



Universidade do Minho
Escola de Engenharia

Débora Sofia dos Santos Ferreira
Spectroscopy systems for the detection of
gastrointestinal dysplasia

Débora Sofia dos Santos Ferreira

Spectroscopy systems for the detection of gastrointestinal dysplasia





Universidade do Minho
Escola de Engenharia

Débora Sofia dos Santos Ferreira

Spectroscopy systems for the detection of gastrointestinal dysplasia

Programa Doutoral em Bioengenharia

Trabalho realizado sob a orientação da

Professora Doutora Graça Minas

e do

Professor Doutor José Higinio Correia

Outubro de 2011

DECLARAÇÃO

Nome

Débora Sofia dos Santos Ferreira

Endereço electrónico: debora@dei.uminho.pt

Telefone: 965104948

Número do Bilhete de Identidade: 12511145

Título dissertação /tese

Spectroscopy systems for the detection of gastrointestinal dysplasia

Orientador(es):

Professora Doutora Graça Minas

Professor Doutor José Higinio Correia

Ano de conclusão: 2011

Designação do Mestrado ou do Ramo de Conhecimento do Doutoramento:

Programa Doutoral em Bioengenharia

É AUTORIZADA A REPRODUÇÃO INTEGRAL DESTA TESE/TRABALHO APENAS PARA EFEITOS DE INVESTIGAÇÃO, MEDIANTE DECLARAÇÃO ESCRITA DO INTERESSADO, QUE A TAL SE COMPROMETE;

Universidade do Minho, 25 de Outubro de 2011

Assinatura: _____

ACKNOWLEDGEMENTS

This Ph.D. thesis represents my most significant professional accomplishment to date. It has required a significant amount of time and effort, but I feel the scientific advancements, together with my professional fulfillment and personal satisfaction, far outweigh the costs. However, none of this would have been possible without the support of my family, colleagues and Professors.

My foremost thank goes to my supervisor, Professor Graça Minas, for her excellent mentorship and support through all phases of my research. Her guidance, incentive, encouragement and availability permitted the important contributions of this thesis.

A grateful thank to my co-supervisor, Professor José Higinio Correia, for his support, discussions and ideas that contributed to the success of this project.

I would also like to thank Professor Michael S. Feld for his valuable advice and support throughout my research at MIT.

A gratifying acknowledgement to Professor Paulo Coutinho and Professor Elisabete Coutinho, from the Physics Department, at University of Minho, for their collaboration and help in spectroscopy experimental measurements. Furthermore, I would like to acknowledge Professor Susana Cardoso, from INESC-MN, for her effort and guidance with the optical filters fabrication.

Many thanks to my colleagues at the GR Harrison Spectroscopy Laboratory, at MIT, for all their support and availability in this project research.

During this incredible journey I had the privilege to have by my side my laboratory colleagues, at the Industrial Electronics Department, who have supported me and have made this a wonderful and fun experience.

Last but not least, I would like to express my gratefulness to my parents, Inácio and Filipa, my sister, Tânia, and my boyfriend, Jorge, for their support, patience, dedication and love. They have provided me important support throughout this amazing challenge, and have been always on my side, even when things didn't always work out. Thank you.

The author, Débora Sofia dos Santos Ferreira, was supported by the Portuguese Foundation for Science and Technology (SFRH/BD/38978/2007). The author would like also to acknowledge the MIT Portugal Program for supporting this work

The detection of gastrointestinal (GI) dysplasia is essential to improve the patient's survival rate. The diagnosis of this condition can be performed using spectroscopy techniques, such as fluorescence and diffuse-reflectance, which have the potential to provide morphological and biochemical information regarding normal and dysplastic tissue.

Research prototypes currently used for those clinical spectroscopy techniques have associated a few drawbacks: they are costly, bulky, too sophisticated and they use optical fibers, which are usually related with low-collection efficiency. Moreover, these catheter-based instruments are invasive and very uncomfortable for the patient.

In this context, the present work had the purpose to develop a miniaturized spectroscopy system, based on those two techniques, that features low-complexity and cost-effectiveness. Furthermore, the integration of optical components in a single chip allows a high level of reliability. Such a system can be integrated in less-invasive devices (e.g., the endoscopic capsules), for an effective and comfortable detection of GI dysplastic lesions.

The developed spectroscopy system core is based on thin-film optical filters and low-cost silicon photodiodes, used for the selection and detection of a few light wavelengths significant for the diagnosis of dysplasia. Thin-film optical filters, centered at specific wavelengths, were designed, fabricated and characterized after the successful demonstration that the use of only 16 spectral bands (within the 350 to 750 nm spectral range) enabled an accurate extraction of tissue information. The feasibility of using the fabricated filters to establish a quantitative spectroscopy diagnosis was proved with measurements on tissue phantoms. Additionally, an even more compact device is proposed for qualitative diagnosis using only two different spectral bands, centered at 420 nm for fluorescence measurements and at 540 nm for diffuse-reflectance measurements. This approach enabled the construction of a diagnostic algorithm for the identification of dysplastic tissues, with a sensitivity and specificity of 77.8% and 97.6%, respectively.

This thesis work was also directed towards the development of a fluorescence and diffuse-reflectance spectroscopy imaging system for excised tissue margins assessment, which results from mucosal resections in the GI tract. In the developed system, wide area imaging is achieved by mechanically scanning an optical probe along the tissue surface, with variable spatial resolution. This medical device can provide real-time feedback regarding the resected mucosal margins, which represents a huge impact in intra-operative diagnosis. The clinical utility of the spectroscopy imaging prototype was successfully demonstrated using

biological samples, i.e., different images containing reliable quantitative tissue information were obtained using analytical models. These images can be subsequently used to establish a diagnosis.

This system may enable the reduction of the patient anxiety, avoiding the follow-up surgery, once a fast and real-time data analysis can be performed inside the operating room.

A detecção de displasia gastrointestinal (GI) é essencial para melhorar a taxa de sobrevivência dos pacientes. O diagnóstico desta condição pode ser efetuado utilizando técnicas de espectroscopia, como a fluorescência e a reflectância difusa, que têm a capacidade de proporcionar informação morfológica e bioquímica acerca dos tecidos normais e dos tecidos com displasia.

Os protótipos, ainda em investigação, actualmente utilizados em espectroscopia clínica e que implementam as técnicas mencionadas, têm associadas várias desvantagens, como por exemplo: têm elevado custo; são demasiado sofisticados e volumosos; e utilizam fibras óticas, que normalmente estão associadas a uma baixa eficiência na recolha de sinal. Para além disso, estes instrumentos baseiam-se em catéteres, o que os torna invasivos e, por isso, desconfortáveis para o paciente.

Neste contexto, o presente trabalho teve como objetivo o desenvolvimento de um sistema baseado nas duas técnicas de espectroscopia acima referidas, que seja simples, de baixo custo e miniaturizado. A integração de componentes óticos num único chip possibilita a obtenção dispositivos óticos mais fiáveis e estáveis. Um sistema com estas características pode ser integrado em dispositivos de diagnóstico menos invasivos (por exemplo, nas cápsulas endoscópicas) para uma detecção eficaz e confortável das lesões displásticas do trato GI.

O elemento principal deste sistema miniaturizado de espectroscopia consiste em filtros óticos baseados em filmes finos e fotodíodos de silício de baixo custo, ambos utilizados para a seleção e detecção de alguns comprimentos de onda importantes para o diagnóstico de displasia. Estes filtros óticos, centrados em comprimentos de onda específicos, foram desenhados, fabricados e caracterizados após ter sido demonstrado que a utilização de apenas 16 bandas espectrais (na gama espectral compreendida entre os 350 e os 750 nm) permitia uma extração correta da informação dos tecidos. A viabilidade de utilizar os filtros fabricados para o estabelecimento de um diagnóstico espectroscópico quantitativo foi também demonstrada com êxito através de medições realizadas em fantomas. Adicionalmente, e tendo em vista o desenvolvimento de um dispositivo ainda mais compacto, foi proposto um diagnóstico qualitativo, ou empírico, utilizando apenas duas bandas espectrais, centradas em 420 nm no caso das medições de fluorescência e em 540 nm no caso das medições de reflectância difusa. Esta abordagem permitiu a construção de um algoritmo de diagnóstico para a identificação de displasia com uma sensibilidade e uma especificidade de 77,8% e de 97,6%, respetivamente.

Desenvolveu-se, igualmente, um sistema espectroscópico de imagem (envolvendo fluorescência e reflectância difusa) para a análise de margens de tecido excisado que resultam de ressecções da mucosa do tracto GI.

Este sistema, através do varrimento mecânico de uma sonda de fibra ótica ao longo da superfície do tecido, com uma resolução espacial variável, possibilita a aquisição de imagens numa vasta área de tecido. Este dispositivo médico pode fornecer uma resposta em tempo real acerca das margens de tecido excisado, o que representa um enorme impacto no diagnóstico intra-operatório. A sua utilidade clínica foi demonstrada, com bons resultados, utilizando amostras biológicas, isto é, foi possível obter imagens contendo informação quantitativa fidedigna acerca dos tecidos, que pode ser subsequentemente utilizada para estabelecer um diagnóstico.

Um sistema como este poderá reduzir a ansiedade dos pacientes e evitar a realização de novas cirurgias, uma vez que logo após a cirurgia, e ainda na sala de operações, pode efectuar-se uma análise aos tecidos.

TABLE OF CONTENTS

1	Introduction.....	1
1.1	Gastrointestinal cancer.....	1
1.1.1	Epidemiology of GI cancer	2
1.1.2	Detection of GI cancer <i>in vivo</i>	4
1.1.3	Detection of GI cancer <i>ex vivo</i>	6
1.2	Optical spectroscopy for GI cancer detection	6
1.3	Motivation and objectives	10
1.4	Organization of the thesis.....	13
	References.....	14
2	Esophagus and Esophageal Cancer.....	19
2.1	Anatomy of the esophagus	19
2.1.1	Macroscopic anatomy.....	19
2.1.2	Microscopic anatomy	20
2.2	Carcinogenesis.....	23
	References.....	26
3	Spectroscopy: Methods and Models.....	29
3.1	Spectroscopy.....	29
3.2	Diffuse-reflectance spectroscopy	31
3.3	Fluorescence spectroscopy	33
3.4	Diffuse-reflectance and fluorescence studies in the esophagus.....	34
3.5	Spectroscopy models.....	36
3.5.1	Diffuse-reflectance spectroscopy	37
3.5.2	Intrinsic fluorescence spectroscopy.....	39
3.6	Spectroscopy models implementation: wavelength reduction study	40
3.6.1	Wavelength reduction analysis.....	41
3.6.2	Wavelength reduction simulations	42
3.6.3	Wavelength reduction measurements using tissue phantoms	48
	References.....	50
4	Miniaturized Spectroscopy System: Components Design and Fabrication	53
4.1	System overview	53
4.2	Thin-film optical filters	56
4.2.1	Basic theory	58

4.2.2	Optical filters design	66
4.2.3	Optical filters simulation results	71
4.2.4	Optical filters fabrication	76
4.2.5	Optical and structural characterization of the filters	83
4.2.6	Optical filters for the near-UV/violet and red regions	87
4.3	Photodiodes and readout electronics	94
	References	98
5	Experimental Results: Optical Filters Ability for Diagnosis.....	101
5.1	Quantitative diagnosis.....	101
5.1.1	Diffuse-reflectance spectroscopy	102
5.1.2	Fluorescence spectroscopy.....	106
5.2	Qualitative diagnosis	109
	References	114
6	Experimental Results: <i>Ex Vivo</i> Spectroscopy System.....	115
6.1	Clinical need.....	115
6.2	System overview	117
6.3	System calibration	119
6.4	Tissue imaging	121
	References	124
7	Conclusions and Future Work	127
7.1	Project overview	127
7.1.1	Miniaturized spectroscopy system	127
7.1.2	<i>Ex vivo</i> spectroscopy system.....	129
7.1.3	Application in endoscopic capsules	129
7.2	Future work	131
	References	132
Annex	Journal Publications	135

LIST OF FIGURES

Figure 1.1:	Distribution of the expected new cases (incidence) and deaths (mortality) for three types of GI cancers in the world, European Union, and Portugal, in 2010 [4].	2
Figure 1.2:	General phases of cancer development [2, 15-17].	4
Figure 1.3:	Spectroscopy results obtained from esophageal tissue using: (a) point spectroscopy (Reprinted from [15, 36], Copyright (2000-2006), with permission from Elsevier); and (b) imaging spectroscopy (Reprinted from [38, 40], Copyright (2005-2006), with permission from Elsevier). In point spectroscopy, the higher intensity lines in the plots (in black) correspond to normal esophageal tissue, whereas the lower intensity lines (in grey) correspond to dysplastic and cancerous tissue sites. In the imaging mode, the left side images were acquired using white-light endoscopy, whereas the right side images were acquired using fluorescence and reflectance imaging spectroscopy. In the right side images, normal mucosa appears as a greenish tone, while dysplastic or cancerous lesions appear as well-contrasted purple or magenta. This way, it is possible to identify lesions that were previously “invisible” in the white-light images.	7
Figure 1.4:	Endoscopic photographs of areas with high-grade neoplasia in BE (no staining and 115× original magnification) viewed using (a) high-resolution endoscopy and (b) NBI. NBI is able to show an irregular, disrupted mucosal pattern and an irregular vascular pattern that can be used to differentiate dysplasia from non-dysplastic tissues. These patterns cannot be well seen using high-resolution white-light endoscopy. Reprinted from [61], Copyright (2006), with permission from Elsevier.	10
Figure 1.5:	(a) Miniaturized system with LEDs as light sources, optical filters and photodiodes for wavelength selection and detection, respectively (not scaled). Data transmission is intended to be wireless. (b) Photograph of the detection system based on an array of silicon photodiodes.	12
Figure 1.6:	(a) Schematic layout and (b) photograph of the ex vivo spectroscopic imaging system.	13
Figure 2.1:	Esophagus: some anatomic considerations. Reprinted by permission from Macmillan Publishers Ltd: GI MOTILITY ONLINE ([5]), Copyright (2006).	20
Figure 2.2:	Stratified squamous epithelium: (a) drawing illustrating the shape and arrangement of cells (BM – basement membrane); (b) H&E ×100 (hematoxylin and eosin stain, 100× original magnification). Reprinted from [7], Copyright (2006), with permission from Elsevier.	21
Figure 2.3:	Structure organization of the esophageal wall: (a) drawing and (b) micrograph illustrating several organizational layers: LM – outer longitudinal layer of muscularis propria; CM – inner circular layer of muscularis propria; G – seromucous gland; MM – muscularis mucosae; SM – submucosa; E – epithelium; Ly – lymphoid aggregates. Reprinted from [7], Copyright (2006), with permission from Elsevier.	22

Figure 2.4:	Transition from normal squamous epithelium to esophageal ADC [3].	25
Figure 2.5:	White-light endoscopic view of BE, showing dysplastic lesions (arrow in the left-side image). Reprinted from [17-18] Copyright (2005-2006), with permission from Elsevier.	25
Figure 3.1:	Examples of different light-tissue interactions: scattering, absorption and fluorescence [5].	30
Figure 3.2:	Molar extinction coefficient spectra of HbO ₂ and Hb. The characteristic peaks of absorption for both forms of hemoglobin are clearly visible [23].	33
Figure 3.3:	Representative diffuse-reflectance spectra for normal (upper line) and dysplastic tissue (bottom line), for (a) the full wavelength range (b) and only 16 wavelengths.	43
Figure 3.4:	Representative intrinsic fluorescence spectra for normal (upper line) and dysplastic tissue (bottom line), for (a) the full wavelength range (b) and only 16 wavelengths.	43
Figure 3.5:	Scatter plots with the (a) reduced scattering coefficient and (b) absorption coefficient, determined for several different wavelengths: 350, 370, 380, 400, 420, 450, 480, 510, 540, 560, 580, 600, 620, 650, 700, and 750 nm. For each of these wavelengths, a different coefficient will be determined in each tissue site: a total of 10 high-grade dysplastic tissue sites and 53 non-dysplastic tissue sites were used, corresponding to 160 (10 times 16) and 848 (53 times 16) different values of reduced scattering and absorption coefficient. Y-axis represents the values of the coefficients extracted with the original spectrum; X-axis represents the values of the coefficients determined with the reconstructed spectrum, using only 16 points. The 45 degree black line represents a perfect agreement between the expected values, from the original spectrum, and the extracted values, from the reconstructed spectrum.	44
Figure 3.6:	Scatter plots with the (a) reduced scattering coefficient and (b) absorption coefficient, determined for several different wavelengths: 350, 370, 380, 400, 420, 450, 480, 510, 540, 560, 580, 600, 620, 650, 700, and 750 nm. Y-axis represents the values of the coefficients extracted with the original spectrum; X-axis represents the values of the coefficients determined with the reconstructed spectrum, using only 10 points.	45
Figure 3.7:	Scatter plots with the tissue parameter values for the six diffuse-reflectance parameters: A_s , B_s , C_s , cHb , α , and $b\vartheta r$, extracted using the full spectrum (expected values) and only 16 wavelengths (extracted values).	46
Figure 3.8:	Scatter plots with the tissue parameter values for two fluorescence parameters: collagen and NAD(P)H, extracted using the full spectrum (expected values) and only 16 wavelengths (extracted values).	47
Figure 3.9:	Reflectance spectra measured from different tissue phantoms (phantom 3: blue line; phantom 4: black line; phantom 5: red line): (a) using the full wavelength range; (b) and only 16 wavelengths. The best fit spectra according to the implemented diffuse-reflectance model are also plotted (dashed lines).	49

Figure 4.1:	Spectroscopy systems. (a) Conventional system with excitation and collection fibers, white-light and UV illumination sources, spectrograph and CCD for detection. (b) Miniaturized system with LEDs as light sources, optical filters and photodetectors for wavelength selection and detection, respectively (not scaled). Data transmission is intended to be wireless.	55
Figure 4.2:	Thin-film multilayer structure [12].	57
Figure 4.3:	Plane wave incident on a thin-film structure [12].	61
Figure 4.4:	Structure with two thin-films and three interfaces (a, b, and c) [12].	64
Figure 4.5:	Structure of a Fabry-Perot filter [12].	67
Figure 4.6:	Schematic diagram of the propagation of light in a Fabry-Perot assembly.	68
Figure 4.7:	Environment setting in the software TFCalc 3.5 for the transmittance simulations of the optical filters.	72
Figure 4.8:	Simulated transmittance spectra for the designed thin-film optical filters, with layer thicknesses indicated in Table 4.1: (a) filters of the near-UV/violet region; (b) filters of the central region of the visible spectrum; (c) filters of the red spectral region.	73
Figure 4.9:	Simulated transmittance spectra for the same thin-film optical filters of Figure 4.8, but with only 7 layers: (a) filters of the near-UV/violet region; (b) filters of the central region of the visible spectrum; (c) filters of the red spectral region.	75
Figure 4.10:	Simulated spectral transmittance for the 540 nm optical filter, with maximum intensity peaks at 540 (regular TiO ₂ thicknesses) and 543 nm (when there is an increase of 1 nm in the thickness of each of the TiO ₂ layers).	76
Figure 4.11:	Geometry of the fully automated deposition system (Nordiko 3000), with a 6-target configuration, allowing sequential deposition of the TiO ₂ /SiO ₂ films. The sample rotates at 15 rpm during deposition, and film thickness uniformity is $\pm 2\%$ over 150 mm diameter area.	77
Figure 4.12:	Assist gun phase space. Triangles indicate the low power beam conditions tested for assisted deposition of TiO ₂ , at 12, 19 and 27 mA. These conditions correspond to a broad and weak beam. The conditions used for ion beam milling (30 mA, +500 V, etch rate $\sim 1 \text{ \AA/s}$) are also shown for comparison.	78
Figure 4.13:	Rutherford Backscattering data obtained at normal incidence, for a 40 nm thick TiO ₂ film deposited on a Si substrate.	78
Figure 4.14:	Comparison between the refractive indices of the <i>Sopra</i> Database and the ones obtained experimentally, for (a) 95 nm thick SiO ₂ and (b) 45 nm thick TiO ₂	79
Figure 4.15:	Simulated spectral transmittance for 6 optical filters in the central region of the visible spectrum.	80
Figure 4.16:	Simulated transmittance spectra for an optical filter with a resonance cavity thickness equal to 164 nm, and with SiO ₂ and TiO ₂ layer thicknesses of 95 and 52 nm, respectively. The two curves are obtained using the refractive indices provided by the <i>Sopra</i> database (n from	

	Sopra database) and the experimental refractive indices (experimental n).....	82
Figure 4.17:	Transmitted peak variation (Δ) as a function of the SiO ₂ resonance cavity thicknesses, when it is used the refractive indices provided by the <i>Sopra</i> database and the experimental refractive indices.	82
Figure 4.18:	Experimental dependence of the SiO ₂ refractive index on the SiO ₂ film thickness.	83
Figure 4.19:	Measured transmittance spectra for the 6 fabricated Fabry-Perot optical filters with the wide band-pass filter included.	83
Figure 4.20:	Comparison between the experimental and the simulated results for 6 optical Fabry-Perot filters: the wavelength of maximum transmittance is shown for each resonance cavity thickness.	84
Figure 4.21:	SEM photograph showing the cross-section of the 560 nm Fabry-Perot optical filter (the designed TiO ₂ and SiO ₂ layer thicknesses were equal to 52 and 95 nm, respectively, while the resonance cavity thickness was equal to 206 nm): (a) magnification 100,000 times; (b) magnification 200,000 times.	85
Figure 4.22:	Surface 3D map of the Fabry-Perot optical filter.	86
Figure 4.23:	AFM image of a thin-film optical filter: (a) 3-D image; (b) 2-D image.	87
Figure 4.24:	Methodology used in the fabrication of the thin-film optical filters.	88
Figure 4.25:	Simulated spectral transmittance for the 400 nm thin-film optical filter, with TiO ₂ and SiO ₂ mirror thicknesses of 36 and 68 nm, respectively, and a resonance cavity with a thickness equal to 136 nm.	89
Figure 4.26:	Experimentally measured spectral transmittance for the 400 nm thin-film optical filter, with TiO ₂ and SiO ₂ mirror thicknesses of 36 and 68 nm, respectively, and a resonance cavity with a thickness equal to 136 nm.	89
Figure 4.27:	Simulated spectral transmittances for the different UV/violet thin-film optical filters using the experimentally measured refractive indices.	90
Figure 4.28:	Comparison between the transmittance obtained using TiO ₂ materials with different refractive indices: “TiO ₂ _n_Sopra” - <i>Sopra</i> database refractive index, and TiO ₂ thickness equal to 30 nm (as in the first simulation, Figure 4.8(a)); “TiO ₂ _n_experimental” - experimentally measured refractive index, and TiO ₂ thickness equal to 36 nm (as in the second simulation, Figure 4.27).	90
Figure 4.29:	Experimentally measured spectral transmittances for the different UV/violet thin-film optical filters with the short-pass filter at 500 nm included in the measurements.	91
Figure 4.30:	Measured transmittance spectra of one violet/blue Fabry-Perot optical filter. The transmittance was measured using a UV-3101PC spectrophotometer. The filter has a maximum intensity peak at 422 nm.....	92
Figure 4.31:	Simulated spectral transmittances for the different thin-film optical filters in the red region using the experimentally measured refractive indices.....	93
Figure 4.32:	Experimentally measured spectral transmittances for the different thin-	

	film optical filters in the red spectral region. The measurements were performed with a high-pass filter at 550 nm on top the thin-film optical filters.	93
Figure 4.33:	Layout of the photodiodes array: (a) <i>n-well/p-epilayer</i> photodiode; (b) <i>n+/p-epilayer</i> photodiode; and (c) <i>p+/n-well</i> photodiode.	96
Figure 4.34:	Simulated spectral transmittance of the 540 nm filter: (a) without the optical effect of the photodiode included; and (b) with the optical effect of the <i>n+/p-epilayer</i> photodiode included.	97
Figure 4.35:	Picture of the fabricated photodiodes array that integrates three types of photodiodes: <i>p+/n-well</i> , <i>n+/p-epilayer</i> , and <i>n-well/p-epilayer</i>	97
Figure 4.36:	Quantum efficiency of the three types of vertical junction photodiodes: (a) <i>n-well/p-epilayer</i> ; (b) <i>n+/p-epilayer</i> ; and (c) <i>p+/n-well</i>	98
Figure 5.1:	Diffuse-reflectance spectra measured with a UV-3101PC spectrophotometer: (a) phantom 1; (b) phantom 2; (c) phantom 3; (d) phantom 4; (e) phantom 5.	103
Figure 5.2:	Diffuse-reflectance spectra measured with the 9 fabricated narrow-band pass optical filters: (a) phantom 1; (b) phantom 2; (c) phantom 3; (d) phantom 4; (e) phantom 5.	104
Figure 5.3:	Original diffuse-reflectance spectra together with the 9 integrated intensity values that will be obtained using the miniaturized spectroscopy system (a trendline was also added to the discrete data points): (a) phantom 1; (b) phantom 2; (c) phantom 3; (d) phantom 4; (e) phantom 5.	105
Figure 5.4:	Comparison, or difference, between the original results (obtained with the UV-3101PC spectrophotometer) and the results obtained using the 9 thin-film optical filters, for the different tissue phantoms.	106
Figure 5.5:	Bulk fluorescence and intrinsic fluorescence (pure furan) measured from two tissue phantoms: (a) phantom with intralipid mass concentration equal to 2%, hemoglobin concentration of 0.25 mg/mL, and furan concentration of 0.25 $\mu\text{g/mL}$; (b) phantom with intralipid mass concentration equal to 2%, hemoglobin concentration of 0.5 mg/mL, and furan concentration of 0.25 $\mu\text{g/mL}$	107
Figure 5.6:	Bulk fluorescence and intrinsic fluorescence (pure furan) measured from two tissue phantoms, together with the two intensity values that would be obtained using the blue optical filter: (a) phantom with intralipid mass concentration equal to 2%, hemoglobin concentration of 0.25 mg/mL, and furan concentration of 0.25 $\mu\text{g/mL}$; (b) phantom with intralipid mass concentration equal to 2%, hemoglobin concentration of 0.5 mg/mL, and furan concentration of 0.25 $\mu\text{g/mL}$	108
Figure 5.7:	Bulk fluorescence spectra and the corresponding intrinsic fluorescence spectra measured from two tissue phantoms: (a) phantom with intralipid mass concentration equal to 2%, hemoglobin concentration of 0.25 mg/mL, and furan concentration of 0.25 $\mu\text{g/mL}$; (b) phantom with intralipid mass concentration equal to 2%, hemoglobin concentration of 0.5 mg/mL, and furan concentration of 0.25 $\mu\text{g/mL}$. The blue spectra in both figures are the fluorescence measured from pure furan in water.	109
Figure 5.8:	Diffuse reflectance (dashed lines) and fluorescence (solid lines) spectra	

	examples. Higher intensity spectra correspond to normal tissue, whereas dysplastic tissue sites exhibit low intensity spectra. For this illustration, reflectance and fluorescence intensity spectra were normalized to their maximum intensity values for a better comparison of their spectral shape (peaks and valleys).....	110
Figure 5.9:	Discrimination of normal from dysplastic tissue sites: (a) ROC curve for the logistic regression algorithm: ROC curve (blue solid line); 45 degree green line (AUC = 0.5). The AUC measures the accuracy of the model to correctly classify normal and diseased tissue. A perfect discrimination is achieved with an AUC value of 1; an AUC value of 0.5 indicates an inability to differentiate the two tissue types. Box plots of the two variables included in the model: (b) fluorescence data from the violet/blue spectral region for the two tissue types; (c) reflectance data from the green spectral region for the two tissue types. Outliers are symbolized by circles.	112
Figure 6.1:	(a) Schematic layout and (b) photographs of the <i>ex vivo</i> quantitative spectroscopy scanning platform; a regular white-light camera is used to take pictures of the samples under analysis.	118
Figure 6.2:	Calibrated reflectance spectra (solid lines) measured on different tissue phantoms. The best fit spectra are also plotted (dashed lines). The characteristic absorption bands of hemoglobin at 420, 540, and 580 nm are clearly visible.	120
Figure 6.3:	Bulk fluorescence spectra (dashed lines) measured on different tissue phantoms. The corresponding intrinsic fluorescence spectra (IFS) are also plotted (solid lines). The blue spectrum is the fluorescence measured from pure furan in water. Note that the calculated IFS spectra, which are independent to the absorbers and scatterers and the raw spectrum of pure furan are well overlapped.	121
Figure 6.4:	White-light picture of the analyzed breast tissue sample with a normal and a malignant area. The dashed square represents the region of interest that will be scanned using the described instrument.	122
Figure 6.5:	Representative QS images of breast tissue taken with the developed spatial high-resolution scanner: a) quantitative map of the scattering parameter A_s (mm^{-1}); b) quantitative map of hemoglobin concentration (mg/dl). Each box represents approximately a 1.2 x 1.2 cm scanning area.	122
Figure 6.6:	Representative QS images of brain cortex taken with the developed spatial high-resolution scanner: (a) total reflectance map (in arbitrary units); (b) quantitative map of the scattering parameter A_s (mm^{-1}); (c) quantitative map of the scattering parameter B_s ; (d) quantitative map of hemoglobin concentration (mg/dl). Each box represents approximately a 1 x 1 cm scanning area.	124
Figure 7.1:	Picture representing the future integration of the miniaturized spectroscopy system in an EC. Example is shown for the collection of diffuse-reflectance data (i.e. illumination using one white LED), and for the integration in a capsule with a single camera. The current capsule CMOS image sensor is represented by the centre black square.....	131

LIST OF TABLES

Table 3.1:	Excitation and emission maxima of some tissue fluorophores.....	34
Table 3.2:	Reflectance parameters extracted from tissue phantoms.....	49
Table 4.1:	Layer thicknesses of the 16 Fabry-Perot optical filters.	71
Table 4.2:	Layer thicknesses of the 6 central Fabry-Perot optical filters.	81
Table 4.3:	Photographs of the 6 fabricated optical filters.	85
Table 5.1:	Tissue phantoms composition and thin-film optical filters used in diffuse-reflectance measurements.....	102
Table 6.1:	Reflectance parameters (A_s , in mm^{-1} , B_s , and cHb in mg/mL) measured from tissue phantoms with different hemoglobin concentrations.....	120
Table 6.2:	Reflectance parameters (A_s , in mm^{-1} , B_s , and cHb in mg/mL) measured from four different tissue sites in the breast tissue sample.....	123

LIST OF SYMBOLS

Symbol	Description	Unit
A_0	Internal reflection at the interface	-
Abs	Absorptance	-
A_s	Parameter A (related to scatterer density)	m^{-1}
B	Magnetic flux density or magnetic induction	T
B_s	Parameter B (related to average scatterer size)	-
$b\vartheta r$	Effective blood vessel radius	m
c	Velocity of light in a vacuum	$m.s^{-1}$
C_{diff}	Correction factor for the vessel packaging effect	-
c_{Hb}	Total concentration of hemoglobin	$mol.L^{-1}$
C_s	Parameter C (related to scattering by small particles)	-
D	Electric displacement	$C.m^{-2}$
d	Physical thickness of the film	m
d_m	Thickness of the mirror layers	m
d_r	Thickness of the resonance cavity	m
d_s	Penetration depth of light in silicon	m
E	Electric field strength	$V.m^{-1}$
F	Function of the Fabry-Perot interferometer	-
f	Frequency	Hz
F_i	Bulk fluorescence	-
f_i	Intrinsic fluorescence	-
g	Anisotropy parameter	-
H	Magnetic field strength	$A.m^{-1}$
h	<i>Plank</i> constant	J.s
H_n	High refractive index	-
I	Photocurrent	A
I_0	Intensity of the incident beam	J.s/m
I_T	Intensity of the transmitted beam	J.s/m
j	Electric current density	$A.m^{-2}$
\mathbf{k}	Wave vector	$rad.m^{-1}$
k	Wavenumber	$rad.m^{-1}$

l	Probe geometry parameter	m
L_n	Low refractive index	-
n	Refractive index	-
n_{air}	Refractive index of air	-
n_{tissue}	Refractive index of tissue	-
OPL	Optical path length	m
P_i	Incident optical power	W
q	Peak order of a Fabry-Perot interferometer	-
q_e	Electron charge	C
R	Reflectance	-
r	Position vector	m
R_0	Diffuse-reflectance in the absence of absorption	-
R_1	Diffuse-reflectance	-
r'_c	Radius of a circular collection spot	m
S	<i>Poynting</i> vector	W.m ⁻²
S_p	Probe geometry constant	-
T	Transmittance	-
t	Time	s
u	Electromagnetic energy density	J.m ⁻³
Y	Optical admittance of a medium or structure	S
α	Oxygen saturation of hemoglobin	-
α_s	Silicon absorption coefficient	m ⁻¹
δ	Phase thickness	rad
ε	Electric permittivity of the medium	F.m ⁻¹
ε_0	Electric permittivity of a vacuum	F.m ⁻¹
ε_1	Extinction coefficient	m ⁻¹ /mol.L ⁻¹
ε_{Hb}	Molar extinction coefficient of the deoxygenated hemoglobin	m ⁻¹ /mol.L ⁻¹
ε_{HbO_2}	Molar extinction coefficient of the oxygenated hemoglobin	m ⁻¹ /mol.L ⁻¹
η	Quantum efficiency	-
θ	Angle	rad
θ_c	Critical angle for total internal reflection	rad
λ	Wavelength	m
λ_0	Reference wavelength	m
λ_m	Emission wavelength	m

λ_x	Excitation wavelength	m
μ	Magnetic permeability of the medium	H.m ⁻¹
μ_0	Magnetic permeability a vacuum	H.m ⁻¹
μ_a	Absorption coefficient	m ⁻¹
μ_a^{blood}	Absorption coefficient of whole blood	m ⁻¹
μ_s	Scattering coefficient	m ⁻¹
μ'_s	Reduced scattering coefficient	m ⁻¹
ν	Velocity of light in a medium	m.s ⁻¹
ρ	Electric charge density	C.m ⁻³
ρ_r	The amplitude reflection coefficient	-
σ	Electric conductivity	S.m ⁻¹
\mathcal{Y}	Optical admittance in a vacuum	S
ϑ	Volume fraction of blood sampled	
ϕ	Phase of the wave	rad
ω	Angular frequency	rad.s ⁻¹

LIST OF TERMS

Term	Designation
ADC	Adenocarcinoma
AFM	Atomic Force Microscope
Ar-O ₂	Argon-Oxygen
AUC	Area Under the Curve
BaSO ₄	Barium Sulfate
BE	Barrett's Esophagus
CCD	Charge-Coupled Device
CMOS	Complementary Metal-Oxide-Semiconductor
DNF	Differential Normalized Fluorescence
DRS	Diffuse-Reflectance Spectroscopy
EC	Endoscopic Capsule
EMR	Endoscopic Mucosal Resection
FS	Fluorescence Spectroscopy
FOV	Field-Of-View
FWHM	Full-Width-Half-Maximum
GERD	Gastroesophageal Reflux Disease
GI	Gastrointestinal
GTG	Grid-To-Grid
HbO ₂	Oxyhemoglobin
Hb	Deoxyhemoglobin
HfO ₂	Hafnium Oxide
HGD	High-Grade Dysplasia
IFS	Intrinsic Fluorescence Spectroscopy
LED	Light-Emitting Diode
LGD	Low-Grade Dysplasia
LVOF	Linear Variable Optical Filter
MIT	Massachusetts Institute of Technology
NAD(P)H	Nicotinamide Adenine Dinucleotide (Phosphate)
NBI	Narrow-Band Imaging
NPV	Negative Predictive Value
PPV	Positive Predictive Value

QS	Quantitative Spectroscopy
ROC	Receiver Operating Characteristic
SCC	Squamous Cell Carcinoma
SEM	Scanning Electron Microscope
Si	Silicon
SiO ₂	Silicon Dioxide
TiO ₂	Titanium Dioxide
UV	Ultraviolet
WHO	World Health Organization
Xe	Xenon

Chapter 1

Introduction

In this Chapter it is presented the epidemiology of gastrointestinal cancers. Current detection methods and its limitations for the detection of gastrointestinal cancer *in vivo* and *ex vivo* are described. The impact of optical spectroscopy techniques for the detection of pre-cancerous lesions, also *in vivo* and *ex vivo*, is then discussed. Finally, the motivation and specific objectives of this project are detailed. The Chapter is concluded with a description of the organization and contents of this thesis.

1.1 Gastrointestinal cancer

According to the World Health Organization (WHO) cancer can be defined as a group of diseases characterized by uncontrolled growth and spread of abnormal cells. When these abnormal cells grow beyond their usual boundaries and spread, cancer can result in death. It is estimated that, worldwide, one in eight deaths is due to cancer, but the global cancer burden is expected to grow. In 2030, 21.4 million new cancer cases are expected to be diagnosed, and

13.2 million cancer related deaths are predicted to occur [1-2].

Cancer occurs mainly due to the exposure of people to carcinogenic agents (in what they eat, drink, inhale, and are exposed at work or in the environment) and biologic factors (virus and bacterial infections), and due to personal habits (alcohol consumption, tobacco smoking, unbalanced diet, physical inactivity), rather than inherited genetic factors. The disease is also associated with social and economic status: risk factors are high in people with least education, and cancer survival is poor in low social classes [2].

Cancers arising in the gastrointestinal (GI) system, including cancers of the oral cavity, esophagus, stomach, colon and rectum, pancreas, and liver, occupy a prominent place in cancer statistics, accounting for significant morbidity and mortality worldwide. As a group, GI malignancies are considered the most common type of human solid cancer worldwide [3]. This section will take an overview of GI cancer, focusing on some of the most common GI cancers in the world: colorectal, stomach, and esophageal cancer [4].

1.1.1 Epidemiology of GI cancer

In 2010, for both sexes and all ages, it was estimated that there were approximately 2.8 million new diagnosed cases of GI cancers and 1.8 million GI cancer deaths in the world (including in the same group colorectal, stomach and esophageal cancers). In Portugal, specifically, for the same year, colorectal cancer was expected to have the highest incidence, with 7,157 new cases diagnosed and 3,813 deaths. Esophageal and stomach cancers occupy, as well, a major place, contributing together for approximately 3 thousand deaths [4]. Figure 1.1 represents the estimated numbers of cancer cases and deaths from these three types of GI cancers in the world, European Union, and Portugal, in 2010.

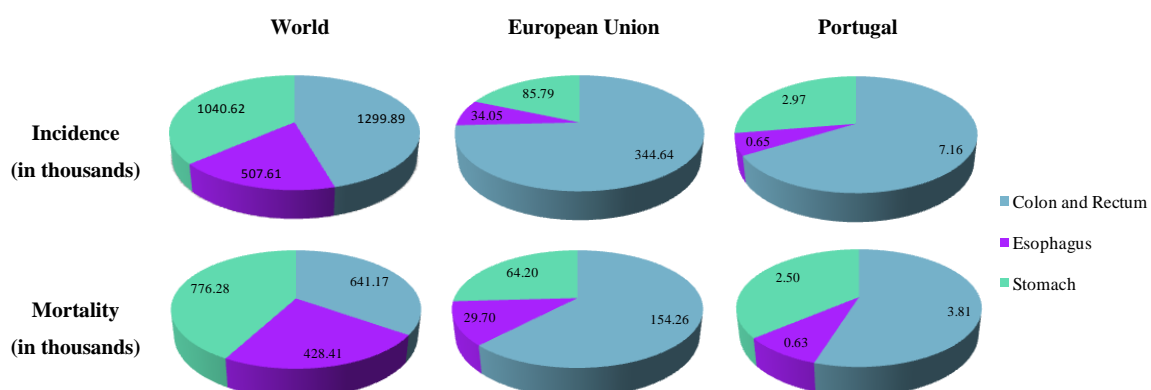


Figure 1.1: Distribution of the expected new cases (incidence) and deaths (mortality) for three types of GI cancers in the world, European Union, and Portugal, in 2010 [4].

Colorectal cancers have high incidence rates in North America, Australia, New Zealand, Japan, and Europe, whereas the lowest rates are verified in Africa and South Central

Asia. Its incidence continues to increase in Asian and Eastern European countries, which may reflect an elevated obesity and smoking prevalence associated with the adoption of western lifestyles. On the other hand, the incidence of colorectal cancers has been decreasing in long-standing economically developed countries, such as the United States. This trend is related to an increased use of screening for the detection and removal of pre-cancerous lesions [1, 3, 5-7]. Risk factors include: personal or family history of colorectal cancer and polyps; personal history of chronic inflammatory bowel disease; obesity and physical inactivity; diet high in red or processed meat; inadequate consumption of fruits and vegetables; alcohol consumption; and, smoking [1, 5-6, 8].

The incidence of stomach cancer varies widely around the world. Still, in general, the highest incidence rates are in Asia and South America, whereas the lowest rates can be found in North America and most parts of Africa. Over the last 50 years, in developed countries of Europe and North America, stomach cancer incidence rates have dropped by more than 80%. This decreasing trend was also verified in Japan (where the rate is still high) and China. An increased consumption of fresh fruits and vegetables, a decreased dependence on salted and preserved foods, a reduction in *Helicobacter pylori* (*H. pylori*) infection, and an increased screening have contributed to this reduction in the number of stomach cancer cases [1, 9-10].

Esophageal cancer incidence varies more around the world than the incidence of any other type of cancer. Still, the highest incidence rates are found in Asia and in East and South Africa [1, 3, 11]. Esophageal cancer can occur in two different ways: squamous-cell carcinoma (SCC), in the middle or upper third of the esophagus; and adenocarcinoma (ADC), in the lower third of the esophagus, or junction of the esophagus and stomach [1, 11]. The incidence of SCC has been increasing in some regions of Asia with a low socio-economic status and nutritional deficiencies, and declining in the United States and other developed countries due to a decrease in the consumption of alcohol and tobacco. In opposition, the incidence of ADC has been increasing in countries such as the United States and England. This trend might be due to an increase in obesity and physical inactivity, chronic gastroesophageal reflux disease (GERD), and Barrett's esophagus (BE), which is a pre-malignant condition that can lead to esophageal cancer [1, 10-12].

As demonstrated in Figure 1.1, the type of GI cancer with the highest incidence rate worldwide and in Portugal, specifically, is colorectal cancer. However, among GI cancers, esophageal cancer is the one with the highest mortality rate. In Portugal, approximately 96% of the patients diagnosed with esophageal cancer die from this disease [4]. In other developed countries the same trend is verified, which emphasizes the high aggressiveness and lethality of this tumor. Also, until the twenty-first century, ADC of the esophagus, in particular, has

increased with a rate of acceleration greater than that of any other cancer (e.g. in the United States it has increased approximately 300% to 500% in the second half of the twentieth century) [11, 13-14]. Therefore, and despite its small incidence numbers, esophageal ADC has become a significant health concern in Western countries due to its increasing incidence and due to the poor prognosis associated with this disease – it remains a deadly tumor [14]. For these reasons, this type of cancer will be the main subject of this thesis in the following Chapters.

1.1.2 Detection of GI cancer *in vivo*

The progress of normal epithelial GI tissues into a malignant tumor involves a series of sequential changes that can be generally divided in five phases: dysplasia; cancer *in situ*; localized invasive tumor; regional lymph node involvement; and distant metastases (Figure 1.2) [2, 15].

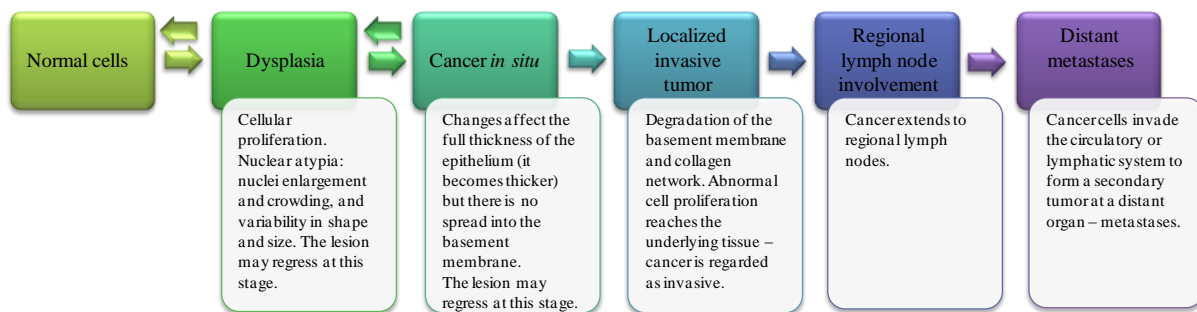


Figure 1.2: General phases of cancer development [2, 15-17].

Cancer survival rates are greatly affected by the phase or stage at which the cancer is diagnosed. The detection of dysplasia is essential for managing GI cancer since the chances of an effective treatment considerably increase if the disease is diagnosed at an early stage, significantly improving the survival rate [16-19]. WHO has estimated that nearly one-third of cancer burden could be decreased if lesions were diagnosed and treated at an early stage. Thus, worldwide, significant healthcare resources are spent each year in screening protocols for an early detection of cancer [16]. However, some types of cancer don't display visible signs and symptoms early in the evolution of the disease (e.g. esophageal cancer) and, therefore, are not amenable to early diagnosis. On the other hand, GI cancer sites with early detection include colon and rectum, and stomach [2].

When colorectal cancer is detected at an early stage the five-year survival rate increases up to 90%. Unfortunately, only 39% of these cancers are diagnosed at its earliest stages, mainly due to underuse of screening. In the case of stomach cancer, it was shown that in the United States survival rates improved from 26% to 63% if the diseased was detected at the dysplastic stage. However, similarly to colorectal cancer, less than 25% of stomach

cancers are diagnosed at an early stage. As previously mentioned, due to the absence of early symptoms, esophageal cancer is usually detected at a late stage, and, as a consequence, most people eventually die from this disease. In the United States the average five-year survival rate is around 18%, whereas in Europe, in average, 11% of patients survive at least five years after diagnosis [1].

Screening for colorectal cancer remains the most important means to reduce morbidity and mortality associated with this type of cancer, and can be performed using several different methods, such as: fecal occult blood testing; flexible sigmoidoscopy; colonoscopy; and, computed tomography colonography. Detailed information about colorectal cancer screening programmes and methods can be found in [1, 3, 6-8, 20-21]. In the majority of countries there are no routine screening tests for stomach cancer. Screening programs, based on upper endoscopy techniques or serum pepsinogen tests, are only available in countries where the incidence of this type of cancer is high (e.g. Japan and Korea) [1, 8, 10, 22]. Similarly, in the esophagus there are no standard screening tests established for the early detection of cancer. Endoscopic screening for SCC may be proposed only for individuals with high consumption of alcohol and tobacco, or with a past history of cancer. For ADC of the esophagus, and despite the increasing incidence and lethality of this cancer, the number of cases remains too small to consider screening [10-11].

After the inspection of visible suspicious tissue sites, an invasive biopsy is usually required to establish a diagnosis. In a biopsy, a few cubic millimeters of tissue from a potentially abnormal site (previously identified by screening techniques or by a physician) are removed for further investigation. Biopsy specimens are then histopathologically evaluated for markers of early cancer: metabolic activity, epithelial thickness, stromal architecture, and nuclear morphology [16-17].

All this detection methodology may be problematic since the majority of early cancerous lesions don't induce visible changes in the tissues, and thus are difficult to detect using the referred standard screening methods: dysplasia is not readily identifiable by direct visual inspection using routine white-light endoscopy techniques. As a consequence, physicians often take a large number of regularly spaced but random biopsies to increase the chances of detecting invisible lesions, which results in sampling errors and high costs associated with the procedure [23].

Moreover, a high number of biopsies and false positive results may lead to unnecessary follow-up procedures and the patient to endure physical and mental discomforts [15, 17, 19, 24-26]. The histopathologic diagnosis and identification of degree of dysplasia is also difficult, as evidenced by low intra- and inter-observer agreement among GI pathologists

[27-29]. Thus, the development and validation of new tools for the detection of dysplasia *in vivo* represents an important priority [15-17].

1.1.3 Detection of GI cancer *ex vivo*

Endoscopic mucosal resection (EMR) has become the treatment of choice for early cancerous lesions of the GI tract, specially the esophagus [30]. Fast and reliable intra-operative diagnosis is critical for the success of these oncological surgeries.

After any cancer tissue resection it has to be ensured that all malignant tissue was removed and for that a surgical pathologist has to examine the tissue margins [31]. Current procedures include visual inspection of the tissue, followed by the assessment of all suspicious sites by frozen sectioning and histological evaluation. This procedure is still not very efficient since, according to a study by the College of American Pathologists [32], a significant number of hospitals do not routinely provide intra-operative feedback to the surgeon within 20 minutes after the tissue is delivered for analyzing. This increases not only the costs but also the risk of morbidity associated with extra time spent by the patient in the operating room. Additionally, frozen section diagnoses are almost always performed on a few “representative” portions of tissue, which may result in discrepancies between the frozen section assessment and the definitive margin status. A definite diagnosis becomes only available once the entire tissue has been processed post-operatively.

A 2005 study suggests that EMR achieves complete excision of dysplastic lesions in only 4% of all cases. This fact implies re-operation for positive surgical margins in a huge percentage of cases, adding significant costs and morbidity to the management of GI cancer [30]. Therefore, there is also a significant technological and clinical need for methods capable of a reliable evaluation of excised tissues in real-time.

1.2 Optical spectroscopy for GI cancer detection

Optical spectroscopy techniques may considerably improve the ability to detect dysplasia. In particular, diffuse-reflectance spectroscopy (DRS) and fluorescence spectroscopy (FS) have been proven to be highly sensitive for the identification of early cancer, by exhibiting different spectral features that can be correlated with normal and cancerous tissue [17, 19, 33]. Such techniques have the ability to reveal biochemical and morphological tissue information that can be used to characterize, in real-time, changes that take place during disease transformation [15, 19]. Diffuse-reflectance and fluorescence signal can be observed and analyzed through spectra (signal plots, usually measured at one specific

tissue point) or images (signal intensity images or maps that are able to cover a wide tissue area). Several studies have successfully applied reflectance and fluorescence point spectroscopy [18, 26, 34-36] and imaging spectroscopy [19, 25, 37-40] for detecting and classifying dysplasia in a variety of GI structures. Figure 1.3 shows some results obtained using point spectroscopy and imaging spectroscopy techniques [15, 36, 38, 40].

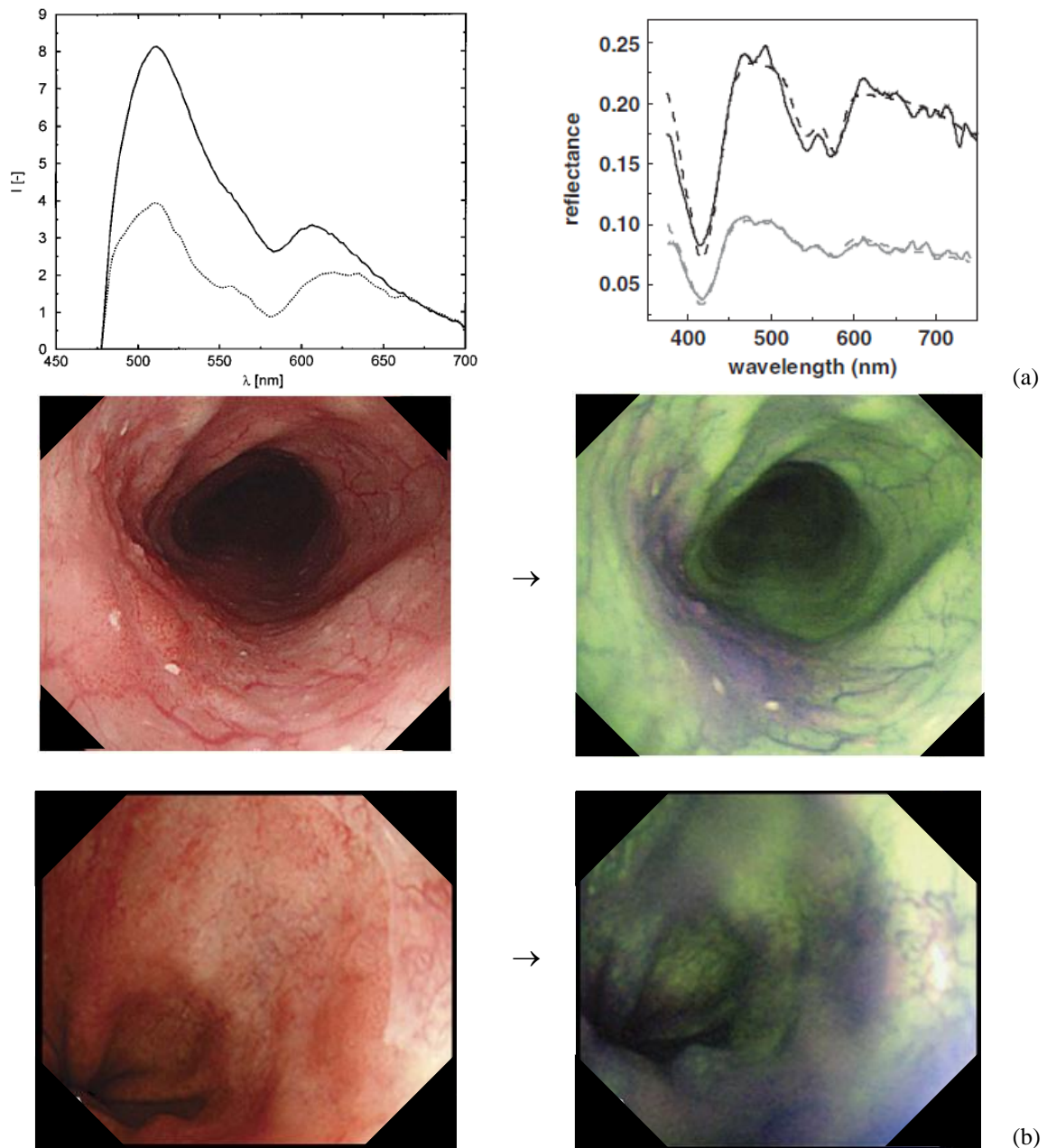


Figure 1.3: Spectroscopy results obtained from esophageal tissue using: (a) point spectroscopy (Reprinted from [15, 36], Copyright (2000-2006), with permission from Elsevier); and (b) imaging spectroscopy (Reprinted from [38, 40], Copyright (2005-2006), with permission from Elsevier). In point spectroscopy, the higher intensity lines in the plots (in black) correspond to normal esophageal tissue, whereas the lower intensity lines (in grey) correspond to dysplastic and cancerous tissue sites. In the imaging mode, the left side images were acquired using white-light endoscopy, whereas the right side images were acquired using fluorescence and reflectance imaging spectroscopy. In the right side images, normal mucosa appears as a greenish tone, while dysplastic or cancerous lesions appear as well-contrasted purple or magenta. This way, it is possible to identify lesions that were previously “invisible” in the white-light images.

Point spectroscopy techniques have the advantage of providing numerical intensity values that enable a quantitative and objective analysis, whereas imaging spectroscopy techniques have the major benefit of allowing an analysis over a wide tissue area. In this last case, the diagnosis is qualitative and based on the visible differences of color. This thesis will focus in point spectroscopy techniques and in the construction of imaging maps using point spectroscopy data.

In DRS, white-light delivered to the tissue is absorbed and multiple scattered by tissue constituents and part of it returns, carrying information about tissue optical properties (scattering, absorption) [15, 41]. Scattering is mainly originated by collagen fibers in connective tissue, whereas absorption is mainly due to hemoglobin [15]. A decrease in tissue scattering and an increase in absorption are generally associated with dysplasia [18-19, 42-44], as will be detailed in Chapter 3.

Epithelial tissues produce fluorescence when excited by ultraviolet (UV) or short-wavelength visible light. This fluorescence is emitted by several fluorophores that are related to the structural arrangement and metabolism of cells. A modification in fluorescence emission may be related to the emergence of pathological conditions [15, 33, 45-46]. Nicotinamide adenine dinucleotide phosphate (NAD(P)H) and collagen are considered fluorescent biomarkers of precancerous changes in epithelial tissues: an increase in NAD(P)H and a decrease in collagen occur with the progression of dysplasia [16, 42]. Also, the fluorescence intensity of dysplastic epithelial tissue is generally lower compared to healthy tissue [42, 47-48], as will be further explained in Chapter 3.

By combining the complementary tissue information provided by diffuse-reflectance and fluorescence, it is achieved a more sensitive and specific diagnosis. These two techniques can be applied for the detection and classification of GI dysplasia using either: a discrimination criteria empirically determined from the acquired spectra (e.g. based on spectra intensity values in different spectral bands); or a model-based approach, which is detailed in Chapter 3, and enables the objective quantification of different tissue morphological and biochemical parameters. These parameters can be subsequently analyzed, using statistical methods, to develop diagnostic algorithms that will be correlated with specific pathological or normal tissue conditions.

Ex vivo imaging strategies using DRS and FS have also been proposed as potential tools for surgical margin assessment of excised specimens [49-51]. Spectral imaging devices for the assessment of excised tissue have two major advantages over traditional practices of surgical margin assessment: real-time analysis in the operating room, with the benefit of reducing patient anxiety and avoid potential follow-up surgery; and, whole area assessment,

with the benefit of reducing the probability of missing an invisible lesion.

Despite all the benefits associated with the use of diffuse-reflectance and fluorescence point spectroscopy techniques for the detection of early cancerous lesions, these are not yet available in commercial instruments. Currently, quantitative tissue diagnosis, using spectroscopy, is only performed with research prototypes. An optically-based endoscopic technique that may improve the early detection of GI cancer and is already commercially available to be used in clinical practice is narrow-band imaging (NBI) [52-55]. This method will be detailed next below.

Detection of early GI cancer using narrow-band imaging

NBI is an optical imaging technique, based on high-resolution endoscopy, which has the ability to enhance the superficial mucosal contrast without the use of staining agents. NBI is based on the optical phenomenon that the depth of light penetration into tissues is dependent on its wavelength. In the visible range, blue light penetrates most superficially (i.e., mucosal imaging) whereas red light penetrates deepest (i.e., submucosal imaging). In NBI, the band-pass ranges of the blue, green, and red components of excitation light are narrowed (blue 400-430 nm, green 530-550 nm, and red 600-620 nm) using optical filters, and the relative intensity of blue light is increased. These bands produce great contrast between microvascular structures and the surrounding mucosa, mainly as a result of the differential optical absorption of light by hemoglobin. Blue light is highly absorbed by hemoglobin enhancing the contrast of superficial mucosal and vascular patterns: structures with high hemoglobin concentration (i.e., blood vessels) absorb the light and thus appear darker, providing contrast to the brighter surrounding mucosa that reflects the light [40, 56-58]. Green light corresponds to another hemoglobin absorption band (less evident than the blue spectral band). While capillaries in the mucosa surface are emphasized by the blue light, deeper submucosal vessels are made visible by the green light [56]. The same way, with red light, deep layers of the mucosa, corresponding to large collecting vessels, can be observed [59].

The use of NBI for the detection of dysplasia in the esophagus has shown that irregular mucosal and vascular patterns, as well as the presence of abnormal blood vessels, are associated with early cancerous lesions [58, 60-61]. NBI techniques also improve the detection of colorectal early cancers [52, 55, 62-63]. In Figure 1.4 it is shown the advantage of using NBI for the visualization of mucosal and vascular patterns, when compared with high-resolution white-light endoscopy [64].

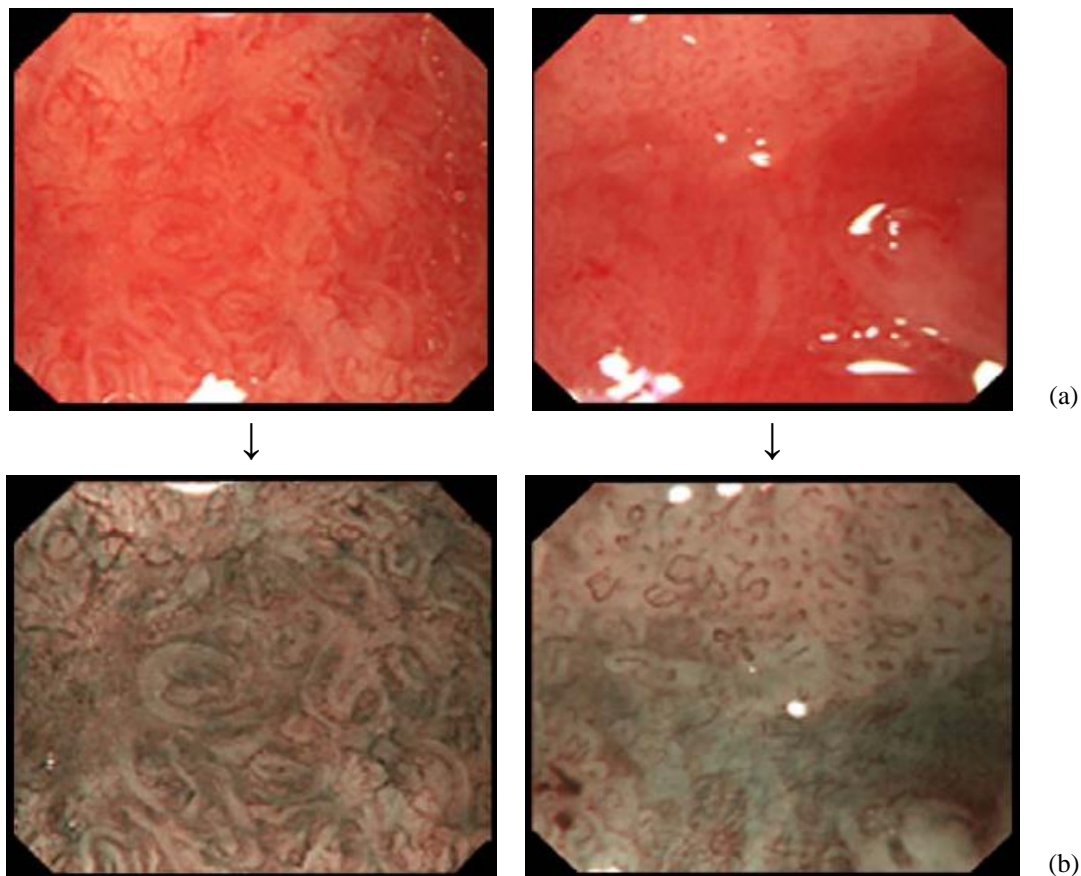


Figure 1.4: Endoscopic photographs of areas with high-grade neoplasia in BE (no staining and 115× original magnification) viewed using (a) high-resolution endoscopy and (b) NBI. NBI is able to show an irregular, disrupted mucosal pattern and an irregular vascular pattern that can be used to differentiate dysplasia from non-dysplastic tissues. These patterns cannot be well seen using high-resolution white-light endoscopy. Reprinted from [61], Copyright (2006), with permission from Elsevier.

However, despite the good results obtained in several clinical studies, NBI is of limited value for primary detection of lesions, being more suitable for targeted detailed inspection of suspected areas. Moreover, this technique relies on improved anatomic resolution and contrast, being considered a surface imaging technique. It requires magnification for optimal use, which is also a limitation [40, 58, 64-65]. This way, the use and further development of detection methods based on functional contrast, with the ability to provide quantitative tissue information, which can also be used as red-flag techniques to identify dysplasia, is of research as well as clinical interest. The optical spectroscopy techniques fulfill these requirements.

1.3 Motivation and objectives

Early cancer detection is a major goal in medicine being the most important factor on which the patient's survival rate depends. Thus, efforts to reduce mortality of GI cancer rely on the detection and complete removal of pre-cancerous or dysplastic lesions [17-19]. These

lesions are usually invisible, and, thus, difficult to identify *in vivo* using standard screening methods, whereas the *ex vivo* identification, after an excision surgery, is difficult to achieve in a timely manner.

DRS and FS have the potential to provide morphological and biochemical information of normal and dysplastic tissue, which can be used to establish a diagnosis. The combination of both techniques should provide a powerful tool for guiding or, ultimately, replacing biopsy during *in vivo* screening for dysplasia, and for *ex vivo*, during surgery, for wide area detection of cancer margins.

In DRS and FS studies performed *in vivo*, costly, bulky, and sophisticated prototypes for data collection are used. These are generally composed by a spectrograph, a high-efficiency detector and optical fibers for light collection from tissues. Such optical set-ups are not portable and compact, which might be cumbersome in the clinical environment. Moreover, regular optical fibers usually have low-collection efficiency, and the placement of the detector at its distal end significantly contributes to light losses. Therefore, the development of a low-complex miniaturized spectroscopy system, without the need of optical fibers, spectrograph, or high-efficiency detectors could potentially increase the collection efficiency, while keeping the same throughput. Additionally, screening techniques using conventional endoscopes have the potential to be replaced by more comfortable and less invasive procedures using small devices, such as the endoscopic capsules (ECs). For that reason, one main goal of this research is the development of a small scale spectroscopy system that can be integrated not only within conventional endoscopes (making them more portable and cost-effective), but also in ECs for the detection of GI dysplastic lesions, adding essential diagnostic functions to current capsule imaging functions. This system is based on light-emitting diodes (LEDs) for illumination, and thin-film optical filters and low-cost silicon photodiodes for the selection and detection of several light wavelengths significant for the diagnosis of GI dysplasia. If successful, the output will be revolutionary in term of diagnostic functions, high-throughput, reduced cost and disposability. Also, the device is envisioned to have a huge clinical impact in early stage cancer management. Figure 1.5 depicts the main components of the miniaturized spectroscopy system.

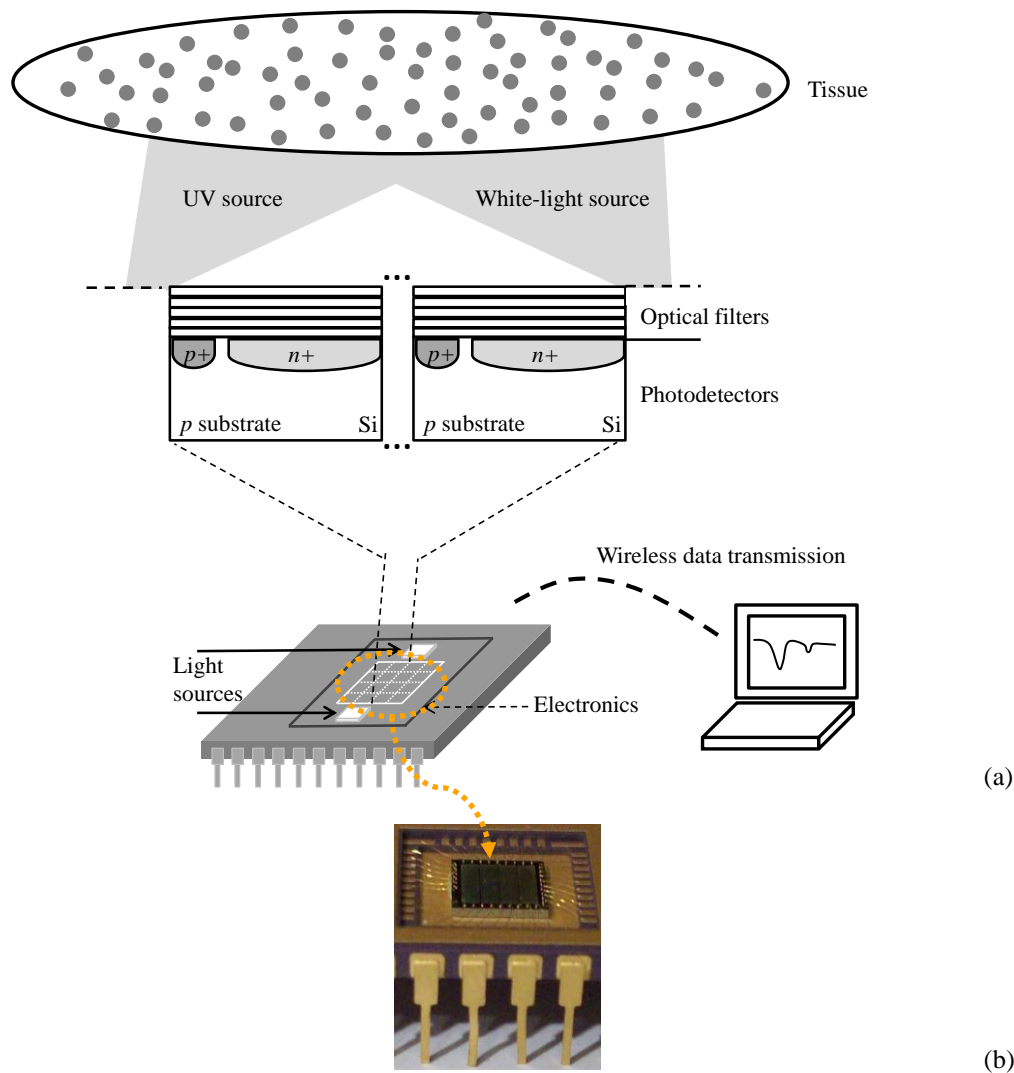


Figure 1.5: (a) Miniaturized system with LEDs as light sources, optical filters and photodiodes for wavelength selection and detection, respectively (not scaled). Data transmission is intended to be wireless. (b) Photograph of the detection system based on an array of silicon photodiodes.

Spectroscopy diagnosis, using current available optical probes, can also be extended to imaging mode, enabling wide area surveillance of tissue. An imaging spectroscopy system can have a significant clinical utility for excised tissue margins assessment by providing structural and biochemical information which correlate to disease state of the tissue. Such a system will be able to reduce patient anxiety and avoid follow-up surgery because a rapid, real-time data analysis can be performed inside the operating room. Moreover, it can reduce the probability of missing a lesion because the whole *ex vivo* tissue area can be assessed. Therefore, this research will also focus on the development of a wide-area *ex vivo* diffuse-reflectance and fluorescence spectroscopy imaging system for comprehensive assessment of surgical margins that result from mucosal resections in the GI tract. In Figure 1.6 the *ex vivo* spectroscopic imaging prototype is presented.

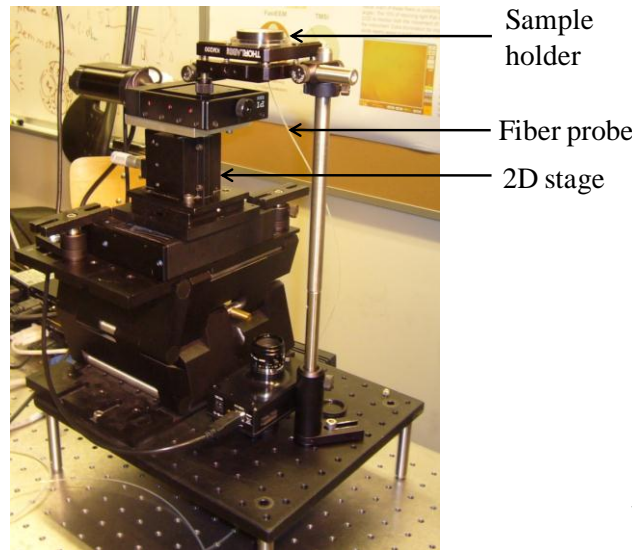
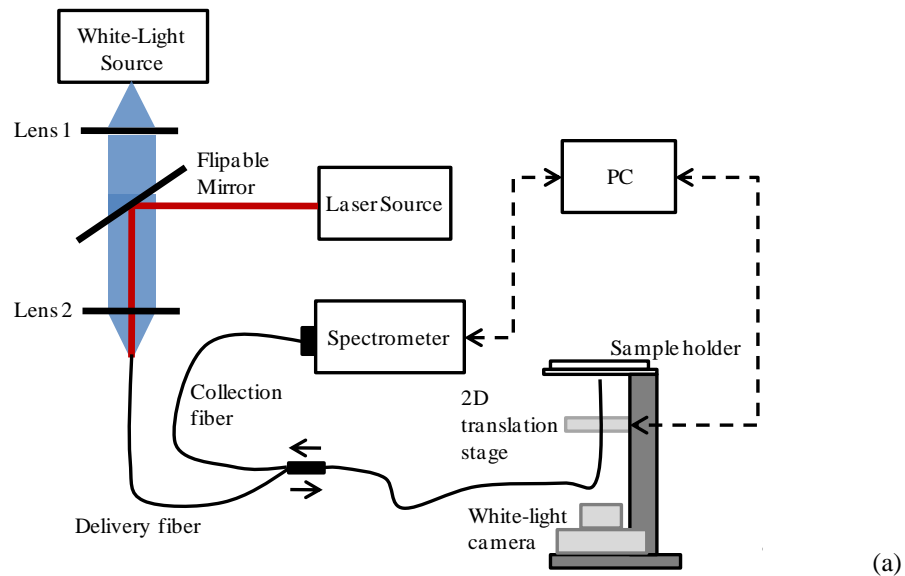


Figure 1.6: (a) Schematic layout and (b) photograph of the *ex vivo* spectroscopic imaging system.

Wide-area imaging of excised tissue is achieved by mechanically scanning an optical probe along the tissue surface, with variable spatial resolution. This medical device can provide real-time feedback regarding the resected mucosal margins, which represents a huge impact in intra-operative diagnosis.

In summary, this thesis research is directed towards two main goals: (1) integration of spectroscopy functions in small and less invasive devices for *in vivo* detection of early cancer in the GI tract; (2) development of an *ex vivo* spectroscopy imaging system for tissue margin assessment in GI oncological surgeries.

1.4 Organization of the thesis

The present Chapter introduces the significance of optical spectroscopy techniques for the detection of early GI cancerous lesions, using both *in vivo* and *ex vivo* methods. The thesis

motivation and objectives are also presented. Chapter 2 generally describes the anatomy of the esophagus and the process involved in the development of esophageal cancer. Some limitations of current esophageal dysplasia detection methods conclude the chapter. Chapter 3 presents the diffuse-reflectance and fluorescence spectroscopy techniques and the corresponding analytical models that are used to extract quantitative tissue information. Chapter 4 deals with the miniaturized spectroscopy system development. The design, fabrication, and characterization of its main components, namely the thin-film optical filters, are also described. Chapter 5 presents the experimental results related to the use of thin-film optical filters for the establishment of a diagnosis, both in a quantitative and qualitative approach. Chapter 6 describes the experimental results obtained with the developed *ex vivo* spectroscopy system for the assessment of excised tissue samples, and discusses the main benefits of this system for oncological surgeries. Finally, conclusions are drawn in Chapter 7 along with some recommendations for future work.

References

- [1] (2011, Accessed June 2011). *Global Cancer Facts & Figures 2nd Edition - American Cancer Society*. Available: <http://www.cancer.org/Research/CancerFactsFigures/GlobalCancerFactsFigures/global-facts-figures-2nd-ed>
- [2] (2002, Accessed June 2011). *National cancer control programmes, policies and managerial guidelines - World Health Organization*. Available: <http://www.who.int/cancer/publications/en/#guidelines>
- [3] J. A. Ajani, P. M. Lynch, and N. A. Janjan, *Gastrointestinal Cancer (M. D. Anderson Cancer Care Series)*, 1st ed. Springer, 2004.
- [4] J. Ferlay, *et al.* (2010, Accessed June 2011). *GLOBOCAN 2008, Cancer Incidence and Mortality Worldwide*. Available: <http://globocan.iarc.fr/>
- [5] M. M. Center, *et al.*, "International Trends in Colorectal Cancer Incidence Rates," *Cancer Epidemiology Biomarkers & Prevention*, vol. 18, pp. 1688-1694, Jun 2009.
- [6] I. Bazensky, *et al.*, "Colorectal cancer: an overview of the epidemiology, risk factors, symptoms, and screening guidelines," *Medsurg Nurs*, vol. 16, pp. 46-51; quiz 52, Feb 2007.
- [7] M. M. Center, *et al.*, "Worldwide variations in colorectal cancer," *CA Cancer J Clin*, vol. 59, pp. 366-78, Nov-Dec 2009.
- [8] S. M. Mahon, "Prevention and screening of gastrointestinal cancers," *Semin Oncol Nurs*, vol. 25, pp. 15-31, Feb 2009.
- [9] P. Bertuccio, *et al.*, "Recent patterns in gastric cancer: a global overview," *Int J Cancer*, vol. 125, pp. 666-73, Aug 2009.
- [10] R. Lambert and P. Hainaut, "Epidemiology of oesophagogastric cancer," *Best Practice & Research in Clinical Gastroenterology*, vol. 21, pp. 921-945, 2007.
- [11] C. J. Lightdale, "Esophageal cancer. American College of Gastroenterology," *Am J Gastroenterol*, vol. 94, pp. 20-9, Jan 1999.
- [12] C. Bosetti, *et al.*, "Trends in oesophageal cancer incidence and mortality in Europe," *International Journal of Cancer*, vol. 122, pp. 1118-1129, Mar 2008.
- [13] H. Pohl, *et al.*, "Esophageal Adenocarcinoma Incidence: Are We Reaching the Peak?,"

- Cancer Epidemiology Biomarkers & Prevention*, vol. 19, pp. 1468-1470, Jun 2010.
- [14] N. J. Shaheen, "Advances in Barrett's esophagus and esophageal adenocarcinoma," *Gastroenterology*, vol. 128, pp. 1554-66, May 2005.
- [15] I. Georgakoudi, "The color of cancer," *Journal of Luminescence* vol. 119-120, pp. 75-83, 2006.
- [16] K. Badizadegan, *et al.*, "Spectroscopic diagnosis and imaging of invisible pre-cancer," *Faraday Discussions*, vol. 126, pp. 265-279, 2004.
- [17] J. W. Tunnell, *et al.*, "Instrumentation for multi-modal spectroscopic diagnosis of epithelial dysplasia," *Technol Cancer Res Treat*, vol. 2, pp. 505-14, Dec 2003.
- [18] I. Georgakoudi, *et al.*, "Fluorescence, reflectance, and light-scattering spectroscopy for evaluating dysplasia in patients with Barrett's esophagus," *Gastroenterology*, vol. 120, pp. 1620-9, Jun 2001.
- [19] C. C. Yu, *et al.*, "Quantitative spectroscopic imaging for non-invasive early cancer detection," *Optics Express*, vol. 16, pp. 16227-39, Sep 2008.
- [20] R. E. Davila, *et al.*, "ASGE guideline: colorectal cancer screening and surveillance," *Gastrointest Endosc*, vol. 63, pp. 546-57, Apr 2006.
- [21] R. A. Smith, *et al.*, "Cancer screening in the United States, 2009: a review of current American Cancer Society guidelines and issues in cancer screening," *CA Cancer J Clin*, vol. 59, pp. 27-41, Jan-Feb 2009.
- [22] K. G. Yeoh, "How do we improve outcomes for gastric cancer?," *Journal of Gastroenterology and Hepatology*, vol. 22, pp. 970-972, Jul 2007.
- [23] L. B. Lovat, *et al.*, "Elastic scattering spectroscopy accurately detects high grade dysplasia and cancer in Barrett's oesophagus," *Gut*, vol. 55, pp. 1078-83, Aug 2006.
- [24] A. M. Rollins and M. V. Sivak, Jr., "Potential new endoscopic techniques for the earlier diagnosis of pre-malignancy," *Best Pract Res Clin Gastroenterol*, vol. 15, pp. 227-47, Apr 2001.
- [25] J. Haringsma, *et al.*, "Autofluorescence endoscopy: feasibility of detection of GI neoplasms unapparent to white light endoscopy with an evolving technology," *Gastrointest Endosc*, vol. 53, pp. 642-50, May 2001.
- [26] L. M. Wong Kee Song, "Optical spectroscopy for the detection of dysplasia in Barrett's esophagus," *Clin Gastroenterol Hepatol*, vol. 3, pp. S2-7, Jul 2005.
- [27] H. Yoon, *et al.*, "Inter-observer agreement on histological diagnosis of colorectal polyps: the APACC study," *Gastroenterol Clin Biol*, vol. 26, pp. 220-4, Mar 2002.
- [28] R. E. Petras, *et al.*, "Barrett's esophagus. A review of the pathologist's role in diagnosis and management," *Pathol Annu*, vol. 26, pp. 1-32, 1991.
- [29] B. J. Reid, *et al.*, "Observer variation in the diagnosis of dysplasia in Barrett's esophagus," *Hum Pathol*, vol. 19, pp. 166-78, Feb 1988.
- [30] M. Mino-Kenudson, *et al.*, "Management of superficial Barrett's epithelium-related neoplasms by endoscopic mucosal resection: clinicopathologic analysis of 27 cases," *Am J Surg Pathol*, vol. 29, pp. 680-6, May 2005.
- [31] A. S. Haka, *et al.*, "In vivo margin assessment during partial mastectomy breast surgery using Raman spectroscopy," *Cancer Research*, vol. 66, pp. 3317-3322, Mar 2006.
- [32] D. A. Novis and R. J. Zarbo, "Interinstitutional comparison of frozen section turnaround time - A College of American Pathologists Q-probes study of 32,868 frozen sections in 700 hospitals," *Archives of Pathology & Laboratory Medicine*, vol. 121, pp. 559-567, Jun 1997.
- [33] J. Haringsma and G. N. Tytgat, "Fluorescence and autofluorescence," *Baillieres Best Pract Res Clin Gastroenterol*, vol. 13, pp. 1-10, Apr 1999.
- [34] T. Vo-Dinh, *et al.*, "Laser-induced fluorescence for esophageal cancer and dysplasia diagnosis," *Ann N Y Acad Sci*, vol. 838, pp. 116-22, Feb 1998.
- [35] G. Bourg-Heckly, *et al.*, "Endoscopic ultraviolet-induced autofluorescence

- spectroscopy of the esophagus: tissue characterization and potential for early cancer diagnosis," *Endoscopy*, vol. 32, pp. 756-65, Oct 2000.
- [36] B. Mayinger, *et al.*, "Light-induced autofluorescence spectroscopy for tissue diagnosis of GI lesions," *Gastrointest Endosc*, vol. 52, pp. 395-400, Sep 2000.
- [37] M. A. Kara, *et al.*, "Endoscopic video autofluorescence imaging may improve the detection of early neoplasia in patients with Barrett's esophagus," *Gastrointest Endosc*, vol. 61, pp. 679-85, May 2005.
- [38] N. Uedo, *et al.*, "A novel videoendoscopy system by using autofluorescence and reflectance imaging for diagnosis of esophagogastric cancers," *Gastrointest Endosc*, vol. 62, pp. 521-8, Oct 2005.
- [39] T. D. Wang, *et al.*, "In vivo identification of colonic dysplasia using fluorescence endoscopic imaging," *Gastrointest Endosc*, vol. 49, pp. 447-55, Apr 1999.
- [40] M. A. Kara, *et al.*, "Endoscopic video-autofluorescence imaging followed by narrow band imaging for detecting early neoplasia in Barrett's esophagus," *Gastrointest Endosc*, vol. 64, pp. 176-85, Aug 2006.
- [41] G. Zonios, *et al.*, "Diffuse reflectance spectroscopy of human adenomatous colon polyps in vivo," *Appl Opt*, vol. 38, pp. 6628-37, Nov 1999.
- [42] I. Georgakoudi, *et al.*, "NAD(P)H and collagen as in vivo quantitative fluorescent biomarkers of epithelial precancerous changes," *Cancer Res*, vol. 62, pp. 682-7, Feb 2002.
- [43] Y. A. DeClerck, "Interactions between tumour cells and stromal cells and proteolytic modification of the extracellular matrix by metalloproteinases in cancer," *European Journal of Cancer*, vol. 36, pp. 1258-1268, Jun 2000.
- [44] A. Couvelard, *et al.*, "Angiogenesis in the neoplastic sequence of Barrett's oesophagus. Correlation with VEGF expression," *J Pathol*, vol. 192, pp. 14-8, Sep 2000.
- [45] N. Ramanujam, "Fluorescence spectroscopy of neoplastic and non-neoplastic tissues," *Neoplasia*, vol. 2, pp. 89-117, Jan-Apr 2000.
- [46] R. S. Dacosta, *et al.*, "Spectroscopy and fluorescence in esophageal diseases," *Best Pract Res Clin Gastroenterol*, vol. 20, pp. 41-57, Feb 2006.
- [47] B. Mayinger, *et al.*, "Light-induced autofluorescence spectroscopy for the endoscopic detection of esophageal cancer," *Gastrointest Endosc*, vol. 54, pp. 195-201, Aug 2001.
- [48] D. C. De Veld, *et al.*, "The status of in vivo autofluorescence spectroscopy and imaging for oral oncology," *Oral Oncol*, vol. 41, pp. 117-31, Feb 2005.
- [49] M. D. Keller, *et al.*, "Autofluorescence and diffuse reflectance spectroscopy and spectral imaging for breast surgical margin analysis," *Lasers Surg Med*, vol. 42, pp. 15-23, Jan 2010.
- [50] V. Krishnaswamy, *et al.*, "Quantitative imaging of scattering changes associated with epithelial proliferation, necrosis, and fibrosis in tumors using microsampling reflectance spectroscopy," *J Biomed Opt*, vol. 14, p. 014004, Jan-Feb 2009.
- [51] N. Ramanujam, *et al.*, "Quantitative spectral reflectance imaging device for intraoperative breast tumor margin assessment," *Conf Proc IEEE Eng Med Biol Soc*, vol. 2009, pp. 6554-6, 2009.
- [52] H. M. Chiu, *et al.*, "A prospective comparative study of narrow-band imaging, chromoendoscopy, and conventional colonoscopy in the diagnosis of colorectal neoplasia," *Gut*, vol. 56, pp. 373-9, Mar 2007.
- [53] E. Dekker, *et al.*, "Narrow-band imaging compared with conventional colonoscopy for the detection of dysplasia in patients with longstanding ulcerative colitis," *Endoscopy*, vol. 39, pp. 216-21, Mar 2007.
- [54] J. E. East, *et al.*, "Narrow band imaging with magnification for dysplasia detection and pit pattern assessment in ulcerative colitis surveillance: a case with multiple dysplasia associated lesions or masses," *Gut*, vol. 55, pp. 1432-5, Oct 2006.
- [55] A. Katagiri, *et al.*, "Narrow band imaging with magnifying colonoscopy as diagnostic

- tool for predicting histology of early colorectal neoplasia," *Aliment Pharmacol Ther*, vol. 27, pp. 1269-74, Jun 2008.
- [56] L. M. Song, *et al.*, "Narrow band imaging and multiband imaging," *Gastrointest Endosc*, vol. 67, pp. 581-9, Apr 2008.
- [57] R. S. DaCosta, *et al.*, "Optical techniques for the endoscopic detection of dysplastic colonic lesions," *Curr Opin Gastroenterol*, vol. 21, pp. 70-9, Jan 2005.
- [58] M. A. Kara, *et al.*, "High-resolution endoscopy plus chromoendoscopy or narrow-band imaging in Barrett's esophagus: a prospective randomized crossover study," *Endoscopy*, vol. 37, pp. 929-36, Oct 2005.
- [59] K. Kuznetsov, *et al.*, "Narrow-band imaging: potential and limitations," *Endoscopy*, vol. 38, pp. 76-81, Jan 2006.
- [60] H. C. Wolfsen, *et al.*, "Prospective, controlled tandem endoscopy study of narrow band imaging for dysplasia detection in Barrett's Esophagus," *Gastroenterology*, vol. 135, pp. 24-31, Jul 2008.
- [61] M. A. Kara, *et al.*, "Detection and classification of the mucosal and vascular patterns (mucosal morphology) in Barrett's esophagus by using narrow band imaging," *Gastrointest Endosc*, vol. 64, pp. 155-66, Aug 2006.
- [62] H. Machida, *et al.*, "Narrow-band imaging in the diagnosis of colorectal mucosal lesions: a pilot study," *Endoscopy*, vol. 36, pp. 1094-8, Dec 2004.
- [63] T. Matsumoto, *et al.*, "Magnifying colonoscopy with narrow band imaging system for the diagnosis of dysplasia in ulcerative colitis: a pilot study," *Gastrointest Endosc*, vol. 66, pp. 957-65, Nov 2007.
- [64] M. A. Kara and J. J. Bergman, "Autofluorescence imaging and narrow-band imaging for the detection of early neoplasia in patients with Barrett's esophagus," *Endoscopy*, vol. 38, pp. 627-31, Jun 2006.
- [65] A. M. Buchner and M. B. Wallace, "Future expectations in digestive endoscopy: competition with other novel imaging techniques," *Best Pract Res Clin Gastroenterol*, vol. 22, pp. 971-87, 2008.

Chapter 2

Esophagus and Esophageal Cancer

In this Chapter it is presented an overview of the macroscopic and microscopic anatomy of the gastrointestinal organ studied in this thesis - the esophagus. The process of esophageal cancer development and the limitations of current dysplasia detection methods conclude this Chapter.

2.1 Anatomy of the esophagus

2.1.1 Macroscopic anatomy

The normal esophagus is a flexible, hollow, muscular tube, with approximately 18 to 22 cm long and an average diameter of 2 cm, that connects the pharynx, in the neck, to the stomach, in the abdomen (Figure 2.1). The esophagus wall is composed of striated muscle in its upper third, smooth muscle in its lower third, and a mixture of striated and smooth muscle in between [1-4]. The pressure in the esophageal lumen is negative compared with the atmosphere. Still, manometric recordings have identified two high-pressure zones that prevent

the backflow of food: the upper and lower esophageal sphincters. These functional zones are located at the upper and lower ends of the esophagus but they are considered physiologic in that there is not a clear anatomic landmark that delineates their limits [3-4].

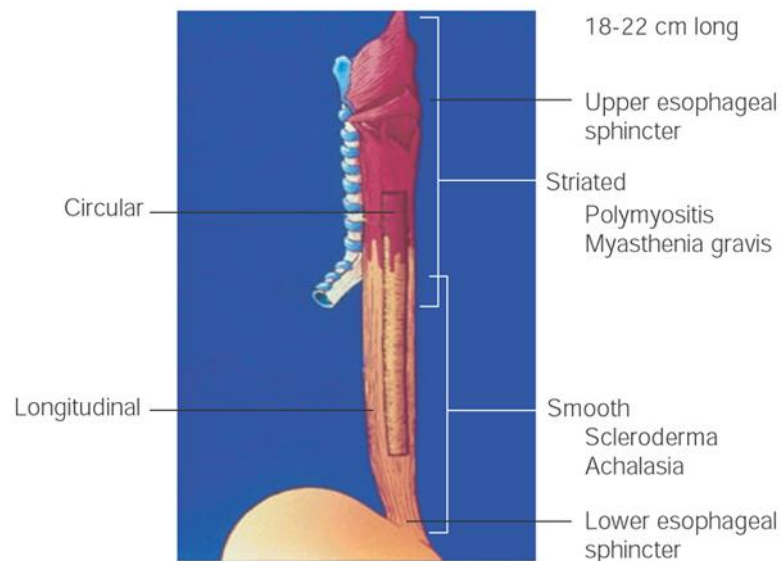


Figure 2.1: Esophagus: some anatomic considerations. Reprinted by permission from Macmillan Publishers Ltd: GI MOTILITY ONLINE ([5]), Copyright (2006).

The main function of the esophagus is to conduct food and fluids from the pharynx toward the stomach: food passes through the esophagus rapidly because of the peristaltic contractions of its musculature, aided by but not dependent on gravity; also, mucus produced by the esophageal mucosa provides lubrication, facilitating the passage of food. In addition, the esophagus prevents passive diffusion of substances from the food into the blood and reflux of gastric contents. These functions require motor activity coordinated with swallowing, namely a wave of peristaltic contraction, relaxation of the lower esophageal sphincter in anticipation of the peristaltic wave, and closure of the lower esophageal sphincter after the swallowing reflex. Maintenance of sphincter tone is necessary to prevent reflux of gastric contents [1, 3-4].

2.1.2 Microscopic anatomy

Epithelial tissue lines the interior of the GI tract. Epithelium consists of closely packed sheets comprising one or more layers of cells that are responsible by several important activities, such as: protection, sensory reception, and the secretion, absorption and transport of molecules [6].

Epithelial cells are bound to adjacent cells by intercellular junctions that provide physical strength and mediate exchange of information and metabolites. All epithelia are supported by a basement membrane that links the epithelial cells to the underlying connective

tissue. Epithelial cells have some degree of polarity with one side facing the basement membrane and underlying supporting tissue (the basal surface) and the other facing outwards (the apical surface) [6-7].

The lining epithelia can be morphologically classified according to: the number of cell layers, the shape of component cells, and the specialization of the apical surface. There are seven categories of epithelia: simple squamous; simple cuboidal; simple columnar; stratified squamous; stratified columnar; pseudostratified columnar; and transitional epithelium. The type of epithelium that lines the inner surface of the esophagus is stratified squamous epithelium (Figure 2.2) [7].

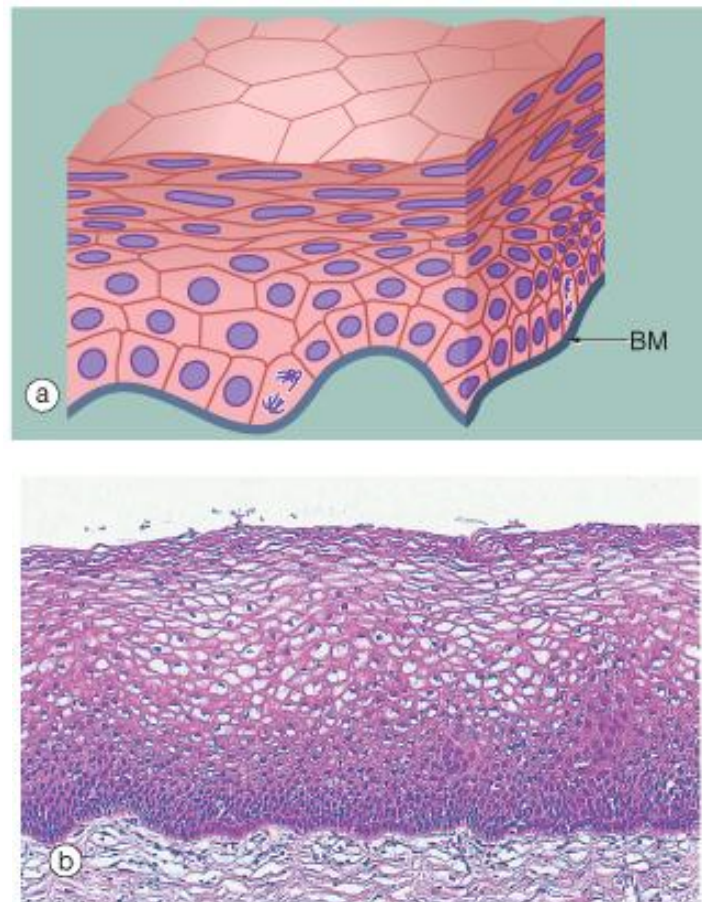
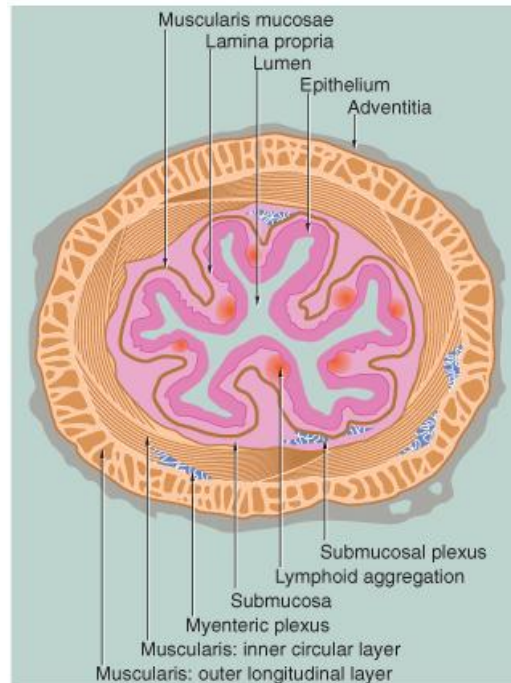


Figure 2.2: Stratified squamous epithelium: (a) drawing illustrating the shape and arrangement of cells (BM – basement membrane); (b) H&E $\times 100$ (hematoxylin and eosin stain, 100 \times original magnification). Reprinted from [7], Copyright (2006), with permission from Elsevier.

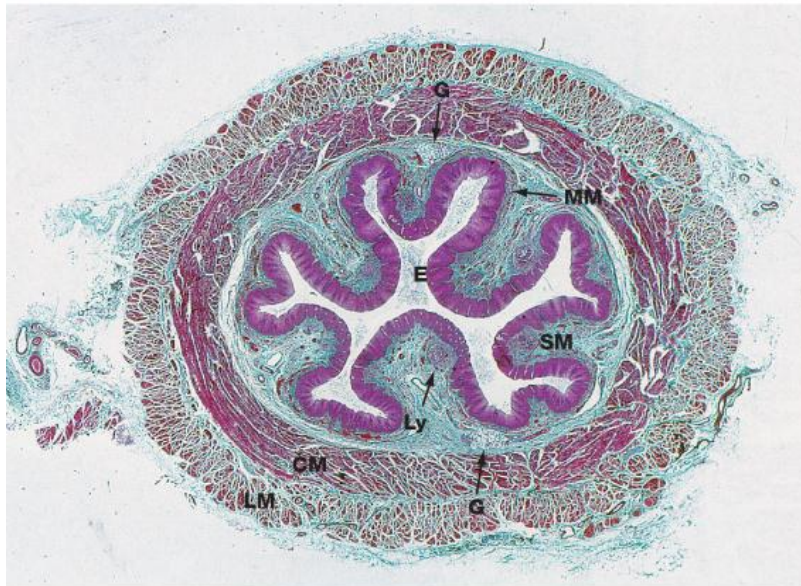
Stratified epithelia are defined as epithelia consisting of two or more layers of cells. Stratified squamous epithelium consists of a variable number of cell layers that mature from a cuboidal basal layer adherent to the underlying basement membrane to a flattened surface layer. The cells resting on the basement membrane typically have a rounded appearance. As the cells move toward the surface, they become increasingly squamous in appearance [7].

Structurally, the wall of the esophagus consists of four organizational layers of cells:

mucosa, submucosa, muscularis propria, and adventitia (Figure 2.3). This structure reflects the general organization of the GI tract, with the exception that the esophagus doesn't have a true serosal outer layer, being covered, instead, by a thin layer of connective tissue [3-5]. The inexistence of a serosal covering allows esophageal infections and tumors to widespread more easily and makes them harder to treat surgically [3-4].



(a)



(b)

Figure 2.3: Structure organization of the esophageal wall: (a) drawing and (b) micrograph illustrating several organizational layers: LM – outer longitudinal layer of muscularis propria; CM – inner circular layer of muscularis propria; G – seromucous gland; MM – muscularis mucosae; SM – submucosa; E – epithelium; Ly – lymphoid aggregates. Reprinted from [7], Copyright (2006), with permission from Elsevier.

The *mucosa* has a smooth, glistening, and reddish surface, being arranged in longitudinal folds that disappear upon distention. It consists of three sub-layers: a nonkeratinizing stratified squamous epithelial layer; lamina propria; and, muscularis mucosae.

The epithelial layer covers almost the entire inner surface of the esophagus, and has mature squamous cells overlying basal cells. The lamina propria is a thin layer of loose connective tissue (corresponding to the non-epithelial portion of the mucosa) above the muscularis mucosae; it is mainly composed by collagen produced by fibroblasts. The muscularis mucosae is a 2 to 3 cell thick layer of longitudinally oriented smooth-muscle bundles that provide support for the lamina propria and the epithelium [3-4, 6].

The *submucosa* consists of a thick layer of supportive connective tissue containing a vascular network, lymphatics, nerve fibers, ganglia, adipose tissue, and submucosal glands [3 - 4, 6].

The *muscularis propria* is responsible for motor function. As mentioned, the upper 5% to 33% of the esophagus is composed of striated (skeletal) muscle fibers, and the distal 33% is composed of smooth muscle. The layers of smooth muscle have different orientations: the inner layer has a circular orientation, whereas the outer layer has a longitudinal orientation [3 - 4, 6].

The *adventitia* is an external fibrous layer that covers the esophagus, being composed by connective tissue, small vessels, lymphatic channels, and nerve fibers [4, 6].

2.2 Carcinogenesis

A *neoplasm*, or *tumor*, can be defined as an abnormal mass of tissue with an uncontrolled and uncoordinated growth, compared with that of normal tissues. *Carcinogenesis* is a multistep process by which normal cells progressively transform into a malignant phenotype, which is characterized by excessive growth, invasiveness, and the ability to form distant metastases [3].

All malignant tumors are commonly known as *cancers*. Cancers of epithelial origin are called *carcinomas*, which may be further classified into *adenocarcinoma* - ADC (when there is glandular growth pattern) and *squamous-cell carcinoma* - SCC (when recognizable squamous cells are produced) [3].

The majority of esophageal ADCs develop in patients with BE, who have an increased risk of developing the disease when compared with the general population. It is estimated that 10 to 40% of esophageal ADCs are linked with BE. This premalignant condition is recognized, nowadays, as the major risk factor for the development of ADC in the lower esophagus [8-13].

Barrett's Esophagus

BE is a complication of long-standing GERD. The reflux of gastric contents into the

esophagus, due to a functional problem in the lower esophageal sphincter, the presence of a hiatal hernia, or a delayed gastric emptying, is the first cause of esophagitis [3, 14]. Reflux esophagitis is characterized by the development of esophageal mucosa injury, with subsequent inflammation, because of the acid-peptic action of gastric juices. BE appears as the most harmful complication of severe esophagitis, but bleeding and the development of stricture may also appear as a consequence. However, it is important to notice that some subjects with severe recurrent esophagitis never develop BE, whereas others with relatively few symptoms and little or no inflammation develop the disease [3, 14].

BE can be defined as a pathological condition in which the distal normal stratified squamous epithelium is replaced by metaplastic columnar epithelium, as a response to prolonged injury (due to an abnormal acidic milieu created by GERD). The replacement of one cell type by another is a process known as *metaplasia*. The pathogenesis of BE is not clear; still, it has been proposed that esophagitis is followed by ingrowth of pluripotent stem cells, that will then differentiate into a columnar epithelium, more resistant to acid-peptic injury [3, 14]. This layer of columnar epithelium is a single-cell layer, whereas in a clinically normal situation the esophageal epithelium is made up of several layers of squamous cells. For this reason, there is a reduction in thickness that makes the underlying blood vessels more visible, giving a reddish appearance to metaplasia [15].

Critical to the pathologic evaluation of patients with BE is the search for dysplasia, which is the precursor lesion of malignancy. BE develops through stages from non-dysplastic metaplasia, followed by increasing grades of dysplasia, and finally ADC [3, 13-14, 16]. The risk of developing ADC increases as the severity of the dysplasia increases.

Dysplasia, which literally means disordered growth, is defined histologically as a neoplastic alteration of the epithelium that does not invade the lamina propria. It is recognized by the presence of cytologic and architectural abnormalities, such as: variation in size and shape of cells (pleomorphism); enlarged, crowded, and stratified hyperchromatic nuclei; neovascularization; and, loss of architectural orientation. It can be classified as high-grade or low-grade [3, 14, 16]. The risk of ADC in low-grade is not well defined, but it was already shown that it is smaller than in high-grade. The lesion is referred to as *cancer in situ* when these changes affect the full thickness of the epithelium [3, 14, 16].

The typical progress from normal squamous epithelium to esophageal ADC is illustrated in Figure 2.4 [3].

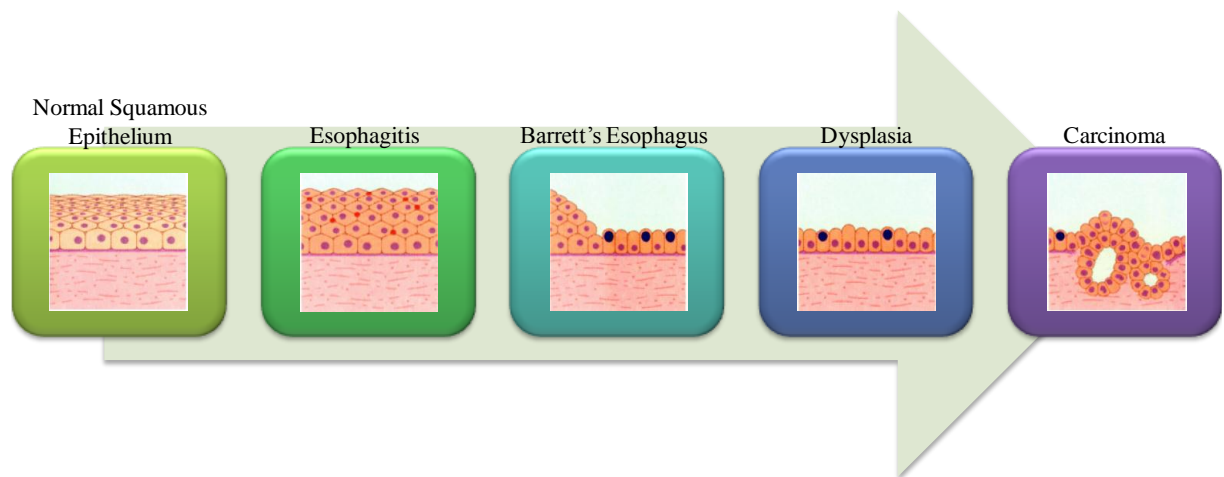


Figure 2.4: Transition from normal squamous epithelium to esophageal ADC [3].

Epithelial dysplasia almost always precedes the appearance of cancer (still, it is important to notice that not all dysplastic lesions necessarily progress to cancer) [3]. The malignant potential of dysplastic cells makes the detection of dysplasia a crucial step in cancer prevention. Unfortunately, and as referred in Chapter 1, the detection of dysplasia is difficult in clinical practice. Figure 2.5 illustrates two images of BE with suspicious dysplastic areas. As the images show, it is hard to detect the dysplastic lesions in a BE mucosa with standard white-light endoscopy [17-18].

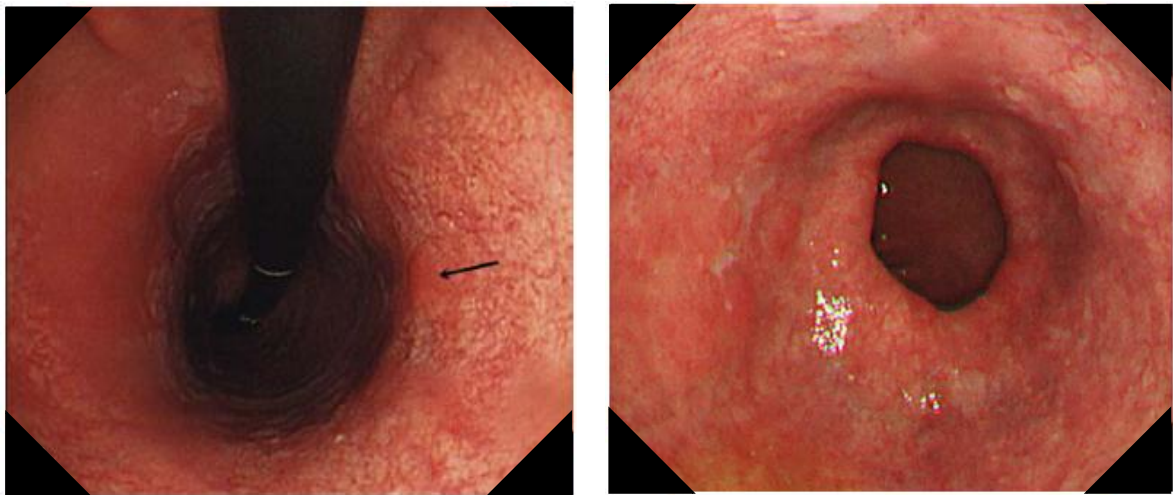


Figure 2.5: White-light endoscopic view of BE, showing dysplastic lesions (arrow in the left-side image). Reprinted from [17-18] Copyright (2005-2006), with permission from Elsevier.

The current validated method to detect dysplasia is based on endoscopy examination followed by biopsy and microscopic examination, i.e. histology, which is the gold standard for analysis of diseased tissue. Patients found to have BE should undergo upper endoscopy surveillance in the hope of detecting malignancy in an early and more curable stage [19-21]. This procedure has limitations since dysplasia is not endoscopically visible. Moreover, dysplastic lesions can be as small as one millimeter, and the probability of detecting such a small lesion in the entire suspected area is not favorable: the portion of tissue sampled may

not be representative of the diseased area. For these reasons, surveillance requires extensive and undirected biopsy, which is prone to sampling errors and associated with high costs. Since biopsy involves removing tissue it is considered an invasive procedure [15, 21].

A dependence on histology also has an inherent time delay between endoscopy and diagnosis, since biopsy samples need to be taken to a pathology laboratory to be analyzed. After the tissue is removed, the sample is fixed in formaldehyde, embedded in paraffin, sliced into sections, and stained with specific dyes. Then the pathologist analyzes the sections with a microscope, looking for patterns of disease (e.g. structural disorganization, increased nuclei size, among others). Overall, these procedure steps together may take hours. This limits the possibility to re-sample or over-sample abnormal or ambiguous areas because the need for further biopsies is not known until the pathologist analyzes the collected samples [15, 21]. Moreover, the histopathological diagnosis can be considered subjective and highly dependent on the pathologist that is performing the analysis [22-25].

Given what was said in the previous paragraph, it is clear that a real-time, more efficient and reliable method for diagnosis of esophageal dysplasia, with potential to guide biopsy, or eventually replace biopsy, is needed. In the next Chapter, two optical spectroscopy techniques will be described that have associated important advantages for the detection of early esophageal cancer: (1) ability to non-invasively probe tissue (without the need for biopsy; for further histopathological evaluation only diseased tissue is removed); (2) no need to process the tissue specimen for histopathological assessment (real-time diagnosis – data can be collected and analyzed in seconds); (3) potential to reveal information beyond what can be provided by standard endoscopy techniques (e.g. biochemical information which often precedes the morphological visible changes); (4) ability to provide quantitative information that can add objectivity to the diagnosis of dysplasia (pathological evaluation is qualitative in nature and thus sometimes subject to low inter-observer agreement).

References

- [1] K. L. Moore, *Clinically oriented anatomy*, 6th ed. Philadelphia Lippincott Williams & Wilkins, 2010.
- [2] R. L. Drake, *et al.*, *Gray's anatomy for students* 1st ed. Philadelphia Churchill Livingstone, 2004.
- [3] R. S. Cotran, *Robbins pathologic basis of disease*, 6th ed. Philadelphia W.B. Saunders Company, 1999.
- [4] B. Kuo and D. Urma. (2006, Accessed July 2011). Esophagus - anatomy and development. *GI Motility Online*. Available: <http://www.nature.com/gimo/contents/pt1/full/gimo6.html>
- [5] H. Mashimo and R. K. Goyal. (2006, Accessed July 2011). Physiology of esophageal motility. *GI Motility Online*. Available:

- <http://www.nature.com/gimo/contents/pt1/full/gimo3.html>
- [6] R. G. Kessel, *Basic medical histology : the biology of cells, tissues, and organs*, 1st ed. New York Oxford University Press, 1998.
 - [7] B. Young, *et al.*, *Wheater's functional histology : a text and colour atlas*, 5th ed. Churchill Livingstone, 2010.
 - [8] N. K. Altorki, *et al.*, "Epidemiology and molecular biology of Barrett's adenocarcinoma," *Semin Surg Oncol*, vol. 13, pp. 270-80, Jul-Aug 1997.
 - [9] I. Georgakoudi, *et al.*, "Fluorescence, reflectance, and light-scattering spectroscopy for evaluating dysplasia in patients with Barrett's esophagus," *Gastroenterology*, vol. 120, pp. 1620-9, Jun 2001.
 - [10] J. F. Flejou, "Barrett's oesophagus: from metaplasia to dysplasia and cancer," *Gut*, vol. 54 Suppl 1, pp. i6-12, Mar 2005.
 - [11] S. R. DeMeester, "Adenocarcinoma of the esophagus and cardia: a review of the disease and its treatment," *Ann Surg Oncol*, vol. 13, pp. 12-30, Jan 2006.
 - [12] K. K. Wang and R. E. Sampliner, "Updated guidelines 2008 for the diagnosis, surveillance and therapy of Barrett's esophagus," *Am J Gastroenterol*, vol. 103, pp. 788-97, Mar 2008.
 - [13] S. Ramel, "Barrett's esophagus: model of neoplastic progression," *World J Surg*, vol. 27, pp. 1009-13, Sep 2003.
 - [14] N. J. Shaheen, "Advances in Barrett's esophagus and esophageal adenocarcinoma," *Gastroenterology*, vol. 128, pp. 1554-66, May 2005.
 - [15] A. H. Kim, "Development of a Real Time Trimodal Spectroscopy Diagnostic Tool for Barrett's Esophagus," Master, Department of Electrical Engineering and Computer Science, Massachusetts Institute of Technology, 2002.
 - [16] M. Conio, *et al.*, "Barrett's esophagus: an update," *Crit Rev Oncol Hematol*, vol. 46, pp. 187-206, May 2003.
 - [17] M. A. Kara, *et al.*, "Endoscopic video autofluorescence imaging may improve the detection of early neoplasia in patients with Barrett's esophagus," *Gastrointest Endosc*, vol. 61, pp. 679-85, May 2005.
 - [18] J. J. Bergman, "The endoscopic diagnosis and staging of oesophageal adenocarcinoma," *Best Pract Res Clin Gastroenterol*, vol. 20, pp. 843-66, 2006.
 - [19] G. W. Falk, "Barrett's esophagus," *Gastroenterology*, vol. 122, pp. 1569-91, May 2002.
 - [20] N. Shaheen and D. F. Ransohoff, "Gastroesophageal reflux, Barrett esophagus, and esophageal cancer: clinical applications," *JAMA*, vol. 287, pp. 1982-6, Apr 17 2002.
 - [21] G. I. Zonios, "Diffuse Reflectance Spectroscopy of Human Colon Tissue," Department of Physics, Massachusetts Institute of Technology, 1998.
 - [22] R. J. Schlemper, *et al.*, "Differences in diagnostic criteria for esophageal squamous cell carcinoma between Japanese and Western pathologists," *Cancer*, vol. 88, pp. 996-1006, Mar 2000.
 - [23] H. Yoon, *et al.*, "Inter-observer agreement on histological diagnosis of colorectal polyps: the APACC study," *Gastroenterol Clin Biol*, vol. 26, pp. 220-4, Mar 2002.
 - [24] R. E. Petras, *et al.*, "Barrett's esophagus. A review of the pathologist's role in diagnosis and management," *Pathol Annu*, vol. 26, pp. 1-32, 1991.
 - [25] B. J. Reid, *et al.*, "Observer variation in the diagnosis of dysplasia in Barrett's esophagus," *Hum Pathol*, vol. 19, pp. 166-78, Feb 1988.

Chapter 3

Spectroscopy: Methods and Models

In this Chapter it is described the two major optical spectroscopy techniques that have been used for the detection of gastrointestinal cancer: diffuse-reflectance and fluorescence. Some of the most relevant studies using these two techniques for the assessment of esophageal tissue, together with their main results, are summarized. The Chapter also deals with the description of some physical models used to analyze the obtained spectral data and to extract quantitative biochemical and morphological information. To conclude, the feasibility of using a few narrow spectral regions for the quantitative extraction of tissue information, used to establish the diagnosis of dysplasia, is discussed.

3.1 Spectroscopy

Optical spectroscopy techniques have the potential to detect endoscopically invisible

early cancerous lesions in epithelial tissues. They make the “invisible visible”. By gathering tissue morphological and biochemical information, spectroscopy techniques are able to establish a diagnosis in a fast, objective and non-invasive way (there is no need to remove, process, and histologically analyze the tissue) [1-2].

In spectroscopy, when tissue is illuminated, several photophysical phenomena can occur as a result of the light-tissue interactions: scattering, absorption, or fluorescence (Figure 3.1). Scattering is the predominant interaction and occurs when light is redirected as a result of variations in the refractive indices of tissue constituents, relative to their surrounding medium [3]. The refractive index is defined as the ratio of the velocity of an electromagnetic wave in vacuum to that in a particular medium [4]. Absorption occurs when a molecule absorbs light without re-emission, whereas fluorescence occurs when a molecule absorbs light and re-emits it at a longer wavelength [1, 5-6].

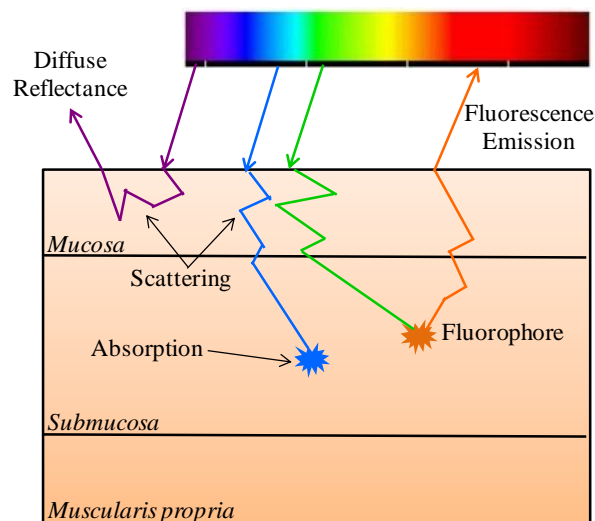


Figure 3.1: Examples of different light-tissue interactions: scattering, absorption and fluorescence [5].

With the progression of dysplasia, changes in the architectural and biochemical properties of tissue perturb tissue absorption, scattering, and fluorescence, thus modifying the characteristics of the re-emitted light [7]. These tissue modifications, which are translated into specific spectroscopic signatures, include [5-6, 8-18]:

(1) the degradation of the extracellular collagen matrix by various proteases, and the loss of basement membrane, which are translated by a decreased scattering and a reduced fluorescence signal from collagen. This degradation facilitates cell invasion and, eventually, a metastatic dissemination;

(2) an increased metabolic activity because of rapid cell division, which results in an increased NAD(P)H fluorescence signal. NAD(P)H is a cellular metabolism related molecule. It is coupled to the production of cellular energy through the oxidation of glucose;

(3) the thickening of the epithelium, which is reflected by a collagen reduced

fluorescence signal and by a decrease in scattering. This occurs because with an increased thickness less incident light is able to reach the underlying collagen fibers;

(4) the angiogenesis process, characterized by the growth of new blood vessels and hence by an increase in blood content, which is translated by an increased absorption by hemoglobin. Increased hemoglobin absorption causes a decrease in the fluorescence emission.

Therefore, by monitoring the light emitted from the tissues (which is a function of light-tissue interactions aforementioned) it is possible to infer about the tissue disease state. Since it is considerably different from healthy tissue in structure and function, dysplasia or cancer, is expected to produce significant changes in the emitted light spectra (as shown in Chapter 1, Figure 1.3(a)). Still, it is important to note that these spectral changes also depend on the type of instrumentation used to collect the data [2, 19].

All the tissue biochemical and morphological information provided by optical measurements represents a valuable tool not only to establish an early diagnosis of a lesion (before macroscopically visible changes take place) but also to understand the biological processes involved in the progression from normal epithelium to dysplasia to cancer [6, 20]. Consequently, the knowledge about these processes can lead to the development of an improved therapeutic intervention [20].

In general, three types of optical spectroscopy technologies are used to assess epithelial tissue: DRS; FS; and Raman spectroscopy. The present thesis will focus on the detection of esophageal dysplasia using two of these modalities: DRS and FS.

3.2 Diffuse-reflectance spectroscopy

DRS measures light that is diffusely reflected from the tissue, i.e. light that is scattered many times before being detected. This scattering is elastic, which means that the scattered light has the same energy as the incident light – energy is conserved. During its travel through the tissue, light can also be absorbed. Thus, the resulting emission spectra will carry information not only about scattering but also about the absorption properties of the medium. This information can then be analyzed and correlated with tissue biochemical composition, morphology, and organization, to establish a diagnosis [10, 20-21].

In this modality, tissue is illuminated using a white-light source. The emitted light is usually collected and dispersed by a spectrograph, and then detected using a charge-coupled device (CCD). The detected diffuse-reflectance signal corresponds to light that has traveled through the tissue in a variety of paths and depths, and thus, the information extracted from the spectrum reflects the properties over a volume of tissue [3, 10, 14, 16].

Scattering

Tissue scattering is originated by variations in the refractive index of tissue constituents, such as collagen fibers, elastin, cell nuclei and membranes, and mitochondrias [1]. Specifically, in epithelial tissues, scattering is mainly due to collagen fibers [9]. The amount of scattering is a function of three factors: (1) the density of particles; (2) the size of the particles compared to the incident wavelength; and (3) the ratio between the refractive index of the particles and the refractive index of the medium [1, 18, 22].

Elastically scattered light can be detected at the tissue surface after being scattered just once (single scattering) or after being scattered many times within the tissue (multiple scattering). The last is the main form of elastic scattering. Re-emitted light that has been scattered many times is known as *diffusely reflected* and is measured from the tissue surface using DRS [1].

In general, a photon travels 0.05 to 0.2 mm in the tissue before it is scattered for the first time by a particle. Multiply scattered photons can penetrate several millimeters into the tissue, ending up traveling the majority of time in the connective tissue (lamina propria and submucosa, see Figure 2.3, Chapter 2) with collagen fibers. Thus, the diffuse-reflectance spectrum translates essentially the properties of the connective tissue [1, 9, 16, 20-21].

Absorption

Tissue absorption depends on the amount of molecules within tissue that absorb light at specific wavelengths. The absorption phenomenon inherently causes a reduction in the amount of incident light that returns to the tissue surface. Tissue components (molecules and atoms) will convert the absorbed light into internal energy and heat [1].

In the epithelial tissue composition there are several absorbers, among which: nucleic acids (with maximum absorption around 260 nm), amino acids (with maximum absorption around 260-280 nm), and hemoglobin. For the esophagus, and epithelial tissues in general, hemoglobin is considered the only major absorber in the visible range [2, 9, 20, 22].

Hemoglobin exists in the tissues in two different forms – oxygenated and deoxygenated, each of one has different absorption features, which are often use to obtain information about tissue oxygenation [20]. Oxyhemoglobin (HbO₂) has maximum absorption peaks around 420, 540, and 580 nm, whereas deoxyhemoglobin (Hb) has its absorption maxima around 430 and 555 nm (Figure 3.2) [9, 23]. The extinction coefficient, ϵ_1 , measures how strong the molecules absorb light at a specific wavelength.

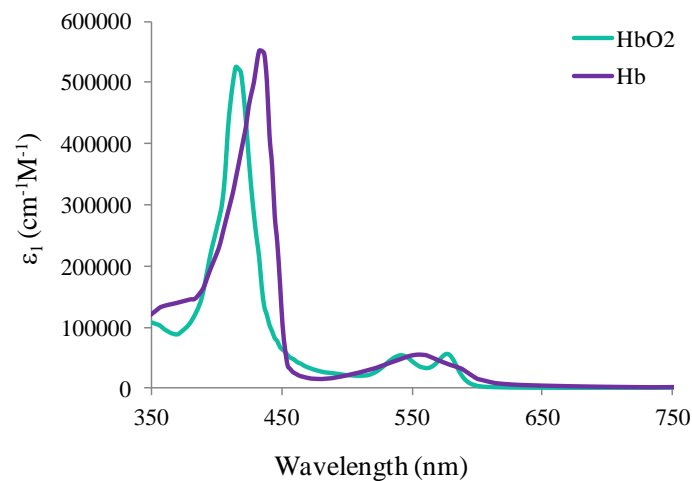


Figure 3.2: Molar extinction coefficient spectra of HbO₂ and Hb. The characteristic peaks of absorption for both forms of hemoglobin are clearly visible [23].

Absorption in tissue is highly dependent on the wavelength, tending to decrease with increasing wavelengths. As a result, the penetration depth of light into the tissue, which directly depends on tissue absorption, increases from the UV to the near-infrared spectral range. Visible light incident into the tissue usually penetrates at a depth of 0.5 to 2.5 mm. However, in the 650 to 1500 nm range, light can penetrate as deep as 10 mm before being collected. This happens because in this spectral range scattering predominates over absorption. In this region, known as *diagnostic or therapeutic window*, tissues are more *transparent* and, thus, it is possible to characterize them beyond surface and subsurface [1-2, 22].

In summary, the measured DRS signal allows to obtain information regarding the tissue structure and its hemoglobin concentration and oxygenation.

3.3 Fluorescence spectroscopy

In FS tissue is illuminated with UV or short-wavelength visible light and the resulting emission is recorded. This emission depends on the fluorophores (biomolecules) present in the tissue, which have different fluorescence emission signals, and on the scattering and absorption properties of the tissue. GI tissue is composed of distinct fluorophores that occur in different concentrations and at different depths. Thus, the tissue layers (mucosa, submucosa and muscularis propria) have distinct fluorophore compositions and, as a consequence, distinct fluorescence emission spectra. Moreover, the fluorophores, which are related to the structure and metabolism of cells, are very sensitive to changes in the tissue microenvironment that may occur during disease development. This way, a modification in the fluorescence emission spectra (intensity and spectral shape) may be correlated to the emergence of pathological conditions [1-2, 5, 20, 24].

In the fluorescence process, the endogenous fluorophores, such as collagen, elastin, tryptophan, or NAD(P)H, absorb light and become excited. When they return to their ground state, the absorbed light is re-emitted at a lower energy in the form of fluorescence. The particular excitation and emission properties of some tissue fluorophores are presented in Table 3.1 [2, 20, 22, 24-25].

Table 3.1: Excitation and emission maxima of some tissue fluorophores.

Fluorophores	Excitation maxima (nm)	Emission maxima (nm)
<i>Amino acids</i>		
Tryptophan	280	350
Tyrosine	275	300
<i>Structural Proteins</i>		
Collagen	325	400
Elastin		
<i>Enzymes and Co-enzymes</i>		
NAD(P)H	290, 340	440, 450
FAD (flavin adenine dinucleotide)	450	515
Porphyrins	400-450	630, 690

Scattering and absorption from tissue particles can significantly affect the measured fluorescence signal, introducing some distortions to the spectra, and ultimately masking the biochemical differences between normal and dysplastic tissues. This makes difficult the extraction of the tissues biochemical composition [2, 6, 16]. Still, and since fluorescence and reflectance spectra are affected similarly by absorption and scattering events, it is possible to remove the mentioned distortions from the fluorescence spectra, using the reflectance spectra, as will be detailed in section 3.5.2. The obtained spectra is known as “intrinsic fluorescence”.

In summary, from the fluorescence signal it is possible to assess the biochemical and morphological composition of tissue, which helps to establish a diagnosis.

3.4 Diffuse-reflectance and fluorescence studies in the esophagus

A few studies have been published about the use of DRS for the detection of esophageal malignancy. Georgakoudi and co-workers have published two different studies using this technique for the detection of dysplasia in patients with known BE [9, 26-27]. In the 2001 study [9], diffuse-reflectance spectra was collected from 16 patients, and then analyzed to obtain information about the scattering and absorption properties of connective tissue. In specific, the data included 26 non-dysplastic BE sites, 7 low-grade dysplastic sites,

and 7 high-grade dysplastic tissue sites. Using DRS, it was possible to differentiate high-grade dysplasia (HGD) from non-dysplastic tissue and low-grade dysplasia (LGD) with a sensitivity and specificity of 86% and 100%, respectively. In 2003, a study enrolling 27 patients also applied DRS for the identification of malignancy [26]. The ability of this technique to establish a diagnosis was again successful demonstrated with sensitivities and specificities of 90-95% and 85-90%, respectively.

In 2006, Lovat *et al.* [27] conducted a study to assess the potential of DRS to detect HGD or cancer in patients with BE. Data was collected from 181 different tissue sites, in a total of 81 patients. DRS was able to differentiate low-risk tissue sites (including clinically normal and low-grade dysplastic tissue sites) from high-risk tissue sites (with histologically confirmed HGD or cancer) with a sensitivity and specificity of 92% and 60%, in that order. Moreover, it was demonstrated the ability of DRS to identify benign lesions in patients with BE: high-risk sites were distinguished from inflammation with a sensitivity and specificity of 79%.

Overall, these studies have shown the potential of DRS as a reliable technique to detect malignant lesions in patients with BE.

Several studies have described the use of FS for the detection of esophageal dysplasia and cancer [9, 12-13, 28-32]. In these reports excitation wavelengths between 330 and 620 nm were used, and the collected emission spectra were analyzed using different methods, such as intensity ratios, area under the fluorescence curve, or principal component analysis. Overall, FS has shown great potential for the discrimination between clinically normal and malignant tissue. A brief description of some of these studies can be found next below.

Panjehpour and co-workers [28] have excited the Barrett's mucosa of 36 patients using 410 nm light. The collected fluorescence spectra were analyzed using differential normalized fluorescence (DNF) indices at 480 nm and 660 nm to differentiate HGD from LGD and healthy tissue. In this method, all fluorescence spectra are normalized to the total integrated light (area under the emission curve). An average normalized fluorescence spectrum, collected from 15 patients with normal esophagus, was used as a baseline. The DNF spectrum of each fluorescence spectrum is achieved by subtracting this baseline from the normalized collected spectrum. The DNF index at 480 or 660 nm corresponds to the magnitude of the DNF spectrum at these wavelengths. The main objective was to find significant differences between the indices of normal and cancerous tissue sites. This methodology was able to correctly identify 96% of non-dysplastic tissue sites, and 90% of high-grade dysplastic tissue sites.

In one study by Georgakoudi *et al.* [9] the potential of intrinsic fluorescence

spectroscopy (IFS) to identify LGD and HGD in 16 patients with known BE was evaluated. A 337 nm nitrogen laser was used as the light source. Other excitation wavelengths were tested, being obtained using different dye cuvettes mounted on a rotating wheel in front of the laser. In particular, emission fluorescence spectra that resulted from an excitation at 337, 397, and 412 nm were modeled and analyzed. Significant differences were found between non-dysplastic and dysplastic tissue sites: at 337 nm excitation the spectral line-shape shifted to the red spectral region as malignancy progressed; and at 397 nm excitation the fluorescence intensity increased in the red spectral region. Based on these findings a diagnostic algorithm was developed that was able to differentiate HGD from non-dysplastic tissue and LGD with a sensitivity and specificity of 100% and 97%, respectively.

In 2001, Mayinger *et al.* [13] used violet-blue light (375-478 nm) to excite normal and malignant esophageal tissue. This study enrolled 13 patients and a total of 129 tissue sites from which fluorescence spectra were collected. The emitted fluorescence spectra were all normalized to the average intensity at a wavelength 657 to 700 nm. This spectral range was used since in this region the fluorescence spectra had the same shape, irrespective of the tissue disease state. Then, a mathematical algorithm was developed based on the ratio of the fluorescence intensity in the wavelength range between 500 and 549 nm. With this algorithm it was possible to diagnose esophageal ADC with a sensitivity and specificity of 97% and 95%, respectively.

IFS was also successfully used to extract quantitative information about two important tissue fluorophores: NAD(P)H and collagen [12]. In this report fluorescence spectra from 7 patients with BE were collected, corresponding to a total of 10 non-dysplastic sites and 5 high-grade dysplastic lesions. Physical models were then applied to the measured spectral data for the quantification of tissue properties. It was found that low collagen and high NAD(P)H fluorescence were associated with high-grade dysplastic lesions when compared with non-dysplastic tissues. With this information it was possible to describe in an objective way significant biochemical changes between normal and dysplastic tissues.

3.5 Spectroscopy models

As described in section 3.4, different methods and models can be applied to analyze spectra and to develop a diagnostic algorithm. These models can be qualitative or empirical (e.g. the ratio of two intensity values), or quantitative. Quantitative models have the huge advantage to quantitatively determine different tissue properties.

Thus, this section will describe the physical models that have been developed to be

applied to the measured diffuse-reflectance and fluorescence spectra to extract physical properties of the tissues. This is performed in order to develop any relevant and useful diagnostic algorithms that provide objective diagnostic differences between normal and malignant tissues, based on physiologically understood quantities of tissue constituents.

3.5.1 Diffuse-reflectance spectroscopy

A well-developed model [10], based on the diffusion approximation to the radiative transfer equation, enables the extraction of quantitative information about tissue constituents that contribute to reflectance. The radiative transfer equation describes light propagation in turbid media. The diffusion approximation assumes that light transport is dominated by scattering, and is not valid in highly absorbing or very dilute samples. Also, for very small source-detector separations (i.e. less than 0.2 mm) the diffusion approximation may not be valid since light may not experience sufficient scattering events before being collected [19]. This model, developed by Zonios *et al.* in 1999 [10], was based on a previous study by Farrell *et al.* [33]. This section will not discuss in detail the Farrell's model, but the reader is referred to the literature for further information [33].

In the Zonios *et al.* model [10] three fundamental approximations were made to model DRS and determine the tissue biochemical and morphological parameters: (1) light is delivered to the tissue in an infinitesimally small point (point source); (2) hemoglobin is the only significant absorber in the visible range; (3) the scattering is modeled as if tissues were homogeneous systems of spherical particles with known refractive index. This last approximation allowed the characterization of tissue scattering in terms of the effective scatterer size and the effective scatterer density. The diffuse-reflectance measured by an instrument can then be expressed as:

$$R_1 = \frac{\mu'_s}{\mu'_s + \mu_a} \left(e^{-\mu_0' z_0} + e^{-\left(1 + \frac{4}{3} A_0\right) \mu_0' z_0} - \frac{z_0}{r'_1} e^{-\mu_0' r'_1} - \left(1 + \frac{4}{3} A_0\right) \frac{z_0}{r'_2} e^{-\mu_0' r'_2} \right) \quad (3.1)$$

where

$$r'_1 = \sqrt{z_0^2 + r_c'^2} \quad (3.2)$$

and

$$r'_2 = \sqrt{\left(1 + \frac{4}{3} A_0\right) z_0^2 + r_c'^2} \quad (3.3)$$

The radius of the circular collection spot, r_c' , is an empirically determined value, derived by calibrating the spectroscopy instrument with a phantom (a physical tissue model,

with known scattering and absorption properties) [19]. Also, in equation 3.1:

$$z_0 = \frac{1}{\mu'_s + \mu_a} \quad (3.4)$$

and

$$\mu_0' = \sqrt{3\mu_a(\mu'_s + \mu_a)} \quad (3.5)$$

where μ'_s and μ_a are the reduced scattering and absorption coefficients of the tissue, respectively.

To account for the refractive index mismatch between the tissue and the surrounding environment (usually air), the term A_0 describes the internal reflection at the interface, and is expressed as the following equation:

$$A_0 = \frac{2 / \left(1 - \left[\left(\frac{n_{tissue}}{n_{air}} - 1 \right) / \left(\frac{n_{tissue}}{n_{air}} + 1 \right) \right]^2 - 1 + |\cos\theta_c|^3 \right)}{1 - |\cos\theta_c|^2} \quad (3.6)$$

where n_{tissue} and n_{air} correspond to the refractive indices of tissue and air, respectively. The critical angle for total internal reflection is defined as θ_c [4].

In the DRS analysis, the experimentally measured reflectance spectra are fit to the described Zonios *et al.* model to determine the values of two key parameters that describe the light-tissue interactions: μ'_s and μ_a . The reduced scattering and absorption coefficients represent the approximate number of scattering or absorption events that a photon undergoes while propagating a certain distance in the medium. The inverse of these coefficients values represents the average distance traveled by a photon before being scattered or absorbed. Both parameters are wavelength-dependent [18].

The reduced scattering and absorption coefficients can be expressed as [3, 34]:

$$\mu'_s(\lambda) = A_s \left(\frac{\lambda}{\lambda_0} \right)^{-B_s} + C_s \left(\frac{\lambda}{\lambda_0} \right)^{-4} \quad (3.7)$$

$$\mu_a(\lambda) = C_{diff}(\lambda) \cdot \vartheta \cdot \mu_a^{blood}(\lambda) \quad (3.8)$$

In equation 3.7, λ is the wavelength and λ_0 is equal to 700 nm (λ_0 is the reference wavelength for the extraction of parameter A_s). The second term is used to accurately model reflectance at wavelengths below 400 nm, in which scattering from Rayleigh particles is significant [3, 34].

For equation 3.8 C_{diff} is a correction factor to account for the *vessel packaging* effect. This effect accounts for alterations in the shape and intensity of hemoglobin absorption peaks, related to the fact that hemoglobin is restrained to finite-sized blood vessels that are more or less transparent to light depending on the incident wavelength. In equation 3.8, $\vartheta =$

$c_{Hb}/2.3 \times 10^{-3}$ and corresponds to the volume fraction of blood sampled. In this expression c_{Hb} is the total concentration of hemoglobin, and 2.3×10^{-3} mol/L is the value assumed for the hemoglobin concentration of whole blood. C_{diff} is defined by:

$$C_{diff}(\lambda) = \left(\frac{1 - \exp[-2 \cdot \mu_a^{blood}(\lambda) \cdot b\vartheta r]}{2 \cdot \mu_a^{blood}(\lambda) \cdot b\vartheta r} \right) \quad (3.9)$$

where $b\vartheta r$ is the effective blood vessel radius and $\mu_a^{blood}(\lambda)$ is the absorption coefficient of whole blood:

$$\mu_a^{blood}(\lambda) = \log_{10} \cdot 2.3 \times 10^{-3} \text{ mol/L} \cdot (\alpha \varepsilon_{HbO_2}(\lambda) + (1 - \alpha) \varepsilon_{Hb}(\lambda)) \quad (3.10)$$

where α is the hemoglobin oxygen saturation; ε_{HbO_2} and ε_{Hb} are the molar extinction coefficient spectra of the oxygenated and deoxygenated hemoglobin, respectively.

As previously mentioned, the measured reflectance spectra are fit to the Zonios *et al.* model, usually over the 350 to 750 nm spectral range, using a nonlinear least-squares fitting algorithm. From the fitting, six DRS parameters, which translate six different tissue properties, are extracted for each spectrum: A_s , related to scatterer density and the overall magnitude of scattering; B_s , related to the average scatterer size; C_s , related to scattering by small particles; c_{Hb} , the total concentration of hemoglobin; $b\vartheta r$, the effective blood vessel radius; and α , the oxygen saturation of hemoglobin.

3.5.2 Intrinsic fluorescence spectroscopy

During propagation through the tissue, fluorescence photons are strongly influenced by the tissue's turbidity (scattering and absorption), which can introduce significant distortions in the spectra lineshape and intensity. As a result, the measured fluorescence (known as bulk fluorescence) is not simply the intrinsic fluorescence from tissue fluorophores, i.e., it is not simply a linear sum of the intrinsic fluorescence of the endogenous fluorophores. This prevents the quantitative extraction of specific biochemical tissue constituents [3, 35].

The IFS algorithm is based on the photon migration model of Wu *et al.* [36] and extracts intrinsic fluorescence spectra combining the fluorescence and diffuse-reflectance spectra measured at the same tissue site. With this algorithm the intrinsic fluorescence can be determined by the ratio of bulk fluorescence to a function of reflectance. Since fluorescence and reflectance photons are affected similarly by scattering and absorption, the division of fluorescence by reflectance allows one to obtain the fluorescence not affected by scattering and absorption (i.e. the effects of turbidity are accounted and corrected).

The analytical model to determine IFS is expressed as [35, 37]:

$$f_i(\lambda_m) = \frac{F_i(\lambda_m)}{\frac{1}{\mu_s(\lambda_x)l} \sqrt{\frac{R_0(\lambda_x)R_0(\lambda_m)}{[e^{S_p(1-g(\lambda_x))} - 1][e^{S_p(1-g(\lambda_m))} - 1]} \frac{R_1(\lambda_x)}{R_0(\lambda_x)} \left(\frac{R_1(\lambda_m)}{R_0(\lambda_m)} + [e^{S_p(1-g(\lambda_m))} - 1] \right)} \quad (3.11)$$

where, S_p and l represent geometric parameters of the spectroscopy instrument, and g is the anisotropy coefficient. The anisotropy coefficient represents the direction of scattering, and can vary from -1 (scattering is in the backwards direction) to 1 (all light is scattered in the forward direction). If $g = 0$, scattering is isotropic.

In equation 3.11, f_i and F_i correspond to the intrinsic and bulk fluorescence, respectively, and λ_x and λ_m are the excitation and emission wavelengths (e.g. $R(\lambda_x)$ is the reflectance at the excitation wavelength). R_1 corresponds to the experimentally measured diffuse-reflectance, whereas R_0 represents the diffuse-reflectance that would be measured in the absence of absorption. R_0 can be calculated using equation 3.1 and setting μ_a to zero. Also, in equation 3.11, the scattering coefficient, μ_s , can be calculated using parameters A_s , B_s and C_s , and coefficient g , with the following expression:

$$\mu'_s = \mu_s(1 - g) \quad (3.12)$$

Typical values of g for tissue are in the range of 0.7 to 0.95 [19, 35].

The combination of the two spectroscopy techniques - DRS and IFS - increases the amount of information that can be obtained from tissues, which in turn potentially improves the diagnostic accuracy of the developed algorithms for the differentiation of dysplastic and normal esophageal tissue.

3.6 Spectroscopy models implementation: wavelength reduction study

As mentioned in Chapter 1, one of the main goals of this thesis is to develop a miniaturized spectroscopy system. In conventional spectroscopy instruments, the discrimination of the different wavelengths is usually achieved in steps of 1 nm, using a spectrograph. However, it is difficult to integrate a spectrograph into a small-scale instrument and, this way, the discrimination of the different wavelengths has to be achieved using other approach: a narrow-band optical filtering system (the full miniaturized spectroscopy system and its components will be described in Chapter 4). As a consequence, this scale-down precludes the discrimination of the intensity at all wavelengths (i.e. with steps of 1 nm), which may be necessary for the quantification of tissue properties, using the described analytical models. To cover the full visible spectrum, it would be necessary to fabricate an extremely high number of filters, thus compromising the device small size.

The use of a few optical filters, centered at discrete locations of the visible spectrum,

would be enough for an empirical diagnosis, based, for instance, in the ratio of the intensity at two different spectral regions (e.g. red and green). This type of analysis is useful and simplifies the diagnostic method. However, the possibility to determine physiological quantities from tissue, by analyzing the measured spectra with analytical models, is a huge benefit of using spectroscopy. For that reason, the miniaturized system should be able to accomplish the quantitative extraction of tissue information. This way, a study was conducted, prior to the optical filtering system design and fabrication, to show the feasibility of using a small number of spectral regions to establish diagnosis. If successful, these results will demonstrate that it is possible to replace the spectrograph, used in conventional systems, by several optical filters.

3.6.1 Wavelength reduction analysis

The possibility of replacing the spectrograph by a series of optical filters for the diagnosis of esophageal dysplasia was investigated using an existing spectroscopy data set, composed by fluorescence and diffuse-reflectance measurements. These data were taken from esophageal tissue using a system described elsewhere [9]. For this study, simulations on wavelength reduction were performed on the data set in order to assess the feasibility of reducing the 400 wavelengths used to perform a quantitative diagnosis (from 350 to 750 nm, in 1 nm steps) to only 16, while still achieving a good accuracy in the extraction of tissue optical properties (sixteen was considered the minimum number of wavelengths from which one could accurately extract tissue information, as will be detailed in section 3.6.2).

For the wavelength reduction analysis, diffuse-reflectance and fluorescence algorithms (detailed in section 3.5) were implemented using MATLAB tools (from The MathWorksTM). Based on previously published results [9], several slightly different combinations of 16 wavelengths were chosen and simulated. For all the simulations the following wavelengths were fixed: 350 and 750 nm (the first and last wavelength in the analysis); 420, 540 and 580 nm (corresponding to HbO₂ absorption peaks); and 700 nm (reference wavelength). The remaining wavelengths were selected within the full visible range. The spacing between selected points must take into account the filters fabrication constraints, namely their FWHM (Full-Width-Half-Maximum), i.e., the filters transmittance spectrum should not considerably overlap. Thus, the best 16 wavelengths group is composed by those 6 fixed points and by 10 more wavelengths that are more or less equally spaced along the visible spectrum and correspond to filters which by design don't overlap.

The diffuse-reflectance and fluorescence data were then processed and data points from all wavelengths were eliminated, with exception for those corresponding to the selected

16 wavelengths. Thus, instead of having a continuous array of 400 wavelengths (from 350 to 750 nm), and the corresponding reflectance and fluorescence intensity values, a discrete set of 16 specific data points is obtained. The remaining spectrum intensities are achieved by linear interpolation within the range of the discrete data set. These newly generated spectra are then used to extract the tissue spectroscopy parameters. In the system to be developed, the 16 optical filters, together with the detection system, will directly provide these 16 intensity values from which the spectra will be reconstructed. In this procedure unknown data points are being calculated, and therefore one must be aware that the results might not be exactly the same as when using the original spectrum. Still, the overall advantages of having a miniaturized system may offset the error.

3.6.2 Wavelength reduction simulations

The selection of wavelengths for the design of the optical filters (each filter will be centered at a different wavelength) was based on simulations of wavelength reduction on an existing spectroscopy data set. The data set consisted of 53 histologically confirmed non-dysplastic tissue sites and 10 high-grade dysplastic esophageal tissue sites. The goal is to investigate if it is possible to accurately extract tissue properties using reflectance and fluorescence intensity values of only 16 wavelengths, and interpolating the remaining spectrum intensities to cover the whole visible range.

For the simulations diffuse-reflectance and fluorescence parameters were extracted from high-grade dysplastic and normal squamous esophageal tissue. Several combinations of 16 wavelengths were simulated. The combination that provided the best results comprises the following discrete points: 350, 370, 380, 400, 420, 450, 480, 510, 540, 560, 580, 600, 620, 650, 700, and 750 nm. As previously mentioned, for the wavelength selection a compromise between the accuracy in parameters extraction and the constraints inherent to the filters fabrication process (e.g. materials, number of layers, FWHM, and maximum transmission) had to be achieved. This wavelength choice is very important for the intended diagnosis and highly depends on the clinical situation for which the system is going to be used for. Since the esophagus is expected as the first application of the microsystem, the used clinical data set is appropriate for the simulations. Representative diffuse-reflectance and intrinsic fluorescence spectra of HGD and non-dysplastic squamous tissue are shown in Figure 3.3 and in Figure 3.4.

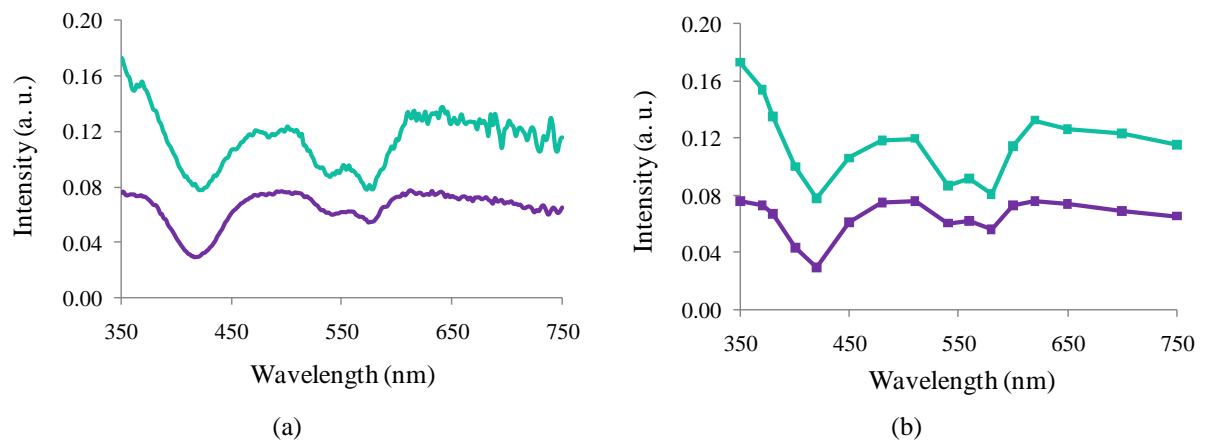


Figure 3.3: Representative diffuse-reflectance spectra for normal (upper line) and dysplastic tissue (bottom line), for (a) the full wavelength range (b) and only 16 wavelengths.

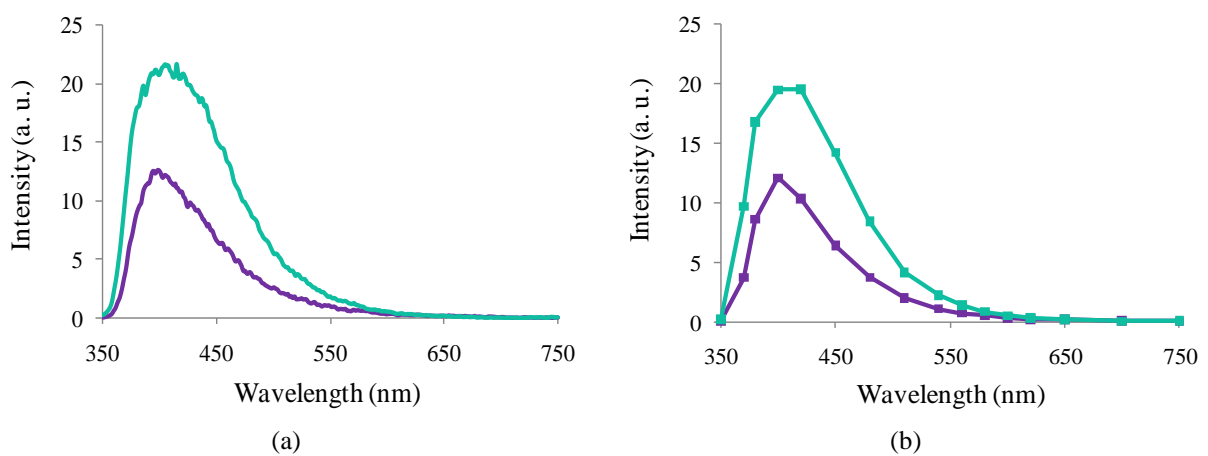


Figure 3.4: Representative intrinsic fluorescence spectra for normal (upper line) and dysplastic tissue (bottom line), for (a) the full wavelength range (b) and only 16 wavelengths.

For the diffuse-reflectance data, the reduced scattering and absorption coefficients, μ'_s and μ_a , respectively, were determined for 16 different wavelengths, using the original spectrum and the reconstructed spectrum of high-grade dysplastic and non-dysplastic tissue sites (Figure 3.5). The algorithm described in section 3.5.1 was used for the calculation of these coefficients. In general, the extracted coefficients obtained using the reconstructed spectrum are in good agreement with the coefficients extracted from the original spectrum, with a strong and positive correlation: correlation coefficients of 0.951 and 0.933 for the reduced scattering coefficient of HGD and non-dysplastic tissue sites, respectively; and, 0.966 and 0.987 for the absorption coefficient of HGD and non-dysplastic tissue sites, in that order. Thus, it is expected that the miniaturized system and the conventional systems will have comparable performance in the quantification of tissue optical information.

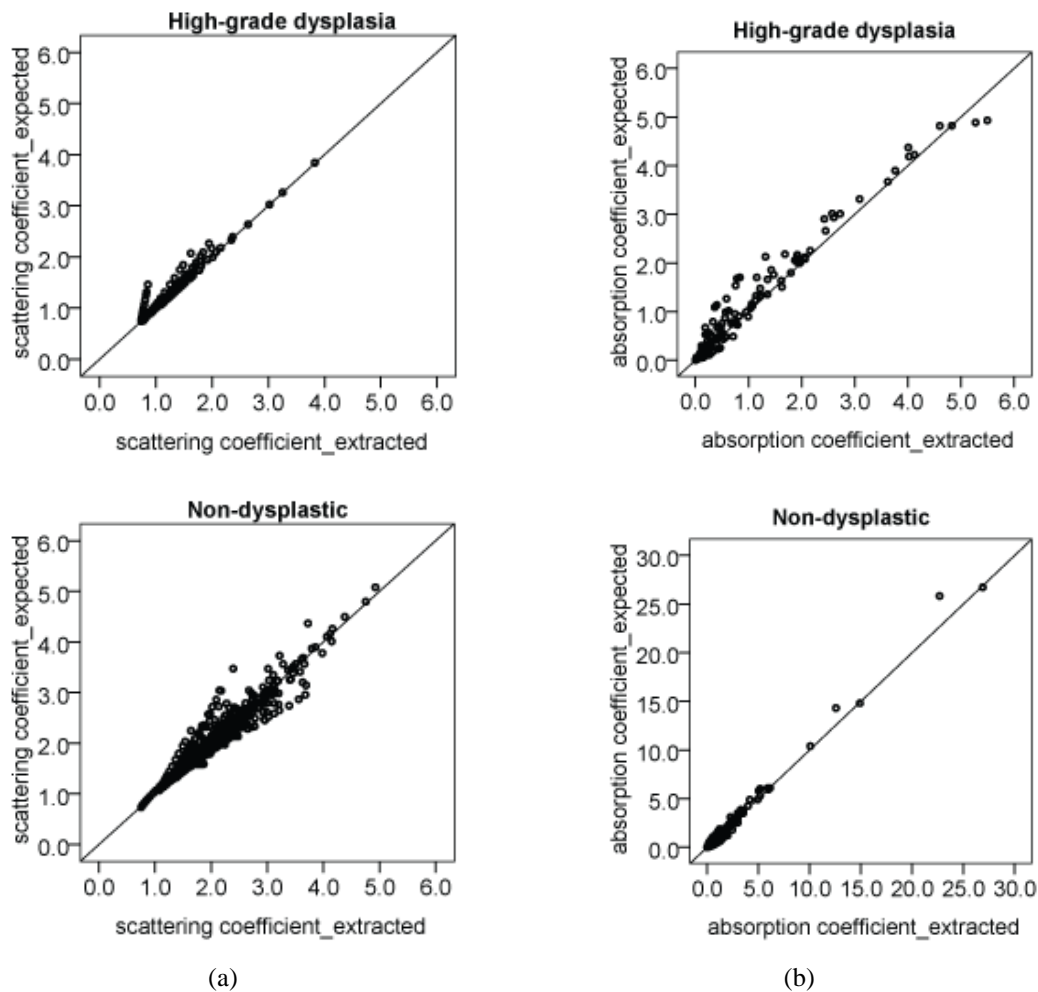


Figure 3.5: Scatter plots with the (a) reduced scattering coefficient and (b) absorption coefficient, determined for several different wavelengths: 350, 370, 380, 400, 420, 450, 480, 510, 540, 560, 580, 600, 620, 650, 700, and 750 nm. For each of these wavelengths, a different coefficient will be determined in each tissue site: a total of 10 high-grade dysplastic tissue sites and 53 non-dysplastic tissue sites were used, corresponding to 160 (10 times 16) and 848 (53 times 16) different values of reduced scattering and absorption coefficient. Y-axis represents the values of the coefficients extracted with the original spectrum; X-axis represents the values of the coefficients determined with the reconstructed spectrum, using only 16 points. The 45 degree black line represents a perfect agreement between the expected values, from the original spectrum, and the extracted values, from the reconstructed spectrum.

An even more reduced number of wavelengths for spectra analysis could be useful to further reduce the size and complexity of the optical filtering system. However a trade-off between this number and an accurate extraction of optical parameters had to be achieved. Sixteen was considered the limit beyond which one could accurately determine those parameters.

For demonstration, Figure 3.6 presents the same results of Figure 3.5 but extracted using only 10 wavelengths (350, 380, 400, 420, 480, 540, 580, 600, 700 and 750), instead of 16. In this approach, the extracted coefficients using the reconstructed spectrum have weaker correlations with the coefficients determined from the original spectrum, when compared with the previous strategy. Specifically, for the reduced scattering coefficient of non-dysplastic

tissue sites, there is a weak and not very significant correlation between the expected and extracted values, with a correlation coefficient of 0.326. From the obtained results it is clear the performance improvement of using 16 over 10 wavelengths for quantitative spectroscopy.

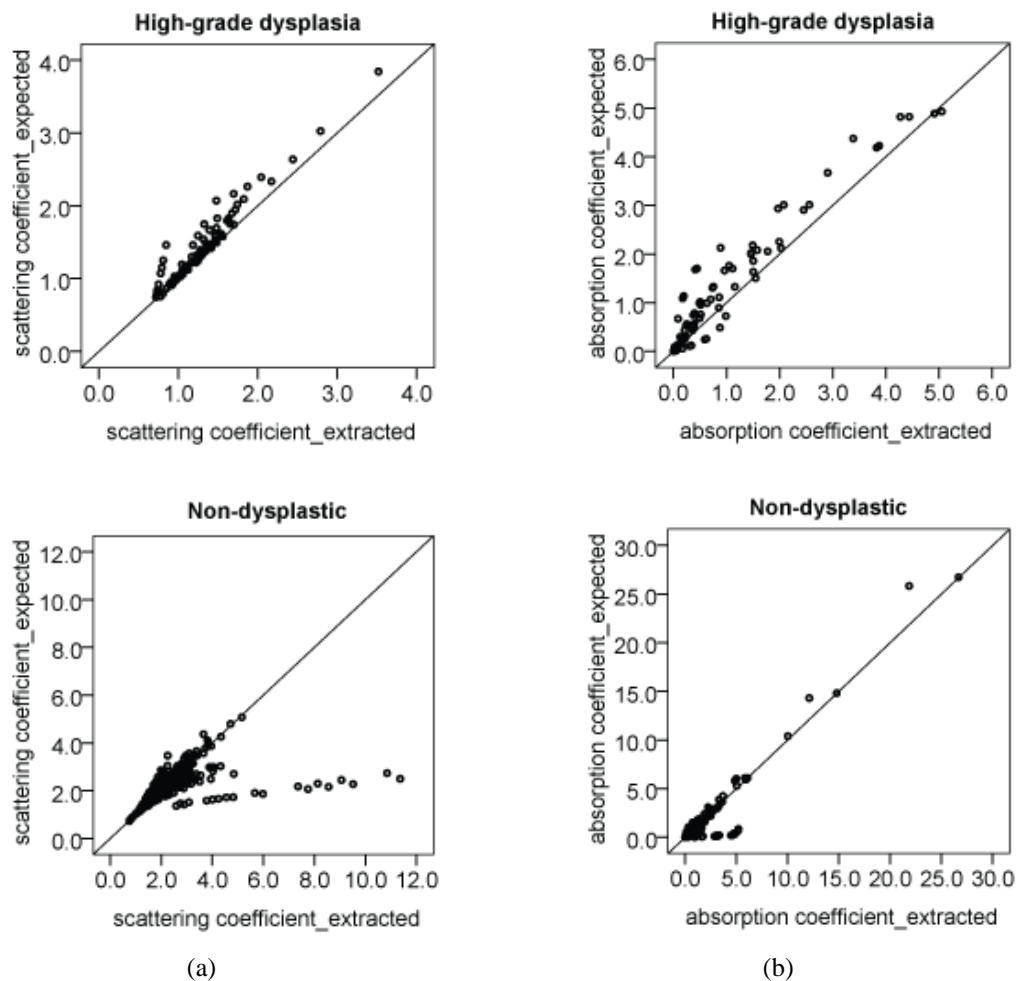


Figure 3.6: Scatter plots with the (a) reduced scattering coefficient and (b) absorption coefficient, determined for several different wavelengths: 350, 370, 380, 400, 420, 450, 480, 510, 540, 560, 580, 600, 620, 650, 700, and 750 nm. Y-axis represents the values of the coefficients extracted with the original spectrum; X-axis represents the values of the coefficients determined with the reconstructed spectrum, using only 10 points.

The theoretical performance of the miniaturized system to extract tissue properties from the reflectance and fluorescence signal was then assessed. Scatter plots displaying the expected (using the full spectrum) and extracted (using only 16 wavelengths) parameter values, or tissue components values, are presented in Figure 3.7 for the six DRS parameters: three parameters extracted from the reduced scattering coefficient (A_s , B_s , and C_s), and three parameters extracted from the absorption coefficient (c_{Hb} , a , and $b\vartheta r$).

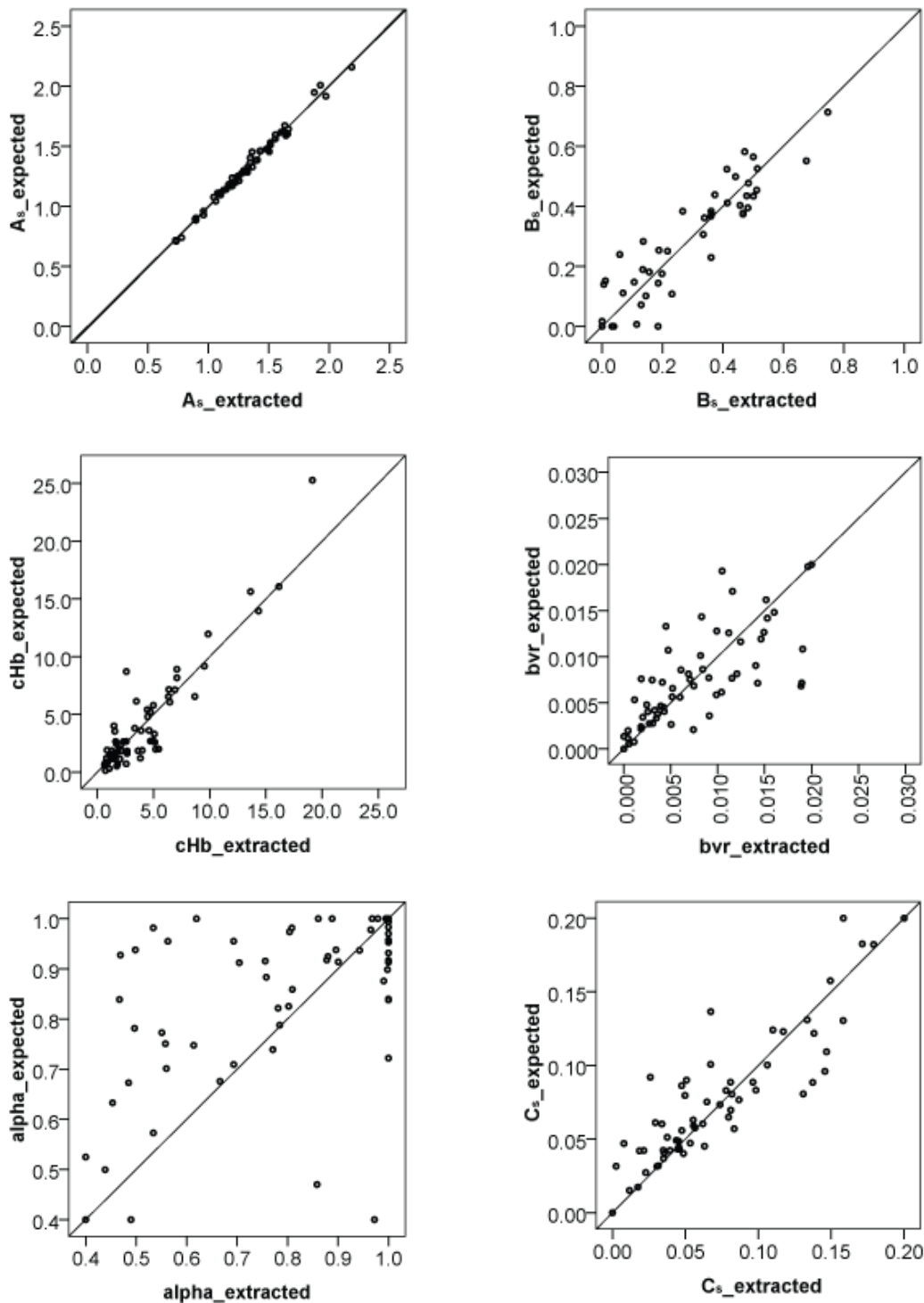


Figure 3.7: Scatter plots with the tissue parameter values for the six diffuse-reflectance parameters: A_s , B_s , C_s , cHb , α , and bvr , extracted using the full spectrum (expected values) and only 16 wavelengths (extracted values).

In Figure 3.8 the correlations between the extracted and expected values of the relative contributions of two fluorophores (collagen and NAD(P)H) for the overall tissue fluorescence are also displayed in scatter plots. These tissue parameters are extracted from the intrinsic fluorescence spectra, which are obtained from the bulk fluorescence spectra in combination with the reflectance spectra, after a tissue excitation using 340 nm light. The intrinsic

fluorescence spectra are then fit using a linear combination of the tissue fluorophore basis spectra. The tissue fluorophores basis spectra are extracted using multivariate curve resolution [34, 38]. For the particular excitation wavelength used (340 nm) the intrinsic fluorescence can be modeled as a linear combination of two spectral components: NAD(P)H and collagen.

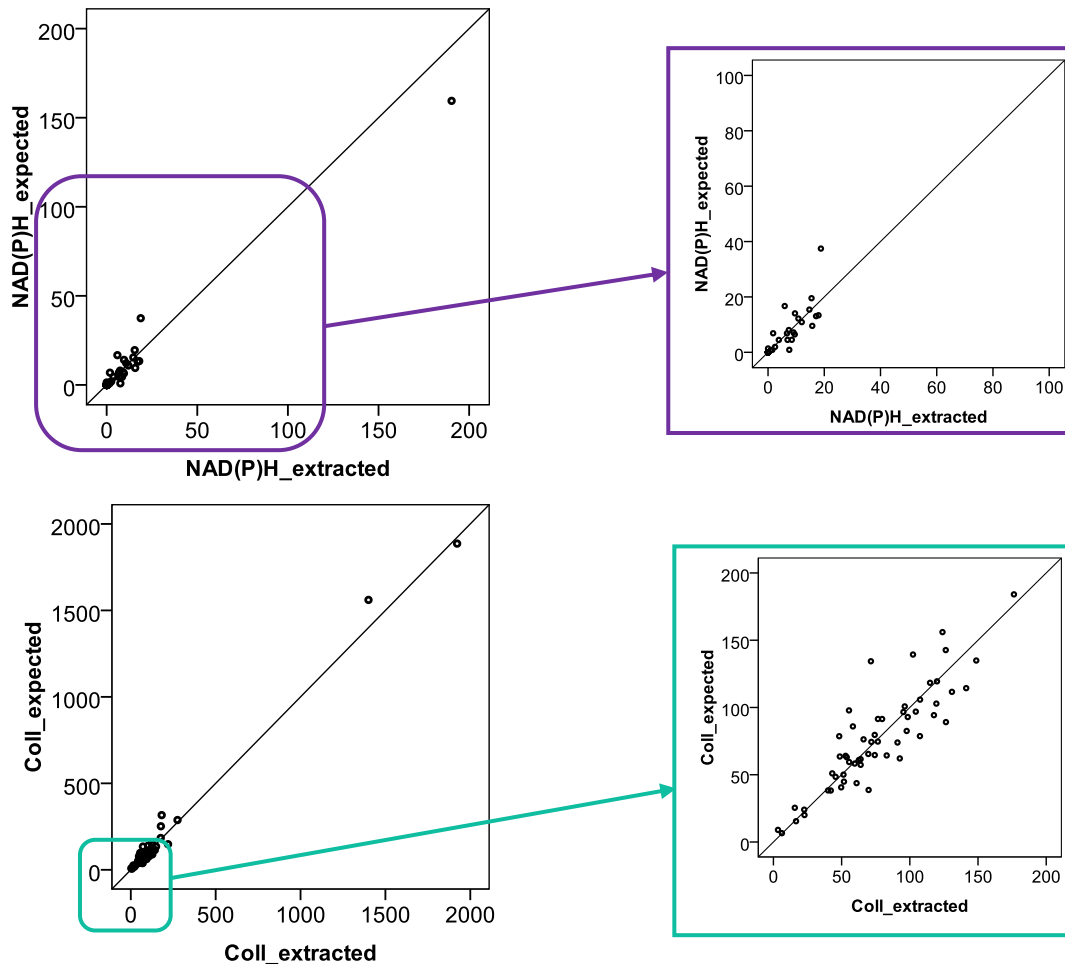


Figure 3.8: Scatter plots with the tissue parameter values for two fluorescence parameters: collagen and NAD(P)H, extracted using the full spectrum (expected values) and only 16 wavelengths (extracted values).

Overall, the reported results demonstrate that reflectance and fluorescence tissue properties can be relatively well determined using a reduced number of wavelengths, and thus these parameters can be used with confidence for the development of predictive models, or diagnostic algorithms, to identify normal and malignant tissues. Still, for some tissue sites, optical parameters could not be accurately extracted, which might be due to loss of spectral information with interpolation. Among the tissue parameters, the oxygen saturation (α) and the vessel packaging ($b\vartheta r$) correspond to the ones with the worst correlation coefficients. In particular, the correlation for the hemoglobin oxygen saturation values can be considered low or not very significant. This way, this tissue property should not be incorporated in the diagnostic algorithms to be developed with the miniaturized system because it cannot be

accurately estimated using a reduced number of wavelengths. For the remaining parameters there is a very strong and positive correlation between the expected and extracted values, with a mean correlation coefficient equal to 0.913.

The use of a different interpolation method could minimize the errors in the quantitative extraction of tissue properties. Therefore, in the future, an alternative approach should be evaluated: a model discretization should be applied and the parameter results should be compared to the ones obtained using linear interpolation.

This rough methodology was applied as an initial approach to select the 16 central wavelengths for fabricating the optical filters, and to demonstrate the feasibility of wavelength reduction for the assessment of tissue optical properties. In general, the 16 selected wavelengths provide good results, and, this way, it is now possible to move to the filters design and fabrication steps.

3.6.3 Wavelength reduction measurements using tissue phantoms

Before starting the filters design, it was decided to test the 16 selected wavelengths in a series of experiments using homogeneous physical tissue models (“phantoms”) with known scattering and absorption parameters. This was done to further evaluate the capability of a miniaturized spectroscopy system to accurately extract tissue optical properties using only 16 wavelengths. These phantoms consist of mixtures of intralipid and hemoglobin at various concentrations (Sigma Aldrich Co.) and water. The intralipid and the water soluble hemoglobin are used for scattering and absorbing, respectively. Two groups of phantoms were measured by DRS: the first was composed by phantoms with different concentrations of hemoglobin and a fixed intralipid concentration; the second consisted of phantoms with variable intralipid concentrations and a fixed hemoglobin amount. A solid sample of barium sulfate (BaSO_4) was used as a reflectance standard. A UV/visible/near-infrared spectrophotometer from Shimadzu (UV-3101PC) was used to measure the wavelength-dependent reflectance spectra from the phantoms.

Several measurements were performed on phantoms in a range of absorbing and scattering concentrations. The collected spectra were normalized by the reflectance spectra measured from the standard to correct for the wavelength dependent response of the system. Figure 3.9 shows the reflectance spectra taken from the same position on different phantoms using the full wavelength range (350-750 nm, with increments of 1 nm) and using only 16 wavelengths. These 16 data points will be the signal that will be read by the photodiodes. Diffuse-reflectance parameters are subsequently extracted using the MATLAB implemented diffuse-reflectance model.

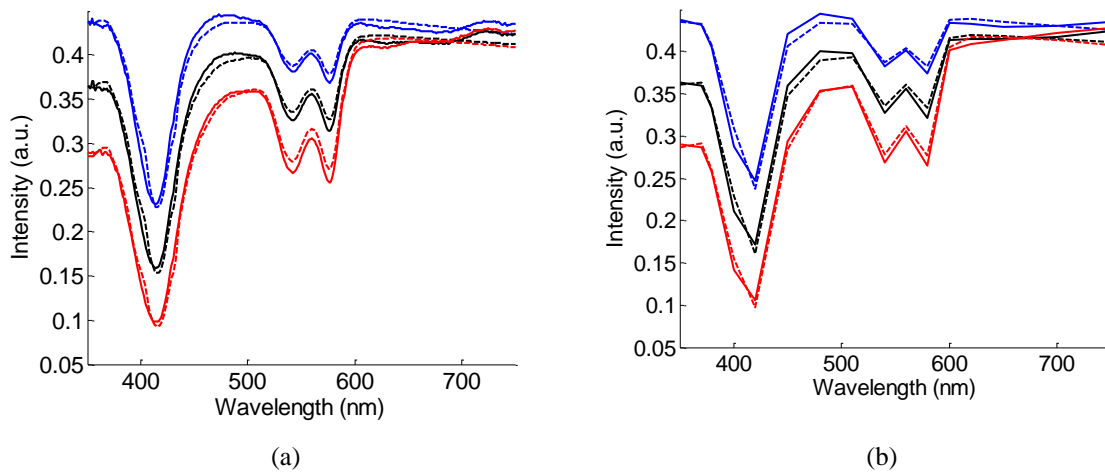


Figure 3.9: Reflectance spectra measured from different tissue phantoms (phantom 3: blue line; phantom 4: black line; phantom 5: red line): (a) using the full wavelength range; (b) and only 16 wavelengths. The best fit spectra according to the implemented diffuse-reflectance model are also plotted (dashed lines).

Table 3.2 summarizes the extracted values for parameters A_s and c_{Hb} , from the different phantoms. The value of A_s increases with intralipid concentration, as expected. The value of c_{Hb} is very similar to the expected value with less than 10% difference. Since all the phantoms were exposed to air during the measurements, the hemoglobin oxygen saturation is set equal to 1.0 for the analysis.

Table 3.2: Reflectance parameters extracted from tissue phantoms.

Phantom	Intralipid mass concentration	Hemoglobin concentration (mg/mL)	Full spectrum		16 wavelengths	
			c_{Hb}	A_s	c_{Hb}	A_s
1	0.5%	0.5	0.496	0.803	0.473	0.811
2	0.5%	1.0	0.954	0.783	0.964	0.782
3	1%	0.25	0.254	1.740	0.245	1.745
4	1%	0.5	0.478	1.650	0.464	1.650
5	1%	1	0.994	1.635	1.047	1.623

The use of the full wavelength range to measure diffuse-reflectance or the use of only 16 wavelengths seems to provide very comparable results in terms of optical properties in tissue physical models, as it was already expected by the previously shown wavelength reduction simulations.

References

- [1] J. W. Tunnell, *et al.*, "Diagnostic Tissue Spectroscopy and Its Applications to Gastrointestinal Endoscopy," *Techniques in Gastrointestinal Endoscopy*, vol. 5, pp. 65-73, 2003.
- [2] N. Ramanujam, "Fluorescence spectroscopy of neoplastic and non-neoplastic tissues," *Neoplasia*, vol. 2, pp. 89-117, Jan-Apr 2000.
- [3] S. McGee, "Non-invasive Detection of Oral Cancer Using Fluorescence and Reflectance Spectroscopy," Harvard-Massachusetts Institute of Technology Division of Health Sciences and Technology, Massachusetts Institute of Technology, 2008.
- [4] E. Hecht, *Optics*, 4th ed. San Francisco: Addison-Wesley, 2001.
- [5] R. S. Dacosta, *et al.*, "Spectroscopy and fluorescence in esophageal diseases," *Best Pract Res Clin Gastroenterol*, vol. 20, pp. 41-57, Feb 2006.
- [6] K. Badizadegan, *et al.*, "Spectroscopic diagnosis and imaging of invisible pre-cancer," *Faraday Discussions*, vol. 126, pp. 265-279, 2004.
- [7] K. Sokolov, *et al.*, "Optical spectroscopy for detection of neoplasia," *Curr Opin Chem Biol*, vol. 6, pp. 651-8, Oct 2002.
- [8] D. Arifler, *et al.*, "Computational analysis of light scattering from collagen fiber networks," *Proceedings of SPIE-OSA Biomedical Optics*, pp. 6628-6634, 2007.
- [9] I. Georgakoudi, *et al.*, "Fluorescence, reflectance, and light-scattering spectroscopy for evaluating dysplasia in patients with Barrett's esophagus," *Gastroenterology*, vol. 120, pp. 1620-9, Jun 2001.
- [10] G. Zonios, *et al.*, "Diffuse reflectance spectroscopy of human adenomatous colon polyps in vivo," *Appl Opt*, vol. 38, pp. 6628-37, Nov 1999.
- [11] M. G. Muller, *et al.*, "Spectroscopic detection and evaluation of morphologic and biochemical changes in early human oral carcinoma," *Cancer*, vol. 97, pp. 1681-92, Apr 2003.
- [12] I. Georgakoudi, *et al.*, "NAD(P)H and collagen as in vivo quantitative fluorescent biomarkers of epithelial precancerous changes," *Cancer Res*, vol. 62, pp. 682-7, Feb 2002.
- [13] B. Mayinger, *et al.*, "Light-induced autofluorescence spectroscopy for the endoscopic detection of esophageal cancer," *Gastrointest Endosc*, vol. 54, pp. 195-201, Aug 2001.
- [14] C. C. Yu, *et al.*, "Quantitative spectroscopic imaging for non-invasive early cancer detection," *Optics Express*, vol. 16, pp. 16227-39, Sep 2008.
- [15] M. C. Skala, *et al.*, "In vivo multiphoton microscopy of NADH and FAD redox states, fluorescence lifetimes, and cellular morphology in precancerous epithelia," *Proc Natl Acad Sci U S A*, vol. 104, pp. 19494-9, Dec 2007.
- [16] J. W. Tunnell, *et al.*, "Instrumentation for multi-modal spectroscopic diagnosis of epithelial dysplasia," *Technol Cancer Res Treat*, vol. 2, pp. 505-14, Dec 2003.
- [17] A. Couvelard, *et al.*, "Angiogenesis in the neoplastic sequence of Barrett's oesophagus. Correlation with VEGF expression," *J Pathol*, vol. 192, pp. 14-8, Sep 2000.
- [18] A. M. Rollins and M. V. Sivak, Jr., "Potential new endoscopic techniques for the earlier diagnosis of pre-malignancy," *Best Pract Res Clin Gastroenterol*, vol. 15, pp. 227-47, Apr 2001.
- [19] G. I. Zonios, "Diffuse Reflectance Spectroscopy of Human Colon Tissue," Department of Physics, Massachusetts Institute of Technology, 1998.
- [20] I. Georgakoudi, "The color of cancer," *Journal of Luminescence* vol. 119-120, pp. 75-83, 2006.
- [21] L. M. Wong Kee Song, "Optical spectroscopy for the detection of dysplasia in Barrett's esophagus," *Clin Gastroenterol Hepatol*, vol. 3, pp. S2-7, Jul 2005.

- [22] R. Richards-Kortum and E. Sevick-Muraca, "Quantitative optical spectroscopy for tissue diagnosis," *Annu Rev Phys Chem*, vol. 47, pp. 555-606, 1996.
- [23] S. Prahl. (Accessed August 2011). *Optical Absorption of Hemoglobin* Available: <http://omlc.ogi.edu/spectra/hemoglobin/>
- [24] R. S. Dacosta, *et al.*, "New optical technologies for earlier endoscopic diagnosis of premalignant gastrointestinal lesions," *J Gastroenterol Hepatol*, vol. 17, pp. S85-104, Feb 2002.
- [25] R. S. DaCosta, *et al.*, "Molecular fluorescence excitation-emission matrices relevant to tissue spectroscopy," *Photochem Photobiol*, vol. 78, pp. 384-92, Oct 2003.
- [26] I. Georgakoudi and J. Van Dam, "Characterization of dysplastic tissue morphology and biochemistry in Barrett's esophagus using diffuse reflectance and light scattering spectroscopy," *Gastrointest Endosc Clin N Am*, vol. 13, pp. 297-308, Apr 2003.
- [27] L. B. Lovat, *et al.*, "Elastic scattering spectroscopy accurately detects high grade dysplasia and cancer in Barrett's oesophagus," *Gut*, vol. 55, pp. 1078-83, Aug 2006.
- [28] M. Panjehpour, *et al.*, "Endoscopic fluorescence detection of high-grade dysplasia in Barrett's esophagus," *Gastroenterology*, vol. 111, pp. 93-101, Jul 1996.
- [29] M. Panjehpour, *et al.*, "Spectroscopic diagnosis of esophageal cancer: new classification model, improved measurement system," *Gastrointest Endosc*, vol. 41, pp. 577-81, Jun 1995.
- [30] G. Bourg-Heckly, *et al.*, "Endoscopic ultraviolet-induced autofluorescence spectroscopy of the esophagus: tissue characterization and potential for early cancer diagnosis," *Endoscopy*, vol. 32, pp. 756-65, Oct 2000.
- [31] T. J. Pfefer, *et al.*, "Temporally and spectrally resolved fluorescence spectroscopy for the detection of high grade dysplasia in Barrett's esophagus," *Lasers Surg Med*, vol. 32, pp. 10-6, 2003.
- [32] T. Vodinh, *et al.*, "In-Vivo Cancer-Diagnosis of the Esophagus Using Differential Normalized Fluorescence (Dnf) Indexes," *Lasers in Surgery and Medicine*, vol. 16, pp. 41-47, 1995.
- [33] T. J. Farrell, *et al.*, "A diffusion theory model of spatially resolved, steady-state diffuse reflectance for the noninvasive determination of tissue optical properties in vivo," *Med Phys*, vol. 19, pp. 879-88, Jul-Aug 1992.
- [34] J. Mirkovic, *et al.*, "Effect of anatomy on spectroscopic detection of cervical dysplasia," *J Biomed Opt*, vol. 14, p. 044021, Jul-Aug 2009.
- [35] M. G. Muller, *et al.*, "Intrinsic fluorescence spectroscopy in turbid media: disentangling effects of scattering and absorption," *Appl Opt*, vol. 40, pp. 4633-46, Sep 1 2001.
- [36] J. Wu, *et al.*, "Analytical model for extracting intrinsic fluorescence in turbid media," *Appl Opt*, vol. 32, pp. 3585-95, Jul 1993.
- [37] Q. Zhang, *et al.*, "Turbidity-free fluorescence spectroscopy of biological tissue," *Opt Lett*, vol. 25, pp. 1451-3, Oct 2000.
- [38] Z. Volynskaya, *et al.*, "Diagnosing breast cancer using diffuse reflectance spectroscopy and intrinsic fluorescence spectroscopy," *J Biomed Opt*, vol. 13, p. 024012, Mar-Apr 2008.

Chapter 4

Miniaturized Spectroscopy System: Components Design and Fabrication

This Chapter describes the miniaturized spectroscopy system that can be integrated in less-invasive medical devices to improve the detection of esophageal dysplasia. This system is based on a narrow-band pass filter array and silicon photodiodes for the selection and detection of different spectral bands significant for diagnosis. The design, fabrication and characterization of the thin-film optical filters that compose the filtering array are exposed. The Chapter is concluded with a brief description of the photodiodes detection system.

4.1 System overview

Different studies have successfully applied DRS and FS for detecting and classifying

dysplasia or cancer in the esophagus [1-7]. The used research prototypes, usually composed by a spectrograph, a detector and optical fibers, are accurate in the identification of dysplasia, and, in some studies, in the quantification of tissue properties.

However, these prototypes (not yet commercially available), designed to perform DRS and FS, suffer from several drawbacks. Regular optical fibers usually have low-collection efficiency, thus requiring high-quantum efficiency detectors (e.g. CCDs). Also, the detector is placed at the distal end of the collection fiber, where considerable light might be lost [8]. In addition, these research prototypes include costly, bulky and sophisticated illumination equipment (e.g. xenon arc lamps, UV lasers). Beyond the disadvantages already listed, catheter-based endoscopy systems using long optical probes are invasive and very uncomfortable for the patient.

Therefore, the development of a low-complexity, miniature, and cost-effective spectroscopy system without the need of optical fibers, spectrograph or CCD cameras could potentially increase the collection efficiency, while simplifying the device. Moreover, such a system could be integrated in small and less-invasive devices, such as the EC, for the assessment of esophageal tissue.

Previous studies have aimed to develop a system with some of these features using LEDs as the illumination sources and photodiodes as the detector [8-9]. Yu *et al.* [9] developed an optical device able to quantitatively assess tissue optical properties using a silicon photodiode for detection. However, a xenon lamp, a monochromator and optical fibers were still used. Lo *et al.* [8] described a spectroscopy system that can integrate LEDs for illumination for wavelength selection, and silicon photodiodes for detection. Even though this study represents a big step towards decreasing the cost and size of conventional spectroscopy systems, only five LED wavelengths are used, which may not be enough to perform quantitative spectroscopy and accurately extract other tissue optical properties besides hemoglobin. The addition of extra LEDs, with an approximate size of 1 mm, can compromise a full integration and size reduction.

In this thesis Chapter it is proposed the development of a potentially robust sub millimeter narrow-band pass filter array that offers prospects for a simplified miniature spectrographic detector that can be integrated, in the future, in a diagnostic device to improve the identification of dysplasia. The proposed miniaturized spectral instrument is based on thin-film optical filters and silicon photodiodes for wavelength selection and signal detection, respectively (Figure 4.1). The narrow-band pass optical filters are centered at 16 specific wavelengths, identified in the feasibility study described in Chapter 3, section 3.6.

Up to the moment, it was not yet developed a miniaturized device that is able to

integrate both FS and DRS functions for early cancer diagnosis. The designed instrument has three major advantages over other spectroscopy systems: (1) it is miniaturized, and thus suitable for a future integration in a less invasive medical device; (2) it integrates components that are compatible with standard microelectronics fabrication techniques (complementary metal oxide semiconductor – CMOS); and, (3) it is able to combine two different spectroscopy techniques – diffuse-reflectance and fluorescence.

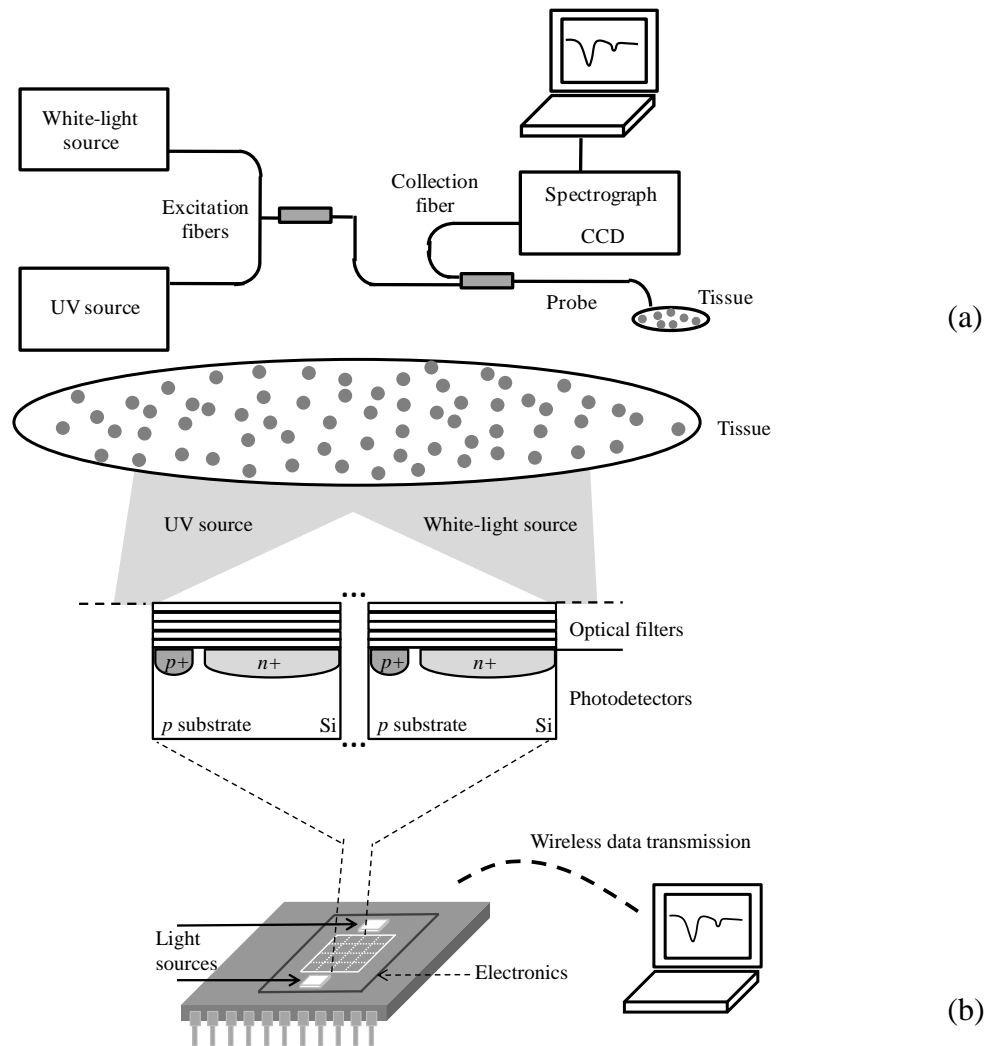


Figure 4.1: Spectroscopy systems. (a) Conventional system with excitation and collection fibers, white-light and UV illumination sources, spectrograph and CCD for detection. (b) Miniaturized system with LEDs as light sources, optical filters and photodetectors for wavelength selection and detection, respectively (not scaled). Data transmission is intended to be wireless.

System components

As previously mentioned, the designed system is composed of thin-film optical filters and silicon photodiodes that will, respectively, select and detect several light wavelengths. Overall, the miniaturized instrument is composed by a 16 narrow-band pass filter array (4 by 4), placed on top of an array of 16 silicon photodiodes. All the 16 filters have a Fabry-Perot multilayer structure made with dielectric materials that are compatible with CMOS fabrication techniques (which is an asset towards the development of a fully miniaturized device, in a

single chip). Also, the use of all-dielectric layers allows a narrow and a high peak transmittance spectral band, as required for the application [10-12]. The reader is referred to section 4.2 for more details about the filters structure and materials.

In addition, commercial small-size UV and white LEDs should be incorporated in the system as the illumination sources for FS and DRS measurements, respectively. UV LEDs are already available at the die level (Nitride Semiconductors Co., Ltd., The Fox Group Inc., among others) whereas white LEDs with high luminous efficiency have already been developed [13]. The use of these components obviates the need for sophisticated and expensive illumination and detection equipment, and optical fibers to deliver and collect light from tissues.

Once a CMOS co-integration process is used, the array area can be scaled down to approximately $200 \times 200 \mu\text{m}^2$. The final encapsulation of the dies on a single chip also requires some space for wiring that will depend on the number of bonding pads (each bonding pad has a maximum size of $100 \times 100 \mu\text{m}^2$) and the encapsulation package. Still, it is expected that the final miniaturized device will not exceed a few millimeters (less than 10 mm^2). The fabrication of the system in a compatible CMOS process will also allow the mass production of the microsystem at reduced costs.

4.2 Thin-film optical filters

The feasibility study described in Chapter 3, section 3.6, provided the group of the 16 wavelengths that better fits the original continuous spectrum. These 16 wavelengths will be selectively detected using thin-film optical filters.

To better understand the performance of thin-film optical filters, it is necessary to accept three statements [12]:

(1) The amplitude of the reflected light at any interface between two media is given by $(1 - \rho_r)/(1 + \rho_r)$, where ρ_r is the ratio of the refractive indices (n). The reflectance is defined as the square of the amplitude.

(2) There is a phase shift of 180° when the reflectance occurs in a medium that has lower refractive index when compared with its adjacent medium; there is a phase shift of 0° when the reflectance occurs in a medium that has higher refractive index when compared with its adjacent medium.

(3) When the light is split into two components by reflection at the top and bottom interfaces of a thin-film, these components will recombine such that: the resultant amplitude is the difference between the amplitudes of the two components, when there is a phase shift of

180° - *beams interfere destructively*; or the resultant amplitude is the sum of the amplitudes of the two components, when there is a phase shift of 0° - *beams interfere constructively*.

As an example, a high-reflective thin-film multilayer structure can be built using a stack of alternate high and low refractive index films, as shown in Figure 4.2.

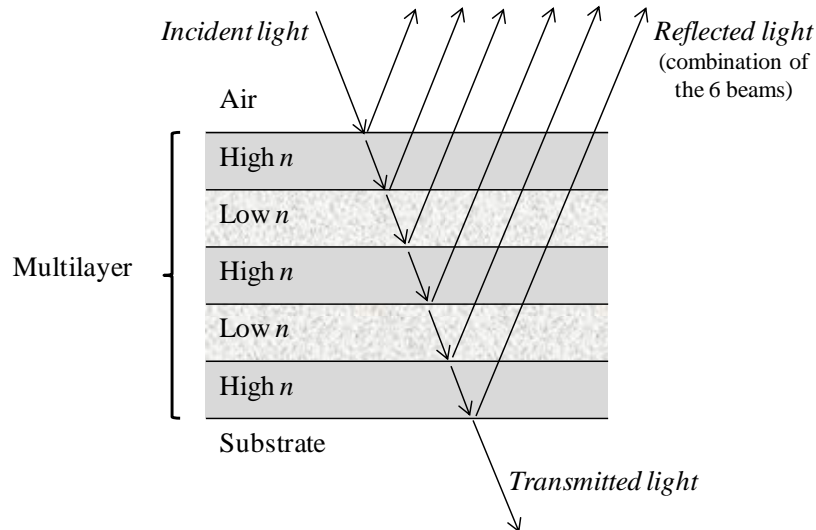


Figure 4.2: Thin-film multilayer structure [12].

In this case, the various components produced by reflection at the different interfaces will reappear at the first interface all in phase, and, therefore, the beams will recombine constructively. This way, it is possible to increase the reflectance of a structure, by increasing only the number of layers.

In these high-reflective structures, the reflectance is high only within a limited range of wavelengths; outside this range, the reflectance drops to low values. This way, the combination of several films or layers with specific thicknesses results in a reflectance spectrum with maxima and minima at specific wavelengths. Due to this behavior, thin-film multilayer structures, such as the one in Figure 4.2, can be used as filters. The filter characteristic in reflection is the complement of that in transmission, when the absorptance equals to zero.

The design of a thin-film multilayer structure to be used as an optical filter is not a straightforward process merely based on calculations of the properties of the multilayer. It is a difficult and time consuming process that requires analytic calculations, computational simulations and a final structure optimization [12].

The first step of this whole process is to develop a possible structure for the filter, using analytical analysis and well-known building blocks. Besides the performance specifications of the filter, the materials to be used are also needed to start the design. The second step involves testing the performance of this initial structure on a computer. The

results will determine if adjustments to the design are needed or not. These adjustments can be done by a computer, or by additional calculations. A final refinement to the filter's design involves an enormous number of parameters, which represent many possibilities of adjustment to match the designed performance with the desired performance. This is, perhaps, the most extensive and cumbersome step.

4.2.1 Basic theory

In this section it will be described some basic theory which is necessary to understand and make the calculations for the design of the multilayer thin-film filters. A summary of the main results will be provided. The reader is referred to the literature for a detailed description of the presented theory [12, 14-15].

Maxwell's equations and electromagnetic waves

Light is an electromagnetic wave, and therefore, the propagation of light in a thin-film multilayer structure is defined by the Maxwell equations. In an isotropic and uniform media these are [12, 15]:

$$\nabla \times E = -\frac{\partial B}{\partial t} \quad (4.1)$$

$$\nabla \times H = j + \frac{\partial D}{\partial t} \quad (4.2)$$

$$\nabla \cdot D = \rho \quad (4.3)$$

$$\nabla \cdot B = 0 \quad (4.4)$$

where E is the electric field strength, H is the magnetic field strength, D is the electric displacement, and B is the magnetic flux density or magnetic induction. Also, j represents the electric current density and ρ the electric charge density.

The electric current density and the electric displacement relate with the electric field strength in the following way:

$$j = \sigma E \quad (4.5)$$

$$D = \varepsilon E \quad (4.6)$$

where σ is the electric conductivity and ε is the electric permittivity of the medium.

The magnetic flux density also relates with the magnetic field strength with the following expression:

$$B = \mu H \quad (4.7)$$

where μ is magnetic permeability of the medium.

In free space, the electric permittivity and magnetic permeability are important constants with the following values:

$$\varepsilon = \varepsilon_0 = 8.854185 \times 10^{-12} \text{ F m}^{-1} \quad (4.8)$$

$$\mu = \mu_0 = 4\pi \times 10^{-7} \text{ H m}^{-1} \quad (4.9)$$

The permittivity of free space can be expressed as:

$$\varepsilon_0 = \frac{1}{(\mu_0 c^2)} \quad (4.10)$$

where c is a constant identified as the velocity of light in a vacuum or in free space: $c = 2.997925 \times 10^8 \text{ m s}^{-1}$.

The following analysis is brief, and for further details the reader is referred to the literature in which this analysis was based [12, 15].

For this analysis, it will be considered a medium free of sources for the electric and magnetic fields, this is, $j = 0$ and $\rho = 0$. The Maxwell's equations for source free media show that the electric and magnetic fields are coupled: variations in the electric field act as a source for the magnetic field, which in turn acts as a source for the electric field, and so on. The electric and magnetic field can be seen as a unique entity (the electromagnetic field) and are mutually compatible: changes in one generate the other.

In this case, equation 4.1 can be solved using equations 4.2, 4.3, 4.6, and 4.7, to obtain the following expression:

$$\nabla^2 E = \mu\varepsilon \frac{\partial^2}{\partial t^2} E \quad (4.11)$$

Using the same procedure, it is possible to obtain the next equation for the magnetic induction:

$$\nabla^2 B = \mu\varepsilon \frac{\partial^2}{\partial t^2} B \quad (4.12)$$

Equations 4.11 and 4.12 are wave equations that can be related to the velocity of light in a medium, v , with the following expression:

$$v = \frac{1}{\sqrt{\mu\varepsilon}} \quad (4.13)$$

The ration between the velocity of light in a vacuum, c , and the velocity of light in a

specific medium, v , defines the refractive index of that medium, n :

$$n = \frac{c}{v} = \sqrt{\frac{\epsilon\mu}{\epsilon_0\mu_0}} \quad (4.14)$$

In general, the magnetic properties of the medium have a negligible effect on the velocity of light propagation. For this reason one can consider $\mu \approx \mu_0$ [15]. This way, the refractive index of a medium is basically determined by its permittivity, ϵ , which depends on the frequency of the incident electromagnetic wave.

Equations 4.11 and 4.12 have the following solutions for plane waves:

$$E = \text{Re}\{E_0 e^{i(\omega t - \mathbf{k}\cdot\mathbf{r} + \phi)}\} \quad (4.15)$$

$$B = \text{Re}\{B_0 e^{i(\omega t - \mathbf{k}\cdot\mathbf{r} + \phi)}\} \quad (4.16)$$

where Re indicates the real part (the physical fields are always given by the real part of the complex fields that appear in the expressions), E_0 and B_0 represent the amplitudes of the oscillations, ω is the angular frequency, ϕ is the phase of the wave, \mathbf{r} is the position vector, and \mathbf{k} is the wave vector, being defined as:

$$|\mathbf{k}| = k = \frac{2\pi n}{\lambda} \quad (4.17)$$

where k is known as the wavenumber.

The frequency, f , and the wavelength, λ , of an electromagnetic wave are given by:

$$f = \frac{\omega}{2\pi} \quad (4.18)$$

$$\lambda = \frac{2\pi}{k} \quad (4.19)$$

An important feature of electromagnetic waves is that they are a form of energy transport. The electromagnetic energy density, u , can be defined as:

$$u = \frac{1}{2}(E \cdot D + B \cdot H) \quad (4.20)$$

The energy flux across unit area, in the wave propagation direction, is known as *Poynting vector*, S :

$$S = E \cdot H \quad (4.21)$$

The optical admittance of a medium is another important concept for the design of thin-film structures: it defines how easy or hard it is for light to pass through it. For free space it can be expressed as:

$$y = \sqrt{\frac{\epsilon_0}{\mu_0}} = 2.6544 \times 10^{-3} \text{ S} \quad (4.22)$$

The optical admittance of a material is numerically equal to its refractive index, n . The optical admittance, or the refractive index, connects the electric and magnetic fields, E and H , respectively, through the following expression:

$$n = \frac{H}{E} \quad (4.23)$$

Thin-film structures

A thin-film structure, with more than one interface or boundary, is schematically represented in Figure 4.3.

For the analysis of light propagation in this thin-film structure, it is convenient to define the direction of incidence of the waves using a symbol + for waves that are in the direction of incidence (i.e. positive-going), and a symbol – for waves that are in the opposite direction (i.e. negative-going) [12, 16].

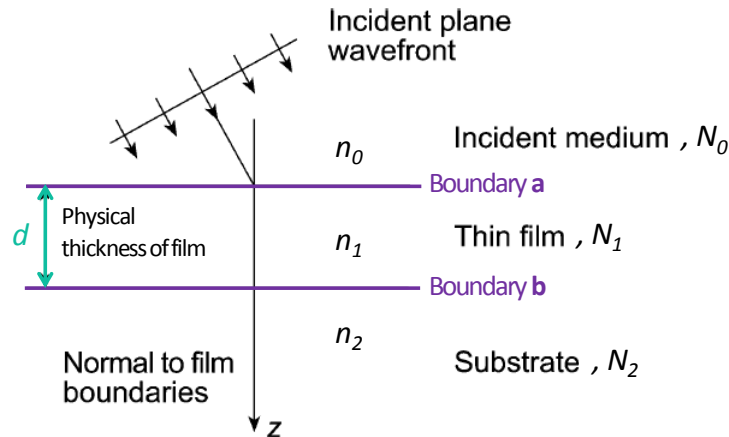


Figure 4.3: Plane wave incident on a thin-film structure [12].

Considering now the interface between the film and the substrate (boundary **b**), there are no negative-going waves in the substrate, and the waves in the film can be summed into one resultant positive-going wave and one resultant negative-going wave. This way, it can be defined:

$$E_b = E_{1b}^+ + E_{1b}^- \quad (4.24)$$

$$H_b = n_1 E_{1b}^+ - n_1 E_{1b}^- \quad (4.25)$$

where

$$E_{1b}^+ = \frac{1}{2} \left(\frac{H_b}{n_1} + E_b \right) \quad (4.26)$$

$$E_{1b}^- = \frac{1}{2} \left(-\frac{H_b}{n_1} + E_b \right) \quad (4.27)$$

$$H_{1b}^+ = n_1 E_{1b}^+ = \frac{1}{2} (H_b + n_1 E_b) \quad (4.28)$$

$$H_{1b}^- = -n_1 E_{1b}^- = \frac{1}{2} (H_b - n_1 E_b) \quad (4.29)$$

The fields at the interface **a**, at the same instant and at the same point, can be determined by changing the phase factors of the waves, in order to allow a shift in the z coordinate, from 0 to $-d$. The phase factor of the positive-going wave will be multiplied by $\exp(\delta)$, while the phase factor of the negative-going wave will be multiplied by $\exp(-\delta)$, where

$$\delta = \frac{2\pi n_1 d \cos\theta}{\lambda} \quad (4.30)$$

d represents the physical thickness of the film, and θ represents the angle of incidence. δ is known as the *phase thickness* and corresponds to the phase shift experienced by the wave as it traverses a distance d normal to the boundary [12, 16].

The optical path length (*OPL*), which is defined as the distance traveled in a thin-film by light, can also be expressed in the following way:

$$OPL = n_1 d \cos\theta \quad (4.31)$$

The values of E and H at interface **a**, can now be defined as:

$$E_{1a}^+ = \frac{1}{2} \left(\frac{H_b}{n_1} + E_b \right) e^\delta \quad (4.32)$$

$$E_{1a}^- = \frac{1}{2} \left(-\frac{H_b}{n_1} + E_b \right) e^{-\delta} \quad (4.33)$$

$$H_{1a}^+ = \frac{1}{2} (H_b + n_1 E_b) e^\delta \quad (4.34)$$

$$H_{1a}^- = \frac{1}{2} (H_b - n_1 E_b) e^{-\delta} \quad (4.35)$$

Using equations 4.32 to 4.35:

$$E_a = E_{1a}^+ + E_{1a}^- = E_b \left(\frac{e^\delta + e^{-\delta}}{2} \right) + H_b \left(\frac{e^\delta - e^{-\delta}}{2n_1} \right) = E_b \cos\delta + H_b \frac{\sin\delta}{n_1} \quad (4.36)$$

$$\begin{aligned} H_a &= H_{1a}^+ + H_{1a}^- = E_b n_1 \left(\frac{e^\delta - e^{-\delta}}{2} \right) + H_b \left(\frac{e^\delta + e^{-\delta}}{2} \right) \\ &= E_b n_1 \sin\delta + H_b \cos\delta \end{aligned} \quad (4.37)$$

These last two equations can be written in matrix notation:

$$\begin{bmatrix} E_a \\ H_a \end{bmatrix} = \begin{bmatrix} \cos\delta & \frac{\sin\delta}{n_1} \\ n_1 \sin\delta & \cos\delta \end{bmatrix} \begin{bmatrix} E_b \\ H_b \end{bmatrix} \quad (4.38)$$

This relation connects the components of E and H at the incident interface, with the components of E and H that are transmitted through the final interface. The 2 by 2 matrix is known as the *characteristic matrix of the thin-film* [12, 16].

The optical admittance of the thin-film structure is defined similarly to equation 4.23:

$$Y = \frac{H_a}{E_a} \quad (4.39)$$

The reflectance of an interface between an incident medium of admittance n_0 and a medium of admittance Y is given by:

$$R = \left(\frac{n_0 - Y}{n_0 + Y} \right) \left(\frac{n_0 - Y}{n_0 + Y} \right) \quad (4.40)$$

Equation 4.38 can be normalized by dividing through by E_b :

$$\begin{bmatrix} \frac{E_a}{E_b} \\ \frac{H_a}{E_b} \end{bmatrix} = \begin{bmatrix} \mathcal{B} \\ \mathcal{C} \end{bmatrix} = \begin{bmatrix} \cos\delta & \frac{\sin\delta}{n_1} \\ n_1 \sin\delta & \cos\delta \end{bmatrix} \begin{bmatrix} 1 \\ n_2 \end{bmatrix} \quad (4.41)$$

where \mathcal{B} and \mathcal{C} are the normalized electric and magnetic fields at the front interface. These quantities are used to extract the properties of the thin-film. From Equations 4.39 and 4.41, it can be written:

$$Y = \frac{H_a}{E_a} = \frac{\mathcal{C}}{\mathcal{B}} = \frac{n_2 \cos\delta + n_1 \sin\delta}{\cos\delta + \left(\frac{n_2}{n_1} \right) \sin\delta} \quad (4.42)$$

From equations 4.40 and 4.42, the reflectance can be calculated:

$$\begin{bmatrix} \mathcal{B} \\ \mathcal{C} \end{bmatrix}$$

known as the *characteristic matrix of the assembly* [12, 16].

All the above analysis was done for a single film. A similar methodology can be applied to an assembly of thin-films. In Figure 4.4 a structure with two thin-films is represented.

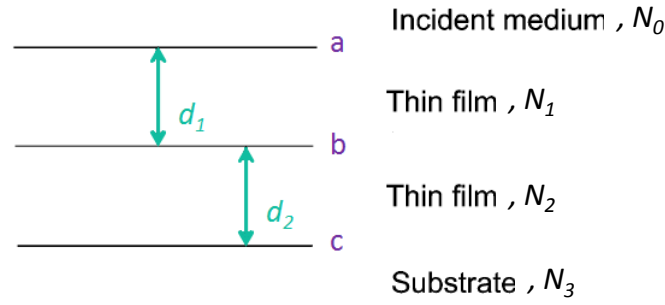


Figure 4.4: Structure with two thin-films and three interfaces (a, b, and c) [12].

The characteristic matrix of the thin-film N_2 can be expressed by:

$$\begin{bmatrix} \cos\delta_2 & \frac{\sin\delta_2}{n_2} \\ n_2\sin\delta_2 & \cos\delta_2 \end{bmatrix} \quad (4.43)$$

Applying equation 4.38, the parameters at the interfaces **b** and **a** can be obtained:

$$\begin{bmatrix} E_b \\ H_b \end{bmatrix} = \begin{bmatrix} \cos\delta_2 & \frac{\sin\delta_2}{n_2} \\ n_2\sin\delta_2 & \cos\delta_2 \end{bmatrix} \begin{bmatrix} E_c \\ H_c \end{bmatrix} \quad (4.44)$$

$$\begin{bmatrix} E_a \\ H_a \end{bmatrix} = \begin{bmatrix} \cos\delta_1 & \frac{\sin\delta_1}{n_1} \\ n_1\sin\delta_1 & \cos\delta_1 \end{bmatrix} \begin{bmatrix} \cos\delta_2 & \frac{\sin\delta_2}{n_2} \\ n_2\sin\delta_2 & \cos\delta_2 \end{bmatrix} \begin{bmatrix} E_c \\ H_c \end{bmatrix} \quad (4.45)$$

The *characteristic matrix of the assembly* is given by:

$$\begin{bmatrix} \mathcal{B} \\ \mathcal{C} \end{bmatrix} = \begin{bmatrix} \cos\delta_1 & \frac{\sin\delta_1}{n_1} \\ n_1\sin\delta_1 & \cos\delta_1 \end{bmatrix} \begin{bmatrix} \cos\delta_2 & \frac{\sin\delta_2}{n_2} \\ n_2\sin\delta_2 & \cos\delta_2 \end{bmatrix} \begin{bmatrix} 1 \\ n_3 \end{bmatrix} \quad (4.46)$$

This result can be generalized and extended for a multilayer of Z layers. The *characteristic matrix of the assembly* is the basis for many thin-film calculations, and is defined by the product of the individual matrices, in the correct order:

$$\begin{bmatrix} \mathcal{B} \\ \mathcal{C} \end{bmatrix} = \left\{ \prod_{r=1}^Z \begin{bmatrix} \cos\delta_r & \frac{\sin\delta_r}{n_r} \\ n_r\sin\delta_r & \cos\delta_r \end{bmatrix} \right\} \begin{bmatrix} 1 \\ n_m \end{bmatrix} \quad (4.47)$$

with

$$\delta_r = \frac{2\pi n_r d_r \cos\theta_r}{\lambda} \quad (4.48)$$

The suffix m denotes the substrate. If the angle of incidence, θ_0 , is known, it is

possible to determine the values of θ_r using the Snell's law:

$$n_0 \sin \theta_0 = n_r \sin \theta_r = n_m \sin \theta_m \quad (4.49)$$

The reflectance, R , of the assembly can be determined using equation 4.40. Replacing the Y and using equation 4.42, the reflectance expression can be re-written:

$$R = \left(\frac{n_0 \mathcal{B} - \mathcal{C}}{n_0 \mathcal{B} + \mathcal{C}} \right) \left(\frac{n_0 \mathcal{B} - \mathcal{C}}{n_0 \mathcal{B} + \mathcal{C}} \right) \quad (4.50)$$

The transmittance, T , into the substrate is given by:

$$T = \frac{\operatorname{Re}(n_m)(1 - R)}{\operatorname{Re}(\mathcal{B}\mathcal{C})} \quad (4.51)$$

Combining equations 4.50 and 4.51, it is possible to obtain the final expression for the transmittance:

$$T = \frac{4n_0 \operatorname{Re}(n_m)}{(n_0 \mathcal{B} + \mathcal{C})(n_0 \mathcal{B} + \mathcal{C})} \quad (4.52)$$

The absorptance, Abs , is a phenomenon that occurs when the incident light in a thin-film is converted to another form of energy, usually heat, inside that thin-film [12, 16]. It can be related to the transmittance and reflectance through the following expression:

$$1 = R + T + Abs \quad (4.53)$$

Therefore, the equation to calculate the absorptance using equations 4.50 and 4.52 can be written:

$$Abs = \frac{4n_0 \operatorname{Re}(\mathcal{B}\mathcal{C} - n_m)}{(n_0 \mathcal{B} + \mathcal{C})(n_0 \mathcal{B} + \mathcal{C})} \quad (4.54)$$

Dielectric thin-films: quarter- and half-wave optical thicknesses

The *characteristic matrix* of a dielectric thin-film, for a normal incidence, can be simplified if the optical thickness (which in a transparent medium is the same as the *OPL*) is an integer number of quarter-wave or half-wave thicknesses.

If $\delta = \pi$, $\cos \delta = 1$ and $\sin \delta = 0$, so that the layer is an integer number of half-wavelengths thick, $(\lambda/2)$, the matrix becomes:

$$\begin{bmatrix} -1 & 0 \\ 0 & -1 \end{bmatrix}$$

This is the unit matrix and has no effect on the reflectance or transmittance of an assembly, this is, the structure behaves as if there were no thin-film layers deposited on the substrate.

If $\delta = \frac{\pi}{2}$, $\cos \delta = 0$ and $\sin \delta = 1$, so that the layer is an odd number of quarter-

wavelengths thick, $(\lambda/4)$, the matrix becomes:

$$\begin{bmatrix} 0 & 1 \\ n & 0 \end{bmatrix}$$

In this case, if a multilayer structure has an admittance Y , the addition of an odd number of quarter-waves of admittance n' will alter the admittance of the whole assembly to n'^2/Y . This way, it is easy to calculate the properties of an assembly of quarter-wave thickness layers. For example, for a stack of three layers, the admittance is:

$$Y = \frac{n'_1 n'_3}{n'_2 n'_m} \quad (4.55)$$

From the above analysis, it is possible to conclude that, at a normal incidence, if the film has an OPL of $\lambda/4$, $3\lambda/4$, ..., $x\lambda/4$, with x being an odd integer number, the reflectance of the assembly will have its maximum or minimum peak, depending if the n of the thin-film is higher or lower than the n of the substrate, respectively. For a thin-film with an OPL of $\lambda/2$, $2\lambda/2$, ..., $x\lambda/2$, with x being an integer number, the reflectance of the structure will not vary compared with the reflectance of the substrate without a deposited thin-film [12, 16].

4.2.2 Optical filters design

As previously explained, it is simpler to calculate the properties of assemblies using quarter- or half-wave optical thicknesses. Thus, the design of the optical filters will be specified in terms of fractions or quarter-waves at a specific reference wavelength. In a multilayer with two different dielectric materials, quarter-wave thickness layers are generally represented by H_n and L_n , depending if the material has the highest (H_n) or lowest (L_n) refractive index. On the other hand, half-wave thickness layers are denoted by $H_n H_n$ or $L_n L_n$ [12].

Next below, it is shown an example of a multilayer structure with half-wave and quarter-wave thickness layers, with air as the incident medium, and glass as the substrate [16]:

$$\text{Incident medium } H_n L_n H_n L_n L_n H_n L_n H_n \text{ Substrate} \quad (4.56)$$

The thin-film stack matrices $(H_n L_n H_n L_n L_n H_n L_n H_n)$ can be written as:

$$\begin{bmatrix} 0 & 1 \\ n & 0 \end{bmatrix} \times \begin{bmatrix} -1 & 0 \\ 0 & -1 \end{bmatrix} \times \begin{bmatrix} 0 & 1 \\ n & 0 \end{bmatrix} = \begin{bmatrix} -1 & 0 \\ 0 & -1 \end{bmatrix}$$

Therefore, from equation 4.46, the *characteristic matrix* of the assembly can be expressed as:

$$\begin{bmatrix} B \\ C \end{bmatrix} = \begin{bmatrix} -1 & 0 \\ 0 & -1 \end{bmatrix} \times \begin{bmatrix} 1 \\ n_m \end{bmatrix}$$

Given that the refractive index of the substrate (glass) is equal to 1.52:

$$B = -1$$

$$C = -1.52$$

The refractive index of the incident medium (air) is equal to 1. The reflectance and transmittance of the structure can be then calculated using equations 4.50 and 4.51:

$$R = 0.0425$$

$$T = 0.9575$$

Structure

A narrow-band optical filter can be built using an assembly of thin-films that produce simultaneously pass and rejection bands. The filtering array for the miniaturized spectroscopy system will have a Fabry-Perot interferometer structure, with a total of 11 layers of dielectric materials. This type of structure allows for a narrow-band thin-film filter: for collimated light, the transmittance will be low for all wavelengths, except for a series of very narrow transmission bands.

The Fabry-Perot interferometers consist of two flat parallel mirrors (reflecting surfaces) separated by a pre-defined distance, d_r , with a resonance cavity in the middle (Figure 4.5) [12, 17].

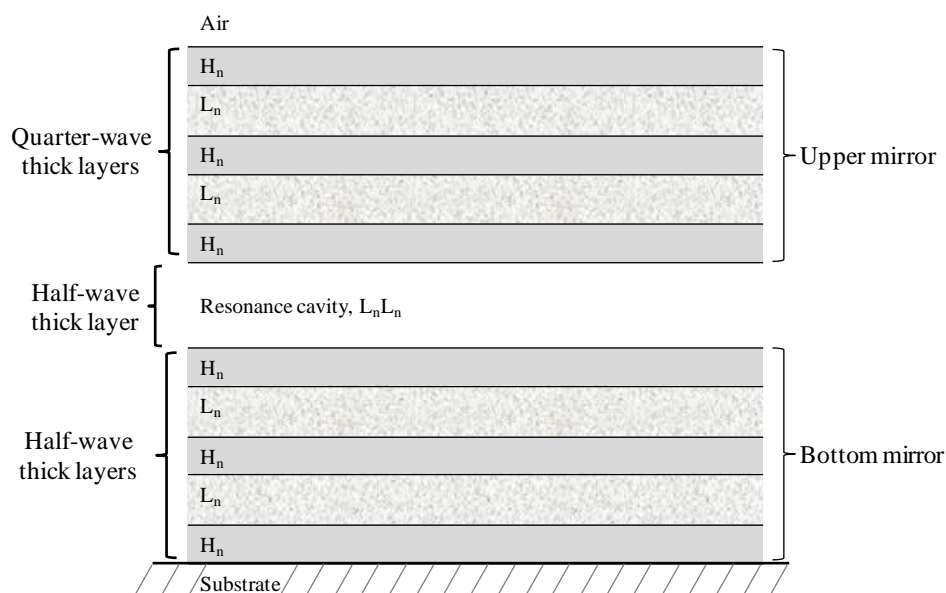


Figure 4.5: Structure of a Fabry-Perot filter [12].

When an incident wave reaches the first surface of the resonance cavity in the Fabry-Perot assembly (Figure 4.6) it is divided into two waves: one reflected (R1) and the other

transmitted into the cavity (first dashed arrow). This transmitted wave will, in turn, reach the second surface of the resonance cavity and again will be divided into two waves: one transmitted (T1) and the other reflected back at the Fabry-Perot in the direction of the first surface (second dashed arrow). This process continues and is repeated along the entire Fabry-Perot assembly. The total transmitted light corresponds to the sum of the contributions of all the transmitted waves (indicated in Figure 4.6 by the letter T).

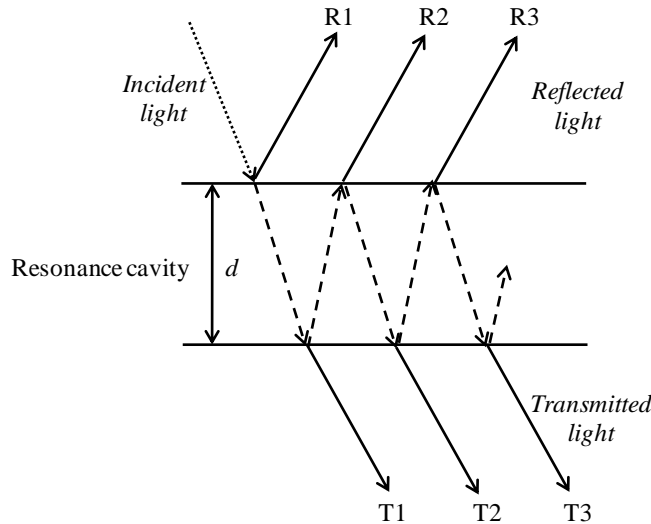


Figure 4.6: Schematic diagram of the propagation of light in a Fabry-Perot assembly.

If the reflectance of mirrors is sufficiently high [12], the total intensity of the light transmitted by the Fabry-Perot filter can be determined using the following expression:

$$I_T = \frac{I_0}{1 + F \sin^2 \delta} \quad (4.57)$$

where I_0 is the intensity of the incident beam, and F is a Fabry-Perot interferometer function, known as *coefficient of finesse*:

$$F = \frac{4R}{(1 - R)^2} \quad (4.58)$$

As F increases, and thus as the mirrors reflectivity increases, the widths of the transmitted peaks become much narrower [12].

When the peaks are very narrow, light is transmitted only if the resonance cavity thickness, d_r , the refractive index, n , and the wavelength, λ , satisfy the following relation:

$$\delta = \frac{2\pi n d \cos \theta}{\lambda} = q\pi \quad (4.59)$$

where q is the peak order.

This way, for a specific separation between the mirrors, the Fabry-Perot filter, will transmit only the wavelength that satisfies equation 4.59. However, it is important to note that

the Fabry-Perot transmission pattern will repeat when δ increases by π .

As a simplified approach to make the filters analytical calculations it will be considered an order of 1 and a normal incidence of light. This way, the separation between the mirrors can be calculated as follows:

$$d_r = \frac{\lambda}{2n} \quad (4.60)$$

where λ is the specific wavelength that will be transmitted by the structure. From this expression, and for the transmission of the same wavelength, the thickness of the quarter-wave layers in the Fabry-Perot assembly can be calculated using the equation:

$$d_m = \frac{\lambda}{4n} \quad (4.61)$$

The transmitted peak FWHM, which corresponds to the width of the band measured at half the peak transmission, can also be determined for large values of F using the following approximation:

$$FWHM = \frac{2}{\sqrt{F}} = \frac{(1-R)}{\sqrt{R}} \quad (4.62)$$

The obtained results in sections 3.6.2 and 3.6.3 showed the viability of using 16 wavelengths to extract tissue biochemical and morphological information. The selection of these 16 wavelengths will be achieved, as already mentioned, using a 16 narrow-band pass optical filter array. An array of 16 optical filters was designed instead of a tunable optical filter since in the latter approach it is hard to guarantee a high degree of flatness and parallelism of the mirrors. A conventional tunable filter usually comprises an air-gap cavity and one movable mirror using, for example, electrostatic actuation. Some include simultaneous displacement sensing, resulting in adjustable mirror spacing. This approach has four disadvantages: (1) fabrication requires complex micromachining, which is difficult to be merged with a standard microelectronics process; (2) large voltages are required for actuation; (3) it is necessary electronics to control the mirrors adjustment, which increases the silicon area; and (4) operation is difficult, mainly for achieving parallelism between the mirrors during the tuning of the filter. A widely used alternative to solve the problem of maintaining parallel mirrors is the one reported here: an array of non-tunable devices with differently sized fixed cavity thicknesses. Such a device is relatively simple to operate. As a drawback, it requires a larger area (proportional to the number of differently sized cavities) when compared to the tunable filter [18-19].

The filtering array is composed of three groups of optical filters to cover different regions of the spectrum: (1) near-UV/violet (350 to 450 nm); (2) central band of the visible spectrum (480 to 600 nm); (3) red (620 to 750 nm). In each group, the quarter-wave layers of

the assembly will all have the same thickness (but, of course, the thickness of the high-refractive index layers is different from the low refractive index layers). This way, in each region, the assembly of thin-films can be easily tuned to transmit a different wavelength by adjusting only the thickness of the resonance cavity, e.g., the 6th layer (Figure 4.5). This enables the fabrication of several optical filters in each region of the spectrum while minimizing the global deposition time.

Materials

The designed filters are all-dielectric assemblies, with the mirrors composed of a stack of TiO₂ (titanium dioxide) and SiO₂ (silicon dioxide) thin-films (high and low refractive index materials, respectively, in the visible spectrum) that offer good performance characteristics: a narrow and high peak transmittance spectral band; high reflectivity; and low absorption losses because of its transparency. Moreover, TiO₂ and SiO₂ have been selected because they can be co-integrated on CMOS, thus being compatible with standard microelectronics fabrication techniques (which is an asset towards the development of a fully miniaturized device, in a single chip). Also, their deposition process is well characterized, and the refractive index of SiO₂ for the spectral band between 350 nm and 750 nm is almost wavelength independent [12, 17, 20-22].

As an approximation for the analytical calculations of the layer thicknesses in each group of filters, equations 4.60 and 4.61 were used, together with the refractive indices provided by the *Sopra* database [23]. Since, in each group, the goal is to tune the filters for different wavelengths by changing only one layer (i.e. the resonance cavity), the thicknesses of the quarter-wave layers have to be calculated using as reference a central wavelength ($\lambda_{\text{reference}}$) in that specific group or region. This is,

(1) For the near-UV/violet region: $\lambda_{\text{reference}}$ is equal to 400 nm; and $n_{\text{SiO}_2} = 1.4701$ and $n_{\text{TiO}_2} = 3.2861$. Therefore, and according to equation 4.61, the thickness of the SiO₂ layers is approximately equal to 68 nm, while the thickness of the TiO₂ layers is approximately equal to 30 nm. The resonance cavity spacing is equal to 136 nm for the transmission of that specific wavelength (i.e. 400 nm).

(2) For the central band of the visible spectrum: $\lambda_{\text{reference}}$ is equal to 550 nm; and $n_{\text{SiO}_2} = 1.4590$ and $n_{\text{TiO}_2} = 2.9544$. This way, and according to equation 4.61 the thickness of the SiO₂ layers can be approximated to 95 nm, while the thickness of the TiO₂ layers can be approximated to 45 nm. The resonance cavity spacing is equal to 190 nm for the transmission of that specific wavelength (i.e. 550 nm).

(3) For the red region: $\lambda_{\text{reference}}$ is equal to 680 nm; and $n_{\text{SiO}_2} = 1.4556$ and

$n_{TiO_2} = 2.8400$. Thus, and according to equation 4.61, the thickness of the SiO_2 layers is approximately equal to 117 nm, while the thickness of the TiO_2 layers is approximately equal to 60 nm. The resonance cavity spacing is equal to 234 nm for the transmission of that specific wavelength (i.e. 680 nm).

After these initial calculations, computational simulations were performed for the structural optimization of the optical filters and for the determination of the other resonance cavity thicknesses, in order to select the remaining 13 wavelengths. All the determined thicknesses are indicated in Table 4.1. It was not possible to determine a thickness for the resonance cavity of the filter centered at 350 nm, as will be explained next in section 4.2.3.

Table 4.1: Layer thicknesses of the 16 Fabry-Perot optical filters.

Maximum wavelength transmission																	
350	370	380	400	420	450	480	510	540	560	580	600	620	650	700	750		
Layer thicknesses (nm)																	
TiO_2	30						45						60				
SiO_2	68						95						117				
TiO_2	30						45						60				
SiO_2	68						95						117				
TiO_2	30						45						60				
SiO_2	-	112	121	136	152	174	140	163	184	199	214	229	189	211	248	285	
TiO_2	30						45						60				
SiO_2	68						95						117				
TiO_2	30						45						60				
SiO_2	68						95						117				
TiO_2	30						45						60				

4.2.3 Optical filters simulation results

The thin-film optics software TFCalcTM 3.5 (Software Spectra, Inc., Portland, OR) was used for the structural optimization of the optical filters through computational simulations that included the materials optical properties. During this step the transmittance peak and bandwidth of the filters (FWHM) were analyzed. The FWHM translates the quality of the filter in terms of its ability to select a narrow band of the electromagnetic spectrum, and therefore, ideally, should be as low as possible. Additionally, the transmittance peak should be high, with at least twice the intensity of any background noise that might appear in the considered spectral range, so that it is possible to clearly discriminate the specific wavelengths, without noise overlap (if it is less, the background noise will significantly affect

the measurements) [12].

For all the simulations the following features were set in the software (Figure 4.7):

(1) a glass substrate with optical properties similar to the glass that will be after used as a substrate in the fabrication process (i.e. Corning® Eagle²⁰⁰⁰™). The substrate thickness equals to 500 μm, and the refractive index equals to 1.5090 at 550 nm;

(2) air as the incident medium;

(3) normal incidence of light in the first surface;

(4) an ideal detector.

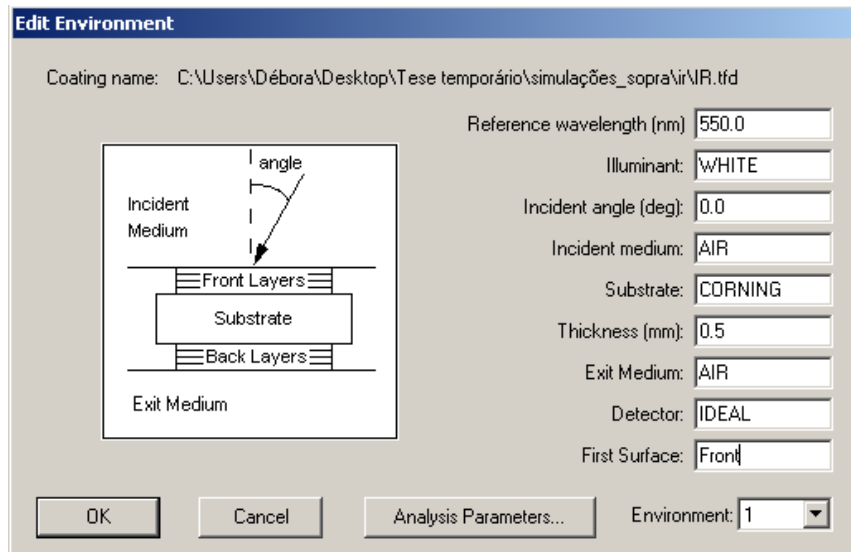


Figure 4.7: Environment setting in the software TFCalc 3.5 for the transmittance simulations of the optical filters.

Simulation results of the filters transmittance for this initial step are presented in Figure 4.8.

For the near-UV/violet and red regions a short-pass filter at 500 nm and a high-pass filter at 550 nm, respectively, were assumed in order to eliminate the tails of the filters far outside these spectral regions. For the central visible region the simulations were performed assuming a wide-band pass filter (200 nm wide) on top of the optical filters.

These three filters can be fabricated, as well, using an assembly of dielectric thin-films. This way, it is possible to deposit the three filters directly on top of each group of narrow-band filters, in the same fabrication process. For example, a 200 nm wide-band pass filter for the 450-650 nm region can be easily obtained with a multilayer structure, composed by 11 layers of SiO₂ and TiO₂, which can be represented by: $L_n H_n L_n H_n L_n H_n L_n H_n L_n H_n L_n$. All these layers have a thickness equal to 88 nm. The multilayer has an average transmittance higher than 90%.

Still, the fabrication of these filters is beyond the scope of this thesis. Therefore, only the different narrow-band interference filters will be fabricated. It is important to notice that

knowing the theory and how to design the filters, and after studying and optimizing the fabrication process for the deposition of the narrow-band filters, the fabrication of the high-, low- and band-pass filters should not be a hard task. For the experimental measurements commercial filters will be used on top of the thin-film optical filters.

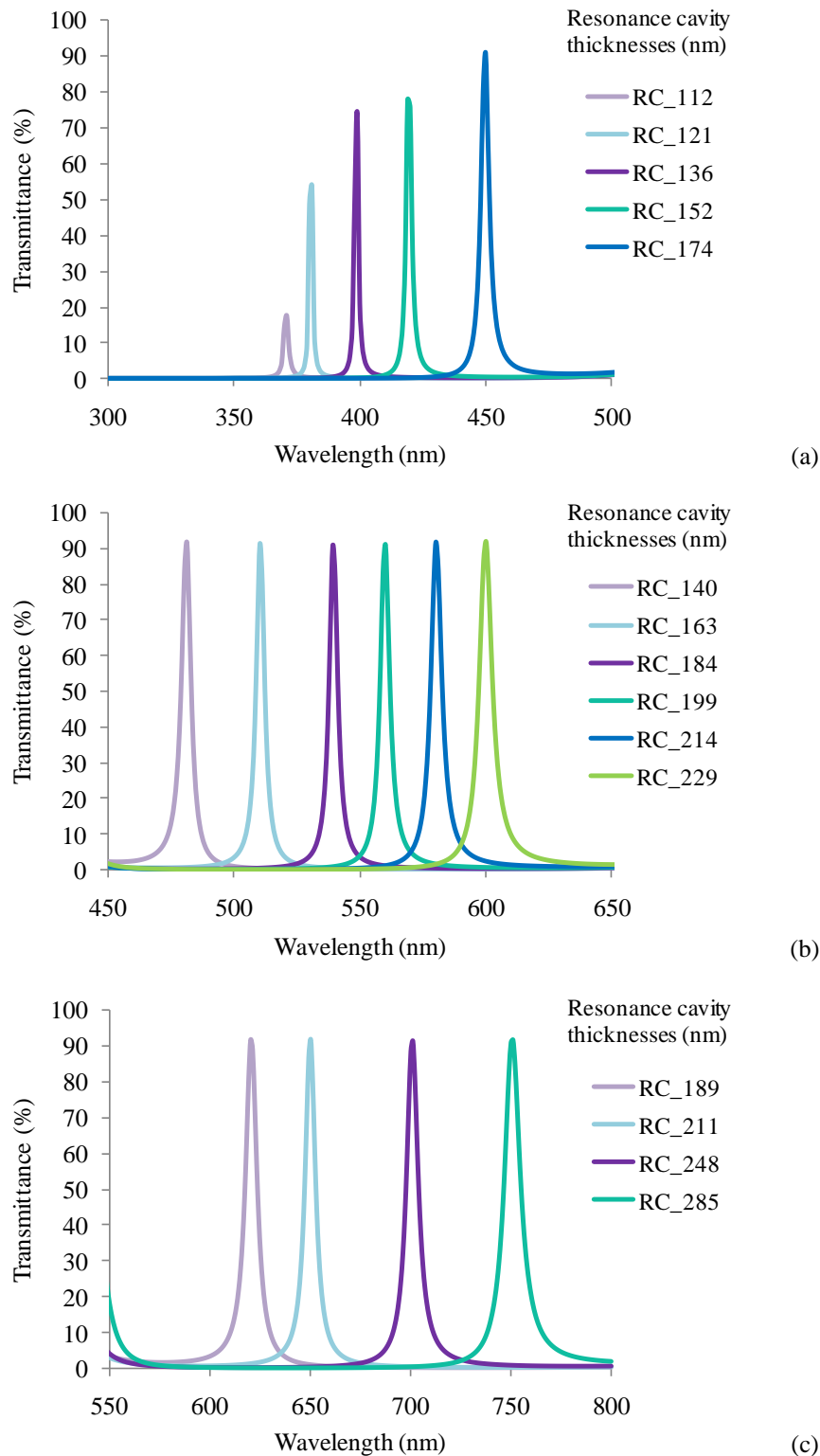


Figure 4.8: Simulated transmittance spectra for the designed thin-film optical filters, with layer thicknesses indicated in Table 4.1: (a) filters of the near-UV/violet region; (b) filters of the central region of the visible spectrum; (c) filters of the red spectral region.

The attenuation of the filter's tails far outside their spectral region can also be achieved by designing photodiodes with higher quantum efficiency in particular regions of the spectrum. This will be discussed in section 4.3.

It was not possible to present the transmittance of the 350 nm optical filter, using the materials and thicknesses indicated in Table 4.1, since the transmittance obtained for this filter in the simulations was smaller than 0.5%. This can be in part explained by the fact that the transmission of the glass used for the substrate (as most glasses) starts decreasing below 370 nm. However, it may also be explained by the properties of the materials being used, namely their refractive indices.

For the remaining 15 filters it can be seen that: each spectral band has a transmittance higher than 90%, except for three filters in the near-UV/violet spectral region, which may due to the same reasons previously indicated for the 350 nm filter; the FWHM is less than 10 nm (average around 6 nm); the transmittance background noise is less than 5%, except for the 750 nm filter; and, the interference of each neighbor peak is less than 10% in each group.

Table 4.1 represents, this way, an assembly of dielectric layers with a specific number of layers and a combination of thicknesses that allows one to obtain a good performance for the optical filters and in accordance with the requirements of the application (e.g. high transmittance, narrow-band pass), as illustrated in Figure 4.8.

If, for example, the filters were designed with 7 layers instead of 11 layers (aiming at faster film deposition), the transmittance peak would not have a significant change, except for the near-UV/violet filters where the transmittance peaks are higher, but the FWHM, the background noise and the neighbor peak interference would be worse, with values around 20 nm, 15% and 50%, respectively, as depicted in Figure 4.9.

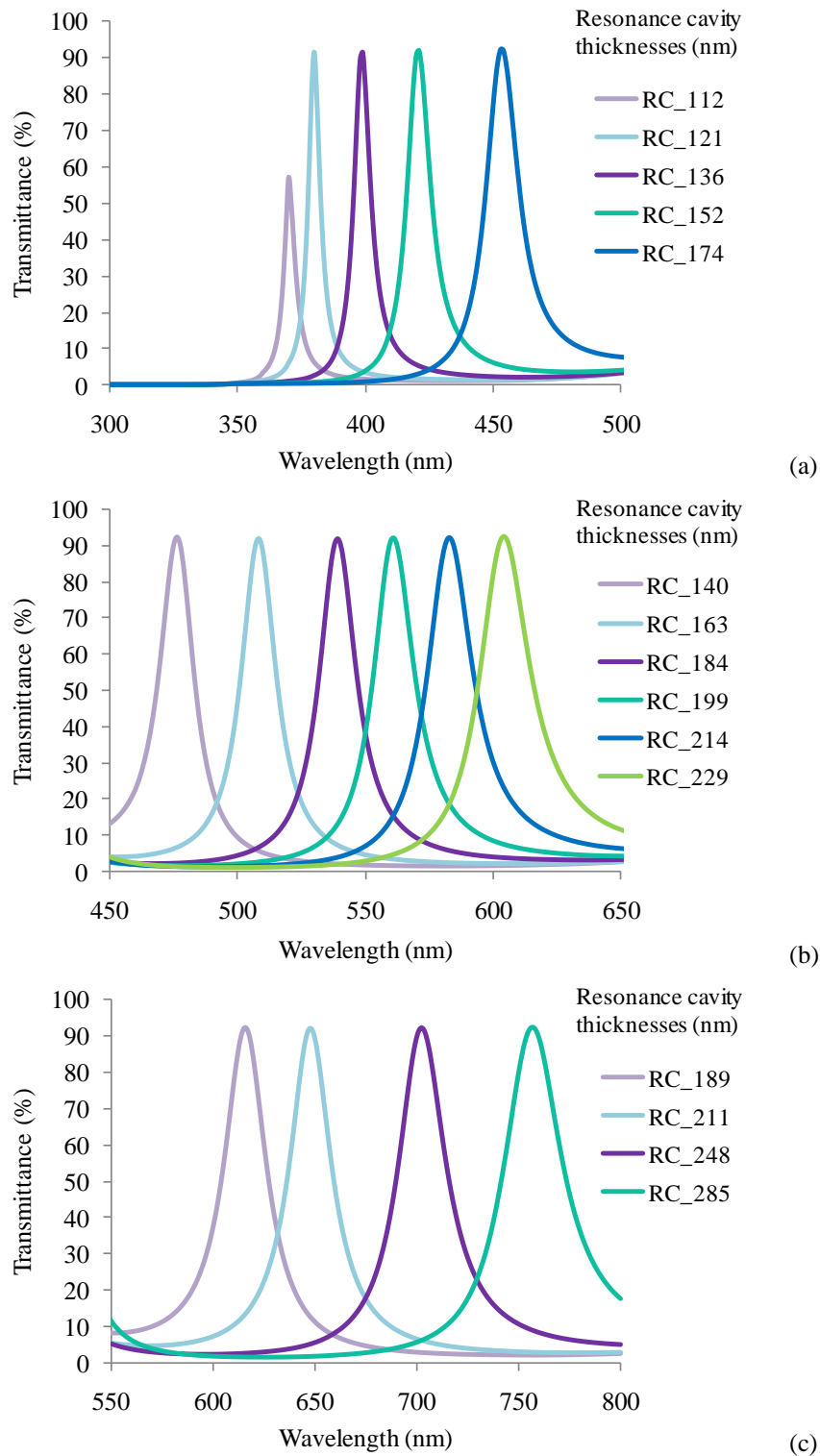


Figure 4.9: Simulated transmittance spectra for the same thin-film optical filters of Figure 4.8, but with only 7 layers: (a) filters of the near-UV/violet region; (b) filters of the central region of the visible spectrum; (c) filters of the red spectral region.

In an initial stage, only 6 of the 16 optical filters (corresponding to the central band of the visible spectra) were fabricated in order to adjust the manufacturing process before proceeding with the fabrication of the remaining filters. Thin-film optical filters fabrication needs to be well controlled and optimized, because the position of the peak is highly sensitive to thickness and refractive indices variation. For example, a thickness variation of only 1 nm

in each of the TiO_2 layers, relative to what was initially designed, is enough to move the peak to a different central wavelength. This is demonstrated in Figure 4.10 where an increase of 1 nm in the thickness of each of the TiO_2 layers significantly affects the central peak position of the 540 nm filter in 3 nm (this effect might be noticed not only in the peak central wavelength, but also in its FWHM and transmission efficiency).

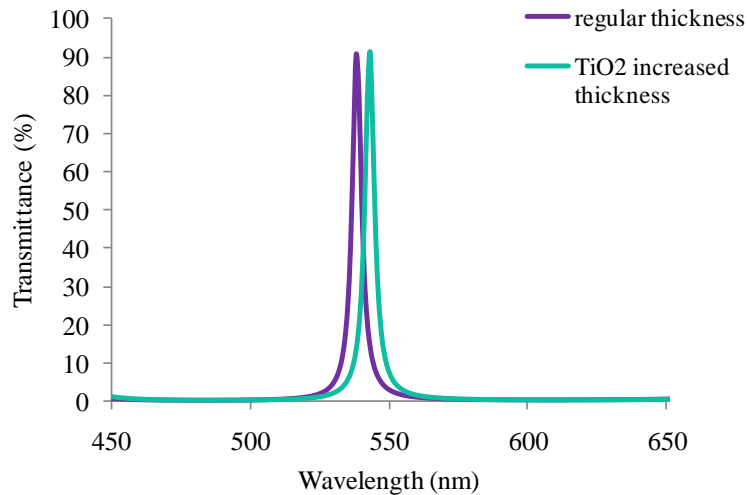


Figure 4.10: Simulated spectral transmittance for the 540 nm optical filter, with maximum intensity peaks at 540 (regular TiO_2 thicknesses) and 543 nm (when there is an increase of 1 nm in the thickness of each of the TiO_2 layers).

4.2.4 Optical filters fabrication

Before starting the deposition of the multilayers, some SiO_2 and TiO_2 thin-films were deposited at INESC-MN by ion beam deposition in a Nordiko 3000 tool equipped with both a deposition and assist guns, in a broad beam architecture [24] compatible with 150 mm diameter wafer deposition and ion milling. This equipment has a 1 nanometer resolution that enables a high level of control of the thicknesses to be deposited, which is very important as mentioned in the previous section.

In Figure 4.11 the geometry used for standard film deposition is illustrated, where the Xenon (Xe) ions created inside the deposition gun (by an external RF coil) are accelerated through a 3-grid assembly (15 cm diameter), into the target, at a pressure of 0.1 mTorr. The SiO_2 films are prepared from a ceramic target, using a Xe beam. Beam distortion caused by charging at the target surface is avoided with a neutralizer (e-beam), which is of major importance for the SiO_2 deposition control, since it assures a stable deposition rate along the several hours of deposition. Deficient neutralization causes different SiO_2 film thickness across the multilayer, that is, the bottom layers (near the substrate) have different thickness than the top layers.

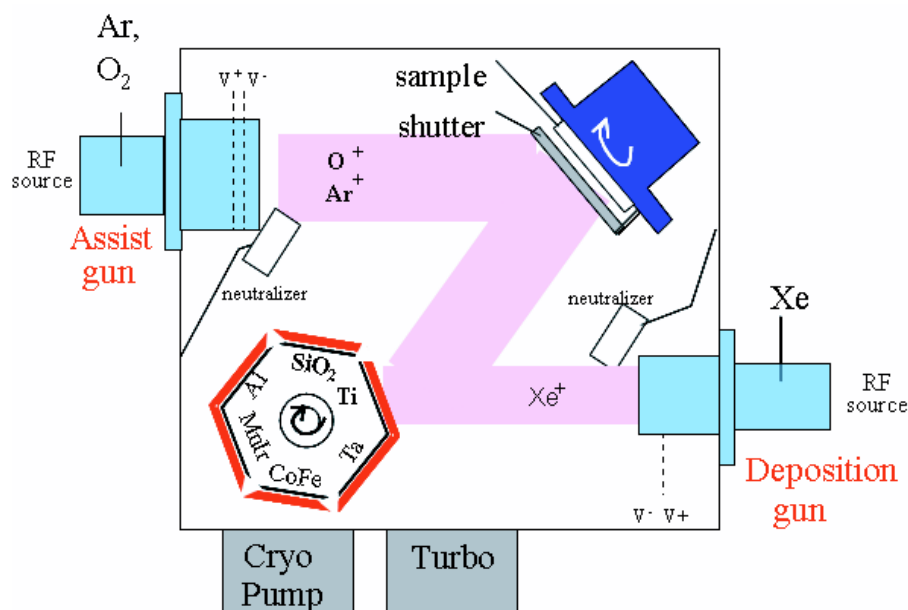


Figure 4.11: Geometry of the fully automated deposition system (Nordiko 3000), with a 6-target configuration, allowing sequential deposition of the TiO₂/SiO₂ films. The sample rotates at 15 rpm during deposition, and film thickness uniformity is $\pm 2\%$ over 150 mm diameter area.

The TiO₂ films were prepared from a Ti metallic target, using ion beam assisted deposition, using a Xe deposition and an Ar-O₂ (argon-oxygen) assist beam extracted from the assist gun through a 3-grid assembly (20 cm diameter), increasing the deposition pressure to 0.3 mTorr. In this work, the assist beam current was maintained in low values to minimize the material etching while depositing.

The focused beam profile is controlled by the beam current (defined as I^+ , measured at the positive grid) and grid voltages (V^+ , V^-), following the relation $I^+ \sim (V^+ + V^-)^{3/2}$, where $(V^+ + V^-)$ is the beam energy [25]. Phase diagram with the conditions to obtain focused or broad beams is plotted in Figure 4.12 for the assist gun, with the beam power calculated as $I^+ \times (V^+ + V^-)$. The films described in this thesis were deposited using the same deposition conditions (22 mA, +1200 V, -300 V, 1.5 sccm Xe), only for the TiO₂ reactive deposition, several lower energy conditions were tested (triangles in the figure). The assist beam energy must be adjusted so that the energy is high enough to promote the Ti film oxidation, but also must be in a range that prevents sputtering from dominating.

Notice that if $V^+ \leq V^-$ the weakly accelerated ions are no longer a beam, reaching the sample by thermal drift (remote plasma oxidation). These, however, are still efficient in oxidizing the Ti films, and the final films have the correct composition, as will be shown below. Also shown in Figure 4.12 are the values used for conventional ion beam milling processes, usually done at high energies (> 26 W), at $\sim 1 \text{ \AA/s}$ (solid curve).

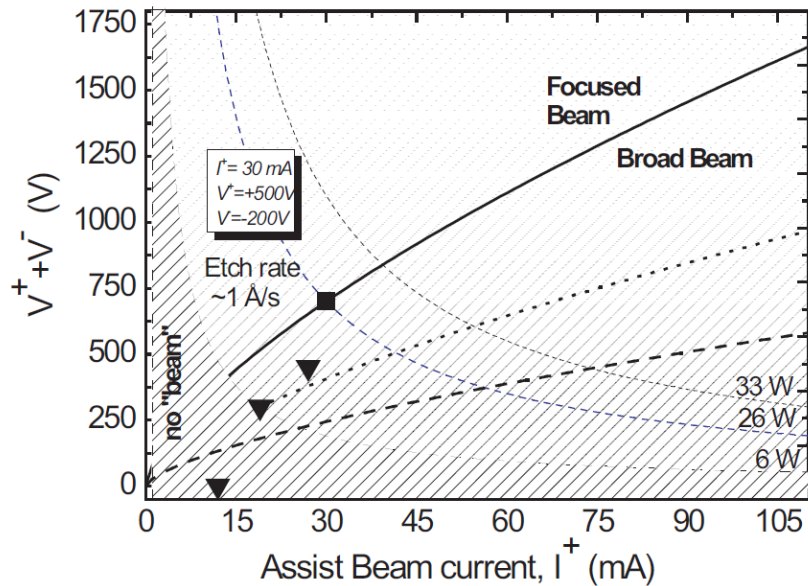


Figure 4.12: Assist gun phase space. Triangles indicate the low power beam conditions tested for assisted deposition of TiO_2 , at 12, 19 and 27 mA. These conditions correspond to a broad and weak beam. The conditions used for ion beam milling (30 mA, +500 V, etch rate $\sim 1 \text{ \AA/s}$) are also shown for comparison.

Simple SiO_2 and TiO_2 films were deposited on silicon (Si) substrates, for deposition rate, composition and refractive index calibration. The composition of TiO_2 films deposited on Si was investigated by Rutherford backscattered spectroscopy (RBS) (at ITN, Sacavém). Figure 4.13 shows the experimental data obtained with a He^+ beam, accelerated at 2 MeV, with a sample-beam angle of 0° and two detectors located at 140° and 180° scattering angles. Fittings of the data [26] indicates a Ti:O ratio of 32.6:67.4, corresponding to a TiO_2 compound. The density was also determined at 3.8 g/cc, which is in agreement with the 4.0 g/cc reported in the literature and indicates a dense thin-film material.

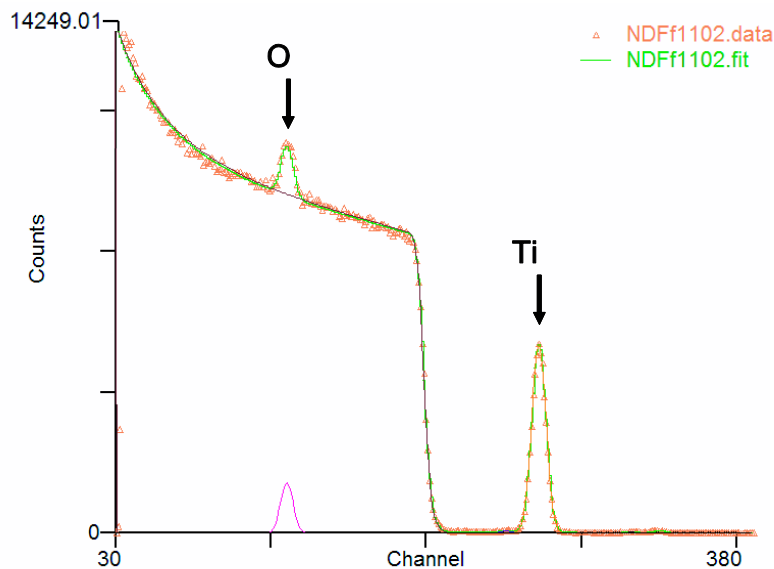


Figure 4.13: Rutherford Backscattering data obtained at normal incidence, for a 40 nm thick TiO_2 film deposited on a Si substrate.

The refractive indices of the dielectric materials used in the deposition process were measured by ellipsometry, on Si/SiO₂ 95 nm thick and Si/TiO₂ 45 nm thick test samples. The variation of the refractive index with the wavelength, in steps of 1 nm, was obtained by spectroscopic ellipsometry using a Nanofilm-ep3se instrument from Accurion (at INL, Braga). The experiments were performed at an angle of incidence of 50°. Optical modeling and data analysis was done with EP4model software package. The refractive index was determined by fitting the ellipsometric parameters with a Cauchy model. Figure 4.14 summarizes the dependence of the refractive index as a function of the wavelength for the SiO₂ and the TiO₂ films (thickness 95 nm and 45 nm, respectively). The variation obtained is in accordance with values reported in the literature for SiO₂ and TiO₂ films [27].

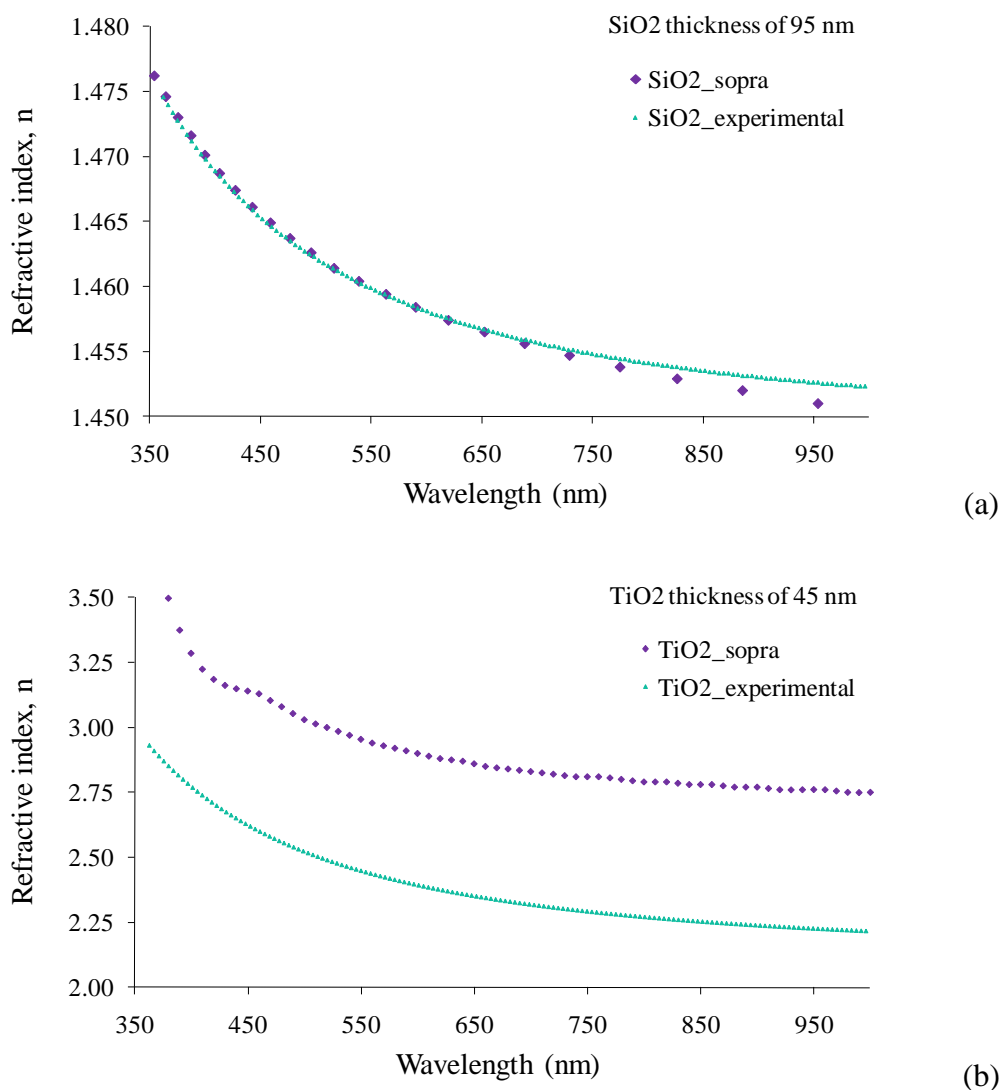


Figure 4.14: Comparison between the refractive indices of the *Sopra* Database and the ones obtained experimentally, for (a) 95 nm thick SiO₂ and (b) 45 nm thick TiO₂.

In addition, Figure 4.14 also compares the refractive indices of the *Sopra* database with the measured refractive indices. After the determination of the real refractive indices of the materials that will be used to fabricate the filters, it can be concluded that, in particular,

the measured refractive indices for the TiO_2 are smaller than the ones used in the initial simulations. This is due to the ratio of the Ti:O compound that was obtained in the deposition process, slightly off-stoichiometry. As a consequence, the layer thicknesses to be used in the multilayers have to be adjusted for maintaining the desired optical properties and performance.

Optical filters design adjustment

After the first theoretical calculations using the refractive indices from the *Sopra* database, the experimental refractive SiO_2 and TiO_2 indices values (presented in Figure 4.14), were used in the analytical and computational code, to adjust the best possible the layer thicknesses. Since the refractive indices obtained for the TiO_2 are smaller than the ones used from the *Sopra* database, the thickness of the TiO_2 mirror layers had to be increased a few nanometers. This way, the new thicknesses for the filters of the central band of the visible spectrum are now equal to 95 nm for the SiO_2 and 52 nm for the TiO_2 layers. Thin-film assemblies with those layers thicknesses were then deposited using the same deposition system.

The resonance cavity thicknesses were also adjusted due to the new SiO_2 refractive indices, in order to obtain the peaks centered at the initial 6 wavelengths. This could be a minor adjustment since the refractive indices from the *Sopra* database and the measured SiO_2 refractive indices are very similar, as it can be seen in Figure 4.14. However, it was decided not to change the SiO_2 mirror layers. Therefore, the changes in the cavity thicknesses were more significant to match the desired peaks.

Table 4.2 summarizes the new layer thicknesses determined for the filters in the central region of the visible spectrum, while Figure 4.15 shows the corresponding simulated transmittance for each filter.

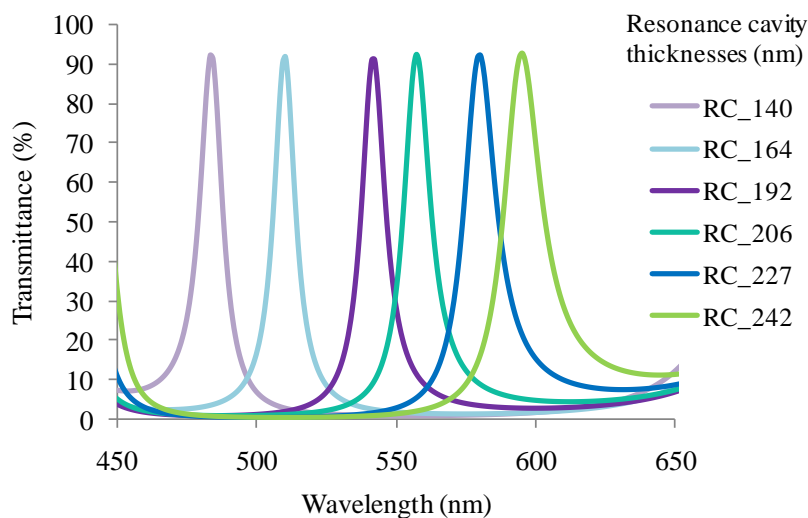


Figure 4.15: Simulated spectral transmittance for 6 optical filters in the central region of the visible spectrum.

Table 4.2: Layer thicknesses of the 6 central Fabry-Perot optical filters.

Maximum wavelength transmission						
480	510	540	560	580	600	
Layer thicknesses (nm)						
TiO ₂	52					
SiO ₂	95					
TiO ₂	52					
SiO ₂	95					
TiO ₂	52					
SiO₂	140	164	192	206	227	242
TiO ₂	52					
SiO ₂	95					
TiO ₂	52					
SiO ₂	95					
TiO ₂	52					

From Figure 4.15, it can be concluded that, using the same optical filters structure, and after the adjustments, each spectral band has a transmittance higher than 90% with a FWHM less than 17 nm (average around 12 nm), a background noise of 15%, except for the 600 nm filter, and a neighbor interference less than 35%, again except for the 600 nm filter. With these results it is possible to conclude that the performance of these filters in terms of a narrow transmission is not as good as in the first simulations. Still, it is an acceptable performance for the interference filters since the maximum transmittance to background noise is about 90/15.

The overall performance of the optical filters could be improved by increasing the total number of dielectric layers, but the fabrication process complexity would also increase. Therefore, it must be achieved a compromise between the filters accuracy to transmit a narrow spectral band and the constraints inherent to the filters fabrication process (e.g. materials, number of layers, FWHM, and maximum transmission).

For a better demonstration of the peak deviation that may occur with a variation of the refractive index, and to better justify the adjustment that was made, Figure 4.16 compares the simulations for a filter with a 164 nm resonance cavity thickness using the refractive indices provided by the *Sopra* database and the experimental refractive indices. The use of the same materials but with slightly different refractive indices causes a peak deviation of approximately 30 nm and different FWHM values.

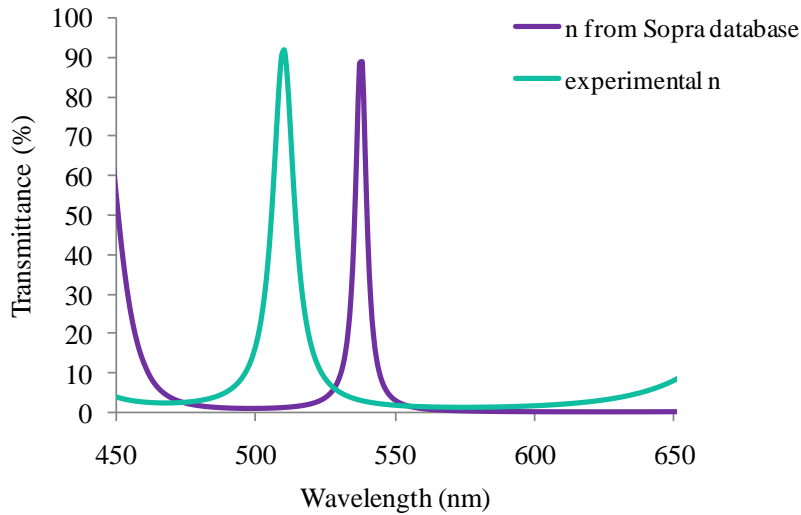


Figure 4.16: Simulated transmittance spectra for an optical filter with a resonance cavity thickness equal to 164 nm, and with SiO₂ and TiO₂ layer thicknesses of 95 and 52 nm, respectively. The two curves are obtained using the refractive indices provided by the *Sopra* database (n from Sopra database) and the experimental refractive indices (experimental n).

This can be better seen in Figure 4.17, where, for each spectral band, it is depicted the peak deviation of using the refractive index of the *Sopra* database materials and the experimental refractive index obtained by measuring the used materials, as a function of the SiO₂ resonance cavity thicknesses. The thicknesses of the mirror layers are kept fixed and equal to 95 nm and 52 nm for the SiO₂ and TiO₂, respectively.

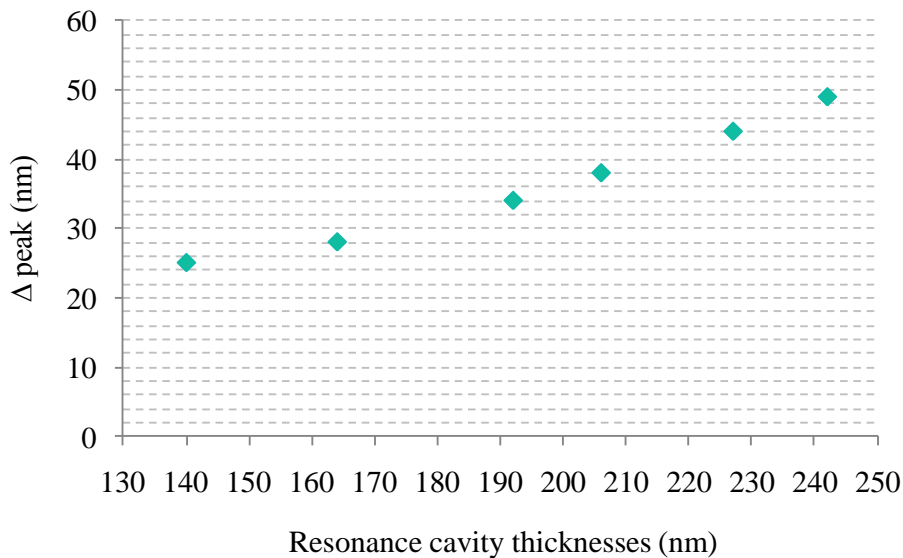


Figure 4.17: Transmitted peak variation (Δ) as a function of the SiO₂ resonance cavity thicknesses, when it is used the refractive indices provided by the *Sopra* database and the experimental refractive indices.

For higher SiO₂ thicknesses the peak deviation is higher. This can lead to the conclusion that the experimental SiO₂ refractive index changes not only with the wavelength, but it also changes with thickness, which is proved by Figure 4.18. Thus one cannot use the same value for thin and thick films.

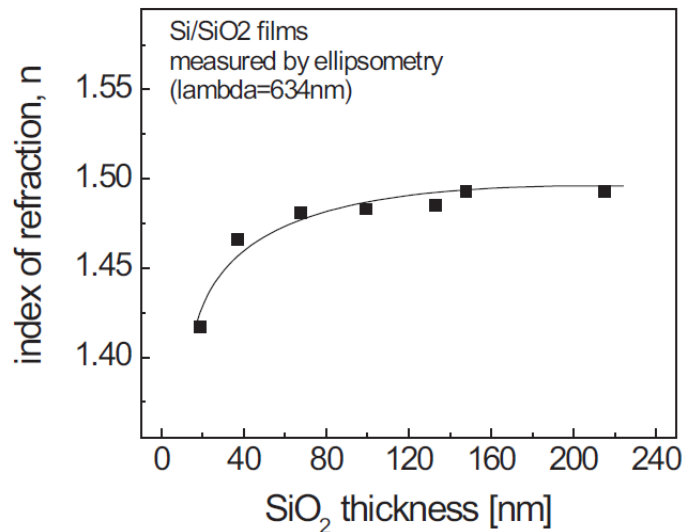


Figure 4.18: Experimental dependence of the SiO₂ refractive index on the SiO₂ film thickness.

The thicknesses of the filters in the near-UV/violet and red regions will also be adjusted in order to compensate for the differences in the refractive indices. However, this will only be done after these first 6 filters are fabricated. The fabrication of the filters is a very complex, time-consuming and prone to errors process. Thus, it is wise to go step by step, so that one can obtain the best results.

4.2.5 Optical and structural characterization of the filters

The 6 optical filters corresponding to the central region of the visible spectrum were fabricated as described in section 4.2.4 but with new layer thicknesses. The optical filter properties, i. e. the filters transmittance, were measured using a spectrophotometer from Shimadzu (UV-3101PC), and are demonstrated in Figure 4.19.

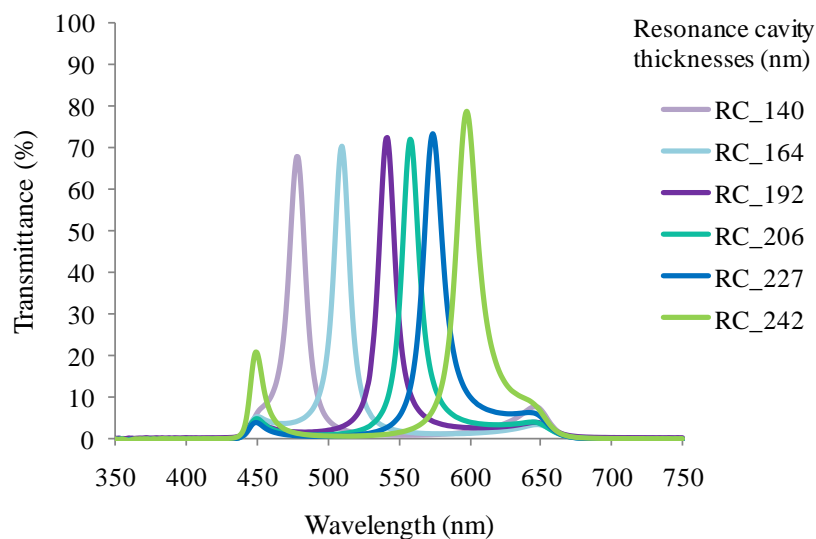


Figure 4.19: Measured transmittance spectra for the 6 fabricated Fabry-Perot optical filters with the wide band-pass filter included.

In order to eliminate the tails of the filters outside the 450-650 nm spectral region, a commercial wide-band pass filter (450-650 nm band, with 96% transmittance) was placed on top of each filter. The comparison between the experimental results and simulated results, in terms of maximum peak transmittance, is shown in Figure 4.20.

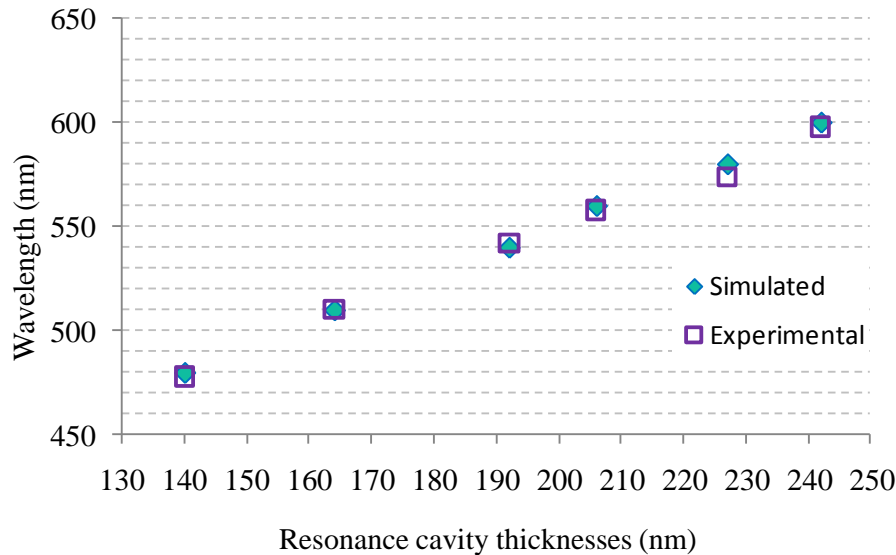








Figure 4.20: Comparison between the experimental and the simulated results for 6 optical Fabry-Perot filters: the wavelength of maximum transmittance is shown for each resonance cavity thickness.

The results of Figure 4.19 show that a multilayer stack of TiO_2 and SiO_2 thin-films for the dielectric mirrors with a SiO_2 resonance cavity is a good option in terms of optical characteristics. The presented results show that each filter is sensitive to a single spectral band, with FWHM less than 20 nm (average around 15 nm) and with transmittances higher than 65%. As mentioned before, the performance of the optical filters could be improved by increasing the number of layers, but the fabrication process complexity would also increase.

Finally, one can conclude from Figure 4.20 that there is a small peak deviation (of approximately 3 nm in average) between the simulated and the measured transmittances. That deviation is within the tolerance of the deposition system, which is about 10% for the fabricated layers range. These differences between the design and the outcome of the fabrication process may also be explained by the etching that might occur in some of the layers immediately below, when the multilayer is deposited. Indeed, the total thickness of the multilayers was measured using a profilometer, and the result was, in average, 2% less than what was initially designed. This event will obviously shift the central transmitted wavelength to the left. As mentioned before, the process needs to be optimized and the deposition rates need to be adjusted.

Table 4.3 shows photographs of the 6 fabricated optical filters. The color differences can be clearly seen according to the spectral band that is transmitted.

Table 4.3: Photographs of the 6 fabricated optical filters.

			
Resonance cavity thickness (nm)	140	164	192
			
Resonance cavity thickness (nm)	206	227	242

The Scanning Electron Microscope (SEM) was then used to characterize the multilayer morphology, structure and quality of interfaces. SEM images of the structure are presented in Figure 4.21.

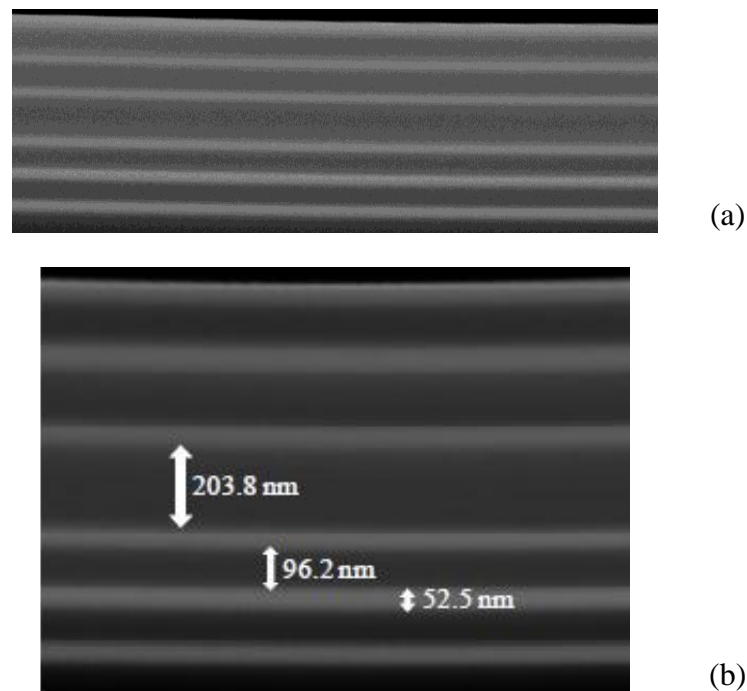


Figure 4.21: SEM photograph showing the cross-section of the 560 nm Fabry–Perot optical filter (the designed TiO_2 and SiO_2 layer thicknesses were equal to 52 and 95 nm, respectively, while the resonance cavity thickness was equal to 206 nm): (a) magnification 100,000 times; (b) magnification 200,000 times.

In these figures it is demonstrated a clear separation between the SiO_2 and TiO_2 layers, with very low interface mixing (brighter layers correspond to elements with high atomic number - TiO_2). Thickness measurements show that the TiO_2 and SiO_2 film thicknesses are in good agreement with the nominal values. It is also shown very good film flatness along the

entire area. Small deviations in the deposited thicknesses in relation to what was designed, namely in the resonance cavity, are caused by instabilities on the beam neutralization during deposition. Both films have amorphous structure and very good adhesion signature on the glass substrate. Notice that the good film flatness shown in Figure 4.21 is extended along the entire sample area, resulting from the very good deposition uniformity of the ion beam N3000 tool ($((\text{maximum}-\text{minimum})/2*(\text{maximum}+\text{minimum})) = \pm 2\%$ over 150 mm wafer areas). This feature allows guarantee the parallelism of the mirrors concerning to the resonance cavity, which is a crucial feature for reproducible optical measurements in narrow-band pass optical filters.

The multilayer surface roughness of the 560 nm filter was also evaluated, in a 400 by 400 μm area, using a profilometer (Dektak 150 Surface Profiler, Veeco Instruments, Inc., Plainview, TX). The surface 3-D map of the optical filter is shown in Figure 4.22.

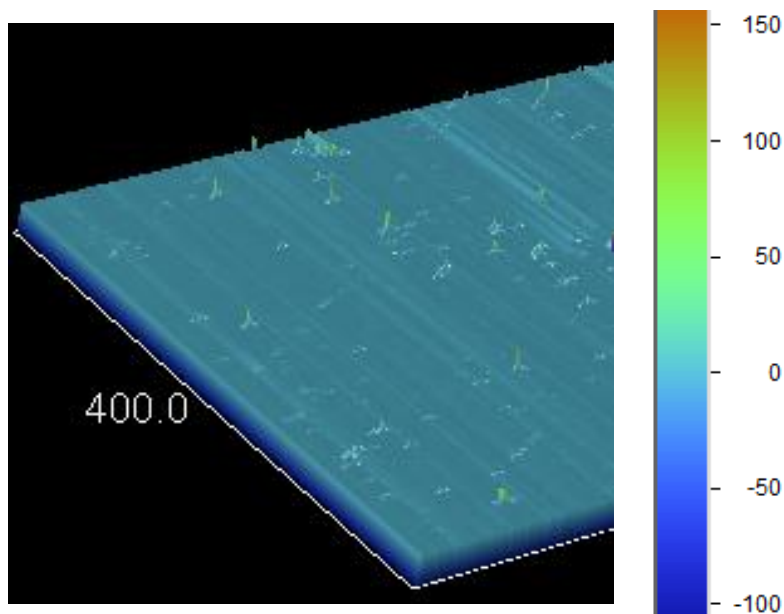


Figure 4.22: Surface 3D map of the Fabry–Perot optical filter.

From Figure 4.22 it can be seen that in general the optical filter's surface is smooth, as would be desirable in order to minimize potential interferences to the incident light beam. Its roughness profile is in average equal to 2.31 nm. Several tiny irregularities inherent to the filters manufacturing process are present in the surface; yet, these are not a major concern due to their small-size. The surface of this filter was also evaluated using an atomic force microscope. The results are displayed in Figure 4.23. In this case, the average surface roughness is equal to 0.41 nm, in an area of 5 μm by 5 μm .

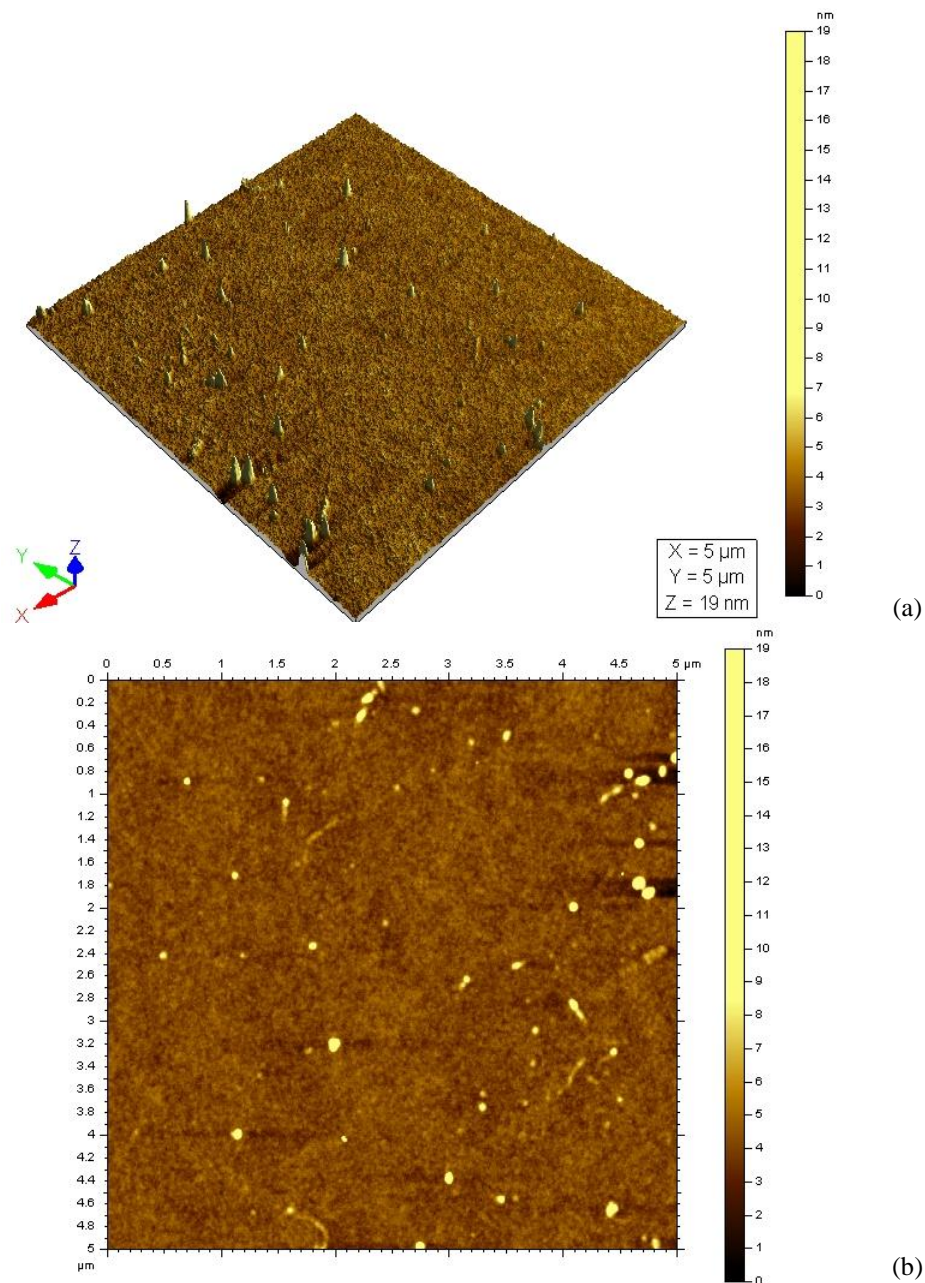


Figure 4.23: AFM image of a thin-film optical filter: (a) 3-D image; (b) 2-D image.

4.2.6 Optical filters for the near-UV/violet and red regions

The filters corresponding to the central region of the visible spectrum were first fabricated and characterized, so that the fabrication process could be optimized before proceeding with the fabrication of the remaining structures. This way, after knowing the real refractive indices of the materials, the deposition process tolerances, and the problems that may occur during the materials deposition (e. g. etching in some of the layers), the structure of the filters centered at the lower and higher wavelengths was adjusted to try to offset these factors.

Design adjustment, fabrication and optical characterization

Until this stage, the whole methodology presented in Figure 4.24 including up to step 7 took about a year to be concluded. The next step (number 8) was related to the adjustment of the structure of the filters in the near-UV/violet region taking into account the previous experience.

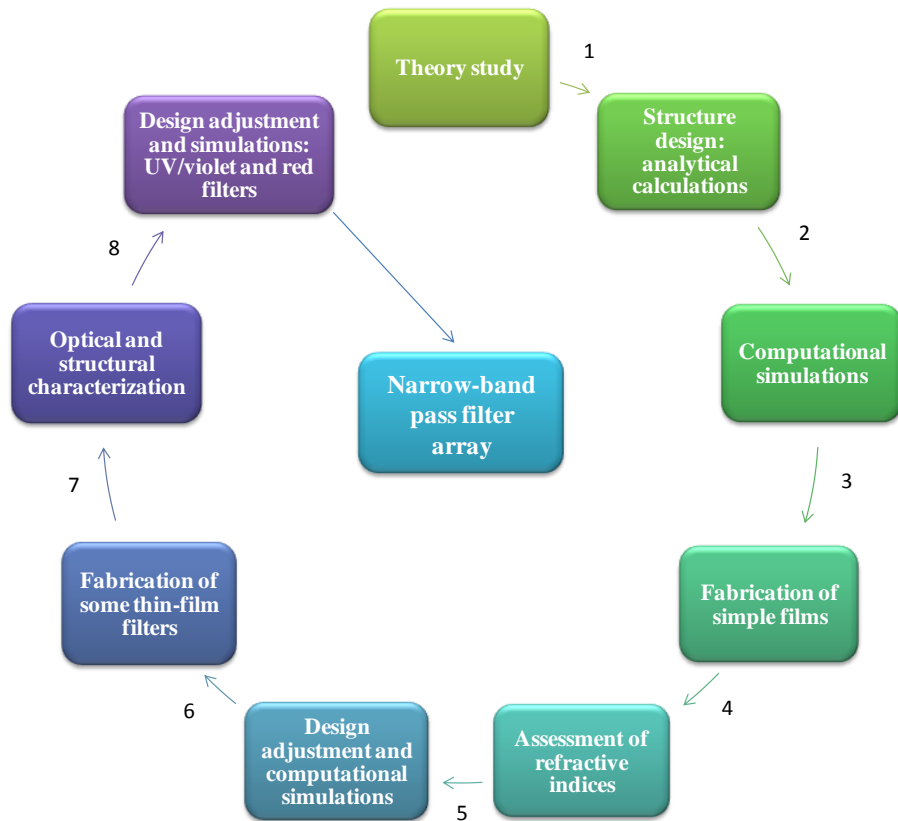


Figure 4.24: Methodology used in the fabrication of the thin-film optical filters.

For the filters of the near-UV/violet region the same approach was used for the structure adjustments: the thicknesses of the TiO₂ mirror layers were increased several nanometers. In a first experiment, only the filter centered at 400 nm was fabricated. In order to keep the filter with its maximum transmittance at 400 nm, and taking into account the new refractive indices, the TiO₂ mirror thicknesses increased from 30 to 36 nm, keeping the same SiO₂ layers. The simulated spectral transmittance for this filter is shown in Figure 4.25.

This specific filter was then fabricated and its optical transmittance is illustrated in Figure 4.26.

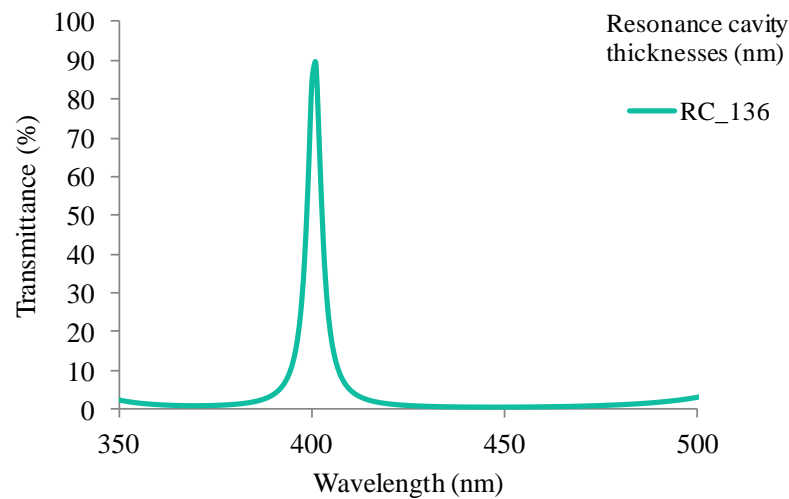


Figure 4.25: Simulated spectral transmittance for the 400 nm thin-film optical filter, with TiO₂ and SiO₂ mirror thicknesses of 36 and 68 nm, respectively, and a resonance cavity with a thickness equal to 136 nm.

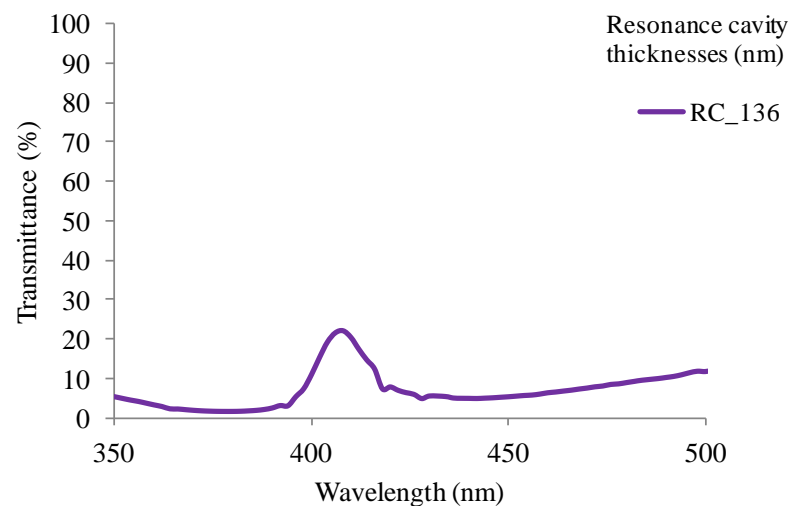


Figure 4.26: Experimentally measured spectral transmittance for the 400 nm thin-film optical filter, with TiO₂ and SiO₂ mirror thicknesses of 36 and 68 nm, respectively, and a resonance cavity with a thickness equal to 136 nm.

It can be concluded from Figure 4.26 that there is a small peak deviation (approximately 6 nm) between the simulated and measured transmittance of the optical filter. This deviation is within the tolerance of the fabrication process. However, the most noticeable feature of the fabricated filter is its small transmittance (less than 30%). The study of this event led to the conclusion that the ratio of the Ti:O compound that was being deposited was slightly off-stoichiometry, which led to the emergence of metallic contaminants in the TiO₂ films. Metallic materials have high absorption losses and, thus, are not suitable for high transmittances.

This particular occurrence was solved and new depositions were performed in order to obtain transmittance peaks at: 350, 370, 380, 400, 420 and 450 nm. The same mirror layers were maintained: 68-nm thick for the SiO₂ and 36-nm thick for the TiO₂ mirror layers. The

resonance cavity thicknesses were changed in order to achieve the desired peaks. The different values of the cavities are indicated in the simulations plot, in Figure 4.27.

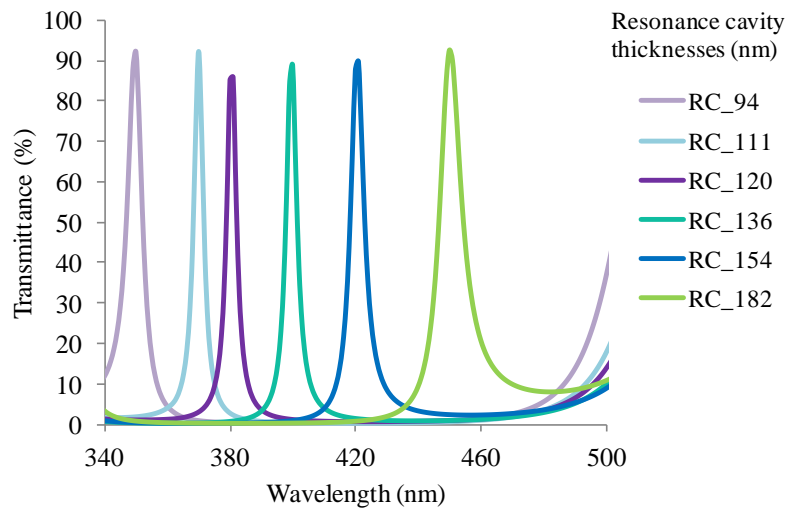


Figure 4.27: Simulated spectral transmittances for the different UV/violet thin-film optical filters using the experimentally measured refractive indices.

It is important to note that with the obtained TiO_2 refractive indices it is now possible to simulate the 350 nm filter since these values are lower when compared with the values of the material used in the initial simulations. This fact has linked a benefit – low absorption by the material (i.e. high transmittance), and also a drawback – loss of selectivity by the multilayer (i.e. high FWHM). For a better illustration, Figure 4.28 shows the optical transmittance simulated using a single layer of TiO_2 over a glass substrate, with layer thicknesses of 30 nm (as used in the first simulation) and 36 nm (as used in the simulation of Figure 4.27). The layer with the low refractive index (i.e. the experimental measured refractive index) has a clear improvement in the transmittance over the violet/blue wavelength range.

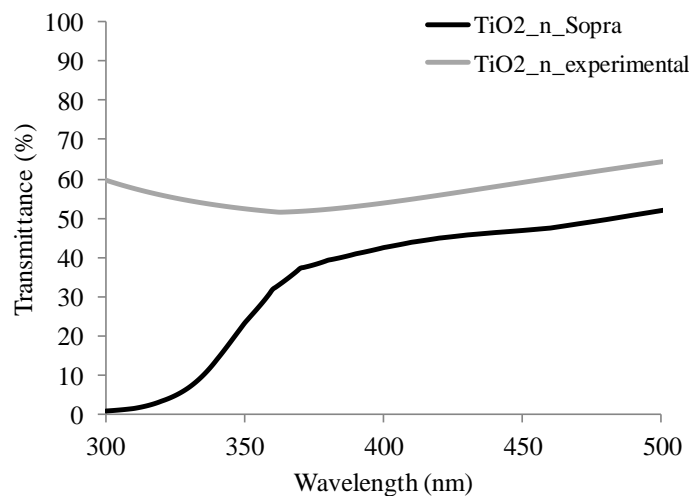


Figure 4.28: Comparison between the transmittance obtained using TiO_2 materials with different refractive indices: “ TiO_2 _n_Sopra” - *Sopra* database refractive index, and TiO_2 thickness equal to 30 nm (as in the first simulation, Figure 4.8(a)); “ TiO_2 _n_experimental” - experimentally measured refractive index, and TiO_2 thickness equal to 36 nm (as in the second simulation, Figure 4.27).

If they exist, the tails of the filters below 350 nm are not a major concern at this time because these correspond to wavelengths far outside the visible range, and, therefore, outside the range of tissues emission (i.e. there won't be a signal emission from tissues in this range, and, thus, even with a high filters transmittance the detected signal will be null).

The optical transmittance measured in the different filters is illustrated in Figure 4.29.

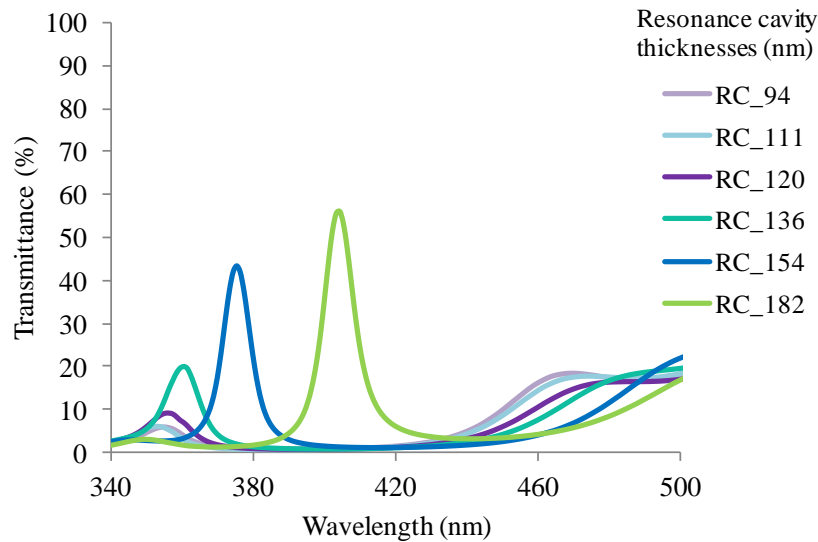


Figure 4.29: Experimentally measured spectral transmittances for the different UV/violet thin-film optical filters with the short-pass filter at 500 nm included in the measurements.

The obtained results are not as good as expected, probably due to modifications in the refractive index of the materials. For the simulations, refractive indices measured from 95-nm thick SiO₂ and 45-nm thick TiO₂ samples were used. However, it is known that these indices also vary with the sample thickness. This way, new refractive indices should have been measured for thinner SiO₂ and, mainly, TiO₂ samples, over the filters transmittance wavelength range, in order to have a simulation as close as possible to the real case.

All the obtained transmittance peaks are deviated to the left and it was not possible to discriminate the different peaks below 350 nm. This is a major limitation in the approach used to design and fabricate all the presented filters. The use of a different structure, instead of a Fabry-Perot structure, an increase in the total number of layers in the assembly, and the use of different materials may potentially improve the chances of obtaining high transmittance filters at low wavelengths. A different approach to build filters in this spectral region will be discussed in the future directions of the last thesis Chapter. According to the results obtained, one of the fabricated filters will be used for the quantitative measurements in this particular spectral range. Even though it hasn't been designed for this specific wavelength, the filter with the 182-nm thick resonance cavity will be used as the 400 nm filter.

Due to the poor results obtained, two more filters were fabricated, for the violet/blue

spectral region, at INESC-MN. In this new design, the TiO₂ mirror layers were kept equal to 45 nm, since the values of the refractive indices available for the computational simulations were measured using TiO₂ samples with a thickness of 45 nm. With this approach one expects to minimize the offset between the design and the outcome of the fabrication process. The other mirror layers of the filters – the SiO₂ layers – were designed to have a thickness of 70 nm.

After the fabrication, the filters were characterized, and good results were obtained for one of the filters (with a cavity thickness of 138 nm) in terms of spectral transmittance. The transmittance performance of this optical filter is shown in Figure 4.30, ove.

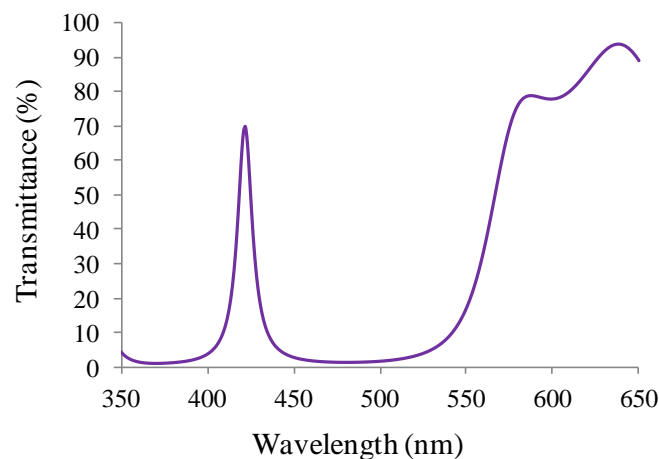


Figure 4.30: Measured transmittance spectra of one violet/blue Fabry-Perot optical filter. The transmittance was measured using a UV-3101PC spectrophotometer. The filter has a maximum intensity peak at 422 nm.

The filters of the red region were then adjusted. A major concern in this adjustment is related to the fact that the SiO₂ and TiO₂ mirror layers of these filters are thicker (117 and 60 nm, respectively) than the ones used to measure the refractive indices, as a function of wavelength, presented in Figure 4.14. This way, and as mentioned before, it is a hard task to adjust the layer thicknesses for unknown refractive indices.

Since for the near-UV/violet group of filters the results were not satisfactory, for this last group of filters it was decided to adjust only the resonance cavity thicknesses and keep the thicknesses of the mirror layers equal to the initial design.

To cover this spectral region only 4 filters are necessary. However, it was possible to deposit 6 more different filters at INESC-MN. Thus, it was decided to only fabricate filters centered at three different wavelengths (620, 650 and 700 nm) and to deposit two different resonance cavity thicknesses for each of them. This was done in order to account for potential deviations between the simulations and the outcome of the fabrication process, once there are some unknown variables in the process (e.g. refractive indices). The 750 nm filter was not fabricated since it is, among the four, the less important wavelength to extract tissue

properties and establish a diagnosis.

From the computational simulations it was possible to conclude that a shift of 20 nm in the transmittance peak to the right or to the left could be obtained, using this particular structure, by increasing or decreasing the resonance cavity thickness by approximately 17 nm, respectively. Given this, 6 different filters were projected, centered at: 620, 640, 650, 670, 680 and 700 nm. The simulated spectral transmittances for these 6 filters, together with the resonance cavity thicknesses, are shown in Figure 4.31.

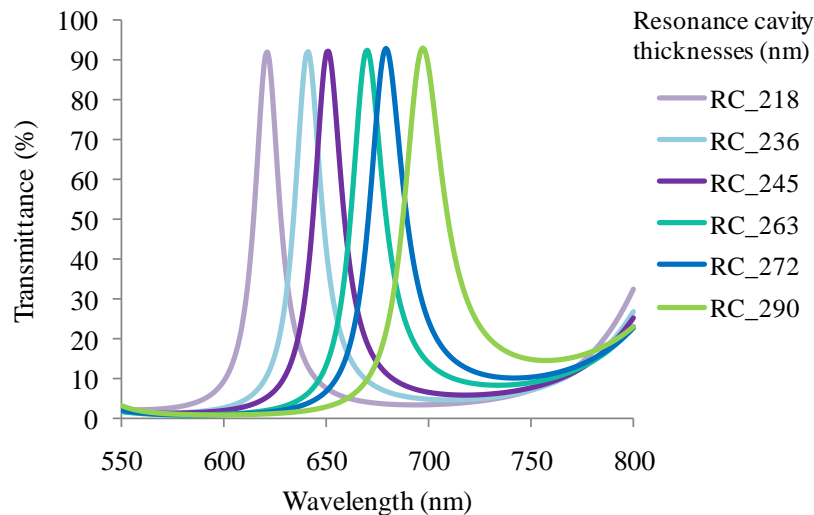


Figure 4.31: Simulated spectral transmittances for the different thin-film optical filters in the red region using the experimentally measured refractive indices.

The filters were finally fabricated and their optical transmittance was measured (Figure 4.32).

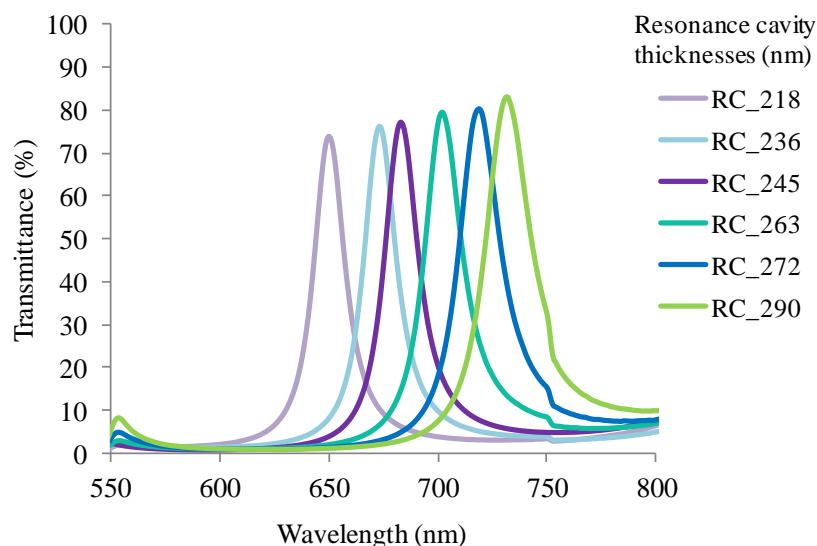


Figure 4.32: Experimentally measured spectral transmittances for the different thin-film optical filters in the red spectral region. The measurements were performed with a high-pass filter at 550 nm on top the thin-film optical filters.

From the results presented in Figure 4.32 it is possible to conclude that the spectral

shape of the fabricated optical filters is in good agreement with the simulations. However, the feature that most stands out is that the filters are all deviated to the right approximately 32 nm. A good aspect is that this deviation is almost constant in all the filters. This means that there is probably a systematic problem in the deposition process, which may be easier to solve than if it was a random, non-uniform problem in some of the filters.

Similarly to what was done in the near-UV/violet case, and even though the filters haven't been designed for these specific wavelengths, the filter with the 218-nm thick resonance cavity will be used as the 650 nm filter, whereas the filter with the 263-nm thick resonance cavity will be used as the 700 nm filter. Unfortunately it was not possible to obtain a filter centered at 620 nm.

For the two filters that are going to be used for the experiments, the results presented in Figure 4.32 show that each filter is sensitive to a single spectral band, with FWHM less than 20 nm, transmittance to background noise less than 10%, and with transmittances higher than 75%. Overall, one can consider the results satisfactory.

4.3 Photodiodes and readout electronics

In the designed miniaturized spectroscopy system, silicon photodiodes are used for signal detection, replacing, this way, the spectrograph and CCD camera that are used in the majority of spectroscopy prototypes for several clinical applications. The photodiodes convert light intensity that is transmitted through the optical filters into a photocurrent. The analog photocurrent signal is converted into a digital signal using a light-to-frequency converter integrated in the same die [20]. The digital output signal, with a suitable format for radio-frequency transmission, will have a frequency proportional to the light intensity emitted by the tissues.

As mentioned before in this Chapter, the integration of optical filters, photodiodes and readout electronics on a single-chip requires the system to fit in a microelectronics process, preferably CMOS. This technology features electronics in a small silicon area and offers low power consumption, an important requirement for the reported application. It is also critical for the economic viability of the detection system. For the miniaturized instrument *pn*-junction photodiodes are used, fabricated in a standard 0.7 μm CMOS process, without additional masks or steps, except for the signal detection in the near-UV/violet spectral region in which the designed photodiodes don't have high quantum efficiency, as will be seen next below. For this spectral band, a photodiode with improved quantum efficiency at low visible wavelengths should be developed in a future step. This will be discussed in Chapter 7.

The CMOS process provides three photosensitive structures as vertical junction photodiodes: *n-well/p-epilayer*, *n+/p-epilayer* and *p+/n-well*. The principle of operation of these three types of photodiodes is very similar. When light shines onto the semiconducting material the photon energy is absorbed. For low photon energies the only effect is that the material heats up. For high photon energies the electrons in the valence band may get sufficient energy to reach the conduction band. This requires the photon energy to be larger than the bandgap of the material between the valence and conduction bands, which in the case of silicon is 1.14 eV. This process creates free electrons in the conduction band and holes in the valence band. These two types of carriers are seen as a photocurrent at the photodiode terminals [28].

The photon energy is wavelength dependent: for relatively larger wavelengths (≥ 950 nm) the photon energy is not high enough to create an electron-hole pair in silicon; for lower wavelengths (< 400 nm) excess carriers are generated very close to the photodiode surface, due to a lower penetration depth. Because the surface recombination rate of electrons and holes is high, only a small part of the generated carriers contribute to photocurrent. Therefore, it is necessary to remove the created electrons from the conduction band. This is done using an inversely polarized *pn*-junction that originates a region deprived of mobile carriers, known as depletion region. The photodiodes should be designed to allow the largest number of photons to be absorbed near or in the depletion region. In an ideal situation, the photons should not be absorbed until they have penetrated as deep as the depletion region, and should be absorbed before they have penetrated beyond it [28].

At a particular wavelength, the photodiodes quantum efficiency (how well they collect the incident light) varies according to their junction depth. In the visible spectrum, the blue light is more efficiently collected by a shallower junction, close to the photodiode surface (*p+/n-well* and *n+/p-epilayer*) and the red light by a deeper junction (*n-well/p-epilayer*). Light with longer wavelengths may penetrate tenths of micrometers deep in the substrate. Despite its shallow junction, the *n+/p-epilayer* photodiode has high-quantum efficiency around 500 nm due to the different doping concentration between the *n* and the *p* side. This extends the *p* side depletion area more deeply [29-30]. Therefore, this photodiode was selected for the detection of the signals filtered by the second group of optical filters (the filters in the central region of the visible spectrum). For the group of filters in the red spectral region, *n-well/p-epilayer* photodiodes are used. The light intensity that passes through the filters in the blue region will be detected, in a first approach, using *p+/n-well* photodiodes, since these cut more efficiently higher wavelengths.

Each filter will be vertically aligned with one photodiode to build the optical channel

for the collection of fluorescence and diffuse-reflectance data in a 4 by 4 array configuration, in order to cover the full 350 to 750 nm range with good quantum efficiency (Figure 4.33). At this stage of the project, the three different photodiodes structures were fabricated. The layout of the detection system is shown in Figure 4.33, designed using the Tanner L-Edit Pro software. Each photodiode has an active area of 100 μm by 100 μm .

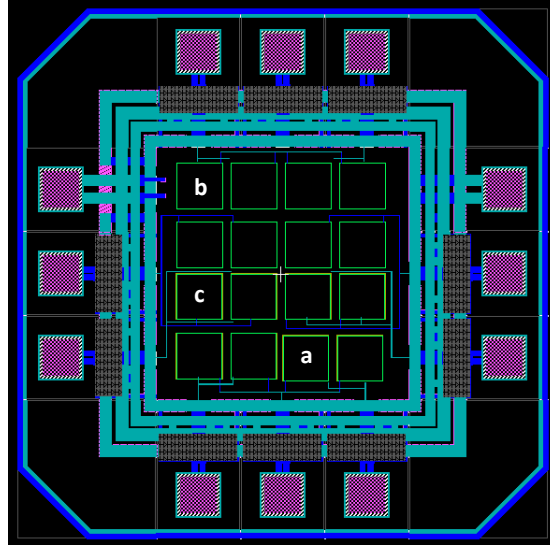


Figure 4.33: Layout of the photodiodes array: (a) *n-well/p-epilayer* photodiode; (b) *n+/p-epilayer* photodiode; and (c) *p+/n-well* photodiode.

The photodiodes photocurrent is proportional to the incident light and can be calculated using the following expression:

$$I = \frac{q_e \eta \lambda P_i}{hc} \quad (4.63)$$

Where q_e is the electron charge, η is the quantum efficiency, λ is the light wavelength, P_i is the incident optical power, h is the *Planck* constant, and c is the velocity of light in a vacuum. The quantum efficiency is defined as the average number of generated electron-hole pairs per incident photon.

The penetration depth of light in silicon, d_s , strongly depends on its absorption coefficient, α , which in turn is wavelength dependent:

$$d_s(\lambda) = \frac{1}{\alpha_s(\lambda)} \quad (4.64)$$

The effect of using a CMOS photodiode to read the spectroscopic signal was demonstrated with new computational simulations for the 540 nm filter. These simulations took into account the optical effect of a *n+/p-epilayer* photodiode. The thickness of the photodiode junction depth is fixed by the microelectronics foundry, and equals to 350 nm. It was also included in the simulations the effect of the first oxide (SiO_2), existent in the CMOS fabrication process, on top of the photodiode. A thickness of 625 nm was assumed for this

oxide (data from the CMOS foundry). Figure 4.34 illustrates the signal attenuation in the violet/blue region to less than 20%. As it was previously mentioned, the collection of out-of-band light by the optical filter that can potentially confound the spectroscopy analysis can be attenuated not only by a wide-band pass filter, but also by the photodiode that will read the signal.

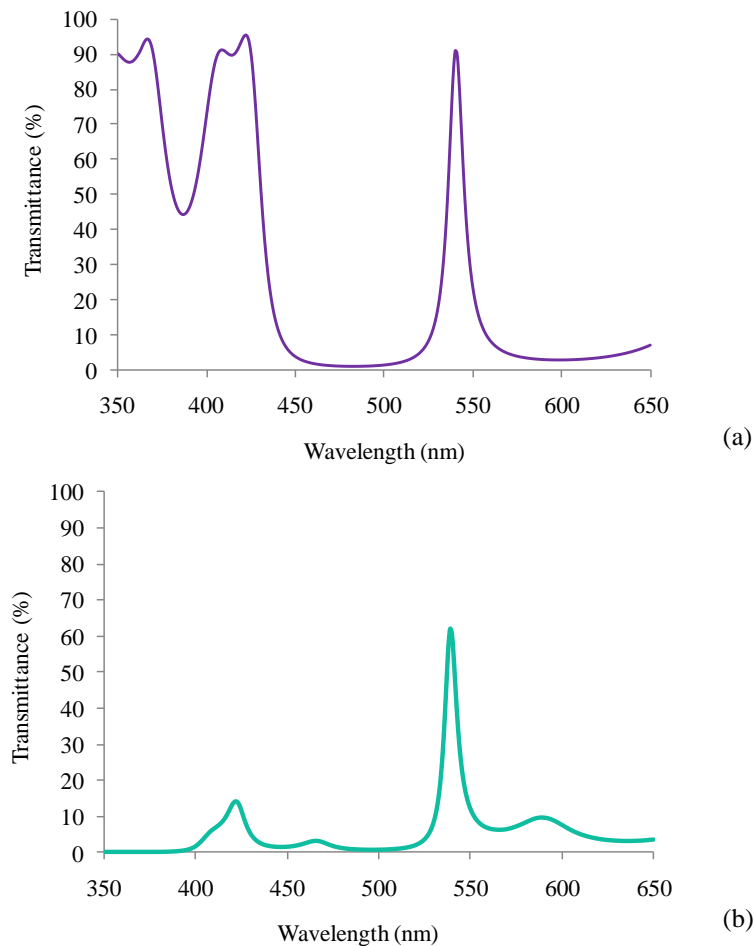


Figure 4.34: Simulated spectral transmittance of the 540 nm filter: (a) without the optical effect of the photodiode included; and (b) with the optical effect of the $n+/p$ -epilayer photodiode included.

The CMOS photodetectors were then fabricated in a 4 by 4 array. In Figure 4.35 a picture of the fabricated array is shown.

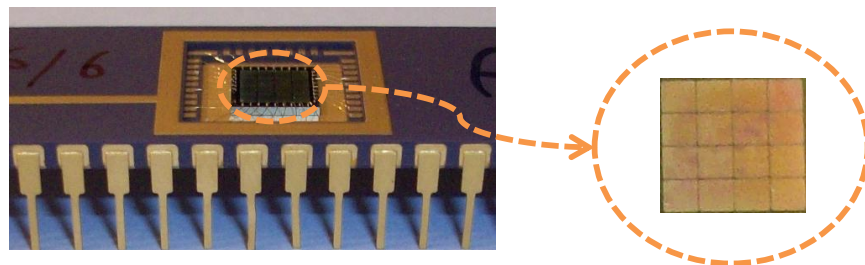


Figure 4.35: Picture of the fabricated photodiodes array that integrates three types of photodiodes: $p+/n$ -well, $n+/p$ -epilayer, and n -well/ p -epilayer.

The spectral response of each type of the fabricated photodiodes was individually measured, using a calibrated commercial photodiode as a reference (Hamamatsu S1336-5BQ).

The quantum efficiency of the three photodiodes was determined from their responsivity, which relates the photocurrent with the incident optical power, and is presented in Figure 4.36. In theory, the typical value of the quantum efficiency in a CMOS photodiode is about 40 to 70% [28].

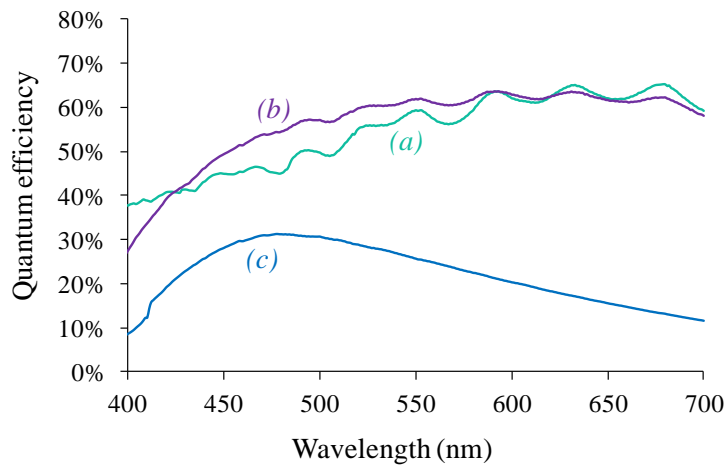


Figure 4.36: Quantum efficiency of the three types of vertical junction photodiodes: (a) *n-well/p-epilayer*; (b) *n+/p-epilayer*; and (c) *p+/n-well*.

According to the results presented in Figure 4.36, it is possible to conclude that, although having a similar quantum efficiency, the *n-well/p-epilayer* photodiode is a little more suitable for the red region of the spectrum, whereas the *n+/p-epilayer* photodiode has a slightly better efficiency in the 500 nm region. Also, the *p+/n-well* photodiode efficiency is increased at low wavelengths when compared with high wavelengths, as would be theoretically expected. Still, the efficiency of this photodiode is not considered good and the photodiode is not suitable for wavelengths below 420 nm. For this reason, other types of photodiodes will be studied in the future for this low wavelength range.

The photocurrent produced by the photodiodes will be read and converted to a digital signal so that the data can be later analyzed. This conversion can be performed using one-bit first-order sigma-delta analog-to-digital converter for each photodiode, such as the one developed by Rocha *et al.* [31]. More details and results about this circuit can be found in the literature [31]. It is just important to mention that the addition of the readout electronics will not significantly increase the size of the chip since the converter can be designed with only 19 small-size MOSFETs [31].

References

- [1] I. Georgakoudi, *et al.*, "Fluorescence, reflectance, and light-scattering spectroscopy for evaluating dysplasia in patients with Barrett's esophagus," *Gastroenterology*, vol. 120, pp. 1620-9, Jun 2001.
- [2] I. Georgakoudi, *et al.*, "NAD(P)H and collagen as in vivo quantitative fluorescent

- biomarkers of epithelial precancerous changes," *Cancer Res*, vol. 62, pp. 682-7, Feb 2002.
- [3] B. Mayinger, *et al.*, "Light-induced autofluorescence spectroscopy for the endoscopic detection of esophageal cancer," *Gastrointest Endosc*, vol. 54, pp. 195-201, Aug 2001.
- [4] T. J. Pfefer, *et al.*, "Temporally and spectrally resolved fluorescence spectroscopy for the detection of high grade dysplasia in Barrett's esophagus," *Lasers Surg Med*, vol. 32, pp. 10-6, 2003.
- [5] G. Bourg-Heckly, *et al.*, "Endoscopic ultraviolet-induced autofluorescence spectroscopy of the esophagus: tissue characterization and potential for early cancer diagnosis," *Endoscopy*, vol. 32, pp. 756-65, Oct 2000.
- [6] M. Panjehpour, *et al.*, "Endoscopic fluorescence detection of high-grade dysplasia in Barrett's esophagus," *Gastroenterology*, vol. 111, pp. 93-101, Jul 1996.
- [7] M. Panjehpour, *et al.*, "Spectroscopic diagnosis of esophageal cancer: new classification model, improved measurement system," *Gastrointest Endosc*, vol. 41, pp. 577-81, Jun 1995.
- [8] J. Y. Lo, *et al.*, "A strategy for quantitative spectral imaging of tissue absorption and scattering using light emitting diodes and photodiodes," *Optics Express*, vol. 17, pp. 1372-84, Feb 2009.
- [9] B. Yu, *et al.*, "Cost-effective diffuse reflectance spectroscopy device for quantifying tissue absorption and scattering in vivo," *J Biomed Opt*, vol. 13, p. 060505, Nov-Dec 2008.
- [10] D. P. Poenar and R. F. Wolffenbuttel, "Optical properties of thin-film silicon-compatible materials," *Appl Opt*, vol. 36, pp. 5122-8, Jul 1997.
- [11] A. Piegari and J. Bulir, "Thin film filters with variable transmittance for spectrometry," *Conf Proc WFOPC 2005: 4th IEEE/LEOS Workshop on Fibres and Optical Passive Components*, pp. 109-144, 2005.
- [12] H. A. Macleod, *Thin-film optical filters*, 3rd ed. Bristol Institute of Physics Publishing, 2001.
- [13] Y. Narukawa, *et al.*, "White light emitting diodes with super-high luminous efficacy," *Journal of Physics D: Applied Physics*, vol. 43, p. 354002, 2010.
- [14] E. Hecht, *Optics*, 4th ed. San Francisco: Addison-Wesley, 2001.
- [15] M. F. S. Ferreira, *Óptica e fotónica*. Lisboa Lidel, 2003
- [16] G. Minas, "Microsistema Laboratorial para Análise de Fluidos Biológicos," Departamento de Electrónica Industrial, Universidade do Minho, 2004.
- [17] G. Minas, *et al.*, "An array of highly selective "Fabry-Perot optical channels for biological fluid analysis by optical absorption using a white light source for illumination," *Journal of Optics a-Pure and Applied Optics*, vol. 8, pp. 272-278, Mar 2006.
- [18] G. Minas, *et al.*, "An array of Fabry-Perot optical-channels for biological fluids analysis," *Sensors and Actuators a-Physical*, vol. 115, pp. 362-367, Sep 2004.
- [19] G. Minas, *et al.*, "An MCM-based microsystem for colorimetric detection of biomolecules in biological fluids," *Ieee Sensors Journal*, vol. 6, pp. 1003-1009, Aug 2006.
- [20] G. Minas, *et al.*, "A lab-on-a-chip for spectrophotometric analysis of biological fluids," *Lab on a Chip*, vol. 5, pp. 1303-1309, 2005.
- [21] A. Piegari and J. Bulir, "Thin film filters with variable transmittance for spectrometry," *Proceedings of WFOPC 2005: 4th IEEE/LEOS Workshop on Fibres and Optical Passive Components*, pp. 109-114, 2005.
- [22] D. P. Poenar and R. F. Wolffenbuttel, "Optical properties of thin-film silicon-compatible materials," *Applied Optics*, vol. 36, pp. 5122-5128, Jul 1997.
- [23] (30th August 2011). *Sopra Download Centre*. Available: <http://www.soprasa.com/index.php>

- [24] V. Gehanno, *et al.*, "Ion beam deposition of Mn-Ir Spin Valves," *IEEE Transactions on Magnetics*, vol. 35, pp. 4361-4367, 1999.
- [25] S. Cardoso, *et al.*, "Ion Beam Assisted deposition of MgO barriers for magnetic tunnel junctions," *Journal of Applied Physics*, vol. 103, p. 07A905, 2008.
- [26] N. P. Barradas, *et al.*, "Simulated annealing analysis of Rutherford backscattering data," *Applied Physics Letters*, vol. 71, pp. 291-293, 1997.
- [27] D. E. Morton, *et al.*, "Optical Monitoring of Thin-films Using Spectroscopic Ellipsometry," in *Society of Vacuum Coaters - 45th Annual Technical Conference* Lake Buena Vista, Florida, 2002.
- [28] S. Radovanovic, *et al.*, *High-speed photodiodes in standard CMOS technology*, 1st ed.: Springer, 2006.
- [29] S. M. Sze, *Physics of semiconductors devices*, 2nd ed. New York: John Wiley & Sons, 1981.
- [30] G. Minas, *et al.*, "On-chip integrated CMOS optical detection microsystem for spectrophotometric analyses in biological microfluidic systems," *ISIE 2005: Proceedings of the IEEE International Symposium on Industrial Electronics 2005, Vols 1- 4*, pp. 1133-1138, 2005.
- [31] J. G. Rocha, *et al.*, "Pixel Readout Circuit for X-Ray Imagers," *IEEE Sensors Journal*, vol. 10, pp. 1740-1745, 2010.

Chapter 5

Experimental Results: Optical Filters Ability for Diagnosis

This Chapter describes the utility of the spectroscopy system based on thin-film optical filters for the diagnosis of GI dysplasia. Two different approaches for the detection of malignancy are presented: (1) a model-based approach, where the full spectrum may be reconstructed from a few discrete data points from which tissue morphological and biochemical parameters can then be quantified (quantitative diagnosis); (2) the use of empirical discrimination criteria based on intensity values in different spectral bands (qualitative diagnosis). Both approaches are validated to be applied once the final prototype is assembled.

5.1 Quantitative diagnosis

As mentioned in Chapter 1 and Chapter 3, point spectroscopy techniques have the uniqueness of allowing a quantitative and objective diagnosis through the acquisition of fluorescence and diffuse-reflectance spectra. Using the full spectra over a wide spectral

region, e.g. from 350 to 750 nm, it is possible to extract several tissue parameters: total hemoglobin concentration and oxygen saturation; collagen and NAD(P)H, or other fluorophores, relative quantities; scatterers density and size [1-5].

The use of the described miniaturized system, based on a few thin-film optical filters, makes impossible the acquisition of a full continuous spectrum. Instead, discrete points are obtained. Still, if the measured points are suitably approximated to the value in the original spectrum, at each particular wavelength, it is possible to reconstruct the original spectrum using interpolation methods (see Chapter 3, sections 3.6.1 to 3.6.3).

5.1.1 Diffuse-reflectance spectroscopy

In Chapter 4, the suitable optical characteristics of the thin-film filters, in terms of structure and transmittance, were demonstrated. The next step involves the performance of diffuse-reflectance measurements on tissue phantoms with different compositions using some of the thin-film optical filters to select specific spectral bands (see Table 5.1). The measurements were performed using a UV-3101PC spectrophotometer. The goal of the study is to determine how accurately each filter is able to detect the diffuse-reflectance signal.

Table 5.1: Tissue phantoms composition and thin-film optical filters used in diffuse-reflectance measurements.

Phantom	Intralipid mass concentration	Hemoglobin concentration (mg/mL)	Thin-film optical filters used (central wavelength, nm)
1	0.5%	0.5	404, 481, 510, 543, 558, 575, 598, 651, 703
2	1%	0.5	
3	1%	1.0	
4	0.5%	0.25	
5	2%	0.25	

For this study, diffuse-reflectance spectra measured from the tissue phantoms without using optical filters were first acquired (Figure 5.1). In all measurements, the characteristic absorption bands of hemoglobin at 420 nm, 540 nm and 580 nm are clearly noticeable.

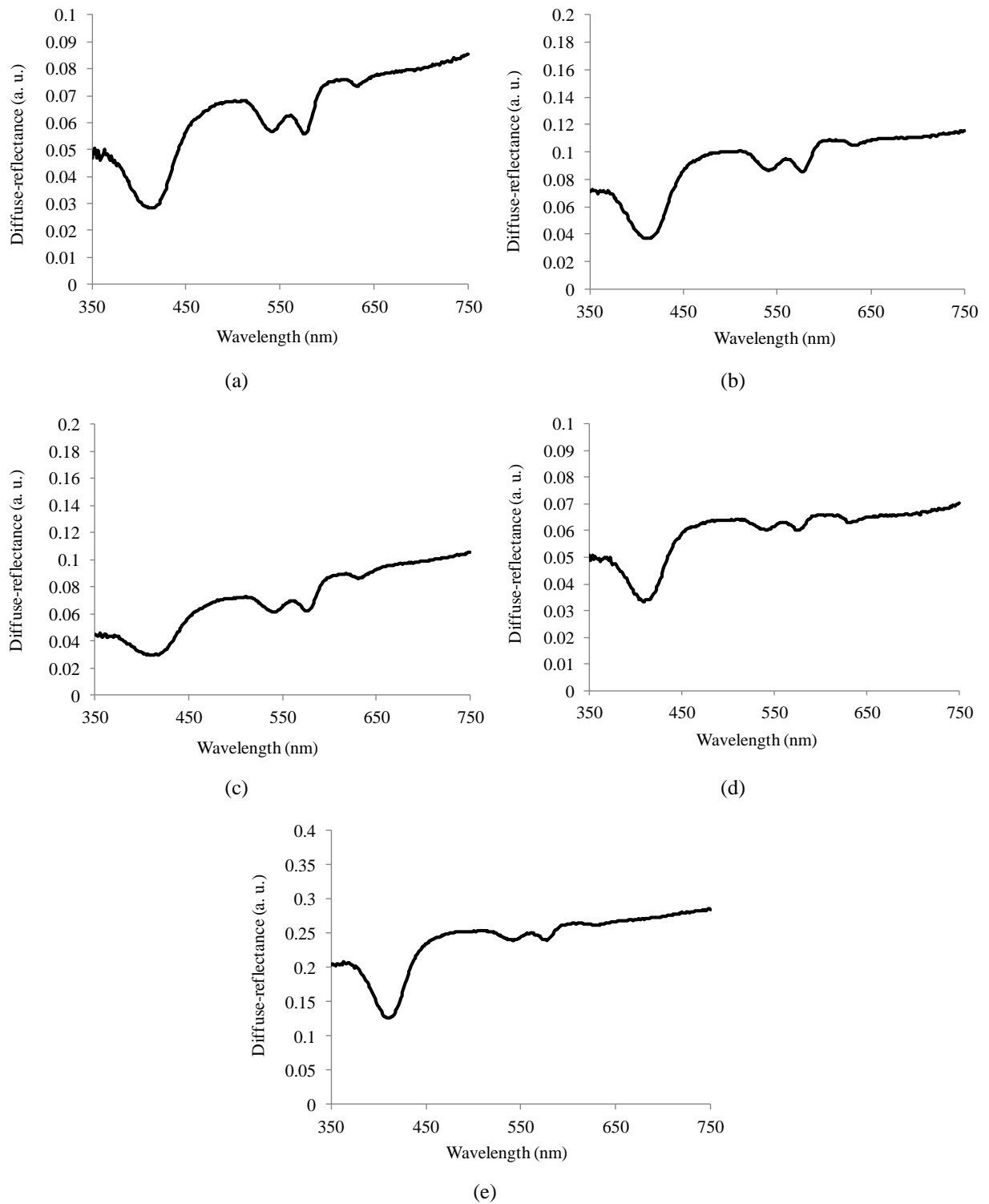


Figure 5.1: Diffuse-reflectance spectra measured with a UV-3101PC spectrophotometer: (a) phantom 1; (b) phantom 2; (c) phantom 3; (d) phantom 4; (e) phantom 5.

After, consecutive DRS measurements using the 9 fabricated filters placed in front of the detection system were performed on all tissue phantoms (Figure 5.2).

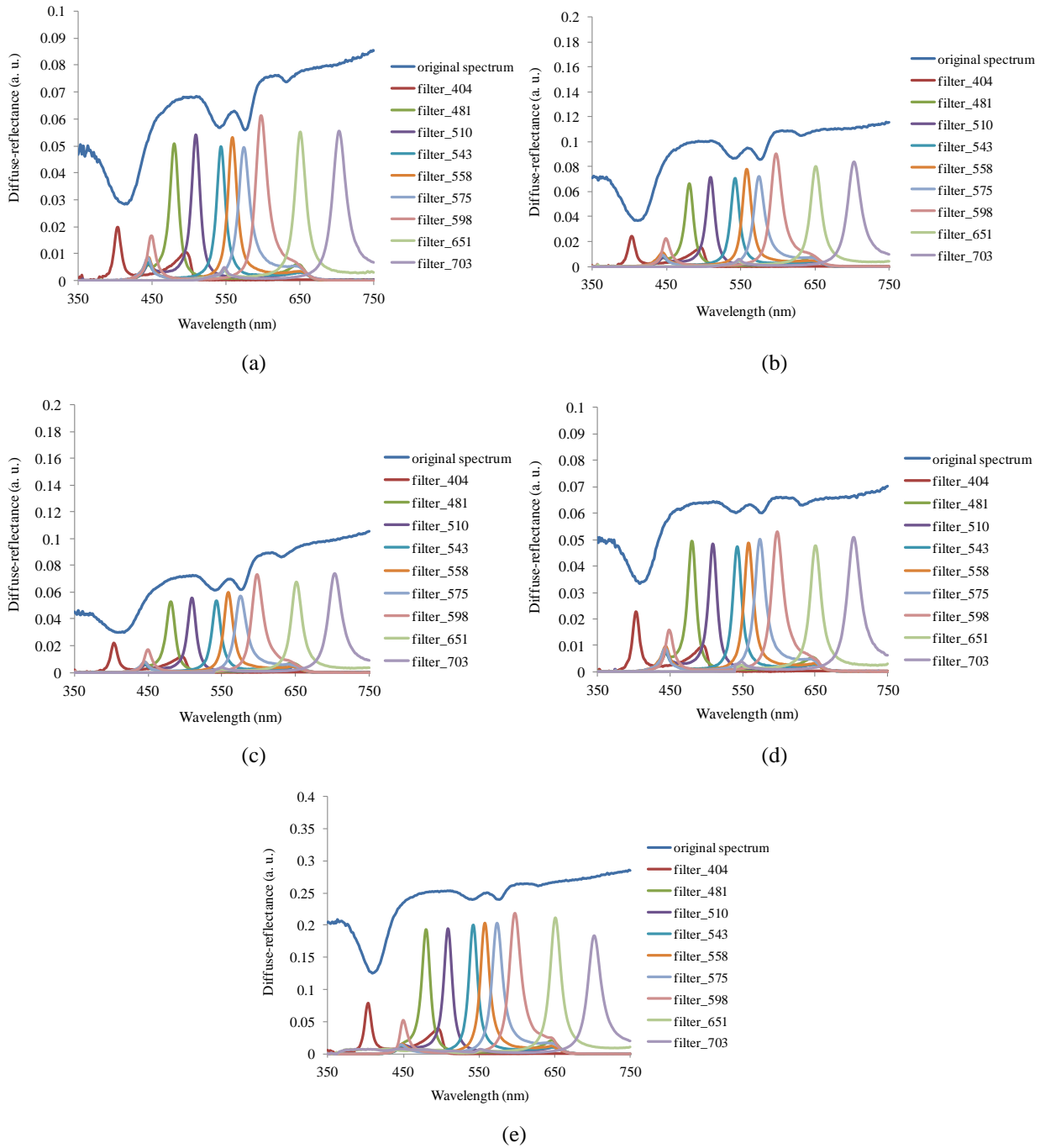


Figure 5.2: Diffuse-reflectance spectra measured with the 9 fabricated narrow-band pass optical filters: (a) phantom 1; (b) phantom 2; (c) phantom 3; (d) phantom 4; (e) phantom 5.

The resulting Gaussian distributed spectra, shown in Figure 5.2, were then integrated. The obtained 9 intensity values, for each phantom, correspond to the signal that will be read in the future by the optical microsensors.

In a further processing, the filters measured transmittance spectra (see Chapter 4, Figures 4.19, 4.29, and 4.32) were also integrated, and the intensities read by the optical microsensors were divided by these 9 values. This way, one can obtain the final 9 data points, for each phantom, that will compose the wavelength-reduced spectrum. In Figure 5.3 these

discrete data points are shown together with the original continuous diffuse-reflectance spectra.

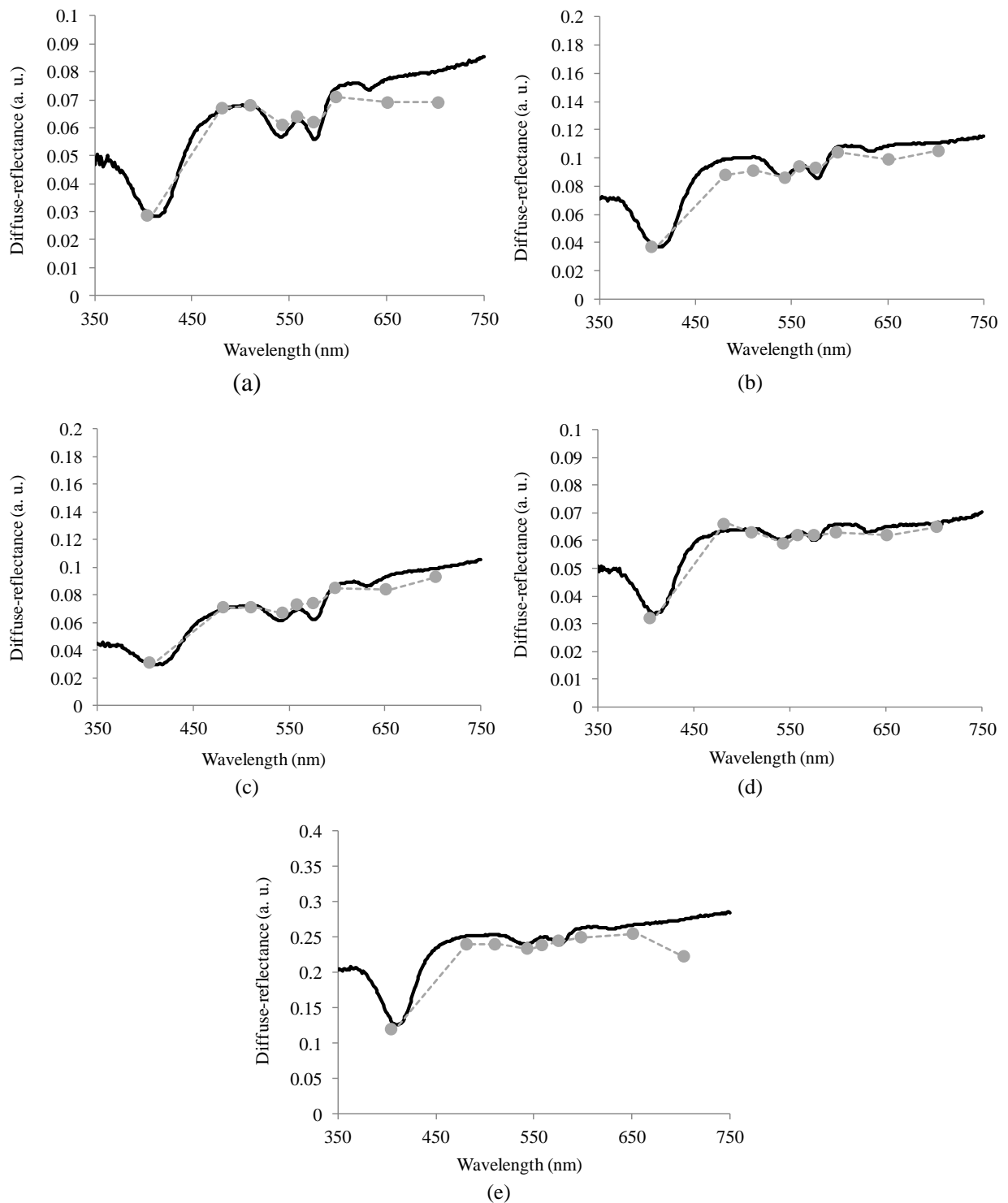


Figure 5.3: Original diffuse-reflectance spectra together with the 9 integrated intensity values that will be obtained using the miniaturized spectroscopy system (a trendline was also added to the discrete data points): (a) phantom 1; (b) phantom 2; (c) phantom 3; (d) phantom 4; (e) phantom 5.

From Figure 5.3 it is possible to conclude that the intensity values obtained with the fabricated thin-film optical filters are similar to the originally obtained diffuse-reflectance intensities measured over the full wavelength range. For a better visualization of the results,

Figure 5.4 shows the comparison between the original results and the results obtained using the thin-film optical filters.

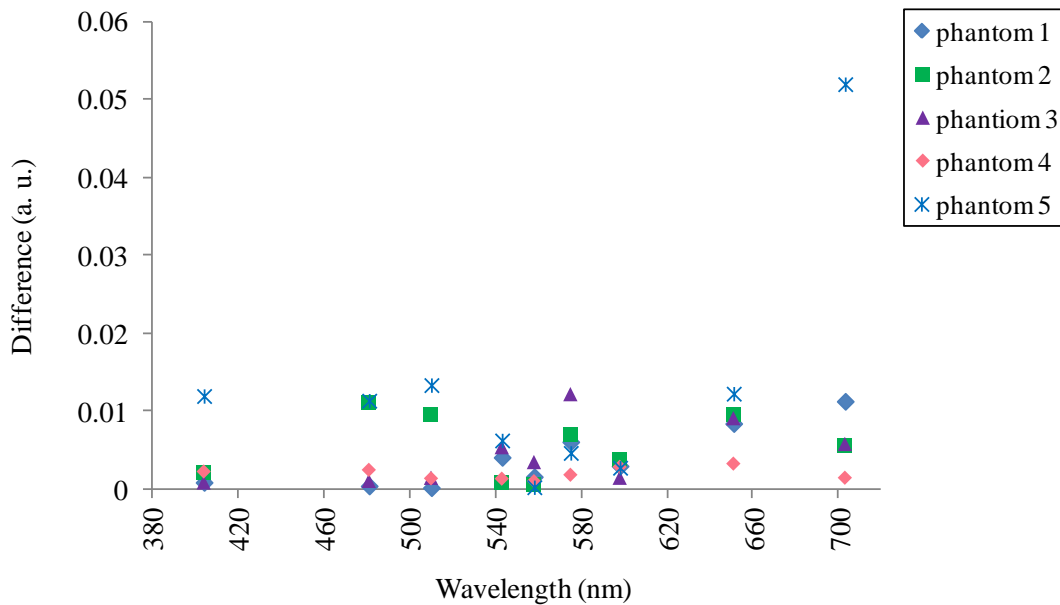


Figure 5.4: Comparison, or difference, between the original results (obtained with the UV-3101PC spectrophotometer) and the results obtained using the 9 thin-film optical filters, for the different tissue phantoms.

The two filters in the red spectral region (centered at 651 and 703 nm) are the filters with the poorest results. On the other hand, the filters centered at 558 nm and 598 nm are the ones that provide the best agreement with the original diffuse-reflectance spectra values.

The divergences that exist between the two measurement approaches are mainly explained by the filters FWHM. Future optimizations to the fabrication process should enable the fabrication of more accurate filters, correctly centered at specific wavelengths, and with a smaller FWHM. Still, currently the mean relative error between the two measurements is less than 5%, while the maximum relative error is around 20%, which means that, overall, it is reasonable to consider that the results validate the possibility of replacing the spectrograph by an array of thin-film narrow-band pass filters for diffuse-reflectance measurements.

5.1.2 Fluorescence spectroscopy

Fluorescence measurements were also performed on two tissue phantoms composed by a different mixture of water based intralipid, hemoglobin, and furan (fluorophore). This fluorescent dye was selected because it has an excitation and emission spectra similar to that of collagen, which, as mentioned in Chapter 3, is an endogenous tissue fluorophore important for diagnosis. The goal of this study was to extract intrinsic fluorescence from bulk fluorescence measurements and, also, to assess the capability of the thin-film optical filters to accurately detect the fluorescence signal.

During this study it was not possible to perform the experiments using the fabricated filters due not only to technical problems with the equipment, but also because the majority of filters in the blue region didn't provide suitable transmittance results to be used, as it was explained in Chapter 4.

However, fluorescence measurements were performed and the algorithm to extract the intrinsic fluorescence (described in Chapter 3) was implemented using MATLAB tools and successfully applied to the measurements, as will be next described next below. A theoretically feasibility study was also executed using the measured transmittance curve of one of the fabricated filters in the blue region (centered at 404 nm) for assessing the performance of this filter when used for fluorescence spectroscopy. For the present analysis, fluorescence measurements were performed on the two phantoms with intralipid, hemoglobin and furan (Sigma Aldrich Co.) - bulk fluorescence, and on a solution of pure furan - equivalent to the intrinsic fluorescence, using a conventional fluorometer (SPEX[®] FluoroLog[®]). The results are shown in Figure 5.5. As it was predicted, the emitted fluorescence intensity decreases as the hemoglobin concentration increases, due to an increase in absorption.

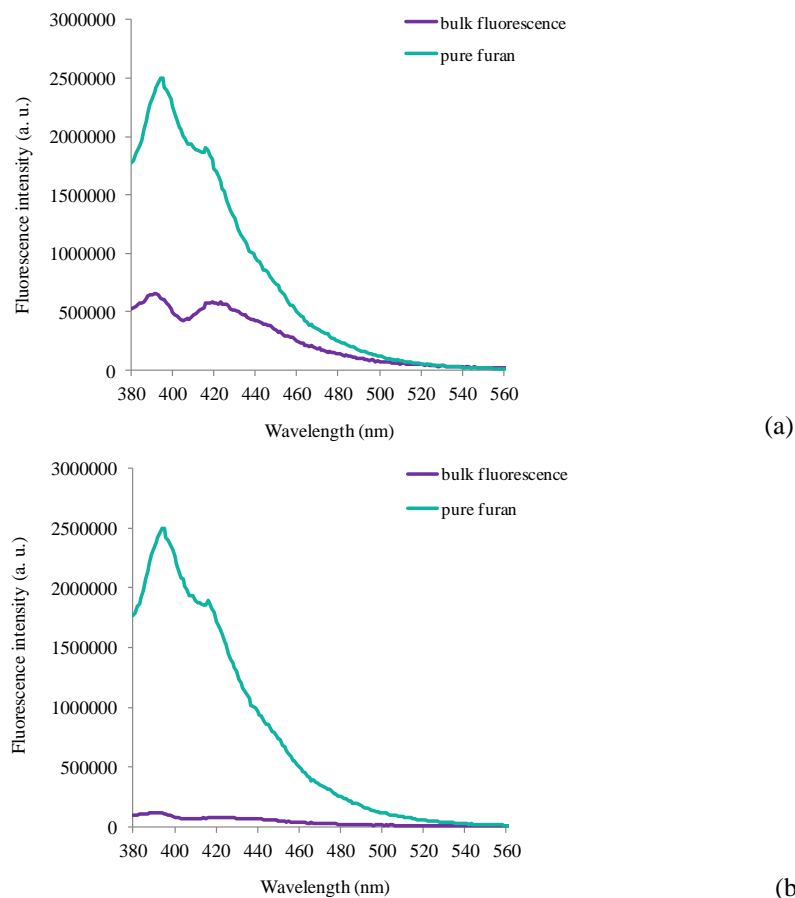


Figure 5.5: Bulk fluorescence and intrinsic fluorescence (pure furan) measured from two tissue phantoms: (a) phantom with intralipid mass concentration equal to 2%, hemoglobin concentration of 0.25 mg/mL, and furan concentration of 0.25 µg/mL; (b) phantom with intralipid mass concentration equal to 2%, hemoglobin concentration of 0.5 mg/mL, and furan concentration of 0.25 µg/mL.

For the feasibility study, the fluorescence measured from the two phantoms was first multiplied by the filter's transmittance curve (see Chapter 4, Figure 4.29). The resulting two Gaussian distributed spectra were then integrated over the fluorescence emission range. This way, the obtained intensity values are equivalent to the signal that will be read by photodiode below the blue filter. After, the filter's transmittance spectrum was also integrated, and the two intensities theoretically read by the photodiode were divided by this value to obtain the final data points. These points are represented in Figure 5.6.

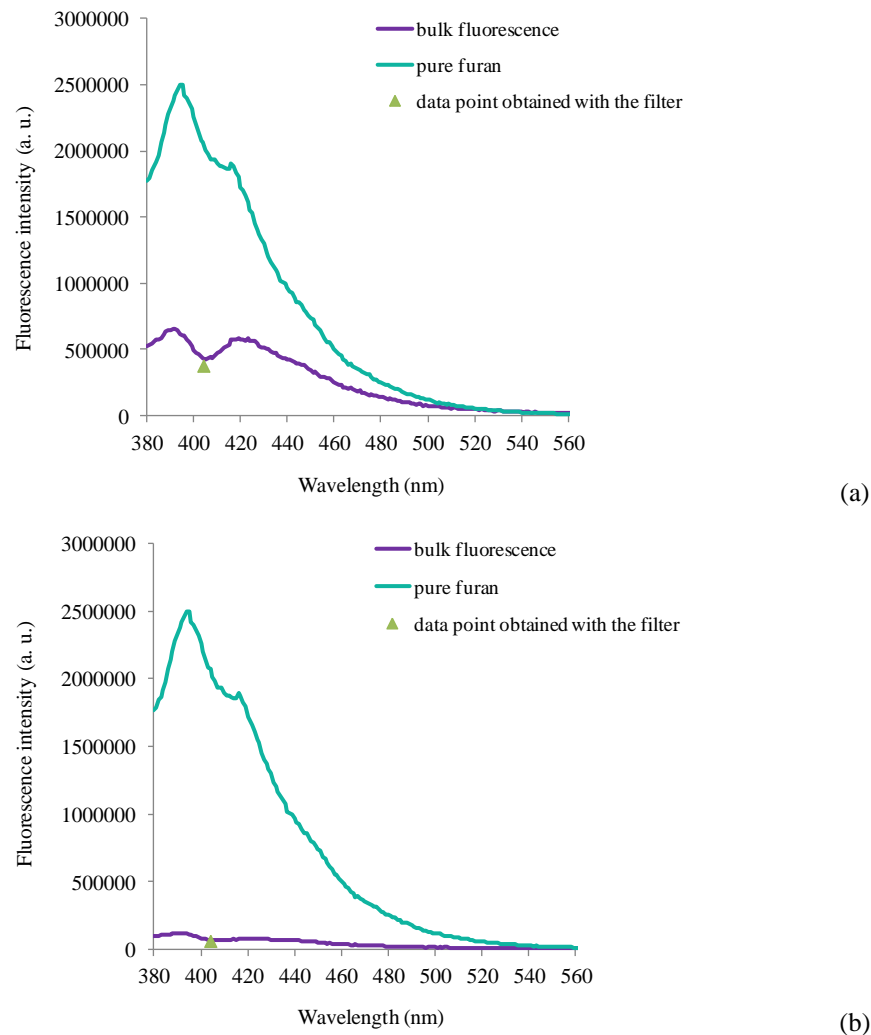


Figure 5.6: Bulk fluorescence and intrinsic fluorescence (pure furan) measured from two tissue phantoms, together with the two intensity values that would be obtained using the blue optical filter: (a) phantom with intralipid mass concentration equal to 2%, hemoglobin concentration of 0.25 mg/mL, and furan concentration of 0.25 $\mu\text{g/mL}$; (b) phantom with intralipid mass concentration equal to 2%, hemoglobin concentration of 0.5 mg/mL, and furan concentration of 0.25 $\mu\text{g/mL}$.

From Figure 5.6 it can be concluded that the intensity values obtained with the optical effect of the filter are similar to the originally obtained bulk fluorescence intensities measured over the full wavelength range. This also validates the possibility of replacing the spectrograph by thin-film optical filters.

The intrinsic fluorescence algorithm was finally applied to the original bulk

fluorescence spectra in order to obtain a spectrum similar to the pure furan spectrum, i.e., not subjected to scattering and absorption effects. The obtained results are shown in Figure 5.7.

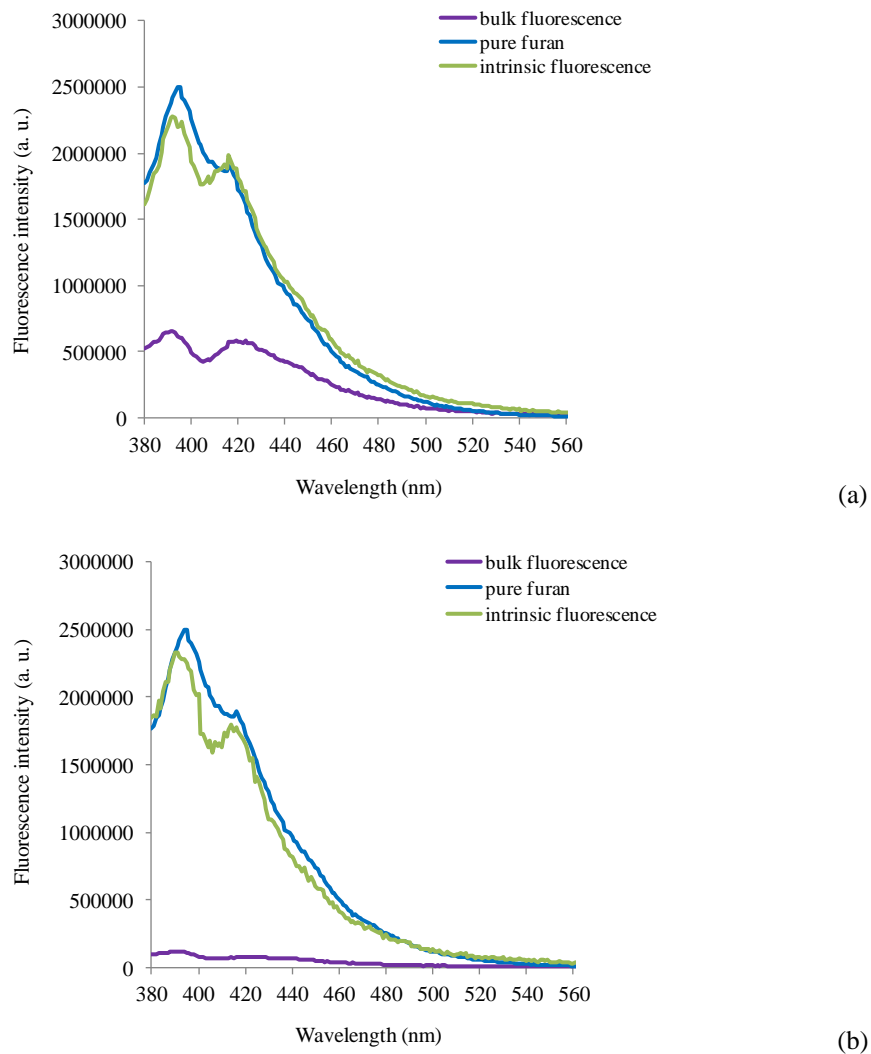


Figure 5.7: Bulk fluorescence spectra and the corresponding intrinsic fluorescence spectra measured from two tissue phantoms: (a) phantom with intralipid mass concentration equal to 2%, hemoglobin concentration of 0.25 mg/mL, and furan concentration of 0.25 $\mu\text{g/mL}$; (b) phantom with intralipid mass concentration equal to 2%, hemoglobin concentration of 0.5 mg/mL, and furan concentration of 0.25 $\mu\text{g/mL}$. The blue spectra in both figures are the fluorescence measured from pure furan in water.

From Figure 5.7 it is possible to conclude that the extracted intrinsic fluorescence spectra, which are independent to the absorbers and scatterers, and the raw spectrum of pure furan are well overlapped. This successfully proves the ability of the algorithm to extract only the tissue fluorophores fluorescence.

5.2 Qualitative diagnosis

A less-complex spectroscopy system can be built using only two optical microsensors. One microsensor will be used for fluorescence measurements, while the other will be used to

collect the reflectance signal. Alternatively, the same array of 16 optical microsensors can be used, but the data analysis can be performed for only two microsensors. This potentially speeds up the analysis. Also, for this less complex approach, data from wavelengths above 650 nm is going to be excluded since it doesn't add significant information for a qualitative diagnosis.

To design the optical microsensors, i.e., to define the two specific transmittance spectral bands of the optical filters, diffuse reflectance and fluorescence data from normal and dysplastic gastrointestinal tissue was used (examples are shown in Figure 5.8). This data set comprised 9 dysplastic tissue sites and 42 normal tissue sites.

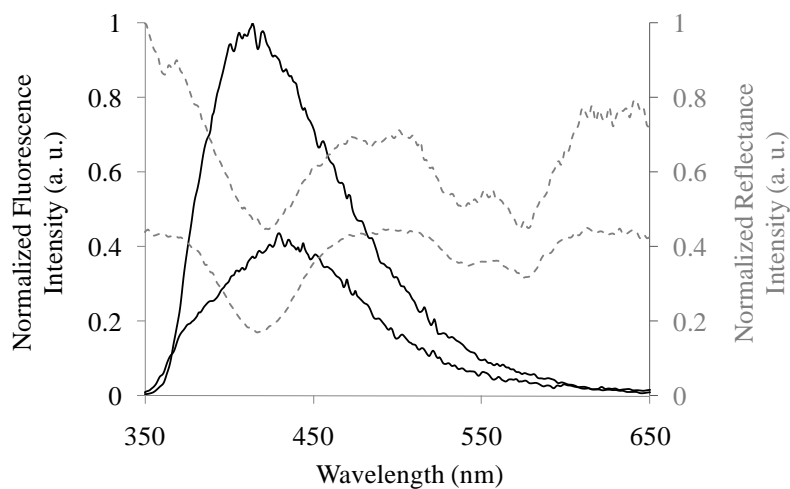


Figure 5.8: Diffuse reflectance (dashed lines) and fluorescence (solid lines) spectra examples. Higher intensity spectra correspond to normal tissue, whereas dysplastic tissue sites exhibit low intensity spectra. For this illustration, reflectance and fluorescence intensity spectra were normalized to their maximum intensity values for a better comparison of their spectral shape (peaks and valleys).

From Figure 5.8, and using only two spectral bands, the optical filters should be able to select one fluorescence band in the violet/blue region of the spectrum (centered at 420 nm) and one reflectance band in the green region of the spectrum (centered at 540 nm). These central wavelengths were selected in order to detect approximately the maximum fluorescence emission of tissues, and to detect one of the hemoglobin absorption peaks in the reflectance signal. A previous study [6] has shown that it is very important to take into account a green reflectance band, to help in the differentiation of inflammation from tumors, and thus reduce the number of false-positives. For this reason, the 540 nm spectral band was selected for the reflectance measurements, instead of the 420 nm spectral band.

For the green region, the filter composed by 52 nm thick TiO_2 and 95 nm thick SiO_2 mirror layers, and with a 192 nm thick resonance cavity was used. For the violet/blue region, the filter composed by 45 nm thick TiO_2 and 70 nm thick SiO_2 mirror layers, and with a 138

nm thick resonance cavity was used.

The tails of the green and violet/blue filters at wavelengths farther from their transmittance peak may raise some concerns. For the violet/blue optical filter the transmittance increases from 550 to 650 nm (see Chapter 4, Figure 4.30). Given that this optical filter is going to be used solely for fluorescence measurements, this collection of out of band light is not a problem once fluorescence emission in this band tends to zero (see Figure 5.8). In turn, the green optical filter tail at low wavelengths will be collecting significant out of band light that will confound the reflectance analysis (see Chapter 4, Figure 4.34(a)). Still, this problem can be exceeded when the effect of the silicon photodiode is integrated in the measurements, as described in Chapter 4, section 4.3 (see Figure 4.34(b)).

The feasibility of using the developed optical microsensors for distinguishing dysplasia from normal tissue was theoretically assessed with a spectral analysis. For this study, the optical filters transmittance curves were used together with spectroscopy diffuse-reflectance and fluorescence data. Histopathology diagnoses are used as the standard against which the spectroscopic-qualitative diagnoses are compared.

In this analysis, all diffuse-reflectance and fluorescence spectra (not normalized) were first multiplied by the green and violet/blue filters measured transmittance curves, respectively (see Chapter 4, Figure 4.30 and Figure 4.34(b)). The resulting Gaussian distributed spectra were then integrated over the full transmittance range (from 350 to 650 nm). The obtained integrated intensity values correspond to the signal that will be read by the photodiodes.

Subsequently, a statistical analysis was performed on the processed spectral data using the Student's *t*-test, the Mann-Whitney test, and the logistic regression model. This analysis is performed in order to extract any relevant diagnostic algorithm that provides diagnostic differences between normal and dysplastic tissues. A statistical software (SPSS) was used for this study.

The Student's *t*-test and the Mann-Whitney test, respectively, were used to compare normally and not normally distributed continuous variables (diffuse-reflectance intensity in the green spectral band, and fluorescence intensity in the violet/blue spectral band) for two distinct groups of tissue sites: dysplastic and normal. A *p*-value less than 0.05 was considered to be statistically significant. For both variables the null hypothesis was rejected. This means that the measured intensity values of diffuse-reflectance at 540 nm, and of fluorescence at 420 nm, are significantly different between the two groups. In nearly all cases, compared with dysplasia, normal tissue sites exhibit significantly higher intensity values, both for diffuse-reflectance and fluorescence, as it was expected. As explained in Chapter 3, a decrease in the

fraction of collagen fibers with progression of dysplasia is translated by low fluorescence intensities, and by a reduced reflectance signal as a result of low scattering. Also, a high hemoglobin concentration, which is characteristic of dysplastic tissues, may attenuate the diffuse-reflectance and endogenous fluorescence signal due to absorption.

The spectral algorithm for classifying tissue as normal or dysplastic was developed by using binary logistic regression. A model with a good predictive capability includes both the diffuse-reflectance and fluorescence data. The accuracy of the final logistic regression model is evaluated by the area under the ROC (Receiver Operating Characteristic) curve (AUC), and the sensitivity and specificity. The box plots of the reflectance and fluorescence variables, as well as the ROC curve for the differentiation of dysplasia from normal tissue are presented in Figure 5.9.

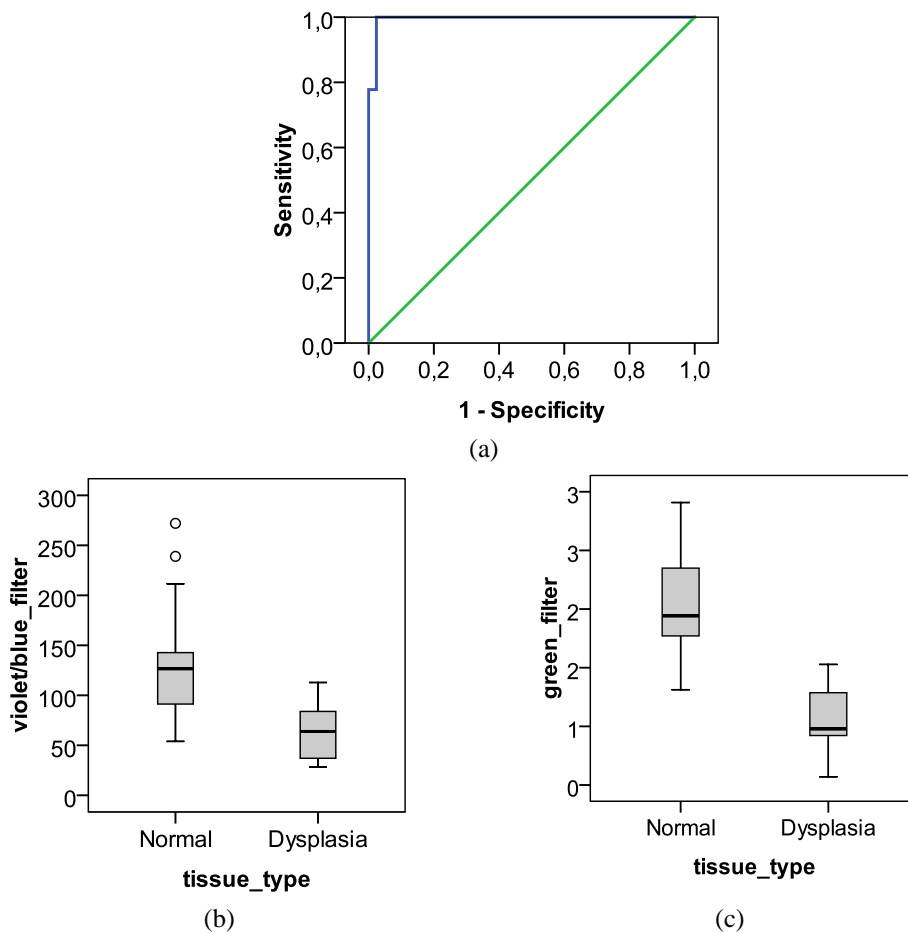


Figure 5.9: Discrimination of normal from dysplastic tissue sites: (a) ROC curve for the logistic regression algorithm: ROC curve (blue solid line); 45 degree green line (AUC = 0.5). The AUC measures the accuracy of the model to correctly classify normal and diseased tissue. A perfect discrimination is achieved with an AUC value of 1; an AUC value of 0.5 indicates an inability to differentiate the two tissue types. Box plots of the two variables included in the model: (b) fluorescence data from the violet/blue spectral region for the two tissue types; (c) reflectance data from the green spectral region for the two tissue types. Outliers are symbolized by circles.

From the results of Figure 5.9 one can say that the violet/blue fluorescence and green diffuse-reflectance intensities are good predictors for the discrimination of tissue disease

status. The model has an overall accuracy of 94.1%. Dysplasia and normal tissue can be distinguished with an AUC, sensitivity, and specificity of 0.995, 77.8%, and 97.6%, respectively. Sensitivity is defined as the fraction of dysplastic tissue sites correctly identified by the model, whereas specificity is defined as the fraction of correctly identified normal tissue sites. The not very high value of sensitivity might be explained by the small number of dysplastic tissue sites used, which is a limitation in this study. The positive predictive value (PPV), which is the probability that a positive result is accurate equals to 87.5%. The negative predictive value (NPV), which is the probability that a negative result is accurate, is equal to 95.3%. A high NPV (low number of false negatives) is very important for an effective clinical practice, especially when the system is going to be used to guide biopsies, since the physician has to be confident that none of the dysplastic lesions are identified as normal, and consequently not subjected to biopsy. A low NPV might be indicative that cancerous tissue is left in the patient without being identified.

Mayinger et al. [7] described a measurement system that uses differences in the fluorescence spectral intensities to identify cancerous tissue in the upper GI tract. Tissues were excited with violet-blue light and fluorescence spectra were collected using an optical fiber and analyzed with a spectrograph. The developed algorithm was based on the intensity ratio in the green and red spectral bands and provided a sensitivity of 97% and a specificity of 95% for the diagnosis of esophageal cancer. However, in his study it was not included data for benign lesions (e.g. inflammations) that might influence fluorescence spectroscopy. Uedo *et al.* [6] found that a superficial neoplasm and an inflamed tissue with edema could be misunderstood using only fluorescence measurements. For this reason, green reflectance information was added to his algorithm, and proved to be helpful for the differentiation of inflammation from tumors. Bourg-Heckly and co-workers [8] also used a fluorescence spectroscopy system for the detection of dysplasia in the upper GI tract. The instrument was composed by a UV xenon lamp, band-pass filters, optical fibers for light delivery and collection, and a spectrometer with a CCD camera for detection. Overall, this optical set-up is not portable and compact to be used in the clinical environment. In this study of Bourg-Heckly, a model based only on the fluorescence intensity ratio at two different wavelengths (390 and 550 nm) was able to discriminate neoplastic tissue from normal mucosa with a sensitivity of 86% and specificity of 95%.

In summary, this study approach has two major benefits when compared to others: (1) there is a combination of diffuse-reflectance and fluorescence information, which combination was shown to be helpful for the discrimination of benign and malignant lesions; (2) it is demonstrated that it is possible to identify dysplastic and healthy tissue sites, with a

suitable sensitivity and specificity, using a much smaller instrument, compared with the instruments used in similar studies.

Despite that the obtained results with only two optical filters are very promising, further study should be done. As an important next step, the performance of the presented diagnostic algorithm should be tested in a large clinical study. Moreover, the overall predictive capability of the model could be improved by adding other fluorescence and reflectance spectral bands as predictors, having this, however, attached the disadvantage of increasing the overall complexity of the system and/or of the data analysis.

References

- [1] I. Georgakoudi, *et al.*, "Fluorescence, reflectance, and light-scattering spectroscopy for evaluating dysplasia in patients with Barrett's esophagus," *Gastroenterology*, vol. 120, pp. 1620-9, Jun 2001.
- [2] C. C. Yu, *et al.*, "Quantitative spectroscopic imaging for non-invasive early cancer detection," *Optics Express*, vol. 16, pp. 16227-39, Sep 2008.
- [3] J. Mirkovic, *et al.*, "Effect of anatomy on spectroscopic detection of cervical dysplasia," *J Biomed Opt*, vol. 14, p. 044021, Jul-Aug 2009.
- [4] Z. Volynskaya, *et al.*, "Diagnosing breast cancer using diffuse reflectance spectroscopy and intrinsic fluorescence spectroscopy," *J Biomed Opt*, vol. 13, p. 024012, Mar-Apr 2008.
- [5] I. Georgakoudi, "The color of cancer," *Journal of Luminescence* vol. 119-120, pp. 75-83, 2006.
- [6] N. Uedo, *et al.*, "A novel videoendoscopy system by using autofluorescence and reflectance imaging for diagnosis of esophagogastric cancers," *Gastrointest Endosc*, vol. 62, pp. 521-8, Oct 2005.
- [7] B. Mayinger, *et al.*, "Light-induced autofluorescence spectroscopy for the endoscopic detection of esophageal cancer," *Gastrointest Endosc*, vol. 54, pp. 195-201, Aug 2001.
- [8] G. Bourg-Heckly, *et al.*, "Endoscopic ultraviolet-induced autofluorescence spectroscopy of the esophagus: tissue characterization and potential for early cancer diagnosis," *Endoscopy*, vol. 32, pp. 756-65, Oct 2000.

Chapter 6

Experimental Results: *Ex Vivo* Spectroscopy System

This Chapter describes an *ex vivo* quantitative spectroscopy scanning platform which enables integration of different optical modalities for the assessment of *ex vivo* tissue properties. The system is intended to be used in operating rooms, with the ultimate goal of imaging excised tissue margins. The clinical utility of the system is demonstrated using *ex vivo* tissue samples. This work was developed at the GR Harrison Spectroscopy Laboratory, at the Massachusetts Institute of Technology (MIT).

6.1 Clinical need

In the majority of Western countries, surgery is the standard treatment for cancers in the GI tract [1]. The introduction of EMR techniques with the ability to remove 2 to 3 cm pieces of mucosa and submucosa represents one of the most important advances in the

treatment of GI cancers over the last ten years [2]. In particular, EMR is the treatment of choice for high-grade dysplasia arising from BE and esophageal ADC [2-3].

EMR has two major benefits: (1) it has a curative ability since it completely removes the diseased mucosa by resecting through the middle or deeper part of the submucosa; (2) it can provide larger and deeper biopsy specimens that allow a more precise determination of the depth of tumor penetration [2, 4]. The depth of tumor penetration is critical to determine the potential for nodal spread [2].

The success of EMR greatly depends on a precise examination of the resected tissue: the location, size, gross appearance, histology, degree of cancer differentiation, depth of cancer invasion, involvement of lymphatics or blood vessels in the submucosa, and cancer involvement of lateral and vertical margins (distance of cancer from the resection margins) must be reported in detail for each specimen [1, 5]. Specifically, lateral and vertical margins of a specimen must be carefully pathologically assessed since EMR of a discrete lesion risks leaving a positive resection margin (i.e. there are cancer cells at the outer edge of the excised specimen) [2].

As mentioned in Chapter 1, this pathological examination is time-consuming, which limits the ability of the surgeon to know within the surgery time if he had removed all the cancerous tissue from the patient (i.e. if there are no positive margins), or if he needs to re-excite more tissue. However, currently, there are no alternative reliable tools to assess tissue intra-operatively [6]. A significant number of oncology surgeries are, this way, concluded before the pathology laboratory results are known [7]. As a major consequence, re-operation due to the existence of positive surgical margins is common, which means that cancer has not been completely removed with the first surgery [6].

Indeed, a study by Mino-Kenudson et al. suggests that EMR only achieves complete excision of Barrett's related cancerous lesions in 4% of all cases [8]. This not only increases healthcare costs but, most important, it increases the risk of morbidity associated with extra time spent by the patient in the operating room. Therefore, there is a significant technological and clinical need for methods and systems capable of a fast and reliable evaluation of excised tissues.

Ex vivo wide-field imaging strategies, based on an optical diagnosis, have already been proposed as potential tools for surgical margin assessment [6, 9-10]. Mahadevan-Jansen and coworkers have successfully applied contact probe autofluorescence and DRS, and a spectral imaging to classify positive and negative margins of excised breast specimens with high sensitivity and specificity [9]. However, a quantitative analysis using images was not performed. Pogue and co-workers used confocal reflectance microscopy and spectrograph to

raster-scan *ex vivo* tumors margins and obtained mainly quantitative scattering parameters associated with tissue morphology [10]. Similar to previous wide area spectroscopic imaging, the non-probe method requires some correction to deal with lines shape spectra if the technique is used to acquire quantitative absorption parameters [9]. A quantitative optical imaging device to assess breast tumor margins was developed by Ramanujam *et al.* [6] using diffuse-reflectance spectroscopy for the extraction of scattering and absorption information. In this work the margin surface is obtained by manually translating an imaging probe that contacts the specimen in a container through pre-drilled holes with 5 mm center to center spacing, which may limit the image resolution.

In this Chapter, it is presented a new and complementary strategy to enable real-time comprehensive assessment of surgical margins in excised GI tissues. This system can have a great impact in esophageal EMR, but it is not limited to this organ. An *ex vivo* spatial high-resolution quantitative spectroscopy (QS) scanning platform for wide area surveillance of tissue has been developed. This QS scanning platform enables integration of different optical modalities which provide quantitative tissue information that correlates to disease state of the surrounding tissue. However, currently the platform only integrates DRS and IFS for the extraction of several spectroscopic parameters, but it is adaptable to assemble many other optical modalities. DRS and IFS have been first implemented on the scanning platform since, and as referred in Chapter 3, they have shown great ability for the detection of dysplasia and cancer in the esophagus.

The design and feasibility studies of the multi-modal scanning platform for an intra-operative medical device, that is able to perform a rapid, real-time, detailed, and reliable quantitative spectroscopic analysis of tissue surfaces, are described in the sections below. The major benefit of this “adaptable scanning platform” concept is that it is not limited to only one optical modality, enabling the selection of the appropriate technique for each margin assessment, or to use a combination of different techniques.

6.2 System overview

Given that *ex vivo* tissue analysis does not have typical restrictions of *in vivo* imaging such as imaging geometry, surface contour, or patient motion, spectroscopic mapping of an arbitrarily wide area is achieved by mechanically scanning an optical probe (the FastEEM probe) in an inverted geometry. Spectroscopic data are then taken one grid at a time, as the probe moves, with variable grid-to-grid (GTG) distance and field of view (FOV).

In the developed instrument, the *ex vivo* tissue surface under examination can have a variable size from 2 square mm to 4 square cm. Still, if necessary, the area for tissue analysis

can be easily increased by including a larger sample holder to the scanning platform. The samples are placed for analysis in a flat platform, which enables an equal pressure across time and an equal distance between probe and tissue throughout the analysis.

The FastEEM contact probe [11] consists of a single light delivery fiber surrounded by six collection fibers that collect light from tissue and deliver it back to the spectrograph (all seven fibers with 200 μm core and $\text{NA} = 0.22$). All fibers are fused together at the tip and polished at 17 degree angle to provide the overlapping of detector and collector optical cones. For spectroscopic scanning, only one of the collection fibers will be used to collect tissue reflectance and fluorescence from a spot size of approximately 500 μm . Wide area coverage is achieved by scanning the spot of illumination light over the tissue, using XY mechanical scanning. The spectroscopic scanning can be performed with variable resolution, which can be as high as a quarter of the spot size since both GTG distance and FOV are controllable.

Figure 6.1 depicts the schematic diagram (a) and the photographs (b) of the developed instrument.

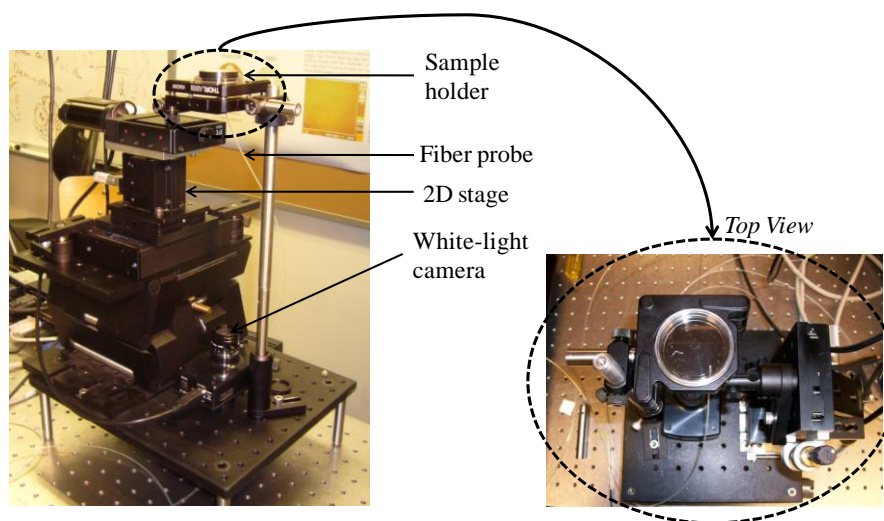
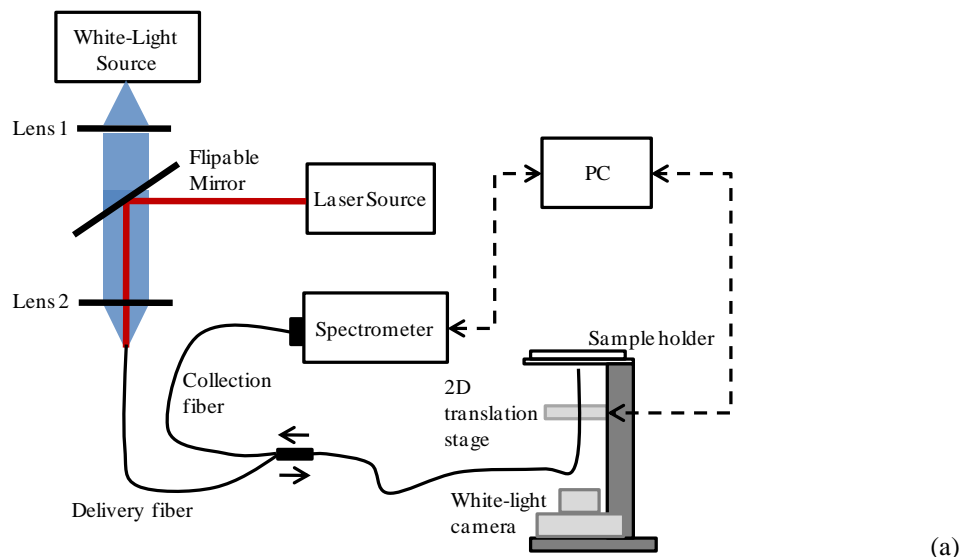


Figure 6.1: (a) Schematic layout and (b) photographs of the *ex vivo* quantitative spectroscopy scanning platform; a regular white-light camera is used to take pictures of the samples under analysis.

To perform DRS measurements, white-light from a 75W CW xenon arc lamp (Oriel Instruments, USA) is coupled via the delivery fiber, to illuminate a “diagnostic spot” of ~0.5 mm in diameter on the tissue sample. DRS signal from the sample is collected, with adjacent collection fibers, and coupled to a spectrometer (USB 2000+, Ocean Optics, USA). A personal computer equipped with Labview 8.5.0 software and DAQ data acquisition board NI PCI-6221 (National Instruments, USA) are used to control and coordinate the various components, including the GTG distance and FOV of the 2-D mechanical scanning (M-605.1DD and M-126.DG1, Physik Instrument, Germany). Spectroscopic data from the spectrometer and 2D stage positions are acquired and then analyzed using model-based diagnostic algorithms [12-13]. This way, the instrument will be able to correlate spectroscopic parameters with disease status in real-time.

Same resources, data handling and data acquisition are utilized for IFS measurements, except the light source is a pulsed diode pumped solid state laser that delivers 355 nm light pulses of duration ~0.6 ns and energy ~0.26 μ J at ~38 kHz (SNV-40F-000, Teem Photonics, France). Note that different measurements are accomplished through switching the excitation sources with an installed flipping mirror. Without any significant changes to the scanning engine, the integration of other optical modalities, such as infrared or Raman spectroscopy, would only require add-on and data acquisition to the platform. This all-in-one device could be a powerful tool in intra-operative clinical tissue diagnostics.

6.3 System calibration

The instrument calibration was performed using liquid phantoms with known scattering, absorption and fluorescence properties. These phantoms were constructed by a mixture of water based intralipid - scatterer - (Fresenius Kabi AG), hemoglobin – absorber - (Sigma Aldrich Co.) and furan – fluorophore - (Lambda Physik) at various concentrations. All the measurements were performed using a wavelength range from 350 to 750 nm for DRS and 380 to 750 nm for IFS.

The accuracy and capability of the system for reflectance measurements was carried on using several combinations of various concentrations of intralipid, furan (0.5 μ g/mL) and hemoglobin (0.6, 1, and 1.5 mg/mL). Reflectance spectra were acquired from one spot in each sample. All the spectra were normalized by a reflectance standard (Labsphere SRS-20) in order to remove spectral distortions and spatial inhomogeneities related with the instrument’s spectral and spatial responses.

Figure 6.2 shows the calibrated DRS spectra, from the same position on the sample, for different phantoms. DRS was used for the extraction of diagnostic information: by fitting

the reflectance spectrum to the diffuse scattering model described by Zonios *et al.* [12], and presented in Chapter 3, three DRS parameters were extracted for each pixel: A_s , the reduced scattering coefficient at the reference wavelength; B_s , related to the average scatter size; and cHb , the total concentration of hemoglobin. However, it is important to notice that in the presented results all the samples were exposed to air and, thus, their estimated oxygen saturation is close to 1.0.

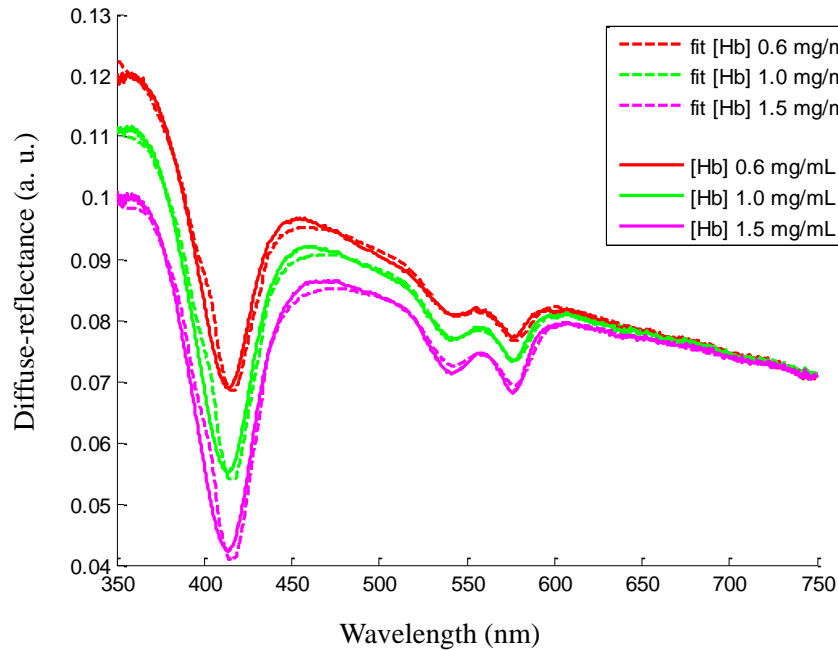


Figure 6.2: Calibrated reflectance spectra (solid lines) measured on different tissue phantoms. The best fit spectra are also plotted (dashed lines). The characteristic absorption bands of hemoglobin at 420, 540, and 580 nm are clearly visible.

Figure 6.2 shows that optimal fits were obtained between the measured and computed spectra from the samples. From the excellence agreement, the computed spectra give the correct values of reflectance spectroscopy parameters, which ensure that the instrument can accurately measure the scatter and absorber parameters. The values for parameters A_s , B_s , and cHb are compiled in Table 6.1.

Table 6.1: Reflectance parameters (A_s , in mm^{-1} , B_s , and cHb in mg/mL) measured from tissue phantoms with different hemoglobin concentrations.

Parameters	$cHb = 0.6$	$cHb = 1.0$	$cHb = 1.5$
A_s	1.072	1.072	1.069
B_s	0.318	0.301	0.254
cHb	0.623	1.004	1.473

The accuracy of fluorescence measurements was then assessed using the same set of phantoms. The fluorescence at each spot is analyzed using IFS: reflectance measurements are

used to correct the bulk fluorescence spectra (affected by scattering and absorption) using the model described by Müller *et al.* [14] (described in Chapter 3) to extract the IFS spectra. Figure 6.3 shows the fluorescence spectrum of pure furan in water (blue line), and the several bulk and IFS spectra measured using phantoms with different hemoglobin concentrations. As expected, the data confirms that bulk fluorescence spectra vary considerably with hemoglobin concentration in opposition to the IFS spectra. The excellent agreement between the IFS spectra and the spectrum of pure furan in water indicates that IFS method can be used to remove the distortions caused by tissue scattering and absorption. These data provide evidence for an accurate calibration of the QS scanning platform.

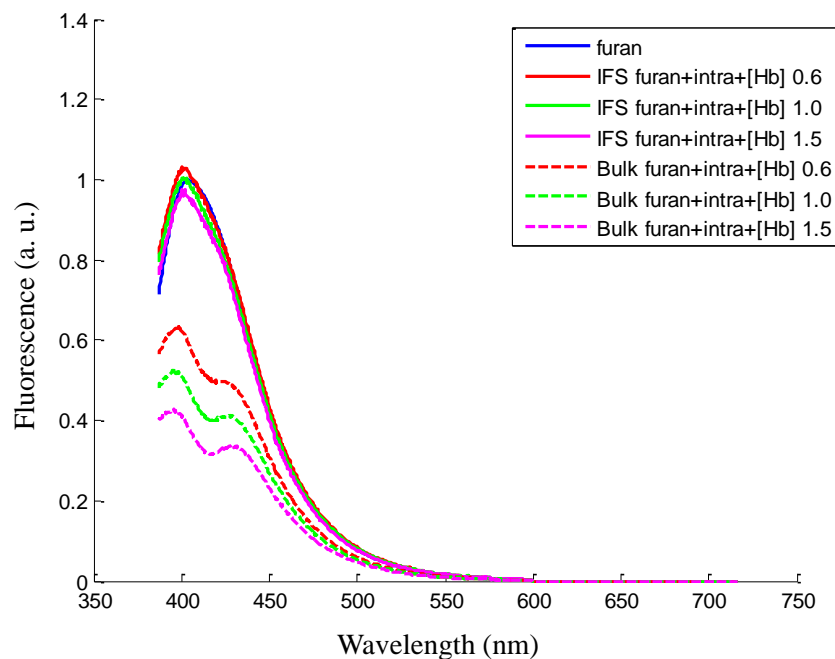


Figure 6.3: Bulk fluorescence spectra (dashed lines) measured on different tissue phantoms. The corresponding intrinsic fluorescence spectra (IFS) are also plotted (solid lines). The blue spectrum is the fluorescence measured from pure furan in water. Note that the calculated IFS spectra, which are independent to the absorbers and scatterers and the raw spectrum of pure furan are well overlapped.

6.4 Tissue imaging

In order to assess the performance of the developed system, in an initial approach, a series of experiments was performed using breast tissue with two previously identified distinct areas: normal and malignant. Figure 6.4 shows a white-light picture of the analyzed tissue specimen. This picture was taken using the white-light camera installed below the sample holder (Figure 6.1).

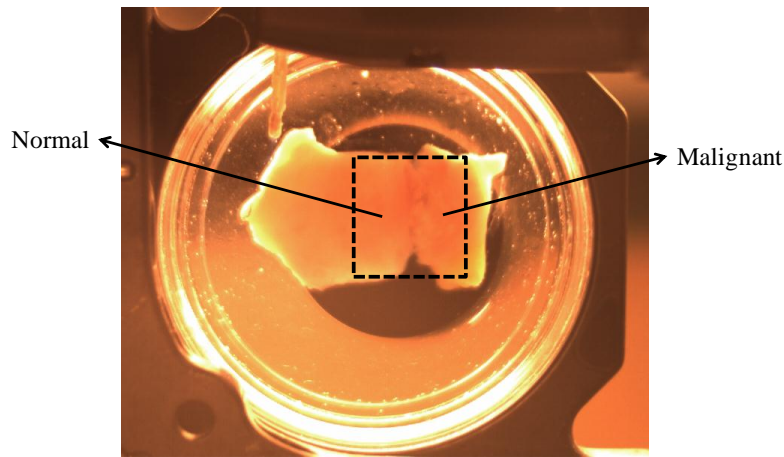


Figure 6.4: White-light picture of the analyzed breast tissue sample with a normal and a malignant area. The dashed square represents the region of interest that will be scanned using the described instrument.

Some parameter maps, extracted from the diffuse-reflectance signal of breast tissue, using the algorithm described in Chapter 3, section 3.5.1, are shown in Figure 6.5 (a) and Figure 6.5 (b). These maps were obtained using a step size of 125 μm , and an integration time of 3 ms at each point.

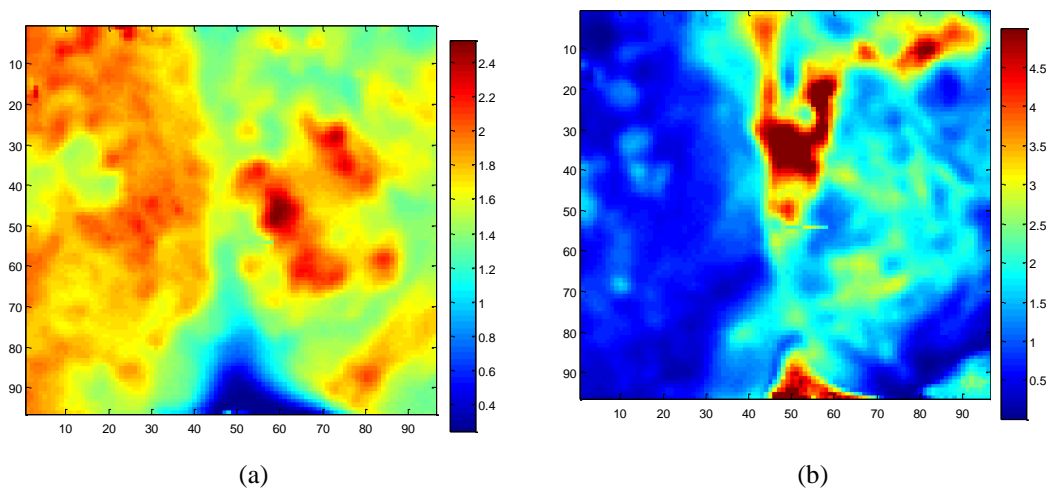


Figure 6.5: Representative QS images of breast tissue taken with the developed spatial high-resolution scanner: a) quantitative map of the scattering parameter A_s (mm^{-1}); b) quantitative map of hemoglobin concentration (mg/dl). Each box represents approximately a 1.2 x 1.2 cm scanning area.

The values for parameters A_s , B_s , and cHb , extracted in two different normal tissue sites and in two different malignant tissue sites, are compiled in Table 6.2.

From Table 6.2, and as theoretically expected, it is possible to conclude that malignant tissue is characterized by lower scattering (low scattering parameter values, A_s) and higher absorption (high hemoglobin concentration values), when compared with normal tissue sites. The extraction of quantitative optical parameters, such as, for example, hemoglobin concentration and collagen, has proven to be helpful for the differentiation of normal and malignant breast tissues. Indeed, a recent study from Volynskaya *et al.* [15] has successfully demonstrated that higher hemoglobin concentrations and higher collagen values were more

likely to be found in ductal carcinoma of breast tissue than in normal breast tissue, and thus could be used as diagnostic parameters.

Table 6.2: Reflectance parameters (A_s , in mm^{-1} , B_s , and cHb in mg/mL) measured from four different tissue sites in the breast tissue sample.

Parameters	Normal tissue		Malignant tissue	
	Site 1	Site 2	Site 3	Site 4
A_s	1.76	1.98	1.67	1.45
B_s	1.37	1.38	1.09	1.2
cHb	0.94	0.94	2.00	3.87

After the first set of experiments, the performance characteristics of the *ex vivo* QS system were demonstrated using an inherently high contrast sample with sharp regional boundaries (a section of formalin-fixed human brain cortex with gray and white matter, with an approximate size of 2 cm by 2 cm). A diffuse-reflectance map of the brain is shown in Figure 6.6 (a), obtained using a step size of 125 μm , and an integration time of 3 ms at each point. In this image, fine detail and high contrast between the gray and white matter of the brain cortex is clearly visible. For demonstration, high-resolution spectral maps of the scattering parameters, A_s and B_s , and measured hemoglobin concentration are shown in Figure 6.6(b), Figure 6.6(c), and Figure 6.6(d), respectively. As expected, it is revealed a higher hemoglobin concentration on gray matter (related with higher blood volume) [16]. These results demonstrate the ability of *ex vivo* QS scanner to provide spectral contrast based on tissue parameters.

The concept of quantitative spectroscopy imaging has been demonstrated with the developed bench-top platform using DRS and small biological samples. However, as previously mentioned, the system is not limited to DRS and IFS. Other modalities, such as Raman and infrared spectroscopy can be readily integrated on the platform to provide additional and complementary tissue information for the establishment of a reliable diagnosis.

In summary, a quantitative multi-modal spectroscopy scanning platform was constructed for assessing *ex vivo* tissue biochemical and morphological information. This developed instrument is suitable for the characterization of surgically excised tissue margins, providing two major benefits over the current practice: (1) reduce patient anxiety and avoid follow-up surgery because on-the-fly real time data analysis can be performed; (2) reduce the probability of missing a lesion because the whole *ex vivo* tissue area can be assessed. The proof of principle has been demonstrated with bench-top prototype for quantitative spectroscopic scanning of biological samples.

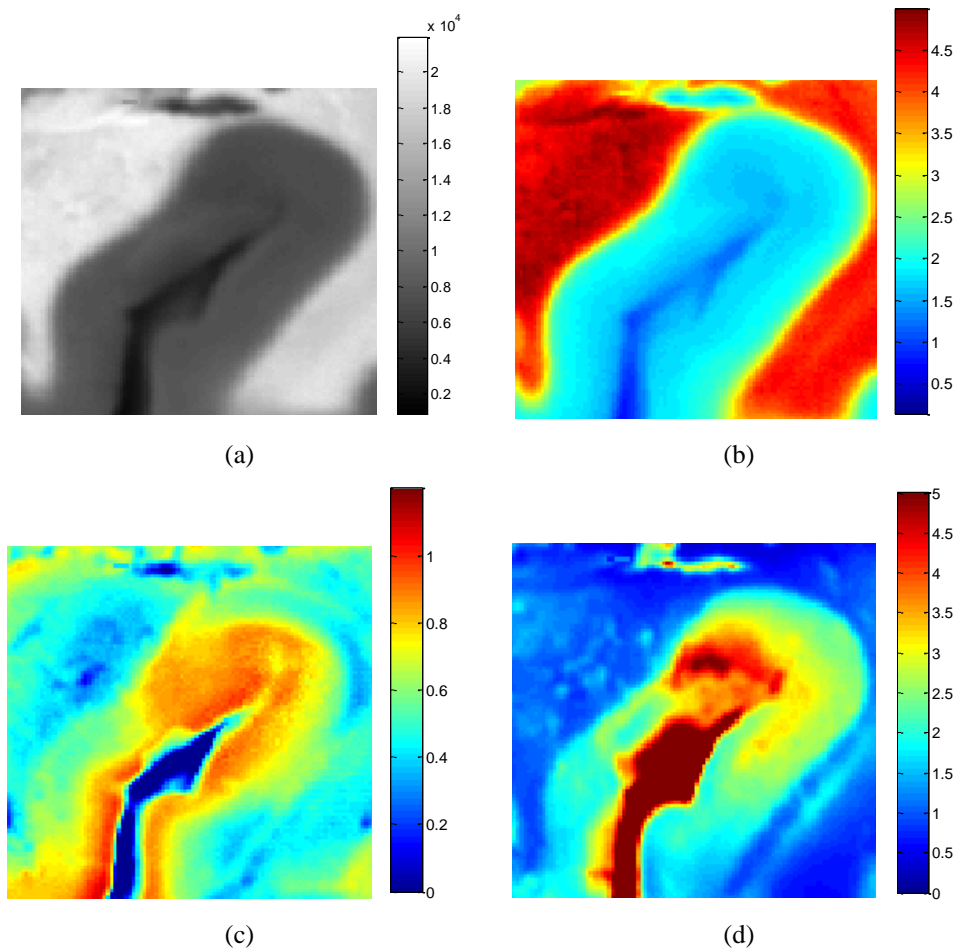


Figure 6.6: Representative QS images of brain cortex taken with the developed spatial high-resolution scanner: (a) total reflectance map (in arbitrary units); (b) quantitative map of the scattering parameter A_s (mm^{-1}); (c) quantitative map of the scattering parameter B_s ; (d) quantitative map of hemoglobin concentration (mg/dl). Each box represents approximately a 1 x 1 cm scanning area.

In the future, and to have a compact clinical unit, several instrumentation and software advances need to be performed: reduction of system size, increase in collection and analysis speed, and improved user interface with diagnostic algorithms. Further investigation is also needed to address the effect of excision in quantitative hemoglobin and fluorophores measurements. For instance, excised specimens contaminated by the presence of surface blood may absorb the majority of reflected light, significantly reducing the reflectance signal [15]. In addition, some fluorophores (e.g. collagen) might be stable in excised tissue, whereas others (e.g. NAD(P)H) might degrade over time, precluding an accurate extraction of its concentration.

References

- [1] R. Soetikno, *et al.*, "Endoscopic mucosal resection for early cancers of the upper gastrointestinal tract," *J Clin Oncol*, vol. 23, pp. 4490-8, Jul 10 2005.
- [2] J. H. Peters and T. A. Watson, "Endoscopic mucosal resection of Barrett's esophagus and Early Esophageal Cancer," *J Gastrointest Surg*, vol. 15, pp. 1299-302, Aug 2011.

- [3] S. V. Kantsevoy, *et al.*, "Endoscopic mucosal resection and endoscopic submucosal dissection," *Gastrointest Endosc*, vol. 68, pp. 11-8, Jul 2008.
- [4] R. M. Soetikno, *et al.*, "Endoscopic mucosal resection," *Gastrointest Endosc*, vol. 57, pp. 567-79, Apr 2003.
- [5] G. G. Ginsberg, "Endoscopic approaches to Barrett's oesophagus with high-grade dysplasia/early mucosal cancer," *Best Pract Res Clin Gastroenterol*, vol. 22, pp. 751-72, 2008.
- [6] J. Q. Brown, *et al.*, "Optical assessment of tumor resection margins in the breast," *IEEE J Sel Top Quantum Electron*, vol. 16, pp. 530-544, Mar 1 2010.
- [7] D. A. Novis and R. J. Zarbo, "Interinstitutional comparison of frozen section turnaround time - A College of American Pathologists Q-probes study of 32,868 frozen sections in 700 hospitals," *Archives of Pathology & Laboratory Medicine*, vol. 121, pp. 559-567, Jun 1997.
- [8] M. Mino-Kenudson, *et al.*, "Management of superficial Barrett's epithelium-related neoplasms by endoscopic mucosal resection - Clinicopathologic analysis of 27 cases," *American Journal of Surgical Pathology*, vol. 29, pp. 680-686, May 2005.
- [9] M. D. Keller, *et al.*, "Autofluorescence and Diffuse Reflectance Spectroscopy and Spectral Imaging for Breast Surgical Margin Analysis," *Lasers in Surgery and Medicine*, vol. 42, pp. 15-23, Jan 2010.
- [10] V. Krishnaswamy, *et al.*, "Quantitative imaging of scattering changes associated with epithelial proliferation, necrosis, and fibrosis in tumors using microsampling reflectance spectroscopy," *Journal of Biomedical Optics*, vol. 14, Jan-Feb 2009.
- [11] J. W. Tunnell, *et al.*, "Instrumentation for multi-modal spectroscopic diagnosis of epithelial dysplasia," *Technol Cancer Res Treat*, vol. 2, pp. 505-14, Dec 2003.
- [12] G. Zonios, *et al.*, "Diffuse reflectance spectroscopy of human adenomatous colon polyps in vivo," *Appl Opt*, vol. 38, pp. 6628-37, Nov 1 1999.
- [13] M. G. Muller, *et al.*, "Intrinsic fluorescence spectroscopy in turbid media: disentangling effects of scattering and absorption," *Applied Optics*, vol. 40, pp. 4633-4646, Sep 1 2001.
- [14] M. G. Muller, *et al.*, "Intrinsic fluorescence spectroscopy in turbid media: disentangling effects of scattering and absorption," *Appl Opt*, vol. 40, pp. 4633-46, Sep 1 2001.
- [15] Z. Volynskaya, *et al.*, "Diagnosing breast cancer using diffuse reflectance spectroscopy and intrinsic fluorescence spectroscopy," *J Biomed Opt*, vol. 13, p. 024012, Mar-Apr 2008.
- [16] L. M. Hamberg, *et al.*, "Measurement of cerebral blood volume with subtraction three-dimensional functional CT," *AJNR Am J Neuroradiol*, vol. 17, pp. 1861-9, Nov-Dec 1996.

Chapter 7

Conclusions and Future Work

This chapter presents the final considerations and major achievements of the developed work. Future work is also proposed for subsequent investigations.

7.1 Project overview

This project had two major goals: (1) the development of a miniaturized spectroscopy system that can be integrated in small and less invasive devices for *in vivo* detection of early cancer in the GI tract; (2) development of an *ex vivo* spectroscopy system for the assessment of tissue margins in oncological surgeries.

7.1.1 Miniaturized spectroscopy system

In this investigation preliminary steps have been taken towards the development of a miniaturized spectroscopy system for the detection of GI dysplasia, by studying, developing

and characterizing its several components and by assessing the clinical impact of such a system.

The proposed miniaturized spectroscopy instrument is based on thin-film optical filters and low-cost silicon photodiodes that are responsible for the selection and detection of the spectroscopy signal, respectively.

Thin-film optical filters, centered at specific wavelengths, were designed and fabricated, after the successful demonstration that using only 16 specific spectral bands enabled an accurate extraction of quantitative tissue information. The fabrication of the filters and its further optimization was a lengthy and complex process, with several problems associated in order to get reasonable results.

The feasibility of using the fabricated filters to establish a quantitative diagnosis was investigated by performing diffuse-reflectance measurements on tissue phantoms. The measurements corresponded to discrete spectral points that were successfully correlated with the phantoms original spectra values. The success of these results enabled an accurate reconstruction of the full spectrum in the 350 nm to 750 nm range using only 16 points. From the reconstructed spectrum, the information about tissue properties could be then reliably extracted using the described spectroscopy analytical models. With the obtained results it was possible to validate the replacement of the spectrograph by an array of thin-film optical filters for spectroscopy measurements.

A different approach, using only two optical filters, was theoretically assessed for the establishment of an empirical diagnosis. It was successfully demonstrated that the use of two spectral bands, one centered at 420 nm for the fluorescence emitted signal, and the other centered at 540 nm for the measured diffuse-reflectance signal, can be useful to differentiate dysplasia from clinically normal tissues. The developed diagnostic algorithm, based on these two spectral bands, is very simple and enabled a sensitivity and specificity of 77.8% and 97.6%, respectively, for the identification of dysplastic tissues. This approach enables the use of a more compact system, but it doesn't provide an insight about the biochemical and morphological properties of the tissue being analyzed, whereas the quantitative approach does.

The development of this work has highlighted the complexity and challenges associated with the scale-down of a spectroscopy instrument. The findings presented show a significant progress towards this final goal and serve as an important guide for how to build a miniaturized spectroscopy system that can be used in the future as a successful spectral diagnostic tool.

As a major clinical advantage, a miniaturized spectroscopy system, such as the one

described in this thesis, could be integrated in small and less invasive devices making the analysis of the GI tract more comfortable to the patient. From the engineering point of view, the integration of different optical components, all in a single chip, enables the achievement of a high level of reliability, when compared to what can be achieved by mounting several discrete optical components (e.g. high optical performance, optimized connections between components due to small-size spacing, fewer losses, less noise, etc.).

7.1.2 *Ex vivo* spectroscopy system

An *ex vivo* spectroscopy system for wide-area assessment of tissue margins in real-time was also developed and evaluated at the GR Harrison Spectroscopy Laboratory, MIT. The *ex vivo* quantitative spectroscopy system is based on a scanning platform which enables integration of different optical modalities for the assessment of tissue properties.

The quantitative spectroscopy scanner prototype combines DRS and IFS to provide a multidimensional image of tissue structural and biochemical properties. The wide area tissue coverage is achieved by mechanically scanning an optical probe. The spectroscopic data is taken one grid at a time with variable spatial resolution and FOV. The *ex vivo* tissue surface under examination can have a variable size (from a few millimeters to about 4 centimeters) since both spatial resolution and FOV can be controlled.

The clinical utility of the system was successfully demonstrated using breast and brain tissue samples: different images containing reliable quantitative tissue information could be obtained using analytical models. This information could be subsequently used to establish a diagnosis.

The introduction of a few improvements in the first prototype (e.g. reduction of system size, increase in collection and analysis speed, improved user interface) can have a huge impact in intra-operative diagnosis. Two major benefits of the system can be pointed out: the reduction of follow-up surgeries because a real-time tissue analysis can be performed; and, the reduction of the probability of missing a lesion because the entire excised tissue area can be evaluated.

7.1.3 Application in endoscopic capsules

The use of conventional endoscopes to perform endoscopy screening has some drawbacks. Among the key problems is the limited flexibility of the endoscope, which is associated to procedural pain, limiting the willingness of the patients to undergo endoscopic procedures, especially for cancer screening. In this sense, the introduction of the EC in 2001

has played an important role since it can greatly reduce the level of discomfort to be tolerated by patients [1-3]. The EC is a pill-sized swallowable camera that travels through the GI tract taking pictures. The use of capsule endoscopy has several advantages over conventional endoscopy: it is non-invasive method; it doesn't require the presence of a physician; it eliminates the need for sedation or insufflation; it offers visual access in a less invasive way to parts of the small intestine that were previously accessed only by surgery; and, it is disposable [3-6].

The accuracy of the EC for detecting BE was already, and successfully, evaluated in several studies, which also compared its performance with the conventional exam [5, 7-11]. The use of the EC appears feasible, safe, and is well tolerated by patients, who, ultimately, prefer this diagnostic method over conventional endoscopy. Still, and because its diagnosis is based mainly on white-light images, capsule endoscopy has the same drawbacks as conventional endoscopy: invisible dysplasia is not detected, even in a high-resolution image. In this context, the addition of spectroscopy functions would offer the possibility of detecting the very earliest mucosal changes at the microstructural and biochemical levels [12].

For that reason, the future integration of the described miniaturized spectroscopy system in an EC would have a huge clinical utility since it would add essential diagnostic functions, e. g. the objective detection of invisible malignant lesions (dysplasia), to current capsule imaging functions. Kfoury and coworkers [13] have attempted to integrate fluorescence imaging functions in a miniaturized capsule endoscope for a non-invasive GI diagnosis. However, the full integrated prototype is still too large (2 cm in diameter and 10 cm in length) to be swallowed and further miniaturization is compromised by the use of several incompatible CMOS IC components.

The miniaturized spectroscopy system described in this work, in a final prototype, is not expected to exceed a few millimeters, and, this way, it can be placed near the current capsule camera with little space adjustment (Figure 7.1). Also, two of the available white LEDs can be kept for tissue illumination during standard images acquisition, whereas the other two must be replaced by one UV and one high luminous efficiency white LED for fluorescence and diffuse-reflectance measurements, respectively.

Also, and as a next step, numerous microsystems (photodiodes plus optical filters) could be built and positioned around the capsule and not only in its front sides (such as the cameras of the commercial capsules), so that a wide tissue area can be assessed. Since point spectroscopy techniques may suffer from undersampling, missing contextual information often needed to distinguish diseased from surrounding normal tissues, the incorporation of optical detectors all around the capsule may solve this drawback [12].

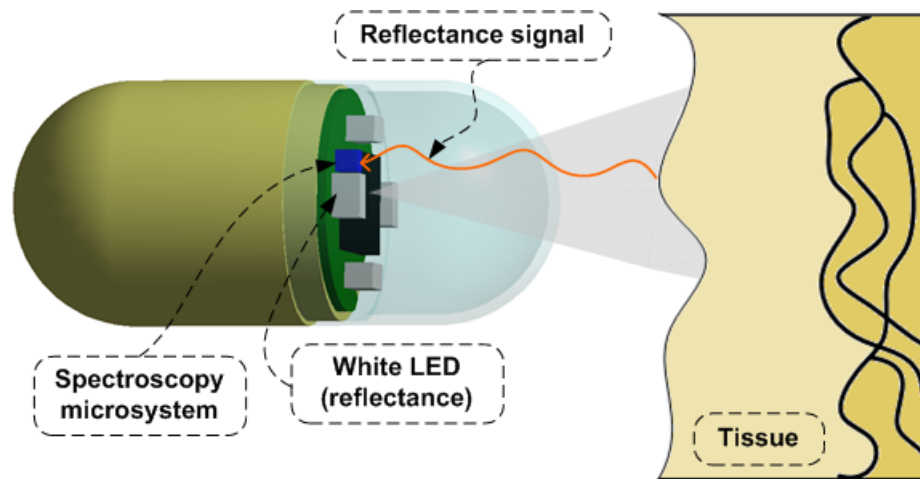


Figure 7.1: Picture representing the future integration of the miniaturized spectroscopy system in an EC. Example is shown for the collection of diffuse-reflectance data (i.e. illumination using one white LED), and for the integration in a capsule with a single camera. The current capsule CMOS image sensor is represented by the centre black square.

7.2 Future work

Epithelial tissues emit fluorescence mainly in the violet/blue region of the spectrum. For this reason, optical filters were proposed to cover this spectral region. Unfortunately, the majority of these filters didn't produce the expected results, i.e. their transmittances were not high enough to enable the discrimination of the different peaks. Moreover, it was demonstrated that the fabricated photodiodes didn't have good quantum efficiency at low visible wavelengths. This way, future work should deal with the improvement of the selection and detection of wavelengths in near-UV/blue wavelength range.

Silicon photodiodes, fabricated in a standard CMOS process, with high sensitivity and selectivity, have already been proposed for this spectral region [14-15]. The selectivity is achieved using a shallow active region, limited by a high potential barrier at a depth of 450 nm. The photodiodes have the maximum responsivity around 400-420 nm, with a quantum efficiency that can go up to 50%.

With a reliable and efficient detection system, the next direction of the project should be the deposition of the optical filters directly on top of the CMOS photodiodes array, and the integration of readout electronics, on the same chip.

Additionally, a CMOS-Compatible Linear Variable Optical Filter (LVOF), such as the one described by Emadi *et al.*, that can be integrated with a CMOS photodiode array and readout circuitry, could be developed in a future step [16-17]. This LVOF structure is also based on a Fabry-Perot resonator, being composed by 21 layers of dielectric materials (SiO_2 and HfO_2). This variable filter can be tuned from UV (where it has high resolution) to near-infrared wavelengths, and, thus, has the potential to replace the 16 individual optical filters

that were developed. Theoretically, it can have a resolution better than 0.2 nm, in the visible range, using some processing techniques. In this sense, the LVOF can have a great impact in the described miniaturized spectroscopy system. Still, further study needs to be done on how to integrate, control and finally perform the intended spectroscopy measurements using this filter.

Future investigations should also be directed for the integration of NBI functions in ECs using thin-film optical filters for the selection of the three excitation bands. In this particular application, it is very important to assess the quality of the acquired images using the ECs and to establish a comparison between these images and the ones acquired using a conventional endoscope with NBI performance. If the images obtained with the two instruments have similar quality and resolution, an important step is given towards providing patients a less invasive diagnosis.

References

- [1] M. Delvaux and G. Gerard, "Capsule endoscopy in 2005: facts and perspectives," *Best Pract Res Clin Gastroenterol*, vol. 20, pp. 23-39, Feb 2006.
- [2] A. Moglia, *et al.*, "Wireless capsule endoscopy: from diagnostic devices to multipurpose robotic systems," *Biomedical Microdevices*, vol. 9, pp. 235-43, Apr 2007.
- [3] D. Fleischer, "Capsule imaging," *Clin Gastroenterol Hepatol*, vol. 3, pp. S30-2, Jul 2005.
- [4] B. Koslowsky, *et al.*, "PillCam ESO in esophageal studies: improved diagnostic yield of 14 frames per second (fps) compared with 4 fps," *Endoscopy*, vol. 38, pp. 27-30, Jan 2006.
- [5] I. M. Gralnek, *et al.*, "Detecting esophageal disease with second-generation capsule endoscopy: initial evaluation of the PillCam ESO 2," *Endoscopy*, vol. 40, pp. 275-9, Apr 2008.
- [6] T. Nakamura and A. Terano, "Capsule endoscopy: past, present, and future," *J Gastroenterol*, vol. 43, pp. 93-9, 2008.
- [7] O. S. Lin, *et al.*, "Blinded comparison of esophageal capsule endoscopy versus conventional endoscopy for a diagnosis of Barrett's esophagus in patients with chronic gastroesophageal reflux," *Gastrointestinal Endoscopy*, vol. 65, pp. 577-583, Apr 2007.
- [8] J. P. Galmiche, *et al.*, "Screening for esophagitis and Barrett's esophagus with wireless esophageal capsule endoscopy: a multicenter prospective trial in patients with reflux symptoms," *Am J Gastroenterol*, vol. 103, pp. 538-45, Mar 2008.
- [9] R. Eliakim, *et al.*, "A novel diagnostic tool for detecting oesophageal pathology: the PillCam oesophageal video capsule," *Aliment Pharmacol Ther*, vol. 20, pp. 1083-9, Nov 2004.
- [10] P. Sharma, *et al.*, "The diagnostic accuracy of esophageal capsule endoscopy in patients with gastroesophageal reflux disease and Barrett's esophagus: a blinded, prospective study," *Am J Gastroenterol*, vol. 103, pp. 525-32, Mar 2008.
- [11] F. C. Ramirez, *et al.*, "Screening of Barrett's esophagus with string-capsule endoscopy: a prospective blinded study of 100 consecutive patients using histology as the criterion standard," *Gastrointest Endosc*, vol. 68, pp. 25-31, Jul 2008.
- [12] R. S. Dacosta, *et al.*, "New optical technologies for earlier endoscopic diagnosis of

- pre-malignant gastrointestinal lesions," *J Gastroenterol Hepatol*, vol. 17 Suppl, pp. S85-104, Feb 2002.
- [13] M. Kfoury, *et al.*, "Toward a miniaturized wireless fluorescence-based diagnostic Imaging system," *Ieee Journal of Selected Topics in Quantum Electronics*, vol. 14, pp. 226-234, Jan-Feb 2008.
- [14] A. Pauchard, *et al.*, "A silicon blue/UV selective stripe-shaped photodiode," *Sensors and Actuators*, vol. 76, pp. 172-177, 1999.
- [15] A. Pauchard, *et al.*, "Integrated microsystem for blue/UV detection," *Sensors and Actuators*, vol. 85 pp. 99-105, 2000.
- [16] A. Emadi, *et al.*, "Fabrication and characterization of IC-Compatible Linear Variable Optical Filters with application in a microspectrometer," *Sensors and Actuators a-Physical*, vol. 162, pp. 400-405, 2010.
- [17] A. Emadi, *et al.*, "CMOS-compatible LVOF-based visible microspectrometer " presented at the Proceedings of the SPIE Conference, Orlando, Florida, USA 2010.

Annex

Journal Publications

D. S. Ferreira, J. Mirkovic, R. F. Wolffenbuttel, J. H. Correia, M. S. Feld, and G. Minas, "Narrow-band pass filter array for integrated opto-electronic spectroscopy detectors to assess esophageal tissue", *Biomedical Optics Express*, vol. 2, 2011, pp. 1703-1716.

D. S. Ferreira, V. Pinto, J. H. Correia, and G. Minas, "Spectroscopic Detection of Gastrointestinal Dysplasia Using Optical Microsensors", *IEEE Transactions on Biomedical Engineering*, vol. 58, 2011, pp. 2633-2639.

The full papers are attached in the following pages.

Narrow-band pass filter array for integrated opto-electronic spectroscopy detectors to assess esophageal tissue

Débora S. Ferreira,^{1,*} Jelena Mirkovic,² Reinoud F. Wolffenbuttel,³ José H. Correia,¹ Michael S. Feld,² and Graça Minas¹

¹Department of Industrial Electronics, University of Minho, Campus de Azurém, 4800-058, Guimarães, Portugal

²George R. Harrison Spectroscopy Laboratory, Massachusetts Institute of Technology, 77 Massachusetts Avenue, Cambridge, Massachusetts 02139, USA

³Faculty of Electrical Engineering, Mathematics and Computer Science, Department of Microelectronics, Delft University of Technology, Mekelweg 4, 2628, CD Delft, The Netherlands

*debora@dei.uminho.pt

Abstract: A strategy for spectroscopy tissue diagnosis using a small number of wavelengths is reported. The feasibility to accurately quantify tissue information using only 16 wavelengths is demonstrated with several wavelength reduction simulations of the existing esophageal data set. These results are an important step for the development of a miniaturized, robust and low-cost spectroscopy system. This system is based on a sub-millimeter high-selective filter array that offers prospects for a simplified miniature spectrographic detector for a future diagnostic tool to improve the diagnosis of dysplasia. Several thin-film optical filters are optimized and fabricated and its spectral performance is shown to be sufficient for the selection of specific wavelength bands.

©2011 Optical Society of America

OCIS codes: (170.3890) Medical optics instrumentation; (170.6510) Spectroscopy, tissue diagnostics; (120.2230) Fabry-Perot; (310.0310) Thin films.

References and links

1. I. Georgakoudi, B. C. Jacobson, J. Van Dam, V. Backman, M. B. Wallace, M. G. Müller, Q. Zhang, K. Badizadegan, D. Sun, G. A. Thomas, L. T. Perelman, and M. S. Feld, "Fluorescence, reflectance, and light-scattering spectroscopy for evaluating dysplasia in patients with Barrett's esophagus," *Gastroenterology* **120**(7), 1620–1629 (2001).
2. J. W. Tunnell, A. E. Desjardins, L. Galindo, I. Georgakoudi, S. A. McGee, J. Mirkovic, M. G. Mueller, J. Nazemi, F. T. Nguyen, A. Wax, Q. G. Zhang, R. R. Dasari, and M. S. Feld, "Instrumentation for multi-modal spectroscopic diagnosis of epithelial dysplasia," *Technol. Cancer Res. Treat.* **2**(6), 505–514 (2003).
3. J. F. Fléjou, "Barrett's oesophagus: from metaplasia to dysplasia and cancer," *Gut* **54**(Suppl 1), i6–i12 (2005).
4. S. Villette, S. Pigaglio-Deshayes, C. Vever-Bizet, P. Validire, and G. Bourg-Heckly, "Ultraviolet-induced autofluorescence characterization of normal and tumoral esophageal epithelium cells with quantitation of NAD(P)H," *Photochem. Photobiol. Sci.* **5**(5), 483–492 (2006).
5. A. J. Cameron, "Management of Barrett's esophagus," *Mayo Clin. Proc.* **73**(5), 457–461 (1998).
6. B. J. Reid, R. C. Haggitt, C. E. Rubin, G. Roth, C. M. Surawicz, G. Van Belle, K. Lewin, W. M. Weinstein, D. A. Antonioli, H. Goldman, W. Macdonald, and D. Owen, "Observer variation in the diagnosis of dysplasia in Barrett's esophagus," *Hum. Pathol.* **19**(2), 166–178 (1988).
7. R. E. Petras, M. V. Sivak, Jr., and T. W. Rice, "Barrett's esophagus. a review of the pathologist's role in diagnosis and management," *Pathol. Annu.* **26**(Pt 2), 1–32 (1991).
8. K. K. Wang, M. Wongkeesong, and N. S. Buttar; American Gastroenterological Association, "American Gastroenterological Association medical position statement: Role of the gastroenterologist in the management of esophageal carcinoma," *Gastroenterology* **128**(5), 1468–1470 (2005).
9. L. M. Wong Kee Song, "Optical spectroscopy for the detection of dysplasia in Barrett's esophagus," *Clin. Gastroenterol. Hepatol.* **3**(7 Suppl 1), S2–S7 (2005).
10. C. C. Yu, C. Lau, G. O'Donoghue, J. Mirkovic, S. McGee, L. Galindo, A. Elackattu, E. Stier, G. Grillone, K. Badizadegan, R. R. Dasari, and M. S. Feld, "Quantitative spectroscopic imaging for non-invasive early cancer detection," *Opt. Express* **16**(20), 16227–16239 (2008).

11. M. Panjehpour, B. F. Overholt, T. Vo-Dinh, R. C. Haggitt, D. H. Edwards, and F. P. Buckley 3rd, "Endoscopic fluorescence detection of high-grade dysplasia in Barrett's esophagus," *Gastroenterology* **111**(1), 93–101 (1996).
12. T. Vo-Dinh, M. Panjehpour, and B. F. Overholt, "Laser-induced fluorescence for esophageal cancer and dysplasia diagnosis," *Ann. N. Y. Acad. Sci.* **838**(Advances in Optical Biopsy and Optical Mammography), 116–122 (1998).
13. T. J. Pfefer, D. Y. Paithankar, J. M. Poneris, K. T. Schomacker, and N. S. Nishioka, "Temporally and spectrally resolved fluorescence spectroscopy for the detection of high grade dysplasia in Barrett's esophagus," *Lasers Surg. Med.* **32**(1), 10–16 (2003).
14. M. A. Ortner, B. Ebert, E. Hein, K. Zumbusch, D. Nolte, U. Sukowski, J. Weber-Eibel, B. Fleige, M. Dietel, M. Stolte, G. Oberhuber, R. Porschen, B. Klump, H. Hörtnagl, H. Lochs, and H. Rinneberg, "Time gated fluorescence spectroscopy in Barrett's oesophagus," *Gut* **52**(1), 28–33 (2003).
15. G. Zonios, L. T. Perelman, V. M. Backman, R. Manoharan, M. Fitzmaurice, J. Van Dam, and M. S. Feld, "Diffuse reflectance spectroscopy of human adenomatous colon polyps *in vivo*," *Appl. Opt.* **38**(31), 6628–6637 (1999).
16. M. G. Müller, I. Georgakoudi, Q. G. Zhang, J. Wu, and M. S. Feld, "Intrinsic fluorescence spectroscopy in turbid media: disentangling effects of scattering and absorption," *Appl. Opt.* **40**(25), 4633–4646 (2001).
17. B. Yu, J. Y. Lo, T. F. Kuech, G. M. Palmer, J. E. Bender, and N. Ramanujam, "Cost-effective diffuse reflectance spectroscopy device for quantifying tissue absorption and scattering *in vivo*," *J. Biomed. Opt.* **13**(6), 060505 (2008).
18. J. Y. Lo, B. Yu, H. L. Fu, J. E. Bender, G. M. Palmer, T. F. Kuech, and N. Ramanujam, "A strategy for quantitative spectral imaging of tissue absorption and scattering using light emitting diodes and photodiodes," *Opt. Express* **17**(3), 1372–1384 (2009).
19. J. Mirkovic, C. Lau, S. McGee, C. C. Yu, J. Nazemi, L. Galindo, V. Feng, T. Darragh, A. de Las Morenas, C. Crum, E. Stier, M. S. Feld, and K. Badizadegan, "Effect of anatomy on spectroscopic detection of cervical dysplasia," *J. Biomed. Opt.* **14**(4), 044021 (2009).
20. Y. Narukawa, M. Ichikawa, D. Sanga, M. Sano, and T. Mukai, "White light emitting diodes with super-high luminous efficacy," *J. Phys. D Appl. Phys.* **43**(35), 354002 (2010).
21. L. Phee, D. Accoto, A. Menciassi, C. Stefanini, M. C. Carrozza, and P. Dario, "Analysis and development of locomotion devices for the gastrointestinal tract," *IEEE Trans. Biomed. Eng.* **49**(6), 613–616 (2002).
22. A. Menciassi, A. Moglia, S. Gorini, G. Pernorio, C. Stefanini, and P. Dario, "Shape memory alloy clamping devices of a capsule for monitoring tasks in the gastrointestinal tract," *J. Micromech. Microeng.* **15**(11), 2045–2055 (2005).
23. M. Quirini, S. Scapellato, P. Valdastri, A. Menciassi, and P. Dario, "An approach to capsular endoscopy with active motion," in *Proceedings of the 29th Annual International Conference of the IEEE EMBS* (Institute of Electrical and Electronics Engineers, New York, 2007), pp. 2827–2830.
24. J. G. Rocha, G. Minas, and S. Lanceros-Mendez, "Pixel Readout Circuit for X-Ray Imagers," *IEEE Sens. J.* **10**(11), 1740–1745 (2010).
25. H. A. Macleod, *Thin-Film Optical Filters* (E.D. Institute of Physics Publishing, 2001).
26. G. Minas, R. F. Wolffenbuttel, and J. H. Correia, "A lab-on-a-chip for spectrophotometric analysis of biological fluids," *Lab Chip* **5**(11), 1303–1309 (2005).
27. G. Minas, R. F. Wolffenbuttel, and J. H. Correia, "An array of highly selective Fabry-Perot optical channels for biological fluid analysis by optical absorption using a white light source for illumination," *J. Opt. A, Pure Appl. Opt.* **8**(3), 272–278 (2006).
28. G. Minas, J. C. Ribeiro, R. F. Wolffenbuttel, and J. H. Correia, "On-Chip integrated CMOS optical detection microsystem for spectrophotometric analyses in biological microfluidic systems," in *Proceedings IEEE Int. Symposium on Industrial Electronics* (Institute of Electrical and Electronics Engineers, New York, 2005), pp. 1133–1138.

1. Introduction

The majority of lower esophageal adenocarcinomas appear in patients with Barrett's esophagus (BE), a premalignant condition in which the normal squamous epithelium is replaced by metaplastic columnar epithelium. Adenocarcinomas develop through increasing grades of dysplasia, which is the precursor lesion of epithelial cancers. Detection of dysplasia is essential for managing this type of cancer since the chances of an effective treatment increase if the disease is diagnosed at an early stage, significantly improving the survival rate [1–4].

Dysplastic lesions arising in BE are difficult to identify and to diagnose using standard methods, such as conventional white-light endoscopy [5]. Therefore, clinicians take systematic patterned biopsies to screen for dysplasia. Moreover, dysplasia can be difficult to diagnose due to the poor intra- and inter-observer agreement among gastrointestinal pathologists [6–9].

Optical techniques, such as diffuse reflectance and fluorescence spectroscopy, provide contrast based on tissue morphology and biochemistry to help differentiate non-dysplastic from dysplastic lesions in BE. These techniques can be used to guide biopsy during white-light endoscopy [1,2,9,10]. Several groups have successfully applied diffuse reflectance and fluorescence spectroscopy for detecting and classifying dysplasia in BE [1,11–14].

Diffuse reflectance spectra can be analyzed using a well-developed analytical model to obtain tissue optical parameters, such as the wavelength dependent scattering parameter, and hemoglobin concentration and oxygen saturation [15]. Intrinsic fluorescence spectroscopy is used to extract the relative contributions of tissue fluorophores, such as NAD(P)H and collagen [16]. These parameters are subsequently correlated to histopathologic diagnosis and analyzed using statistical methods to develop quantitative diagnostic algorithms.

Research prototypes designed to perform diffuse reflectance and fluorescence spectroscopy are generally accurate in the quantification of tissue parameters and in diagnosis. However, these prototypes suffer from several drawbacks. Regular optical fibers usually have low collection efficiency, thus requiring high quantum efficiency detectors (such as charge coupled device cameras - CCDs). In addition, these research prototypes (not yet commercially available) include costly, bulky and sophisticated illumination equipment (xenon arc lamps, UV lasers). Therefore, the development of a low complexity, miniature, and cost-effective spectroscopy system without the need of optical fibers, spectrograph or CCD cameras could potentially increase the collection efficiency, while simplifying the device. Previous studies have aimed to develop a system with some of these features using LEDs (light-emitting diodes) as the illumination sources and photodiodes as the detector [17,18]. Yu *et al.* [17] developed an optical device to quantitatively assess tissue optical properties using a silicon photodiode for detection. However, a xenon lamp, a monochromator and optical fibers were still used. Lo *et al.* [18] described a spectroscopy system that can integrate LEDs for illumination and wavelength selection, and silicon photodiodes for detection. Even though this study represents a big step towards decreasing the cost and size of conventional spectroscopy systems, only five LED wavelengths are used, which may not be enough to accurately extract other physiological parameters besides hemoglobin. The addition of extra LEDs can compromise a full integration and size reduction.

In this study we propose the development of a potentially robust sub-millimeter narrow-band pass filter array that offers prospects for a simplified miniature spectrographic detector for a future spectrographic diagnostic tool to improve diagnosis of dysplasia.

In this paper we describe a strategy for spectroscopy diagnosis using a reduced number of wavelengths. The long term goal of this study is the development of a simple spectral instrument based on thin-film optical filters and silicon photodiodes for signal detection. Here we focus on diffuse reflectance spectroscopy. Nevertheless, the instrument has potential for fluorescence measurements which is the subject of future work.

2. Diffuse reflectance spectroscopy model

In diffuse reflectance spectroscopy (DRS) white-light is delivered to the tissue and photons are absorbed and elastically scattered multiple times by tissue constituents. The detected scattered photons carry information about tissue structure and composition. Using a well-developed model based on the diffusion approximation [15], quantitative information about tissue constituents that contribute to reflectance can be extracted. In this method, the reflectance spectra are fit to the Zonios *et al.* [15] model to determine the values of the reduced scattering, $\mu'_s(\lambda)$, and absorption, $\mu_a(\lambda)$, coefficients of the tissue (in mm^{-1}). These coefficients can be expressed as [19]:

$$\mu'_s(\lambda) = A \left(\frac{\lambda}{\lambda_0} \right)^{-B} + C \left(\frac{\lambda}{\lambda_0} \right)^{-4}, \quad (1)$$

$$\mu_a(\lambda) = C_{diff}(\lambda) \cdot \mathcal{G} \cdot \mu_a^{blood}(\lambda). \quad (2)$$

In Eq. (1), λ is the wavelength (in μm) and λ_0 is equal to $0.7 \mu\text{m}$ (λ_0 is the reference wavelength for the extraction of parameter A). The second term is used to accurately model reflectance at wavelengths below $0.4 \mu\text{m}$.

For Eq. (2) C_{diff} is a correction factor to account for the *vessel packaging* effect (related to the fact that hemoglobin is restrained to blood vessels that are more or less transparent to light depending on the incident wavelength), and $\theta = c_{Hb} / 150$ and corresponds to the volume fraction of blood sampled, where a hemoglobin concentration of 150 mg/mL is assumed for whole blood. C_{diff} is defined by:

$$C_{diff}(\lambda) = \left\{ \frac{1 - \exp[-2 \cdot \mu_a^{blood}(\lambda) \cdot b\mathcal{G}r]}{2 \cdot \mu_a^{blood}(\lambda) \cdot b\mathcal{G}r} \right\}, \quad (3)$$

where $b\mathcal{G}r$ is the effective blood vessel radius (in mm) and $\mu_a^{blood}(\lambda)$ is the absorption coefficient of whole blood (in mm^{-1}):

$$\mu_a^{blood}(\lambda) = \log 10 \cdot 150 \text{ mg} / \text{mL} \cdot [\alpha \varepsilon_{HbO_2}(\lambda) + (1 - \alpha) \varepsilon_{Hb}(\lambda)], \quad (4)$$

where α is the hemoglobin oxygen saturation; ε_{HbO_2} and ε_{Hb} are the molar extinction coefficient spectra of the oxygenated and deoxygenated hemoglobin, respectively.

The measured reflectance spectra in the data set used in the present study were fit over the 350 to 750 nm range using a nonlinear least-squares fitting algorithm. From the fitting six DRS parameters are extracted at each tissue spot: A , related to scatterer density (mm^{-1}); B , related to the average scatterer size; C , related to scattering by small particles; c_{Hb} , the total concentration of hemoglobin (mg/mL); $b\mathcal{G}r$, the effective blood vessel radius (mm); and α , the oxygen saturation of hemoglobin.

3. Instrumentation

The designed system will be composed of thin-film optical filters and silicon photodiodes that will, respectively, select and detect several light wavelengths. In addition, commercial small-size ultraviolet (UV) and white LEDs will be incorporated in the system as the illumination sources for fluorescence and diffuse reflectance spectroscopy, respectively. UV LEDs are already available at the die level (Nitride Semiconductors Co., Ltd., The Fox Group Inc., among others) whereas white LEDs with high luminous efficacy have already been developed [20]. The use of these components eliminates the need for expensive illumination and detection equipment (high-power xenon arc lamp, CCD camera, spectrograph), and optical fibers to delivery and collect light from tissues.

This miniaturized spectroscopy system could be integrated in standard clinical endoscopes making these instruments more compact and portable. Its dimensional advantage can also enable a future integration in a smaller and less invasive device, such as the endoscopic capsule. Once a CMOS co-integration process is used, the dimensions of each optical microsensor (thin-film optical filter and photodiode) can be scaled down to $50 \times 50 \mu\text{m}^2$ to enable integration into an endoscopic capsule. The fabrication of the system in a compatible CMOS process will also allow the mass production of the microsensors at reduced costs. With this integration essential diagnostic functions will be added to current capsule imaging functions. In this particular application, numerous microsystems should be built and positioned around the capsule and not only in its front (such as the cameras of the commercial capsules), so that a wide tissue area can be assessed. It is known that the majority of

endoscopes that integrate spectroscopy functions use point spectroscopy instead of imaging spectroscopy. Despite of being a promising method for detecting early stage cancer, point spectroscopy techniques suffer from undersampling, missing contextual information often needed to distinguish diseased from surrounding normal tissues. Incorporating optical detectors all around the capsule may solve this drawback. The promising developments in the field of the capsule locomotion and stopping mechanisms [21–23] will make it possible to place the capsule into gentle contact with the tissue when data are taken. The use of a detection system directly in contact with the tissue enables collection of most of the reemitted light, which represents a significant advantage over conventional systems [17,18]. Figure 1 depicts the several components of a conventional and a miniaturized spectroscopy system.

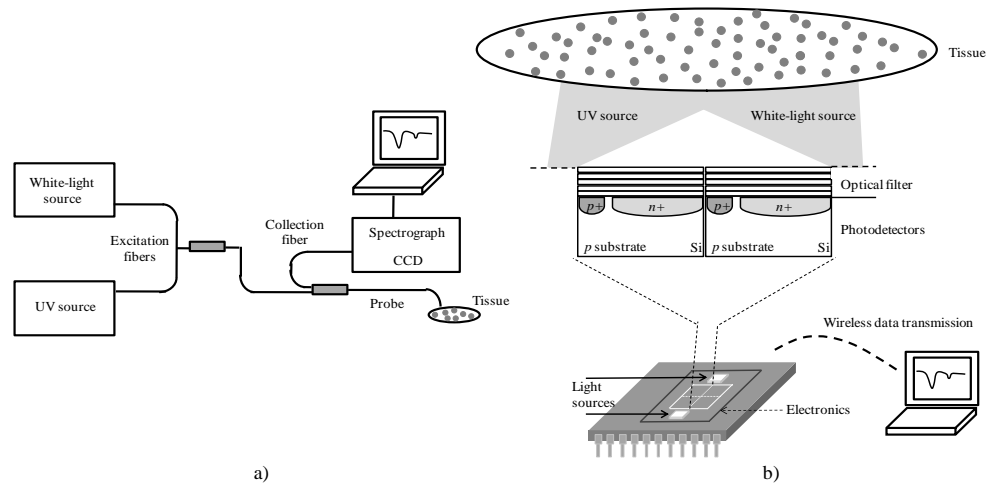


Fig. 1. Spectroscopy systems. (a) Conventional system with excitation and collection fibers, white-light and UV illumination sources, spectrograph and CCD for detection. (b) Miniaturized system with LEDs as light sources, optical filters and photodetectors for wavelength selection and detection, respectively (not scaled). Data transmission is intended to be wireless.

3.1 Wavelength reduction analysis

The possibility of replacing the spectrograph by a series of optical filters in the 350 to 750 nm spectral range was first investigated using an existing diffuse reflectance data set. These data were taken from esophageal tissue using a system described elsewhere [1]. For this study, simulations on wavelength reduction were performed on the data set in order to assess the feasibility of reducing the 400 wavelengths used to perform diagnosis to only 16, while still achieving a good accuracy in the extraction of tissue optical properties (sixteen was considered the minimum number of wavelengths from which one could accurately extract tissue information, as will be detailed in section 4.1).

If that is feasible, the optical microsensors used for light collection will be composed by a 16 narrow-band pass filter array (4 by 4), placed on top of an array of silicon photodiodes. The array area will be approximately $200 \times 200 \mu\text{m}^2$. The final encapsulation of the dies on a single chip will also require some space for wiring that will depend on the number of bonding pads (each bonding pad has a maximum size of $100 \times 100 \mu\text{m}^2$) and the encapsulation package. Each optical microsensors will be collecting different wavelength bands from slightly different locations in the tissue surface. However, since the maximum center to center separation of photodiodes will be around $150 \mu\text{m}$ it is reasonable to believe that no significant spatial heterogeneity will be introduced across wavelengths. Moreover, the analog photodiodes array readout electronics signals will be converted to digital using a compact Sigma-delta converter, already studied by the research group [24]. Each photodiode will have one converter. It is important to notice that the addition of readout electronics will not increase the size of the

optical microsensors since this converter can be designed with only 19 MOSFETs [24]. This scheme will be able to make a conversion in less than 1 microsecond. Thus, in order to avoid any potential spatial heterogeneity that might occur, the position of the optical array might be slightly moved to scan the tissue area under analysis, enabling several measurements, in different locations, by each optical microsensor. With this approach a matrix with 16 different spectral measurements in each specific location can be obtained.

For the wavelength reduction analysis, diffuse reflectance algorithms (section 2) were implemented using MATLAB tools (from The MathWorksTM). Based on previously published results [1], several slightly different combinations of 16 wavelengths were chosen and simulated. For all the simulations the following wavelengths were fixed: 350 and 750 nm (the first and last wavelength in the analysis); 420, 540 and 580 nm (corresponding to oxy-hemoglobin absorption peaks); and 700 nm (reference wavelength). The remaining wavelengths were selected to cover the full visible range. The spacing between selected points must take into account the filters fabrication constraints, namely their FWHM (Full-Width-Half-Maximum), i.e., the filters transmittance spectrum should not considerably overlap. Thus, the best 16 wavelengths group is composed by those 6 fixed points and by 10 more wavelengths which are more or less equally spaced along the spectrum, corresponding to filters which by design don't overlap.

The diffuse reflectance data were then processed and data points from all wavelengths were eliminated, with exception for those corresponding to the selected 16 wavelengths. Thus, instead of having a continuous array of 400 wavelengths (from 350 to 750 nm), and the corresponding reflectance intensity values, a discrete set of 16 specific data points is obtained. The remaining spectrum intensities are achieved by linear interpolation within the range of the discrete data set. This newly generated spectrum is then used to extract the tissue spectroscopy parameters. In the system to be developed, optical microsensors will directly provide these 16 intensity values from which the reflectance spectrum will be reconstructed. In this procedure unknown data points are being calculated, and therefore one must be aware that the results might not be exactly the same as when using the original spectrum. Still, the overall advantages of having such a miniaturized system may offset the error.

The feasibility study outputs the group of the 16 wavelengths that better fits the original continuous spectrum. These 16 wavelengths will be selectively detected using one stack of TiO₂ and SiO₂ thin-films, as detailed next below.

3.2 Thin-film optical filters

A 16 narrow-band optical filter array has been designed based on Fabry-Perot thin-film optical resonators. In addition to the optical filter array only a white-light and a UV source for reflectance and fluorescence illumination, respectively, will be required, thus avoiding a full spectrograph. The filtering system should be designed to yield a narrow-band pass around the selected wavelengths. This way, the instrument will have the high selectivity, at the desired wavelength, required for the application.

The Fabry-Perot resonators consist of two flat parallel mirrors separated by a pre-defined distance, with a resonance cavity in the middle. The thickness of the resonance cavity determines the transmitted wavelength. In this study, the mirrors are dielectric mirrors composed of a stack of TiO₂ and SiO₂ thin-films (high and low refractive index materials, respectively, in the visible spectrum) that offer good performance characteristics with high reflectivity and low absorption losses [25–27]. The refractive indexes of these materials (for a TiO₂ thickness of 52 nm and a SiO₂ thickness of 95 nm) were measured by ellipsometry (Table 1). Titania and silica have been selected because of the IC (integrated circuit) compatibility and the well characterization of their deposition process. Also, the refractive index of SiO₂ for the spectral band between 350 nm and 750 nm is almost wavelength independent (1.476 to 1.455, respectively, with variations smaller than 3%).

Table 1. Measured Refractive Indexes (n) of the Dielectric Materials SiO₂ and TiO₂

Wavelength (nm)	350	370	380	400	420	450	480	510
n of SiO ₂	1.476	1.473	1.472	1.470	1.468	1.465	1.463	1.462
n of TiO ₂	2.931	2.889	2.834	2.77	2.699	2.62	2.556	2.504
Wavelength (nm)	540	560	580	600	620	650	700	750
n of SiO ₂	1.460	1.459	1.459	1.458	1.458	1.457	1.456	1.455
n of TiO ₂	2.461	2.434	2.411	2.39	2.375	2.351	2.318	2.294

The selected wavelengths for this study are closely spaced. Hence, the optical filters must be highly selective with a FWHM less than 20 nm to avoid misidentification in the analysis by possible overlapping of emitted wavelengths.

4. Results and discussion

4.1 Wavelength reduction simulations

The selection of wavelengths for the design of thin-film optical filters was based on simulations of wavelength reduction on an existing diffuse reflectance data set. The data set consisted of 53 histologically confirmed non-dysplastic tissue sites and 10 high-grade dysplastic esophageal tissue sites. The goal is to investigate if it is possible to accurately extract tissue properties using reflectance intensity values of only 16 wavelengths, and interpolating the remaining spectrum intensities to cover the whole 350 to 750 nm range.

For the simulations diffuse reflectance parameters were extracted from high-grade dysplastic and normal squamous esophageal tissue. Several combinations of 16 wavelengths were simulated. The combination that provided the best results comprises the following discrete points: 350, 370, 380, 400, 420, 450, 480, 510, 540, 560, 580, 600, 620, 650, 700, and 750 nm. For this wavelength selection a compromise between the accuracy in parameters extraction and the constraints inherent to the filters fabrication process (e.g. materials, number of layers, FWHM, and maximum transmission) had to be achieved. This wavelength choice is important for the intended diagnosis and will be dependent on the clinical situation for which the system is going to be used for. Since the esophagus is expected as the first application of the microsystem, the used clinical data set is suitable for the simulations. Examples of DRS spectra of high-grade dysplasia and non-dysplastic squamous tissue are shown in Fig. 2.

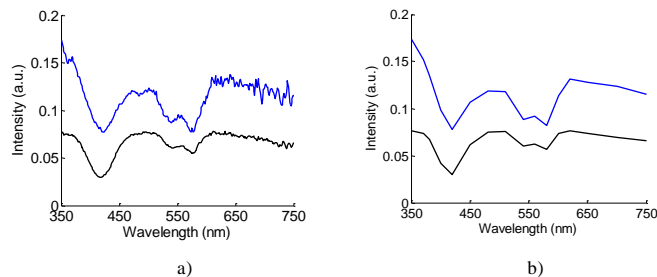


Fig. 2. Examples of DRS spectra for normal (upper line) and high-grade dysplastic tissue (bottom line), for (a) the full wavelength range (original spectrum) (b) and only 16 wavelengths (reconstructed spectrum).

The reduced scattering and absorption coefficients were determined for 16 different wavelengths, using the original spectrum and the reconstructed spectrum of high-grade dysplastic and non-dysplastic tissue sites (Fig. 3). In general, the extracted coefficients using the reconstructed spectrum are in good agreement with the coefficients extracted from the original spectrum, with a strong and positive correlation: correlation coefficients of 0.951 and

0.933 for the reduced scattering coefficient of high-grade dysplasia and non-dysplastic tissue sites, respectively; and, 0.966 and 0.987 for the absorption coefficient of high-grade dysplasia and non-dysplastic tissue sites, in that order. Thus, it is expected that the miniaturized system and the conventional systems will have very comparable performance in the quantification of tissue optical information.

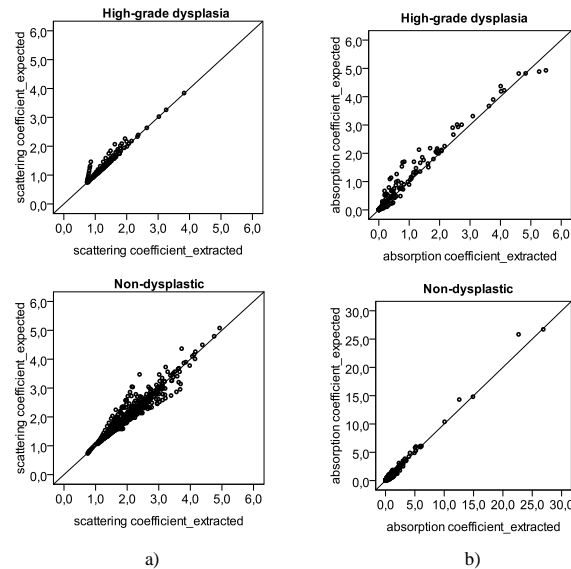


Fig. 3. Scatter plots with the (a) reduced scattering coefficient and (b) absorption coefficient, determined for several different wavelengths: 350, 370, 380, 400, 420, 450, 480, 510, 540, 560, 580, 600, 620, 650, 700, and 750 nm. For each of these wavelengths, a different coefficient will be determined in each tissue site: a total of 10 high-grade dysplastic tissue sites and 53 non-dysplastic tissue sites were used, corresponding to 160 (10 times 16) and 848 (53 times 16) different values of reduced scattering and absorption coefficient. Y-axis represents the values of the coefficients extracted with the original spectrum; X-axis represents the values of the coefficients determined with the reconstructed spectrum, using only 16 points. The 45 degree black line represents a perfect agreement between the expected values, from the original spectrum, and the extracted values, from the reconstructed spectrum.

An even more reduced number of wavelengths for spectra analysis would be useful to further reduce the size and complexity of the optical microsensors. However a trade-off between this number and an accurate extraction of optical parameters had to be achieved. Sixteen was considered the limit beyond which one could accurately determine those parameters.

For demonstration, Fig. 4 presents the same results of Fig. 3 but extracted using only 10 wavelengths (350, 380, 400, 420, 480, 540, 580, 600, 700 and 750), instead of 16. In this approach, the extracted coefficients using the reconstructed spectrum have weaker correlations with the coefficients determined from the original spectrum, when compared with the previous strategy. Specifically, for the reduced scattering coefficient of non-dysplastic tissue sites, there is a weak and not very significant correlation between the expected and extracted values, with a correlation coefficient of 0.326. From the obtained results it is clear the performance improvement of using 16 over 10 wavelengths for quantitative spectroscopy.

The theoretical parameters extraction performance of the miniaturized system was then assessed. Scatter plots displaying the expected (using the full spectrum) and extracted (using only 16 wavelengths) parameter values are presented in Fig. 5 for four DRS parameters: two parameters extracted from the reduced scattering coefficient (A and B), and two parameters extracted from the absorption coefficient (c_{Hb} and b_{9r}).

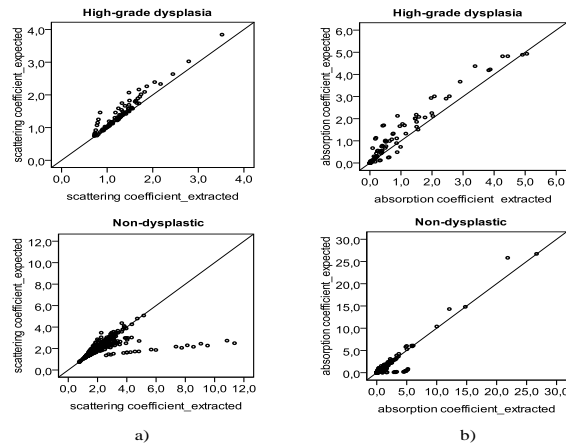


Fig. 4. Scatter plots with the (a) reduced scattering coefficient and (b) absorption coefficient, determined for several different wavelengths: 350, 370, 380, 400, 420, 450, 480, 510, 540, 560, 580, 600, 620, 650, 700, and 750 nm. Y-axis represents the values of the coefficients extracted with the original spectrum; X-axis represents the values of the coefficients determined with the reconstructed spectrum, using only 10 points.

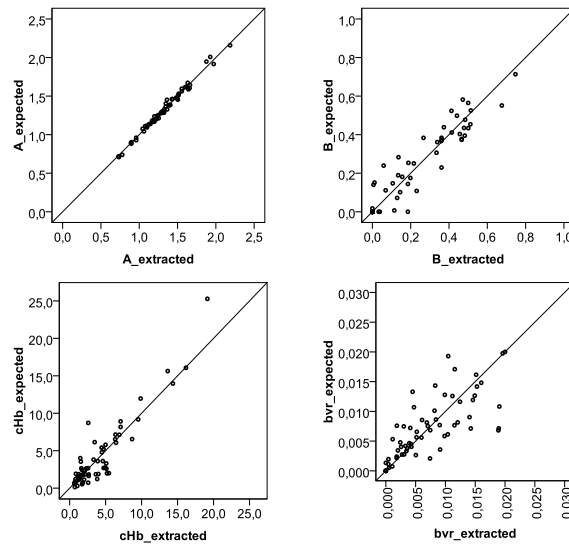


Fig. 5. Scatter plots with the tissue parameter values for four DRS parameters: A , B , c_{Hb} (hemoglobin concentration), and bvr (effective blood vessel radius), extracted using the full spectrum (expected values) and only 16 wavelengths (extracted values).

Overall, the reported results demonstrate that reflectance tissue parameters can be relatively well determined using a reduced number of wavelengths, and thus these parameters can be used with confidence for the development of predictive models to identify normal and malignant tissues. Still, for some tissue sites, optical parameters could not be accurately extracted, which might be due to loss of spectral information with interpolation. The use of a different interpolation method could minimize this error. Also, in further studies an alternative approach will be evaluated: a model discretization will be applied and the parameter results will be compared to the ones obtained using linear interpolation.

This rough methodology is applied as an initial approach to select the 16 central wavelengths to fabricate the optical filters, and to demonstrate the feasibility of wavelength reduction for the assessment of tissue optical properties.

4.2 Optical filtering system

The obtained results show the viability of using 16 wavelengths to extract tissue biochemical and morphological information. The selection of these wavelengths can be achieved using a 16 narrow-band pass optical filter array. This array is composed of three groups of optical filters to cover different regions of the spectrum: near-UV/violet (350 to 450 nm); red (620 to 750 nm); central band of the visible spectrum (480 to 600 nm). Thin-film optics software TFCalc™ 3.5 was used for the structural optimization of the optical filters. Simulations were performed using the previously measured refractive indexes (Table 1). In each group, the filters are composed by 11 layers of TiO₂ and SiO₂, and can be easily tuned to a different wavelength by adjusting the thickness of the resonance cavity, e.g., the 6th layer (Table 2). This enables the fabrication of several optical filters in each region of the spectrum while minimizing the global deposition time.

Table 2. Layer Thicknesses of the 16 Fabry-Perot Optical Filters

	Maximum wavelength transmission															
	350	370	380	400	420	450	480	510	540	560	580	600	620	650	700	750
	Layer thicknesses (nm)															
TiO ₂	36						52						72			
SiO ₂	68						95						116			
TiO ₂	36						52						72			
SiO ₂	68						95						116			
TiO ₂	36						52						72			
SiO ₂	94	110	120	136	154	182	140	164	192	206	227	242	182	210	255	301
TiO ₂	36						52						72			
SiO ₂	68						95						116			
TiO ₂	36						52						72			
SiO ₂	68						95						116			
TiO ₂	36						52						72			

Meanwhile, 6 of the 16 optical filters were fabricated in order to adjust the manufacturing process before proceeding with the fabrication of the remaining filters. Thin-film optical filters fabrication needs to be well controlled and optimized, because the position of the peak is highly sensitive to thickness variation. For example, a thickness variation of only 1 nm in each of the TiO₂ layers, relative to what was initially designed, is enough to move the peak to a different central wavelength. As demonstrated in Fig. 6, an increase of 1 nm in the thickness of each of the TiO₂ layers significantly affects the central peak position of the 540 nm filter (this effect might be noticed not only in the peak central wavelength, but also in its FWHM and transmission efficiency). For that reason, the filters were deposited by Ion Beam Deposition (IBD) in a 1 nanometer resolution system (Nordiko 3000).

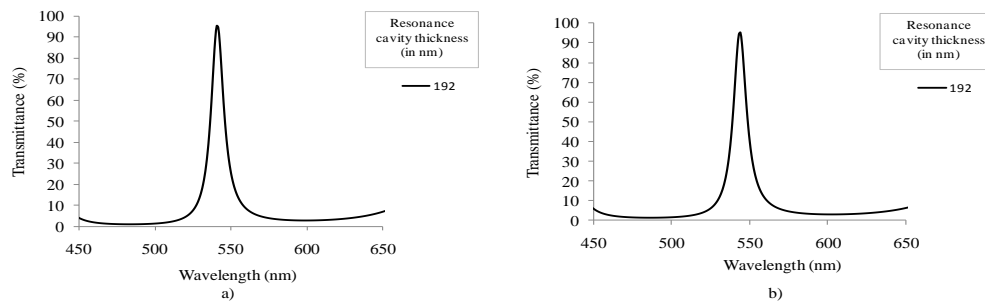


Fig. 6. Simulated spectral transmittance for the 540 nm optical filter, with maximum intensity peaks at: (a) 540 and (b) 543 nm, when there is an increase of 1 nm in the thickness of each of the TiO₂ layers.

Prior to filters fabrication, simple SiO₂ and TiO₂ films were deposited on silicon substrates to calibrate deposition rates and indexes of refraction. Subsequently, multilayer filters were deposited on a glass substrate.

The fabricated narrow-band pass filters were analyzed by cross section SEM (Scanning Electron Microscope) in order to assess layer thicknesses and interface quality between the SiO₂ and TiO₂ layers. Figure 7 depicts the cross-section of one of the analyzed optical filters (filter with peak centered at 560 nm).

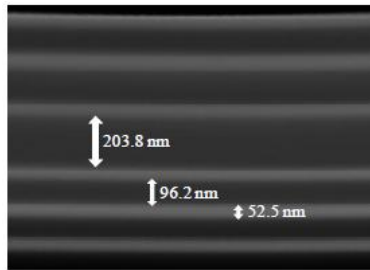


Fig. 7. SEM photograph showing the cross-section of the Fabry-Perot optical filter with the peak centered at 560 nm (magnification 200,000 times).

Figure 7 demonstrates the clear separation between the SiO₂ and TiO₂ layers, with very low interface mixing (brighter layers correspond to TiO₂). The mirrors thicknesses are in good agreement with the outlined values, whereas the resonance cavity thickness is slightly lower than what was initially designed (206 nm). Very good film flatness is shown along the entire area. This feature allows guarantee the parallelism of the mirrors concerning to the resonance cavity, which is crucial for reproducible optical measurements.

The transmittance of the fabricated filters was then assessed using a spectrophotometer from Shimadzu (UV-3101PC), and is demonstrated in Fig. 8. All the measurements were performed with the placement of a wide-band pass filter (200 nm wide) on top of the optical filters. This wide-band pass filter eliminates the tails of the filters outside the 450-650 nm spectral region. At this stage, this filter was fabricated on a glass substrate and placed on top of the 6 Fabry-Perot optical filters. In the final device, a thin-film wide-band pass filter will be processed directly on top of the narrow-band optical filters array, and its effect will be combined in the measurements with the optical effect of the silicon photodiodes. A wide-band pass filter is easily obtained with a multilayer structure, composed by 11 layers of SiO₂ and TiO₂, which can be represented by: SiO₂/TiO₂/ SiO₂/TiO₂/ SiO₂/TiO₂/ SiO₂/TiO₂/ SiO₂/TiO₂/SiO₂. All these layers have a thickness equal to 88 nm.

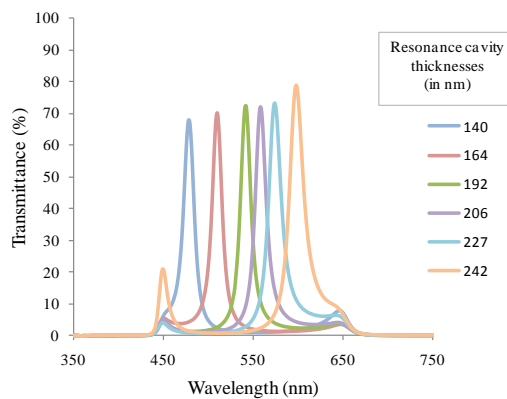


Fig. 8. Measured transmittance spectra for the 6 fabricated Fabry-Perot optical filters with the wide-band pass filter included.

Optical spectra measurements show that a multilayer structure composed of $(\text{TiO}_2, \text{SiO}_2)^2 \text{TiO}_2 / \text{SiO}_2 / \text{TiO}_2 (\text{SiO}_2, \text{TiO}_2)^2$ is the best option in terms of optical characteristics and fabrication process. The results show that each filter is sensitive to a specific spectral

band, with FWHM < 20 nm, and a ratio of maximum transmittance to background noise greater than 70/20. The FWHM translates the quality of the filter in terms of its ability to select a narrow band of the electromagnetic spectrum, and therefore, ideally, should be as low as possible. Additionally, the transmittance peak should be high, with at least twice the intensity of any background noise that might appear in the considered spectral range, so that we can clearly discriminate the specific wavelengths, without noise overlap (if it is less, the background noise will significantly affect the measurements) [25]. The filters peaks are slightly deviated from what was designed, being centered at: 478; 510; 540; 558; 574; and 598 nm. These differences between the design and the outcome of the fabrication process are mainly explained by the etching that might occur in some of the layers immediately below, when the multilayer is deposited. Indeed, the total thickness of the multilayers was measured using a profilometer, and the result was 2% less than what was initially designed. This event will obviously shift the central transmitted wavelength. As mentioned before, the process is being optimized and adjustments on the deposition rates are on-going. The overall performance of the optical filters could be improved by increasing the number of dielectric layers, but the fabrication process complexity would also increase.

The integration of optical filters, photodiodes and readout electronics on a single-chip requires the system to fit in a microelectronic process, preferably CMOS. The CMOS process provides three photosensitive structures as vertical junction photodiodes. At a particular wavelength, their quantum efficiency varies according to their junction depth. For this particular spectral region, we will use *pn*-junction photodiodes fabricated in a standard 0.7 μm CMOS process, without additional masks or steps.

As an example, a simulation of the optical transmittance for the 540 nm filter was performed taking into account the effect of the previously described wide-band pass filter and the effect of using a *n + /p-epilayer* photodiode to read the signal. Previous studies from our group have shown the fabrication and characterization of this type of photodiode [28]. The thickness of the photodiode junction depth is fixed by the microelectronics foundry, and equals to 350 nm (this junction depth is included in the simulations). Figure 9(a) depicts the transmittance of the filter without the optical effect of the wide-band pass filter and photodiode, whereas Fig. 9(b) illustrates the transmittance of the narrow-band pass filter with both effects included in the simulation. From Fig. 9(b) it is clear the signal attenuation below 450 nm and after 650 nm to less than 12%. Also, the maximum transmittance is lower due to the effect of the wide-band pass filter and photodiode. This approach enables the collection of spectroscopy data only around the filter central wavelength.

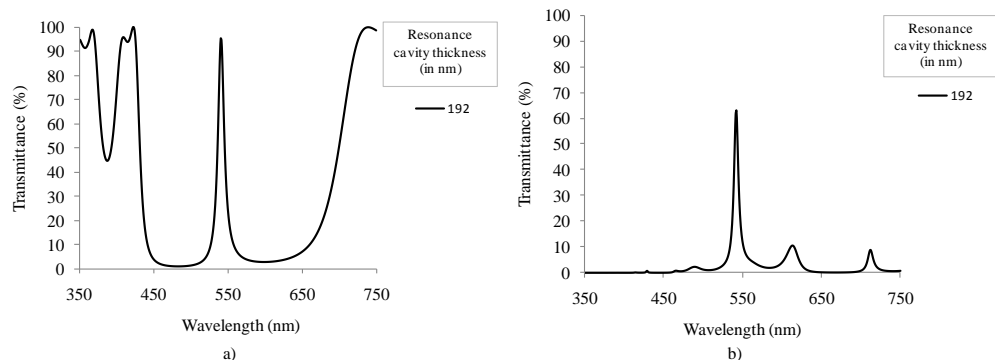


Fig. 9. Simulated transmittance spectra for the 540 nm Fabry-Perot optical filter: (a) not including and (b) including the optical effect of the wide-band pass filter and the *n + /p-epilayer* photodiode.

A new study was carried out for assessing the performance of the fabricated optical filters when used for spectroscopy. This study consisted in measuring diffuse reflectance spectrum from a tissue phantom using the fabricated optical filters (together with the wide-band pass

filter) placed in front of the UV-3101PC spectrophotometer detector, to determine how accurately each filter could detect the diffuse reflectance signal. The phantoms consist of a mixture of intralipid and hemoglobin (Sigma Aldrich Co.) and water. The intralipid and the water soluble hemoglobin are used for scattering and absorbing, respectively. All the collected spectra were normalized by the reflectance spectra measured from a standard (solid sample of BaSO₄) to correct for the wavelength dependent response of the system.

For this study, a diffuse reflectance spectrum measured from the tissue phantom without using optical filters was first acquired (Fig. 10(a)). After, consecutive diffuse reflectance measurements using each of the fabricated filters in front of the detection system were performed on the same tissue phantom (Fig. 10(b)). The resulting 6 Gaussian distributed spectra were integrated over the full wavelength range. The obtained 6 intensity values correspond to the signal that will be read by the optical microsensor. In a further processing, the filters transmittance spectra (Fig. 8) were also integrated, and the intensity read by the optical microsensor was divided by these 6 values. This way, one can obtain the final 6 data points that will compose the wavelength-reduced spectrum (Fig. 10(c)).

The intensity values obtained with the fabricated filters are similar to the originally obtained reflectance intensities measured over the full wavelength range, except for the 540 and 580 nm valleys that are not as noticeable as desired. This divergence might be explained by the filters FWHM. The on-going optimizations to the fabrication process should enable the fabrication of more accurate filters, correctly centered at the specific wavelengths, and with a smaller FWHM. Overall, it is reasonable to consider that the results validate the possibility of replacing the spectrograph by an array of thin-film narrow-band pass filters.

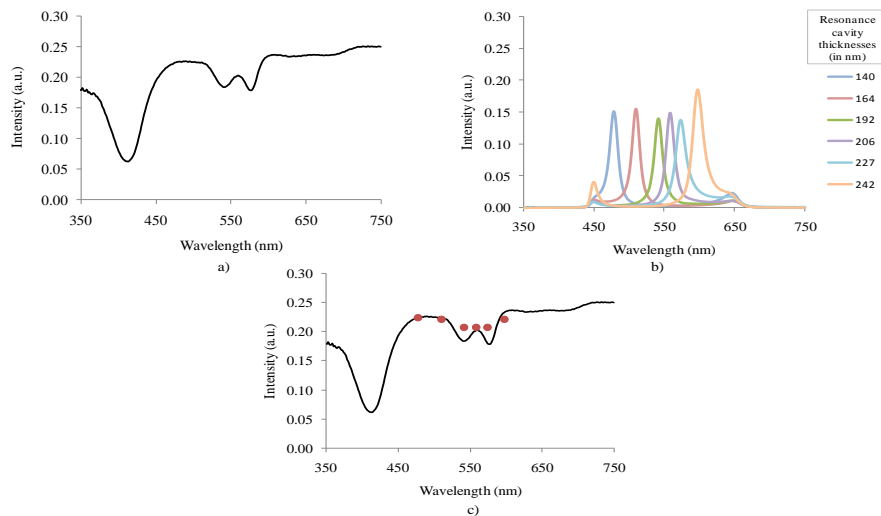


Fig. 10. Diffuse reflectance spectra: (a) measured with the UV-3101PC spectrophotometer; (b) measured with the 6 fabricated narrow-band pass optical filters; and, (c) together with the 6 integrated intensity values that will be obtained using the miniaturized system.

5. Conclusions

Diffuse reflectance spectroscopy is used to analyze tissue and to extract quantitative information. This study demonstrates that it is possible to obtain tissue properties accurately using a small number of wavelengths. These results represent an important step towards the development of a much smaller, simpler, and cost-effective device compared with the conventional spectroscopy prototypes, and with similar throughput.

The wavelength-reduction simulations were performed using real esophageal tissue data and the values of tissue properties obtained with the selected 16 wavelengths are comparable with those obtained using 400 wavelengths. However, it is important to notice the significance

of wavelength selection which may be different when using the system for other tissue types. After this feasibility study, thin-film narrow-band pass filters were fabricated and its optical performance was assessed. Reflectance measurements, performed on tissue phantoms, using the full wavelength range and the fabricated optical filters provided comparable results.

Overall, the results show the feasibility of replacing the spectrograph in a conventional system by a series of narrow-band pass optical filters in the new spectroscopy system. Also, with a future integration of LEDs for illumination and silicon photodiodes for detection, the instrument will be fully miniaturized while still providing similar results in terms of quantitative diagnostic information. The described results open the way to explore the integration of the developed instrument into endoscopic devices with clinical potential. Due to its reduced size, it could be incorporated in standard endoscopes making it more compact and portable. Moreover, it has a potential to be integrated, in the future, into smaller, less-invasive devices, such as the endoscopic capsules. The future directions include: filter optimization (specified band pass, FWHM, signal-to-noise ratio, and reliable reproducibility); assembling the 16 filters with the silicon photodiodes (in a 4 by 4 array), on a single-chip with readout electronics; accommodate on the same chip UV and white-light miniaturized sources.

Acknowledgments

This research was supported by the Portuguese Foundation of Science and Technology under the MIT|Portugal Program (SFRH / BD / 38978 / 2007) and PTDC/BIO/70017/2006.

Spectroscopic Detection of Gastrointestinal Dysplasia Using Optical Microsensors

D. S. Ferreira*, *Student Member, IEEE*, V. C. Pinto, J. H. Correia, *Member, IEEE*,
and G. Minas, *Senior Member, IEEE*

Abstract—The detection of dysplasia in the gastrointestinal tract can be performed using optical microsensors based on thin-film optical filters and silicon photodiodes. This paper describes two optical microsensors that can be used for spectroscopy data collection in two different spectral bands (one in the violet/blue region and the other in the green region) for which two optical filters were designed and fabricated. An empirical analysis of gastrointestinal spectroscopic data using these specific spectral bands is performed. The obtained results show that it is possible to accurately differentiate dysplastic lesions from normal tissue, with a sensitivity and specificity of 77.8% and 97.6%, respectively. Therefore, the developed filters can be used as a tool to aid in diagnosis. The small size of the optical microsensors can enable, in the future, integration in endoscopic capsules.

Index Terms—Diffuse-reflectance, Fabry–Perot optical filters, fluorescence, spectroscopy tissue diagnosis.

I. INTRODUCTION

GASTROINTESTINAL (GI) cancers, in particular cancers of the esophagus, stomach, and colorectum, are among the fifth leading causes of cancer-related deaths worldwide [1]. These epithelial cancers are usually preceded by dysplastic changes. An early identification of cancer is very important since the chances of an effective treatment considerably increase when the disease is detected at the dysplastic stage, improving the survival rate [2], [3]. The World Health Organization has estimated that nearly one-third of cancer burden could be decreased if lesions were diagnosed and treated at its earliest stages. Unfortunately, dysplastic lesions are difficult to detect using standard screening methods: dysplasia is not readily identifiable by visual inspection during routine endoscopy. As a consequence, physicians often take a large number of undirected

biopsies to increase the chances of detecting invisible lesions, which results in sampling errors and high costs associated with the procedure [2]–[4].

Optical techniques may overcome some limitations of current screening methods and enhance detection of dysplasia *in vivo*. Diffuse-reflectance and fluorescence spectroscopy have been proven to be highly sensitive for the identification of dysplasia, by exhibiting different spectral features that can be correlated with normal and cancerous tissue [2], [3]. Such techniques have the ability to reveal biochemical and morphological tissue information that can be used to characterize changes that take place during disease transformation [3], [4].

Several studies have successfully applied diffuse-reflectance and fluorescence spectroscopy for detecting and classifying dysplasia in a variety of GI structures [5]–[7]. In these studies, data collection is performed using costly and bulky clinical instruments, usually composed by a spectrograph, a detector, and optical fibers. This instrument configuration has some drawbacks: regular optical fibers might have low collection efficiency, thus requiring high quantum efficiency detectors (such as charge-coupled device (CCD) cameras), and, the detector is placed at the distal end of the collection fiber, where considerable light might be lost [8]. Moreover, catheter-based endoscopy systems are invasive and very uncomfortable for the patient. The development of a miniature spectroscopy system without using optical fibers, spectrograph or CCDs would enable integration in small and less-invasive devices for GI tract evaluation. Kfourri *et al.* [9] have already developed a miniaturized fluorescence imaging device for noninvasive diagnosis of diseases in the GI tract. However, the full-integrated prototype is still too large (2 cm in diameter and 10 cm in length), and further miniaturization is compromised by the use of several incompatible CMOS IC components. Also, only fluorescence images are acquired to perform diagnosis. To the best of our knowledge, it was not yet developed a miniaturized device that integrates both fluorescence and diffuse-reflectance functions for early cancer diagnosis.

In this study, it is described a strategy for the detection of dysplasia in the upper GI tract and proposed the development of a low complexity, miniaturized device for spectroscopy data collection (fluorescence together with diffuse-reflectance). This system, named as *optical microsensor*, is based on thin-film optical filters and CMOS silicon photodiodes, for the selection and detection of two different spectral bands that are significant for the identification of GI dysplastic lesions. This approach requires the development of two optical filters, one of which will be used for fluorescence measurements, while the other will be

Manuscript received March 15, 2011; revised May 11, 2011; accepted June 6, 2011. Date of publication June 23, 2011; date of current version August 19, 2011. This work was supported by ADI with reference FCOMP-01-0202-FEDER-005358, by FEDER funds through the “Programa Operacional Factores de Competitividade—COMPETE”, and by national funds by Fundação para a Ciência e a Tecnologia, with project reference PTDC/BIO/70017/2006, and the MIT/Portugal Program (SFRH/BD/38978/2007). *Asterisk indicates corresponding author.*

*D. S. Ferreira is with the Centro Algoritmi, University of Minho, Campus de Azurém, 4800-058 Guimarães, Portugal (e-mail: debora@dei.uminho.pt).

V. C. Pinto, J. H. Correia, and G. Minas are with the Centro Algoritmi, University of Minho, Campus de Azurém, 4800-058 Guimarães, Portugal (e-mail: vpinto@dei.uminho.pt; higino.correia@dei.uminho.pt; gminas@dei.uminho.pt).

Color versions of one or more of the figures in this paper are available online at <http://ieeexplore.ieee.org>.

Digital Object Identifier 10.1109/TBME.2011.2160263

used to collect the reflectance signal. Both filters will have a Fabry–Perot multilayer structure made with dielectric materials that are Si compatible, thus compatible with standard microelectronics fabrication and processing techniques (which is an asset toward the development of a fully miniaturized device, in a single chip). Also, the use of all-dielectric layers allows a narrow and a high peak transmittance spectral band, as required for the application [10]–[12].

The proposed device has three major advantages over previous systems: 1) it is miniaturized and, thus, suitable for a future integration in a less-invasive medical device (e.g., endoscopic capsule); 2) it integrates components that are compatible with standard microelectronics fabrication and processing techniques; and 3) it combines two different spectroscopy techniques: diffuse-reflectance and fluorescence.

II. DIFFUSE-REFLECTANCE AND FLUORESCENCE SPECTROSCOPY

In diffuse-reflectance spectroscopy, white light delivered to the tissue is absorbed and multiple scattered by tissue constituents and part of it returns, carrying information about tissue optical properties (scattering and absorption) [4], [13]. Scattering is mainly originated by collagen fibers in connective tissue, whereas absorption is mainly due to hemoglobin. The major hemoglobin absorption peaks are nearly the 420 nm and 540–580 nm regions [4]. A decrease in scattering is associated with increasing dysplasia: epithelial thickness increases, and therefore the amount of light propagating to the connective tissue with collagen is reduced. Additionally, with dysplasia some enzymes are released that will cleave the collagen cross links [3], [14]. An increased hemoglobin concentration, which translates into an increased absorption, may be associated with angiogenesis that is proved to be linked with some types of early cancers [15].

Epithelial tissues produce fluorescence when excited by ultraviolet (UV) or short-wavelength visible light. This fluorescence is originated by several fluorophores that are related to the structural arrangement and metabolism of cells. Each fluorophore is excited by a specific wavelength and has particular emission characteristics, supplying different biochemical information. A modification in fluorescence emission may be related to the emergence of pathological conditions. The dominant fluorescent tissue layer is the submucosa, where collagen and elastin emit around the 400 nm spectral band [4], [16], [17]. NAD(P)H and collagen are considered fluorescent biomarkers of precancerous changes in epithelial tissues [14]. An increase in NAD(P)H is associated with an increase in cellular metabolic activity and proliferation, both of which occur with the progression of dysplasia. A decrease in collagen can be an indicator of loss of structural integrity and is translated by low fluorescence intensity. Thus, fluorescence intensity of dysplastic epithelial tissue is generally lower compared to healthy tissue [14], [18], [19]. This concept, together with diffuse-reflectance signal information, can be used to distinguish the presence and absence of malignancy.

An empirical analysis of fluorescence and diffuse-reflectance signal from GI tissue is described. The intensity of fluorescence

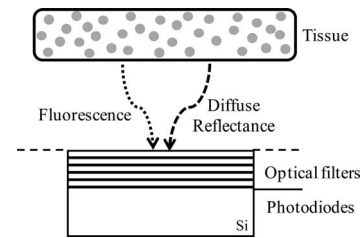


Fig. 1. Cross-sectional view of the optical microsensor with optical filters and photodiodes (not scaled).

and diffuse-reflectance within only two specific spectral bands will be used for the discrimination of dysplastic and normal tissue.

III. DESIGN OF THE OPTICAL MICROSENSOR

An optical microsensor for spectroscopy data collection was designed (see Fig. 1). This device is based on thin-film optical filters and silicon photodiodes that will, respectively, select and detect several light wavelengths of interest for the diagnosis of GI dysplasia. The use of these components obviates the need for expensive and sophisticated detection equipment and optical fibers for light collection from tissues. In addition, small-size UV and white light-emitting diodes (LEDs) could be incorporated in the instrument as the illumination sources for fluorescence and diffuse-reflectance measurements, respectively.

The designed microsensor can be scaled down to a few millimeters, and like that has potential to be integrated in very small and thus less-invasive devices, such as the endoscopic capsule. For this particular application, a control of the capsule direction and distance to the tissue surface has first to be achieved. Promising developments in this field have already been made, which may allow, in the future, to place the capsule into gentle contact with the tissue, in a controlled way, to collect spectroscopy data [20], [21]. This placement of the detection system close to the sample allows us collecting most of the reemitted light.

Concerning power supply requirements, for the proposed optical microsensor, it will be similar to the one used in commercial endoscopic capsules. A 50-mAh capacity with a 3-V nominal voltage would be used, being enough for 6-h work. Also, it is important to notice that the illumination sources will not spend more energy than the one currently available since when the UV LEDs are turned ON, the white LEDs are turned OFF and vice versa.

A. Optical Filters Structure and Materials

The detection of specific spectral bands requires the use of thin-film optical filters placed on top of silicon photodiodes. The filtering system is based on Fabry–Perot thin-film optical resonators. These consist of two flat parallel mirrors separated by a specific distance, with a resonance cavity in the middle (see Fig. 2). The thickness of the resonance cavity determines the transmitted wavelength band, as explained by the equation $\lambda q = 2nd$, where n is the refractive index of the cavity medium, d is the cavity length or thickness, λ is the transmitted wavelength,

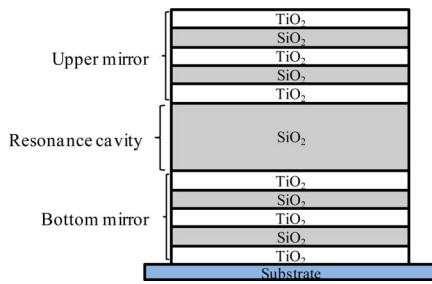


Fig. 2. Designed Fabry-Perot resonator, composed by 11 layers, and with dielectric mirrors.

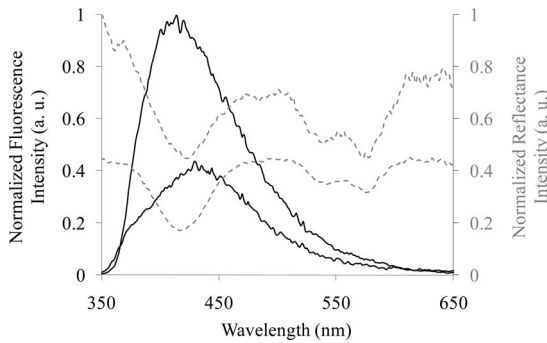


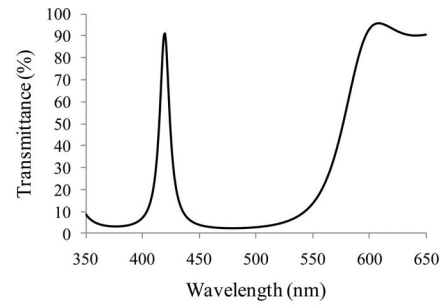
Fig. 3. Diffuse-reflectance (dashed lines) and fluorescence (solid lines) spectra examples. Higher intensity spectra correspond to normal tissue, whereas dysplastic tissue sites exhibit low-intensity spectra. For this illustration, reflectance and fluorescence intensity spectra were normalized to their maximum intensity values for a better comparison of their spectral shape (peaks and valleys).

and q is the interference order. For the designed filters (see Fig. 2), the mirrors are dielectric mirrors composed of a stack of TiO_2 and SiO_2 thin-films (materials with high and low refractive index in the visible spectrum, respectively) which offer good optical performance characteristics, high transmittance and low full-width half-maximum (FWHM), with low-absorption losses [12], [22].

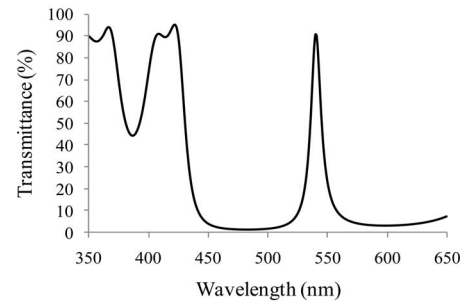
B. Optical Filters Simulations

To design the optical microsensors, i.e., to define the two specific transmittance spectral bands of the optical filters, diffuse-reflectance and fluorescence data from normal and dysplastic GI tissue were used (examples are shown in Fig. 3). This dataset comprised nine dysplastic tissue sites and 42 normal tissue sites.

From Fig. 3, and using only two spectral bands, the optical filters should be able to select one fluorescence band in the violet/blue region of the spectrum (centered at 420 nm) and one reflectance band in the green region of the spectrum (centered at 540 nm). These central wavelengths were selected in order to detect approximately the maximum fluorescence emission of tissues, and to detect one of the hemoglobin absorption peaks in the reflectance signal. Previous studies [23] have shown that it is very important to take into account a green reflectance band, to help in the differentiation of inflammation from tumors, and thus reduce the number of false positives. For this reason, the 540 nm spectral band was selected for the reflectance measurements, instead of the 420 nm spectral band.



(a)



(b)

Fig. 4. Simulated spectral transmittance of the two Fabry-Perot optical filters: (a) violet/blue region; (b) green region. Maximum intensity peaks at (a) 420 and (b) 540 nm.

For the violet/blue region, the mirrors are composed by 45 nm-thick TiO_2 and 70 nm-thick SiO_2 layers, whereas for the green region, the mirrors are composed by 52 nm-thick TiO_2 and 95 nm-thick SiO_2 layers. The resonance cavity thickness, i.e., the sixth layer, is equal to 138 and 192 nm for the violet/blue and green filter, respectively. In each spectral region, the optical filters can be easily tuned to a different central wavelength by adjusting only the thickness of the sixth layer, and keeping the same mirror layers. Thus, it would be possible to produce a filter centered at 450 nm by simply increasing the cavity thickness from 138 to 180 nm, or to create a filter centered at 500 nm by reducing only the cavity thickness from 192 to 155 nm. This procedure enables the fabrication of several optical filters in each region of the spectrum, whereas, minimizing the global deposition time.

Thin-film optics software TFCalc 3.5 (Software Spectra, Inc., Portland, OR) was used for the structural optimization of the optical filters. In Fig. 4, the simulated transmittances for the two Fabry-Perot optical channels are presented.

The simulated results show that each filter is sensitive to its specific spectral band, with FWHM less than 12 nm. Also, the peaks transmittance is higher than 90%. However, the tails of both filters at wavelengths farther from its transmittance peak may raise some concerns. For the violet/blue optical filter, the transmittance increases from 550 to 650 nm. Given that this optical filter is going to be used solely for fluorescence measurements, this collection of out-of-band light is not a problem once fluorescence emission in this band tends to zero (see Fig. 3). On the other hand, as it is designed, the green optical filter will be collecting significant out-of-band light that will confound the reflectance analysis. Still, this problem can also be exceeded

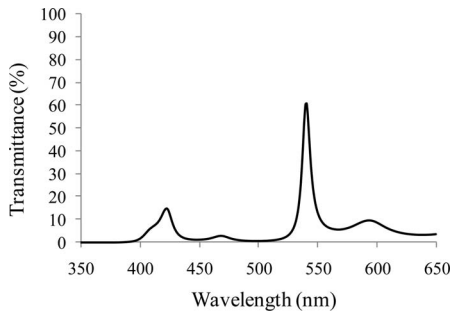


Fig. 5. Simulated spectral transmittance of the green filter with the optical effect of the $n+/p$ -epilayer photodiode included.

when the effect of the silicon photodiode is integrated in the measurements, together with the green filter, to produce the final device.

The integration of optical filters, photodiodes, and readout electronics on a single chip requires the system to fit in a microelectronic process, preferably CMOS. This technology features electronics in a small silicon area and offers low power consumption, an important requirement for the reported application. For the violet/blue spectral band, a photodiode with improved quantum efficiency at low-visible wavelengths is being designed. Regarding the green spectral band, we will use p-n junction photodiodes fabricated in a standard $0.7\text{-}\mu\text{m}$ CMOS process, without additional masks or steps.

The CMOS process provides three photosensitive structures as vertical junction photodiodes. At a particular wavelength, their quantum efficiency varies according to their junction depth. In the visible spectrum, blue light is more efficiently collected by a shallower junction ($p+/n$ -well and $n+/p$ -epilayer) and red light by a deeper junction (n -well/ p -epilayer). However, despite its shallow junction, the $n+/p$ -epilayer photodiode has high quantum efficiency around 550 nm due to the different doping concentration between the n - and the p -side. This extends the p -side depletion area more deeply [24]. Therefore, this photodiode was selected for the microsystem. The green optical filter will be vertically aligned with the photodiode to build the optical channel for the collection of reflectance data. A detailed characterization of the fabricated $n+/p$ -epilayer photodiode can be found in [24].

New computational simulations were then performed for the green optical filter taking into account the effect of using an $n+/p$ -epilayer photodiode to read the signal. The thickness of the photodiode junction depth is fixed by the microelectronics foundry, and equals to 350 nm. Fig. 5 illustrates the signal attenuation in the violet/blue region to less than 20%. The peak transmittance is also lower than what was initially simulated due to the optical effect of the detector.

IV. RESULTS AND DISCUSSION

A. Thin-Film Optical Filters Characterization

Before the optical filters fabrication, single layers of SiO_2 and TiO_2 were deposited on silicon substrates to calibrate deposition rates and indexes of refraction. After, the multilayer filters were

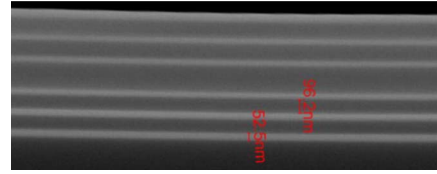


Fig. 6. SEM photograph showing the cross section of the green Fabry-Perot optical filter (magnification 100 000 times).

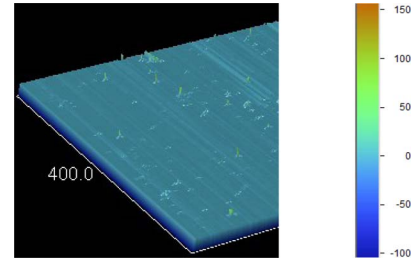


Fig. 7. Surface 3-D map of the green Fabry-Perot optical filter.

deposited by ion-beam deposition on a glass substrate using a Nordiko 3000 deposition tool. Multilayer filters were analyzed by a cross-sectional scanning electron microscope (SEM) in order to assess layer thicknesses and interface quality between the different layers (see Fig. 6).

In Fig. 6, it is noticeable the separation between the SiO_2 and TiO_2 layers, with very low interface mixing (brighter layers correspond to elements with high atomic number— TiO_2). The film thicknesses are in good agreement with the outlined values. It is also shown very good film flatness along the entire area. This feature allows us to guarantee the parallelism of the mirrors concerning to the resonance cavity, which is crucial for reproducible optical measurements.

The multilayer surface roughness was also evaluated, in a 400 by 400 μm area, using a profilometer (Dektak 150 Surface Profiler, Veeco Instruments, Inc., Plainview, TX). The surface 3-D map for the green optical filter is shown in Fig. 7.

From Fig. 7, it can be seen that, in general, the optical filter's surface is smooth, as would be desirable in order to minimize potential interferences to the incident light beam. Its roughness profile is in average equal to 2.31 nm. Several tiny irregularities inherent to the filters manufacturing process are present in the surface; yet, these are not a major concern due to their small size.

Finally, the transmittance performance of the optical filters was assessed (see Fig. 8). Optical spectra measurements on the filters show that they are sensitive to their particular spectral band. However, the violet/blue filter peak is slightly deviated from what was initially simulated, being centered at 422 nm, which is explained by the fabrication process tolerance. This process has a tolerance of 2% in the thickness of the thin-film layers being deposited, which is more evident in the SiO_2 : some SiO_2 layers might have been deposited about 1 or 2 nm thicker than what was initially designed; an increase in the layers thickness shifts the spectral peak to the right. Still, this is a very small deviation that does not affect the performance of the overall

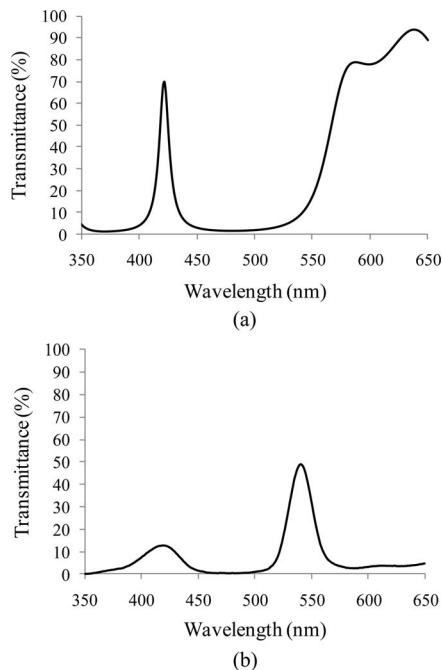


Fig. 8. Measured transmittance spectra of the two Fabry-Perot optical filters: (a) violet/blue filter, measured with the UV-3101 PC spectrophotometer (a CMOS photodiode is currently being designed and optimized for this spectral region); (b) green filter (measured with the fabricated $n+ip$ -epilayer photodiode). Maximum intensity peaks at (a) 422 and (b) 540 nm.

system. This filter spectral shape is in good agreement with the simulations, with a maximum transmittance around 70% and an FWHM of 12 nm. The FWHM of the green filter is a little wider than expected by computational simulations (around 23 nm). Its ratio of maximum transmittance to background noise is greater than 50/15, which is acceptable for the interference filter since the transmittance peak has more than twice the intensity of any background noise that appears in the considered spectral range.

The overall performance of the optical filters could be improved by increasing the number of dielectric layers, but the fabrication process complexity would also increase. Therefore, it must be achieved a compromise between the filters accuracy to perform diagnosis and the constraints inherent to the filters fabrication process (e.g., materials, number of layers, FWHM, and maximum transmission).

B. Diffuse-Reflectance and Fluorescence Spectra Analysis

A new strategy based on the use of only two spectral bands for the detection of dysplasia in the upper GI tract was studied. The feasibility of using the developed optical microsensors for distinguishing dysplasia from normal tissue was theoretically assessed with a spectral analysis. For this study, the optical filters transmittance curves were used together with spectroscopy diffuse-reflectance and fluorescence data. Histopathology diagnoses are used as the standard against which the spectroscopic-qualitative diagnoses are compared.

In this analysis, all diffuse-reflectance and fluorescence spectra (not normalized) were first multiplied by the green and violet/blue filters measured transmittance curves, respectively (see

Fig. 8). The resulting Gaussian distributed spectra were then integrated over the full transmittance range (from 350 to 650 nm). The obtained integrated intensity values correspond to the signal that will be read by the photodiodes.

Subsequently, a statistical analysis was performed on the processed spectral data using the Student's t -test, the Mann-Whitney test, and the logistic regression model. This analysis is performed in order to extract any relevant diagnostic algorithm that provides diagnostic differences between normal and dysplastic tissues. A statistical software (IBM[®] SPSS[®]) was used for this study.

The Student's t -test and the Mann-Whitney test, respectively, were used to compare normally and not normally distributed continuous variables (diffuse-reflectance intensity in the green spectral band and fluorescence intensity in the violet/blue spectral band) for two distinct groups of tissue sites: dysplastic and normal. A p -value less than 0.05 was considered to be statistically significant. For both variables, the null hypothesis was rejected. This means that the measured intensity values of diffuse-reflectance at 540 nm, and of fluorescence at 420 nm, are significantly different between the two groups. In nearly all cases, compared with dysplasia, normal tissue sites exhibit significantly higher intensity values, both for diffuse-reflectance and fluorescence, as it was theoretical expected. As explained in Section II, a decrease in the fraction of collagen fibers with progression of dysplasia is translated by low fluorescence intensities, and by a reduced reflectance signal as a result of low scattering. Also, a high hemoglobin concentration, which is characteristic of dysplastic tissues, may attenuate the diffuse-reflectance and endogenous fluorescence signals due to absorption.

The spectral algorithm for classifying tissue as normal or dysplastic was developed by using binary logistic regression. A model with a good predictive capability includes both the diffuse-reflectance and fluorescence data. The accuracy of the final logistic regression model is evaluated by the area under the receiver operating characteristic (ROC) curve (AUC), and the sensitivity and specificity. The box plots of the reflectance and fluorescence variables, as well as the ROC curve for the differentiation of dysplasia from normal tissue are presented in Fig. 9.

From the results of Fig. 9, one can say that the violet/blue fluorescence and green diffuse-reflectance intensities are good predictors for the discrimination of tissue disease status. The model has an overall accuracy of 94.1%. Dysplasia and normal tissue can be distinguished with an AUC, sensitivity, and specificity of 0.995, 77.8%, and 97.6%, respectively. Sensitivity is defined as the fraction of dysplastic tissue sites correctly identified by the model, whereas specificity is defined as the fraction of correctly identified normal tissue sites. The not very high value of sensitivity might be explained by the small number of dysplastic tissue sites used, which is a limitation in this study. The positive predictive value, which is the probability that a positive result is accurate equals to 87.5%. The negative predictive value (NPV), which is the probability that a negative result is accurate, is equal to 95.3%. A high NPV (low number of false negatives) is very important for an effective clinical

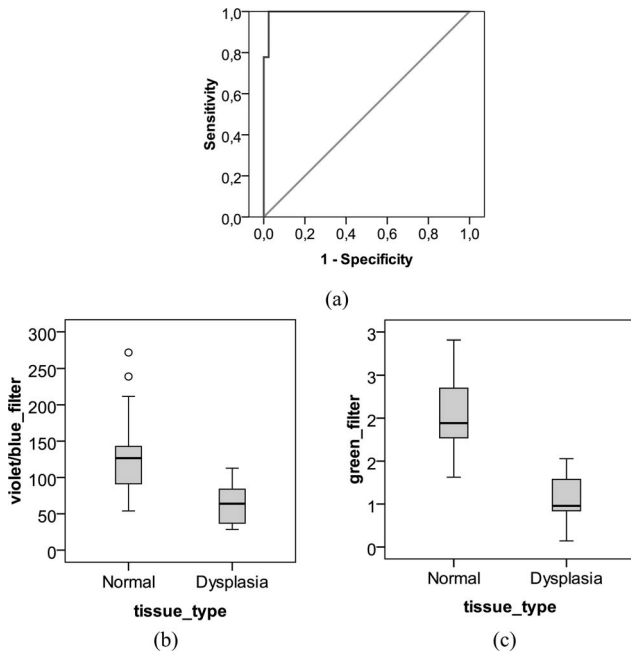


Fig. 9. Discrimination of normal from dysplastic tissue sites. (a) ROC curve for the logistic regression algorithm: ROC curve (blue solid line); 45° green line (AUC = 0.5). The AUC measures the accuracy of the model to correctly classify normal and diseased tissue. A perfect discrimination is achieved with an AUC value of 1; an AUC value of 0.5 indicates an inability to differentiate the two tissue types. Box plots of the two variables included in the model. (b) Fluorescence data from the violet/blue spectral region for the two tissue types. (c) Reflectance data from the green spectral region for the two tissue types. Outliers are symbolized by circles.

practice, especially when the system is going to be used to guide biopsies, since the physician has to be confident that none of the dysplastic lesions are identified as normal, and consequently not subjected to biopsy. A low NPV might be indicative that cancerous tissue is left in the patient without being identified.

Mayinger *et al.* [18] described a measurement system that uses differences in the fluorescence spectral intensities to identify cancerous tissue in the upper GI tract. Tissues were excited with violet-blue light and fluorescence spectra were collected using an optical fiber and analyzed with a spectrograph. The developed algorithm was based on the intensity ratio in the green and red spectral bands and provided a sensitivity of 97% and a specificity of 95% for the diagnosis of esophageal cancer. However, in this study, it was not included data for benign lesions (e.g., inflammations) that might influence fluorescence spectroscopy. Uedo *et al.* [23] found that a superficial neoplasm and an inflamed tissue with edema could be misunderstood using only fluorescence measurements. In this study, the addition of green reflectance information proved to be helpful for the differentiation of inflammation from tumors.

Bourg-Heckly *et al.* [6] also used a fluorescence spectroscopy system for the detection of dysplasia in the upper GI tract. The instrument was composed by a UV xenon lamp, bandpass filters, optical fibers for light delivery and collection, and a spectrometer with a CCD camera for detection. Overall, this optical setup is not portable and compact, which might be cumbersome in the clinical environment. In this study, a model based only on the flu-

orescence intensity ratio at two different wavelengths (390 and 550 nm) was able to discriminate neoplastic tissue from normal mucosa with a sensitivity of 86% and specificity of 95%.

In our study, we not only combine information from diffuse-reflectance and fluorescence, which combination was shown to be helpful for the discrimination of benign and malignant lesions, but we also demonstrate that it is possible to identify dysplastic and healthy tissue sites, with a suitable sensitivity and specificity, using a much smaller instrument, compared with the instruments used in similar studies. Replacing the spectrograph by thin-film optical filters and the CCDs by silicon photodiodes will enable the development of a more portable, low cost, and simple spectroscopy system, with similar throughput.

The obtained results with only two optical filters are very promising but further study should be done. As an important next step, the performance of the presented diagnostic algorithm should be tested in a large clinical study using the optical microsensor incorporated in a conventional endoscope. This optical microsensor must have not only the optical filters post-processed directly on top of the CMOS photodiodes but also the readout electronics, all bonded together on the same chip. A separated fabrication was used as a first approach, since it enabled the characterization and optimization of the different parts.

V. CONCLUSION

Diffuse-reflectance and fluorescence spectroscopy proved to be sensitive methods for the detection of early cancerous lesions in the GI tract. This study reports a new approach for the identification of dysplasia using a simple and miniaturized system for spectroscopy data collection. The proposed device is based on thin-film optical filters and silicon photodiodes for the selection and detection of two spectral bands that will provide information for diagnosis.

An empirical study was performed using spectroscopy data from dysplastic and normal GI tissue sites to demonstrate the feasibility of replacing the spectrograph in standard clinical prototypes by two optical filters in the miniaturized system. The spectral performance of the fabricated interference filters was shown to be sufficient for the intended final goal. The overall results have proven that healthy and diseased tissue can be differentiated with a sensitivity and specificity of 77.8% and 97.6%, respectively.

It is reasonable to envision an important clinical utility for the proposed optical microsensor since due its reduced size it could be incorporated in a standard endoscope making it more compact and portable. Moreover, it could also be, in the future, integrated in an endoscopic capsule platform for guiding biopsy of invisible lesions in the GI tract. With this device, the sampling error and healthcare costs associated with unnecessary biopsies could be significantly reduced.

ACKNOWLEDGMENT

The authors would like to thank Prof. A. C. Braga for the helpful discussions in statistics.

REFERENCES

- [1] J. Ferlay, H. R. Shin, F. Bray, D. Forman, C. Mathers, and D. M. Parkin. (2010). *GLOBOCAN 2008, Cancer Incidence and Mortality Worldwide: IARC CancerBase No. 10*. Lyon, France: Int. Agency Res. Cancer. [Online]. Available at <http://globocan.iarc.fr/>.
- [2] J. W. Tunnell, A. E. Desjardins, L. Galindo, I. Georgakoudi, S. A. McGee, J. Mirkovic, M. G. Mueller, J. Nazemi, F. T. Nguyen, A. Wax, Q. Zhang, R. R. Dasari, and M. S. Feld, "Instrumentation for multi-modal spectroscopic diagnosis of epithelial dysplasia," *Technol. Cancer Res. Treat.*, vol. 2, pp. 505–514, 2003.
- [3] C. C. Yu, C. Lau, G. O'Donoghue, J. Mirkovic, S. McGee, L. Galindo, A. Elackattu, E. Stier, G. Grillone, K. Badizadegan, R. R. Dasari, and M. S. Feld, "Quantitative spectroscopic imaging for non-invasive early cancer detection," *Opt. Exp.*, vol. 16, pp. 16227–16239, 2008.
- [4] I. Georgakoudi, "The color of cancer," *J. Lumin.*, vol. 119–120, pp. 75–83, 2006.
- [5] B. Mayinger, P. Horner, M. Jordan, C. Gerlach, T. Horbach, W. Hohenberger, and E. G. Hahn, "Light-induced autofluorescence spectroscopy for tissue diagnosis of GI lesions," *Gastrointestinal Endoscopy*, vol. 52, pp. 395–400, 2000.
- [6] G. Bourg-Heckly, J. Blais, J. J. Padilla, O. Bourdon, J. Etienne, F. Guillemain, and L. Lafay, "Endoscopic ultraviolet-induced autofluorescence spectroscopy of the esophagus: Tissue characterization and potential for early cancer diagnosis," *Endoscopy*, vol. 32, pp. 756–765, 2000.
- [7] B. Mayinger, M. Jordan, P. Horner, C. Gerlach, S. Muehldorfer, B. R. Bittorf, K. E. Matzel, W. Hohenberger, E. G. Hahn, and K. Guenther, "Endoscopic light-induced autofluorescence spectroscopy for the diagnosis of colorectal cancer and adenoma," *J. Photochem. Photobiol. B: Biol.*, vol. 70, pp. 13–20, 2003.
- [8] J. Y. Lo, B. Yu, H. L. Fu, J. E. Bender, G. M. Palmer, T. F. Kuech, and N. Ramanujam, "A strategy for quantitative spectral imaging of tissue absorption and scattering using light emitting diodes and photodiodes," *Opt. Exp.*, vol. 17, pp. 1372–1384, 2009.
- [9] M. Kfour, O. Marinov, P. Quevedo, N. Faramarzpour, S. Shirani, L. W. C. Liu, Q. Fang, and M. J. Deen, "Toward a miniaturized wireless fluorescence-based diagnostic imaging system," *IEEE J. Sel. Topics Quantum Electron.*, vol. 14, no. 1, pp. 226–234, Jan./Feb. 2008.
- [10] A. Piegari and J. Bulir, "Thin film filters with variable transmittance for spectrometry," in *Proc. 4th IEEE/LEOS Workshop Fibres Opt. Passive Compon.*, Jun. 2005, pp. 109–144.
- [11] D. P. Poenar and R. F. Wolfenbuttel, "Optical properties of thin-film silicon-compatible materials," *Appl. Opt.*, vol. 36, pp. 5122–5127, 1997.
- [12] H. A. Macleod, *Thin-Film Optical Filters*, 3rd ed. London, U.K.: Inst. Phys. Publishing, 2001.
- [13] G. Zonios, L. T. Perelman, V. Backman, R. Manoharan, M. Fitzmaurice, J. Van Dam, and M. S. Feld, "Diffuse reflectance spectroscopy of human adenomatous colon polyps in vivo," *Appl. Opt.*, vol. 38, pp. 6628–6637, 1999.
- [14] I. Georgakoudi, B. C. Jacobson, M. G. Müller, E. E. Sheets, K. Badizadegan, D. L. Carr-Locke, C. P. Crum, C. W. Boone, R. R. Dasari, J. Van Dam, and M. S. Feld, "NAD(P)H and Collagen as in vivo quantitative fluorescent biomarkers of epithelial precancerous changes," *Cancer Res.*, vol. 62, pp. 682–687, 2002.
- [15] A. Couvelard, F. Paraf, V. Gratio, J. Y. Scoazec, D. Héning, C. Degott, and J. F. Fléjou, "Angiogenesis in the neoplastic sequence of Barrett's oesophagus. Correlation with VEGF expression," *The J. Pathology*, vol. 192, pp. 14–18, 2000.
- [16] N. Ramanujam, "Fluorescence spectroscopy of neoplastic and non-neoplastic tissues," *Neoplasia*, vol. 2, pp. 89–117, 2000.
- [17] R. S. Dacosta, B. C. Wilson, and N. E. Marcon, "Spectroscopy and fluorescence in esophageal diseases," *Best Pract. Res. Clin. Gastroenterol.*, vol. 20, pp. 41–57, 2006.
- [18] B. Mayinger, P. Horner, M. Jordan, C. Gerlach, T. Horbach, W. Hohenberger, and E. G. Hahn, "Light-induced autofluorescence spectroscopy for the endoscopic detection of esophageal cancer," *Gastrointestinal Endoscopy*, vol. 54, pp. 195–201, 2001.
- [19] D. C. De Veld, M. J. Wities, H. J. Sterenborg, and J. L. Roodenburg, "The status of in vivo autofluorescence spectroscopy and imaging for oral oncology," *Oral Oncol.*, vol. 41, pp. 117–131, 2005.
- [20] A. Menciassi, A. Moglia, S. Gorini, G. Pernorio, C. Stefanini, and P. Dario, "Shape memory alloy clamping devices of a capsule for monitoring tasks in the gastrointestinal tract," *J. Micromech. Microeng.*, vol. 15, pp. 2045–2055, 2005.
- [21] M. Quirini, S. Scapellato, P. Valdastris, A. Menciassi, and P. Dario, "An approach to capsular endoscopy with active motion," in *Proc. IEEE Eng. Med. Biol. Soc. Conf.*, 2007, pp. 2827–2830.
- [22] G. Minas, R. F. Wolfenbuttel, and J. H. Correia, "An array of highly selective Fabry–Perot optical-channels for biological fluid analysis by optical absorption using a white-light source for illumination," *J. Opt. A: Pure Appl. Opt.*, vol. 8, pp. 272–278, 2006.
- [23] N. Uedo, H. Iishi, M. Tatsuta, and T. Yamada, "A novel videoendoscopy system by using autofluorescence and reflectance imaging for diagnosis of esophagogastric cancers," *Gastrointestinal Endoscopy*, vol. 62, pp. 521–528, 2005.
- [24] G. Minas, J. C. Ribeiro, R. F. Wolfenbuttel, and J. H. Correia, "On-chip integrated CMOS optical detection microsystem for spectrophotometric analyses in biological microfluidic systems," in *Proc. IEEE Int. Symp. Ind. Electron.*, Jun. 2005, pp. 1133–1138.



D. S. Ferreira (S'09) received the M.Sc. degree in biomedical Engineering (major in medical electronics) from the University of Minho, Guimarães, Portugal, in 2007, where she has been working toward the Ph.D. degree in the Department of Industrial Electronics, under the MITPortugal Program, since October 2007.

Her research interests include spectroscopy for tissue diagnosis, biomedical microdevices, and optical microsensors.



V. C. Pinto is currently working toward the M.Sc. degree in micro/nano Technologies in the Department of Industrial Electronics, University of Minho, Guimarães, Portugal.

Her research interests include microfabrication techniques for microfluidic devices and thin-film characterization.



J. H. Correia (S'96–M'00) received the B.Sc. degree in physical engineering from the University of Coimbra, Coimbra, Portugal, in 1990, and the Ph.D. degree at the Laboratory for Electronic Instrumentation, Delft University of Technology, The Netherlands, in 1999, working in the field of microsystems for optical spectral analysis.

He is currently a Full Professor in the Department of Industrial Electronics, University of Minho, Guimarães, Portugal. He was the General-Chairman of Eurosensors 2003 and MME 2007, Guimarães.

His research interests include micromachining and microfabrication technology for mixed-mode systems, solid-state integrated sensors, microactuators, and microsystems.



G. Minas (S'96–M'05–SM'11) received the B.Sc. degree in industrial electronics engineering in 1994, the M.Sc. degree in 1998, and the Ph.D. degree in 2004, all from the University of Minho, Guimarães, Portugal.

Her thesis work was in cooperation with the Laboratory for Electronic Instrumentation, Delft University of Technology, Delft, The Netherlands, and dealt with lab on a chips for biological fluids analysis. Between 1995 and 2004, she was a Lecturer, and from 2004 to 2010, an Assistant Professor in the Department of Industrial Electronics, University of Minho, where she has been an Associate Professor since 2010, where she is involved in biomedical microdevices research, in general, and on lab-on-a-chip devices with on-chip integration of electronic circuits, optical filters, sensors, biosensors, and microactuators.